

Energy-selective neutron imaging for materials science

THÈSE N° 6514 (2015)

PRÉSENTÉE LE 16 FÉVRIER 2015

À LA FACULTÉ DES SCIENCES ET TECHNIQUES DE L'INGÉNIEUR
LABORATOIRE DE MÉTALLURGIE MÉCANIQUE
PROGRAMME DOCTORAL EN SCIENCE ET GÉNIE DES MATÉRIAUX

ÉCOLE POLYTECHNIQUE FÉDÉRALE DE LAUSANNE

POUR L'OBTENTION DU GRADE DE DOCTEUR ÈS SCIENCES

PAR

Steven Luc X PEETERMANS

acceptée sur proposition du jury:

Prof. P. Mural, président du jury
Prof. H. Van Swygenhoven, Dr E. H. Lehmann, directeurs de thèse
Prof. M. Stampanoni, rapporteur
Prof. M. Strobl, rapporteur
Prof. W. Treimer, rapporteur



ÉCOLE POLYTECHNIQUE
FÉDÉRALE DE LAUSANNE

Suisse
2015

Knowledge is like a sphere,
The greater its volume,
The larger its contact with the unknown.
— Blaise Pascal

To my parents,
Luc and Betty

Acknowledgements

I would like to thank Dr. Eberhard Lehmann and Prof. Helena Van Swygenhoven for their continuous supervision, guidance and concerns that marked the road leading to this document. Thanks again, Eberhard, for introducing me into the world of neutron imaging and its community, international, high-level and multidisciplinary where I always felt welcome and well-acknowledged.

Naturally I owe my gratitude to the neutron imaging and activation group, every door always open to advice on all possible matters. One door deserves to be mentioned explicitly: thank you Dr. Anders Kaestner, for the scientific brain storms and more base, help with all my computing issues.

I'm also indebted to the materials science and simulation group, its PhD students, post-docs and scientists, current and former, for all interactions on professional and social level (or both in Châtel).

Then there are the hidden stakeholders in this work who should not be forgotten: our group technician Jan Hovind, always ready to make a last minute sample holder and the department secretary Renate Bercher, worth her weight in gold (or gummi bears).

The user support has been very rewarding, people coming up with new problems, stimulating the development and spreading of new methods in neutron imaging - I think of Dr. Francesco Grazzi and Dr. Floriana Salvemini in particular as well as the members of the Center for X-ray Tomography of the Ghent University (UGCT), always up for a barbecue in the dark once the tomography was running.

Of course there were also the persons supporting me during my experiments and analyses. Thank you Dr. Winfried Kockelmann, Dr. Joe Kelleher and Dr. Saurabh Kabra at the Rutherford Appleton Laboratory and Dr. Wolfgang Ludwig at the European Synchrotron Radiation Facility (ESRF).

Finally, this goes without saying, my thoughts drift towards the friends and family, who ceaselessly supported me in this personal and professional endeavour.

Villigen, 21 October 2014

S. P.

Abstract

Neutron imaging is a highly versatile method that allows for non-destructive insight in the three-dimensional materials' distribution of a sample of interest and its change over time. It has been used to tackle problems in numerous fields, virtually separating fossil from surrounding rock, studying water management in running fuel cells, alloy mixing and air entrapments in friction stir welding of two different alloys and numerous others.

Neutron imaging evaluates the exponential attenuation of a neutron beam upon transmission through an object, summarized by the Lambert-Beer law. The detected image contrast varies depending on traversed material thickness and inherent interaction properties described by the cross-section. Recording neutron projections under various sample rotation angles, one can reconstruct the three-dimensional material distribution with computed tomography.

In case of crystalline materials, the periodic ordering of the nuclei into crystal lattices will give rise to coherent elastic scattering or diffraction of a neutron beam only for specific combinations of incident beam energy, angle and crystal lattice spacing.

Traditionally the full polychromatic beam spectrum coming from a spallation or reactor source is used, giving high neutron flux and low image exposure times. However, as a consequence the energy-dependent behaviour - the footprint of the crystallographic sample properties - are averaged out over the beam spectrum. When imaging is performed with the spectrum limited to a short wavelength band, also known as energy-selective imaging, one can investigate the spectral dependence of the cross-section and use it as a new option for tuning the image contrast.

In the time-of-flight approach, a pulse of neutrons is allowed to travel a certain distance and the recorded arrival time is a measure for their speed and thus their energy. Alternatively, dealing with a continuous stream of neutrons of all energies, one can pick out a short wavelength band of interest using a monochromator, discarding all other neutrons. Several types exist, with various levels of final beam monochromaticity. A neutron velocity selector is a rotating drum with twisted lamellae coated with a strong neutron absorber. Depending on its rotation speed, only neutrons of a particular velocity (and thus energy) are transmitted. A double crystal monochromator uses a crystal to diffract a wavelength of interest out of the direct beam into a well-defined direction. A similar, second crystal then diffracts it back in the original beam direction. Developed in different areas of condensed matter research with neutrons, these monochromators have been characterized for use in neutron imaging. The beam divergence, necessary to illuminate a large samples, was also shown to induce variations in beam spectrum

Abstract

across the field-of-view. A hybrid solution of a velocity selector in combination with crystal wavelength bandwidth filters to increase monochromaticity, called *TESI*, was also explored.

Neutron scattering can sometimes stand in the way of accurately determining material content from transmission data. Scattered neutrons might still hit the detector, suggesting increased transmission and leading to an underestimation of the amount of material present. Local variations in crystal properties and thus cross-section moreover can not be discerned from material thickness or density variations in a neutron projection image. Energy-selective imaging at very low energies, where no diffraction can occur anymore, is shown to be a solution.

In case of single crystals, an energy-scan will yield for each pixel a cross-section pattern that is a thumb print of the local crystal orientation and mosaicity. Through comparison with simulated crystal cross-section patterns, this information can be extracted. It can be mapped quantitatively at previously unattainable spatial resolution and speed compared to traditional neutron diffraction methods with pencil beam scanning. Even overlap of a few crystals in the neutron beam projection direction can be handled.

To resolve the cross-section pattern well enough for such method to work, very high energy-resolution is required. It can be reached with time-of-flight, but hardly when using a monochromator. However, one can think of the crystal as monochromator in itself, diffracting out neutrons of particular energies depending on its orientation. It thus provides an easier and faster option for characterization. When the crystal is fully illuminated by the neutron beam, projections of the crystal by the diffracted neutrons are formed. Rotating the sample, projections under various sample angles can again be obtained, from which crystal shape can be reconstructed in 3D. The position of the crystal on the detector is indicative of its orientation. In case of multiple crystallites, diffraction projections have additionally to be grouped depending on their grain of origin, yielding a 3D grain orientation map in the end.

In summary, during this work the infrastructure for energy-selective neutron imaging has been developed and characterized. New methods have been introduced that probe new crystallographic sample properties previously unavailable in neutron imaging, their application illustrated with various examples ranging from meteorites to turbine blades. A bridge has been formed between neutron diffraction and imaging, but more work can still be done to further develop methods, introduce simulations and expand the application range.

Key words: Neutron imaging · neutron tomography · energy-selective · diffraction contrast imaging · topography · monochromator · crystal

Zusammenfassung

Neutronen Imaging ist eine vielseitige Methode, die es erlaubt, zerstörungsfrei Proben und deren 3-dimensionalen, inneren elementaren Aufbau sowie zeitabhängige Prozesse innerhalb einer Probe zu studieren. Die Methode wurde bereits in vielen Forschungsfeldern wie der virtuellen Separierung von Fossilien und umgebendem Gestein oder Legierungsmischungen und Lufteinschlüssen in verschiedensten Schweissnähten erfolgreich eingesetzt.

Wie das Lambert-Beer Gesetz besagt arbeitet das Neutronen Imaging mit der exponentiellen Abschwächung eines Neutronenstrahls beim Durchdringen einer Probe. Der detektierte Kontrast ist dabei abhängig von der durchdrungenen Probendicke und des materialspezifischen Wirkungsquerschnitts. Durch Bilder von verschiedenen Rotationswinkeln einer Probe ist es möglich, eine 3-dimensionale Rekonstruktion der Materialverteilungen innerhalb einer Probe mittels Computertomographie zu erstellen.

In kristallinen Materialien kann ein Neutronenstrahl am periodischen Kristallgitter kohärent gestreut oder diffraktiert werden. Dies ist abhängig von der Energie sowie des Einfallswinkels der Neutronen aber auch der Kristallgitterparameter. Klassisch wird für das Imaging ein polychromatischer Strahl verwendet, um hohen Fluss und niedrige Belichtungszeiten zu ermöglichen. Da aber die Eigenschaften von kristallinen Proben energieabhängig sind, mitteln sich diese bei der Nutzung eines polychromatischen Strahls heraus. Die Nutzung eines schmalen Energiebandes von Neutronen, auch bekannt als energiewerkzeug Imaging, ermöglicht es hingegen, die spektralen Abhängigkeiten von Wirkungsquerschnitten zu untersuchen und eröffnet ein neues Feld, um unter anderem den Kontrast zu verbessern.

Der „time-of-flight“-Ansatz nutzt die unterschiedlichen Geschwindigkeiten der Neutronen mit verschiedenen Energien, indem nur zu einer bestimmten Zeit gemessen wird, nach welcher nur bestimmte Neutronen (mit bestimmten Energien) den Detektor erreichen. Alternativ kann ein Energieband aus einem kontinuierlichen Neutronenstrahl geschnitten werden, indem man einen Monochromator benutzt. Hier gibt es verschiedenste Möglichkeiten mit verschiedensten Energiebandbreiten. Ein Geschwindigkeitsselektor ist eine rotierende Trommel mit gebogenen, absorbierenden Lamellen, welche frequenzabhängig nur Neutronen einer bestimmten Geschwindigkeit (Energie) passieren lassen. Ein Doppelkristall-monochromator nutzt die Reflexion einer bestimmten Wellenlänge durch einen ersten Kristall aus dem polychromatischen Strahl und einer zweiten Reflexion zurück in die ursprüngliche Strahlrichtung. Beide Arten von Monochromatoren sind für den Gebrauch beim Neutronen Imaging charakterisiert worden. Die für die Belichtung von grossen Proben nötige Strahldivergenz und

deren Einfluss auf Variationen im Energiespektrum des Strahls wurde ebenfalls untersucht. Die Kombination eines Geschwindigkeitsselektors und eines Kristallfilters, hier TESI genannt, wurde ebenfalls erforscht.

Neutronenstreuprozesse können die quantitative Auswertung von Transmissionsdaten erschweren. Gestreute Neutronen können immer noch den Detektor, allerdings an einer anderen Stelle (Pixel) treffen, was zu einer höheren Intensität und einer Unterschätzung der Materialdicke führen kann. Des Weiteren kann im der Projektion nicht mehr zwischen sich ändernden Kristalleigenschaften (Wirkungsquerschnitten) und lokalen Dicke- oder Dichtevariationen unterschieden werden. Energieselektives Imaging bei niedrigen Energien, bei denen keine Diffraktion mehr auftritt, kann hier als Lösungsansatz dienen.

Im Falle eines Einkristalls liefert ein Energiescan ein genaues Muster von Wirkungsquerschnitten in jedem Pixel, was einen exakten Fingerabdruck der lokalen Kristallorientierung und Mosaikstruktur darstellt der durch den Vergleich mit simulierten Kristallwirkungsquerschnitten gewonnen werden kann. Diese Information kann qualitativ mit einer bisher nicht möglichen räumlichen Auflösung und Geschwindigkeit abgebildet werden im Vergleich zum traditionellen Rastern von diffraktiven Neutronentechniken. Sogar der Überlapp von mehreren Kristallen in Strahlrichtung kann akzeptiert und ausgewertet werden.

Um in der Lage zu sein, das Muster der Wirkungsquerschnitte auflösen zu können ist eine äusserst hohe Energieauflösung nötig, welche durch die Nutzung des „time-of-flight“ Ansatzes erreicht werden kann. Die Energieauflösung der anderen vorgestellten Methoden hingegen ist dafür nicht ausreichend. Ein weiterer Ansatz ist es, den Kristall selber als Monochromator nutzen. Dieser diffraktiert bestimmte Wellenlängen, abhängig von seiner Orientierung, aus dem Neutronenstrahl. Dies ermöglicht eine schnellere und einfachere Charakterisierung. Ist der Kristall voll Belichtet, so entstehen Abbildungen des Kristalls aus diffraktierten Neutronen. Wird der Kristall nun rotiert, kann aus verschiedenen Winkeln eine 3-dimensionale Rekonstruktion des Kristalls allein aus den diffraktierten Neutronen erfolgen. Im Falle von mehreren Kristalliten müssen die verschiedenen Projektionen abhängig von ihrem Ursprung gruppiert werden, um eine 3-dimensionale Kornorientierungskarte zu generieren.

Abschliessend ist festzuhalten, dass durch diese Arbeit die Infrastruktur für Energieselektives Imaging entwickelt und realisiert wurde. Neue, vorher unbekannte, Methoden, welche die Möglichkeit eröffnen Kristalleigenschaften untersuchen zu können wurden eingeführt und an verschiedenen Proben wie Meteoriten und Turbinenschaufeln demonstriert und etabliert. Eine Brücke zwischen Diffraktion und Imaging könnte gebaut werden, auch wenn es weiterhin viele Möglichkeiten der Verbesserung und Weiterentwicklung gibt. Besonders im Bereich der Simulationen und der Anwendungsbeispiele ist hier weiterhin ein grosses Potential vorhanden.

Stichwörter: Neutron imaging · Neutrontomographie · Energieselektiv · Diffraktion · Topographie · Monochromator · Kristall

Contents

Acknowledgements	i
Abstract (English/Deutsch)	iii
List of symbols	xi
Glossary	xiii
Prelude	1
1 Neutron imaging	3
1.1 Neutron sources	3
1.1.1 Fission - Research reactors	3
1.1.2 Spallation	5
1.1.3 Other sources of free neutrons	7
1.2 Digital radiography	8
1.3 Why neutrons?	10
1.4 Computed tomography	11
1.4.1 Direct, analytical method: Filtered backprojection	11
1.4.2 Algebraic reconstruction techniques	12
1.5 Imaging beamline layout	14
1.6 Imaging detector systems	17
1.6.1 Film and imaging plates	17
1.6.2 Scintillator based systems	18
1.6.3 Microchannel plate detectors	19
1.7 The need for energy-selective neutron imaging	20
2 Neutron interaction with matter	21
2.1 Cross-sections	21
2.2 Interaction with a single nucleus	22
2.2.1 Absorption	22
2.2.2 Scattering	24
2.3 Scattering from a rigid array of nuclei	26
2.4 Scattering from a rigid crystal lattice	29
2.4.1 Describing a crystal lattice	29

Contents

2.4.2	Single crystal cross-section	30
2.4.3	Powder cross-section	33
2.5	Scattering from a crystal lattice with thermal motion	34
2.5.1	Phonons and the Debye model	34
2.5.2	Elastic scattering cross-section	35
2.5.3	Inelastic scattering cross-section	37
2.6	Application to neutron imaging	38
3	Energy-resolving capability for neutron imaging	41
3.1	Time of flight	41
3.2	Filters	42
3.3	Mechanical neutron velocity selector	43
3.3.1	Principle	43
3.3.2	Experiments	44
3.3.3	Device description	45
3.3.4	Results and discussion	47
3.3.5	The velocity selector at ANTARES	50
3.3.6	Conclusion	51
3.4	Double Crystal Monochromator	52
3.4.1	Device description	52
3.4.2	Spatial variation of the spectrum across the field of view	53
3.4.3	Higher order contamination of the spectrum	54
3.5	TESI - a Transmission based monochromator for Energy-Selective Imaging	56
3.5.1	Principle	56
3.5.2	Design	57
3.5.3	Calibration	58
3.5.4	Imaging characteristics	59
3.6	Discussion and conclusion: energy-selective imaging at pulsed or continuous sources?	61
4	Quantification by energy-selective neutron imaging	65
4.1	The trouble with quantification	65
4.2	Existing quantification strategies	67
4.3	Principle of energy-selective imaging past the Bragg cut-off	68
4.3.1	Proof of principle: radiography of an iron step wedge	69
4.3.2	Proof of principle: tomography of a step cylinder	71
4.3.3	Discussion and outlook	72
4.4	Application 1: Historical copper alloy composition	73
4.4.1	Problem setting	73
4.4.2	Experimental set-up	74
4.4.3	Evaluation strategy	75
4.4.4	Results and discussion	76
4.4.5	Conclusion	79

4.5	Application 2: Integrity of copper discs for SwissFel C-band cavity production .	79
4.5.1	Problem setting	79
4.5.2	Initial examination at NEUTRA	80
4.5.3	Energy-selective neutron imaging at BOA	80
4.5.4	Conclusion	81
4.6	Summary	81
5	Energy-selective neutron imaging of crystals	83
5.1	Quantitative analysis of a single crystal wavelength scan	83
5.1.1	Experiment	83
5.1.2	Evaluation strategy	84
5.1.3	Considerations for tomographic extension	91
5.2	Monochromatic imaging of oligocrystals	92
5.3	Application 1: monochromator crystals for CAMEA	93
5.3.1	Introduction	93
5.3.2	Experiment	94
5.3.3	Results and discussion	95
5.3.4	Conclusion	96
5.4	Application 2: morphological and phase analysis of iron-nickel meteorites . . .	96
5.4.1	Introduction	96
5.4.2	Materials and experimental set-up	97
5.4.3	Principle	98
5.4.4	Results and discussion	99
5.4.5	Conclusion	103
6	Neutron diffraction contrast imaging	105
6.1	Motivation	105
6.2	A double detector set-up for neutron diffraction contrast imaging	107
6.3	Neutron diffraction contrast radiography	109
6.3.1	Introduction	109
6.3.2	Experiment	110
6.3.3	Results and discussion	110
6.3.4	Conclusion	114
6.4	Neutron diffraction contrast tomography of a single crystal	115
6.4.1	Experiment	115
6.4.2	Method	116
6.4.3	Results and discussion	118
6.5	Neutron diffraction contrast tomography of a polycrystal	121
6.5.1	Introduction	121
6.5.2	Properties of a cold neutron imaging beam for DCT	122
6.5.3	Experiment	125
6.5.4	Data processing	125
6.5.5	Results and discussion	126

Contents

6.6 Summary	130
7 Epilogue	131
7.1 Summary	131
7.2 Transmission or diffraction? Continuous or pulsed?	132
7.3 Outlook	135
A Total macroscopic cross sections	137
B Matrix elements in simulating the Laue pattern	139
Bibliography	141
Index	155
Curriculum Vitae	157

List of Symbols

α	Tilt angle of the velocity selector blades
$\mathbf{a}_1, \mathbf{a}_2, \mathbf{a}_3$	Base vectors of the crystal unit cell
b	Scattering length
d	Sample thickness <i>or</i> Crystal lattice plane spacing
ϵ	Efficiency
E	Energy
eV	electronVolt ($1 \text{ eV} = 1.602 \times 10^{-19} \text{ J}$)
f	Scattering amplitude
F	Structure factor
Γ	Resonance width
γ	Gamma particle <i>or</i> tilt between the velocity selector axis and neutron beam direction
h	Planck's constant ($6.626 \times 10^{-34} \text{ Js}$)
I_0	incident neutron beam intensity
I	Beam intensity (attenuated) <i>or</i> the Quantum number for the nuclear spin (chapter 2)
k_B	Boltzmann constant ($1.38 \times 10^{-23} \text{ J/K}$)
\mathbf{k}	Wave vector
$\boldsymbol{\kappa}$	Scattering vector
λ	Wavelength
L	Length, e.g. Source to detector distance <i>or</i> Velocity selector drum length
ℓ	Quantum number of the angular momentum
M	Molar mass
N_A	Avogadro's constant (6.022×10^{23} particles per mole)
\mathbf{n}	Normal vector
ρ	Mass density
s	Spectrum
Ω	Solid angle
ω	Angular frequency
θ	Angle, usually the Bragg angle
θ_D	Debye temperature
\mathbf{r}	Position of the nucleus
R	Velocity selector radius
σ	Microscopic cross-section
Σ	Macroscopic cross-section

List of Symbols

S_{fg}	Similarity between two functions f and g
T	Transmission
t	time
τ	Reciprocal lattice vector
v	Velocity
V	Nuclear potential
ψ	Wave function of the neutron

Glossary

BCC Body Centered Cubic.

CT Computed Tomography.

DAXM Differential Aperture X-ray Microscopy.

DC Dark Current.

DCM Double Crystal Monochromator.

DCT Diffraction Contrast Tomography.

ESRF European Synchrotron Radiation Facility.

FCC Face Centered Cubic.

FOV Field Of View.

FWHM Full Width at Half Maximum.

IFW Leibnitz Institut für Festkörper- und Werkstofforschung.

MCP Microchannel Plate.

MVS Mechanical Neutron Velocity Selector.

nDCT neutron Diffraction Contrast Tomography.

NDT Non-destructive Testing.

NRMSE Normalized Root Mean Square Error.

PG Pyrolytic Graphite.

SANS Small Angle Neutron Scattering.

Glossary

SNR Signal to Noise Ratio.

TESI Transmission based Energy-Selective Imaging.

TOF Time-of-Flight.

UGCT Center for X-ray Tomography of the Ghent University.

XRF X-ray Fluorescence.

Prelude

When a neutron beam passes through a material, it is attenuated depending on the material type and thickness it encounters along its path. When fully illuminating the object of interest in a parallel neutron beam, one can thus capture a shadow image or *radiograph* to study the spatial variation in sample property: one performs neutron imaging. Recording a series of digital radiographs whilst rotating the sample, one can reconstruct the three-dimensional material distribution and make a *computed tomography*. Moreover, neutron imaging is a non-destructive testing (NDT) method, lending itself perfectly for in-situ studies and investigations of unique and priceless objects.

Neutron imaging is nowadays routinely applied at large scale facilities world wide and has solved problems in numerous fields ranging from e.g. water formation and transport in operating fuel cells, to virtually separating fossils from the rock they are embedded in. It is a rapidly evolving field, with new developments continuously being made. Neutron grating interferometry allows access to phase shift and beam decoherence in a material, fast stroboscopic imaging for cyclic processes, polarized neutron imaging is sensitive to magnetic fields. In this work, the imaging method suite is now further expanded with energy-selective neutron imaging to study spatial variation in crystallographic material properties.

The basics of standard neutron imaging are described in **chapter one**. It serves as a foundation later on expanded in infrastructure and analysis for energy-selective neutron imaging. The general features such as neutron sources, typical beamline layout, detection systems, image formation process and tomographic reconstruction methods are discussed. The probability of interaction is however dependent on the energy of the incident neutrons, a feature averaged out in standard polychromatic neutron imaging.

It is the goal of this thesis, to investigate the energy-dependent material response and develop new tools and methods to unlock the mapping of linked crystallographic sample properties to neutron imaging.

In **chapter two**, the energy-dependence of the cross-section which describes the neutron interaction in matter is investigated in more detail. Given combinations of crystal orientation and incident neutron wavelength, dictated by Bragg's law, will give rise to diffraction of neutrons out of the direct beam. Monochromatic neutron imaging can thus access spatial variation in crystallographic properties.

How to obtain energy-resolving capability in neutron imaging is the subject of **chapter three**. At pulsed sources, one can use the time of flight method, where one records the neutron arrival time after the pulse which is representative of its velocity and thus energy. At continuous sources, one has to use a monochromator to select a small band out of the generated energy continuum. As this work was carried out at the SINQ continuous neutron source operated at the Paul Scherrer Institut (CH), focus is on the later. Different monochromator types were investigated and their performance towards energy-selective neutron imaging characterized.

We then have all the theoretical and experimental background to deal with new applications of energy-selective imaging, little explored so far and for the first time investigated in this work. The first one deals with a quantification problem in neutron imaging: some of the neutrons scattered in the sample will still hit the detector. Such contributions lead to erroneous conclusions on material content as tabulated or calculated reference cross sections assume all scattered neutrons removed from the direct beam. However, for many engineering materials, scattering contributions can be experimentally suppressed by energy-selective imaging in their so-called absorption range. This is the subject of **chapter four**.

Many engineering materials are polycrystalline in practice. In the case of energy-selective imaging of samples with few crystallites much larger than the detector resolution, the subject of **chapter five**, spatial variation in intensity will be observed across the sample between those grains oriented as such that they fulfill Bragg's law, and those that do not. Such grain mapping was first performed qualitatively with a broad energy-range. Subsequent work under time-of-flight conditions with high energy resolution allowed for more quantitative spatial mapping of such properties as crystallite orientation, mosaicity,...

However, the required energy resolution is higher than achievable with monochromators at continuous sources. Alternatively, one can think of the crystal(lite) as a monochromator in itself, diffracting neutrons out of the direct beam. In capturing these diffracted neutrons, one obtains projections of the crystallites responsible. These too can be reconstructed, yielding a three-dimensional mapping of crystallites' shape and orientation. This neutron diffraction contrast tomography (nDCT) is discussed in **chapter six**.

To conclude this work, a critical evaluation and applicability of the developed methods is undertaken in light of the new time-of-flight imaging beamlines currently under construction or given the go-ahead.

1 Neutron imaging

In this chapter the basics of neutron imaging are introduced. First, the production of neutrons through fission and spallation is discussed. The neutron beam is attenuated according to the Beer-Lambert law when traversing a sample. This is exploited to obtain sample information in 2D (radiography) or 3D (tomography). The two main tomographic reconstruction algorithm classes, filtered backprojection and algebraic reconstruction techniques, are discussed. The required experimental infrastructure for a successful imaging instrument able to conduct such experiments is then covered. Finally, the opportunities for going beyond standard neutron imaging and motivation for this work are announced.

1.1 Neutron sources

1.1.1 Fission - Research reactors

The most widespread man made source of neutrons is the neutron induced fission reactor. Heavy nuclei are bombarded with neutrons, breaking up into lighter fission fragments and releasing tremendous amounts of energy. Fissile materials such as ^{235}U and ^{239}Pu have a high probability of breaking apart after capture of a slow thermal neutron, having an energy of 25 meV. In case of ^{235}U a highly excited ^{236}U is formed, which generally splits up immediately into two fission products of masses centered around 95 amu and 135 amu, two to three free neutrons and prompt gamma rays. About 200 MeV of energy is released in the process¹, most of which is carried away as kinetic energy of the fission products and converted into heat upon their collision with the surrounding material. Some of these fission products are highly radioactive and slowly decaying, causing a nuclear waste problem. The released neutrons have a mean kinetic energy of around 2 MeV. However, the probability for such a fast neutron to induce a new fission reaction is very low compared to a thermal neutron. The fissile material is therefore surrounded by a moderator, usually water, heavy water or graphite. When fast neutrons collide with the moderator nuclei, they transfer a large fraction of their energy into the recoil of the latter. After several collisions, the neutron energy spectrum features a Maxwellian distribution around the moderator temperature, i.e. they are thermalized and will induce new fission reactions. Carefully balancing neutron generation through fission and neutron losses (absorption, neutrons leaving the reactor geometry) one obtains a sustainable

¹The energy stored in chemical bonds as a reference, is in the order of a few eV, i.e. a million times lower.

chain reaction (figure 1.1). The initial neutrons for starting up the chain reaction in a reactor loaded with new fuel elements are provided by an external radioactive source that can be brought into the core [1] (see also section 1.1.3).

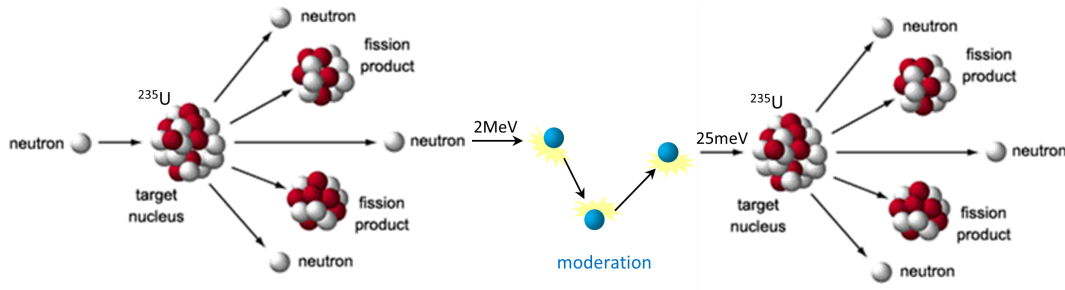
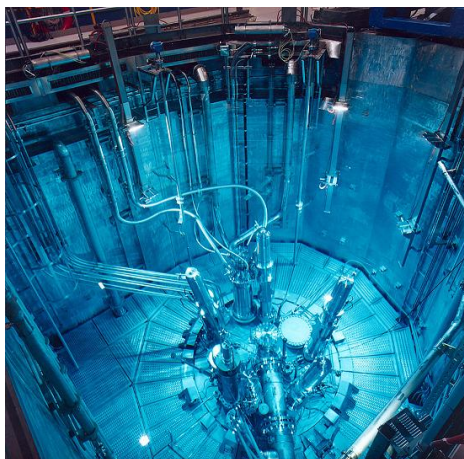


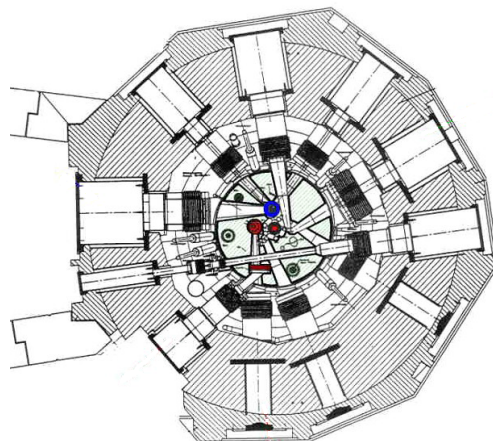
Figure 1.1: Schematic overview of a sustainable neutron induced fission reaction (edited from [2]).

The design of fission reactors is optimized for either heat production as in nuclear power plants or neutron yield in research reactors for scientific usages such as neutron imaging. An example is the FRM II research reactor operated by the *Technische Universität München* in Germany (figure 1.2). It features a 93% enriched ^{235}U fuel element, moderated by a surrounding heavy water tank and the whole placed in a water pool for cooling and shielding. Several secondary sources are present to change the final neutron energy spectrum supplied to different beamlines. Of relevance to neutron imaging is a 20 l tank of liquid D_2 at 25 K, further moderating the neutrons to energies around 5 meV. The beam ports are typically placed close to the core for the highest neutron flux intake, but tangential to it to avoid high gamma radiation background.

Other operational world class imaging beamlines at reactor sources include CONRAD II at the BER II reactor in Berlin (Germany), CG-1D at the HFIR reactor in Oak Ridge (USA) and DINGO at OPAL in Sydney (Australia).



(a)



(b)

Figure 1.2: View into the reactor pool (a) and layout (b) of the FRM II research reactor [3, 4].

1.1.2 Spallation

Another way of releasing neutrons from nuclei is by spallation reactions. When a heavy nucleus is hit by a high energy proton beam of several hundreds of MeV, neutron emission takes place by intra-nuclear cascade followed by de-excitation. A 1 GeV proton has a corresponding de Broglie wavelength of 0.1 fm. As such, it does not 'see' the target nucleus as a whole, but rather the individual nucleons that it consists of. In a direct reaction, it will transfer its incidence energy in a cascade of elastic nucleon-nucleon collisions. Nucleons (e.g. neutrons) that obtain high enough energy can escape from the nucleus. Lighter hadrons such as pions are produced as well. The rest of the energy is distributed equally between the remaining nucleons and a highly excited nucleus remains. In a second stage this nucleus de-excites, mainly by neutron evaporation and also some emission of light charged particles (protons, deuterons, α particles). Alternatively, the excited nucleus can split up into two fission fragments of similar mass which in turn can undergo neutron evaporation. The de-excited nucleus is usually radioactive and will decay until a stable end state is reached. The whole process is illustrated schematically in figure 1.3.

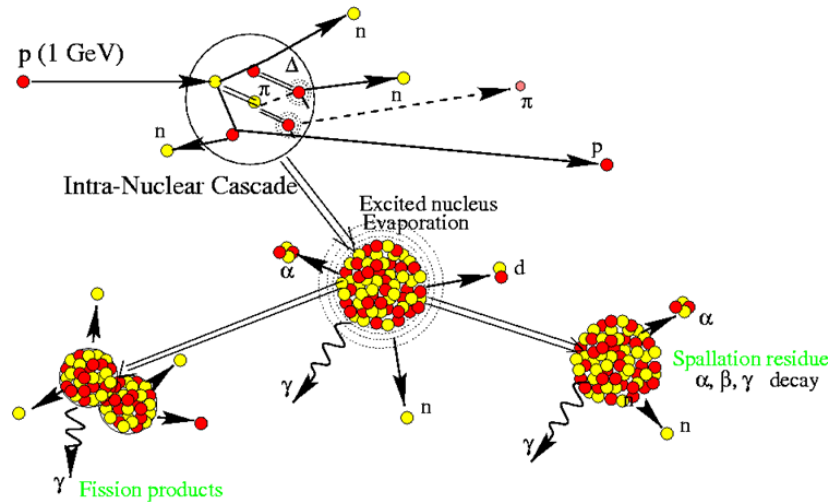


Figure 1.3: Schematic overview of a spallation reaction: intra-nuclear cascade followed by de-excitation through fission or neutron evaporation and final radioactive decay until a stable state is reached [5].

The total number of neutrons produced per incident particle, the neutron multiplicity, is roughly linear with the target's mass number (and thus the number of present nucleons) and slowly increases with the incident proton energy [6], illustrated in figure 1.4. The final neutron energy spectrum contains all energies up to the incident proton beam one. A moderator can be present to shift the spectrum towards thermal and cold neutron energies depending on the application.

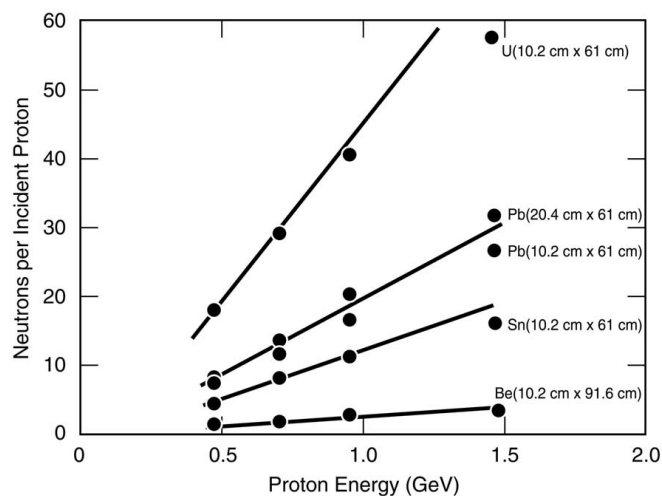


Figure 1.4: Neutron yield as a function of incident proton beam energy for various target materials [7].

The Paul Scherrer Institut in Switzerland, where most of this work was carried out, is home of the SINQ spallation neutron source [8]. A quasi continuous neutron beam is produced by a 570 MeV, 1.5mA proton beam impacting on a lead spallation target at 51 MHz repetition rate. The neutron yield lies around 10 neutrons/proton according to figure 1.4. Moderation and cooling is provided by the enclosing heavy water tank. These thermal neutrons are used to feed the NEUTRA imaging beam line. A smaller tank of liquid D_2 is also present to additionally generate cold neutrons (figure 1.5).

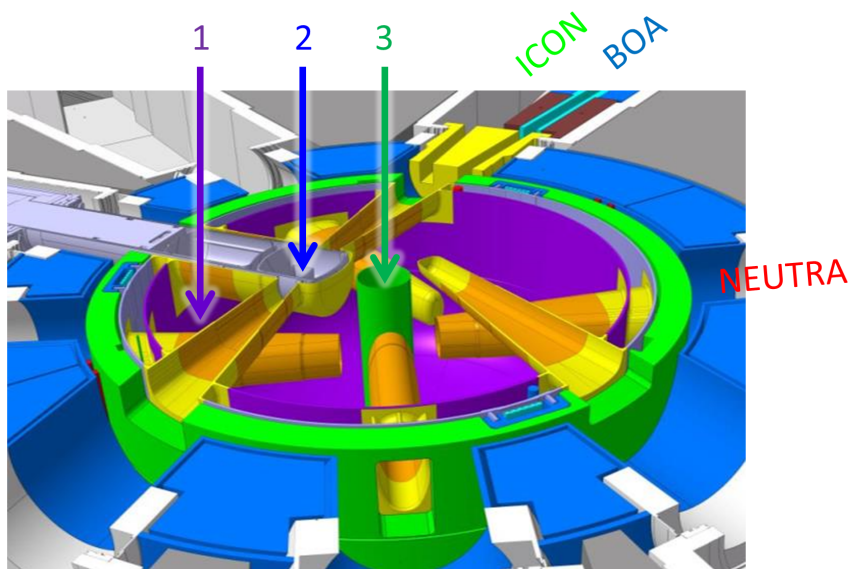


Figure 1.5: Layout of the SINQ spallation neutron source with label 1 pointing out the thermal moderator, 2 the cold source, 3 the spallation target.

This is what the beam port of the ICON beam line for Imaging with COLD Neutrons looks

onto, featuring a resultant colder spectrum than NEUTRA. The BOA beamline for neutron Optics and other Applications, including imaging, looks indirectly at the cold source through a neutron bender which effectively cuts off any thermal component in the beam spectrum. The spectrum of these beamlines for imaging are shown in figure 1.6.

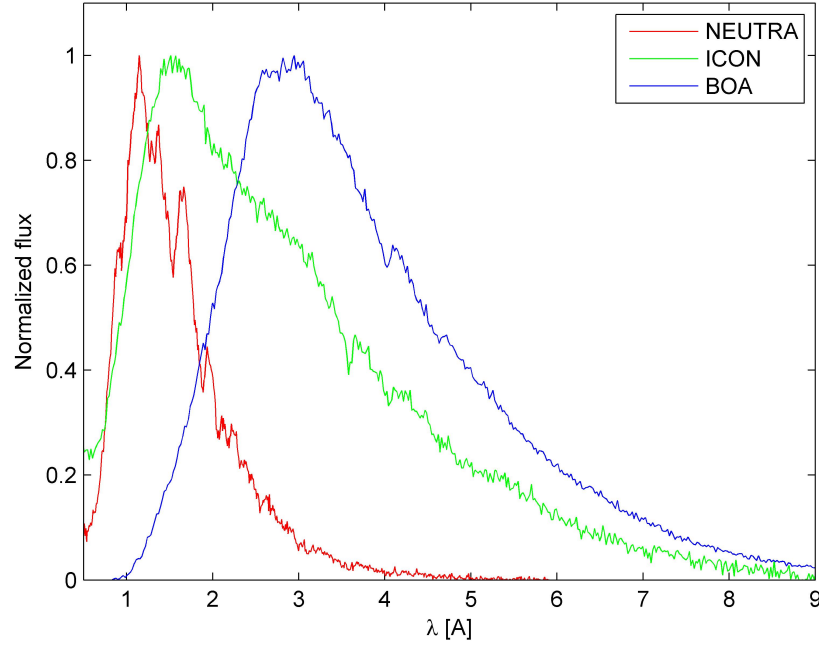


Figure 1.6: Neutron spectrum at the different imaging beamlines present at SINQ, normalized to their peak intensity: NEUTRA (thermal), ICON (cold with a thermal component) and BOA (cold).

Several new imaging instruments at other spallation neutron sources are currently scheduled or under construction: RADEN (formerly known as ERNIS) at JPARC (Japan), IMAT at ISIS (UK), VENUS at SNS (USA) and ODIN at the ESS (Sweden). However, these are all pulsed sources with high energy-resolving capability through time of flight (see chapter 3).

1.1.3 Other sources of free neutrons

There are several other methods to produce free neutrons, though in practice they are rarely used for neutron imaging purposes due to their low neutron flux.

One can make use of radioactive sources [9] such as ^{252}Cf , with a half life for neutron decay of 85.5 years. Alternatively, one can create neutrons via a two-step process as in an $^{241}\text{Am}/^9\text{Be}$ source. The Americium decays by emitting an alpha particle, which is captured by the Beryllium and stabilization occurs through neutron emission. When Chadwick discovered the neutron in 1932, he did it using a combination of Polonium as an α emitter and Beryllium [10]. Alternatively, $^{124}\text{Sb}/^9\text{Be}$ can be used as a (γ, n) neutron source. Fast neutrons are always the result and further moderation is required.

Instead of a proton accelerator and spallation target, a more compact and technologically simpler method is to have an electron beam of several tens of MeV impact on a heavy metal target. Brehmsstrahlung is produced of all energies up to the electron beam energy. These high energy photons in turn can be used to produce neutrons through (γ, n) reactions. An example is the 45 MeV electron linac of the Hokkaido university, with lead target and liquid H_2 moderator. It is used for pulsed neutron imaging, though the flux at the sample position is only on the order of 10^3 n/s/cm²/kW [11].

1.2 Digital radiography

When a neutron beam of intensity I passes through an infinitely thin slab of material, thickness dx , it will be attenuated along the way. The intensity reduction dI will be proportionate to the incident intensity and the thickness. Denoting the proportionality constant Σ , the process can be written as a simple differential equation:

$$dI = -\Sigma I dx \quad (1.1)$$

$$\frac{dI}{dx} = -\Sigma I \quad (1.2)$$

Solving it for a macroscopic sample of thickness d and incident neutron beam intensity I_0 , we obtain the well known Lambert-Beer law

$$I = I_0 e^{-\Sigma d} \quad (1.3)$$

The parameter Σ represents the interaction probability of the beam with the material that leads to its attenuation. For neutrons, it is called the macroscopic cross-section. It is often decomposed into the nuclei density N and a microscopic cross-section σ , which is then a property of the nucleus: $\Sigma = N\sigma$. The density of nuclei can be estimated using the material's mass density ρ , the molar mass M and Avogadro's constant $N_A = 6.022 \times 10^{23}$ particles/mole:

$$\Sigma = N\sigma = \frac{\rho N_A}{M} \sigma \quad (1.4)$$

When using a large neutron beam that covers the entire sample, in combination with a two dimensional detector, one can apply the Lambert-Beer law to each neutron ray through the sample hitting a detector pixel at coordinate (x, y) . A neutron image or radiograph is thus obtained.

The transmission image $T(x, y)$ is found as the ratio (taken pixelwise) of the image with sample $I(x, y)$ and without $I_0(x, y)$, the latter also known as the flat field or open beam image. As such non-uniformities in intensity across the field of view (due to incident beam intensity profile, scintillator texture, lens aberrations, etc.) is eliminated. A dose normalization takes care of the small temporal fluctuations in source intensity between the images inevitably taken at different times. This is as simple as normalizing both images based on the intensity level in a region D outside of the sample. A correction is also made for the Dark Current (DC), an offset in the intensity levels due to the detector electronics:

$$\begin{aligned} I' &= I - DC \\ I'_0 &= I_0 - DC, \end{aligned}$$

so

$$T(x, y) = \frac{I'(x, y)}{I'_0(x, y)}, \quad (1.5)$$

with I'_0 the open beam image normalized to the sample image dose².

$$I'_0(x, y) = I'_0(x, y) * \frac{\iint_D I'(x, y) dx dy}{\iint_D I'_0(x, y) dx dy}. \quad (1.6)$$

The procedure is illustrated schematically in figure 1.7.

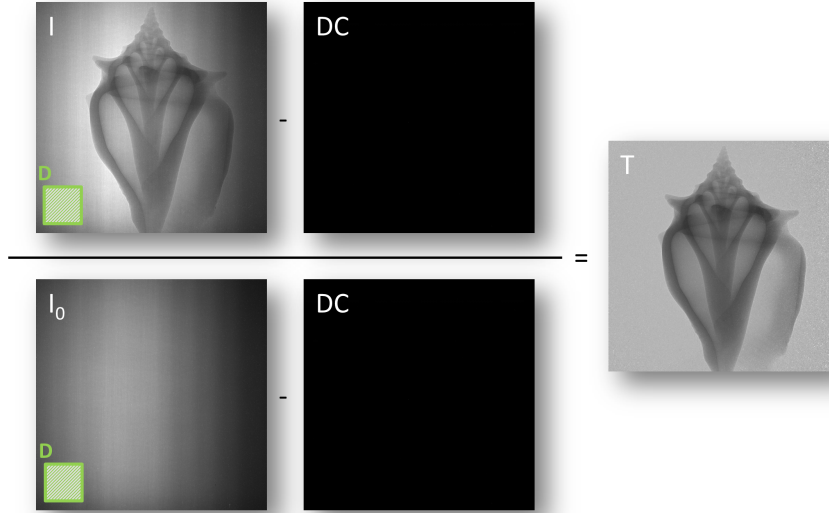


Figure 1.7: Taking the ratio of the image with and without sample - dose normalized based on a region D and dark current offset DC corrected - yields the transmission image T .

Neutron radiography thus allows to investigate the spatial variation in sample thickness if the material (macroscopic cross-section) is known

$$d(x, y) = -\frac{1}{\Sigma(x, y)} \ln T(x, y) \quad (1.7)$$

or material distribution if the thickness is known

$$\Sigma(x, y) = -\frac{1}{d(x, y)} \ln T(x, y). \quad (1.8)$$

²One can equivalently work with the sample image normalized to the open beam dose.

1.3 Why neutrons?

The Lambert-Beer law also holds for other types of penetrating radiation. In case an X-ray beam is used, it is more common to speak of an attenuation coefficient μ instead of a cross-section Σ . Though similar in principle, it is highly complementary in practice due to the different interaction mechanisms involved. X-rays interact with the electrons in each atom, thus the attenuation coefficient increases with the atomic number. Neutrons on the other hand carry no charge, they do not 'see' the electrons and interact mainly with the atomic nucleus³, showing a much more capricious trend. This is illustrated for a selected number of elements in figure 1.8, a comprehensive table of macroscopic cross-sections and attenuation coefficients for all elements can be found in appendix A. Compared to X-rays, some light elements (e.g. hydrogen) interact much more strongly with neutrons, translating in an increased sensitivity to small amounts (e.g. water management in fuel cells [12]). Metals on the other hand interact less with a neutron beam and larger samples can be probed.

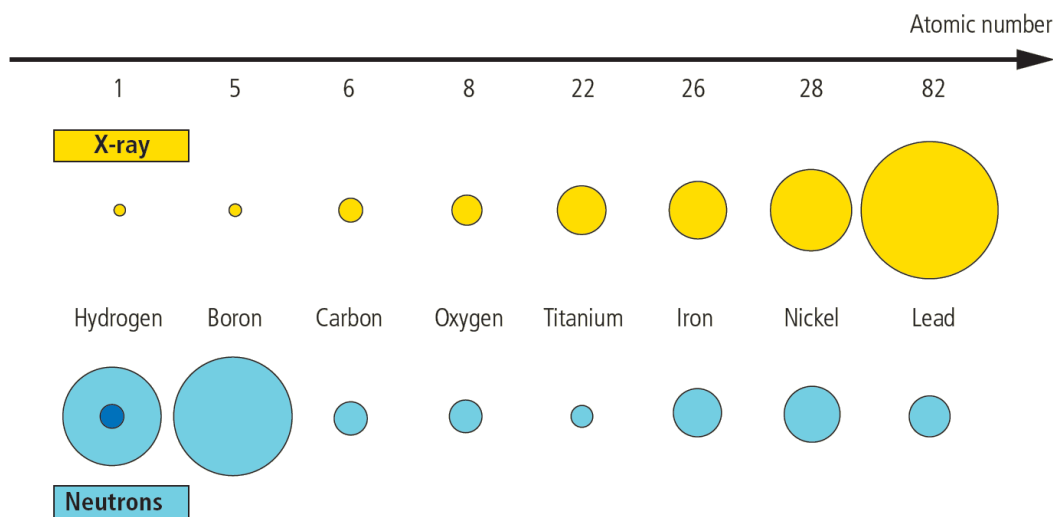


Figure 1.8: Interaction probabilities of selected materials with X-rays and neutrons, depicted schematically by a difference in disk area [13].

An example of the complementarity in attenuation contrast is demonstrated in figure 1.9 showing the radiograph of a computer hard disk using the different types of radiation. Whereas the X-ray image features high attenuation for the metallic conductors, the neutron beam is mainly attenuated by the plastic microchip housings and printed circuit board resin - both hydrogenous substances.

³They do however possess a magnetic moment, which leads to some interaction with the electronic shell. However, it is of no relevance to the topics investigated in this work and shall not be considered further.

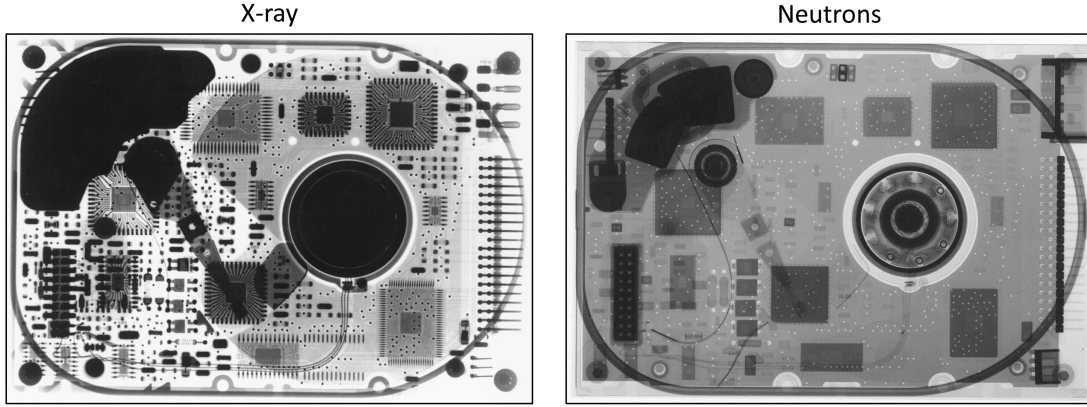


Figure 1.9: Radiographs of a computer hard disk, made using X-rays (left) and neutrons (right).

1.4 Computed tomography

Tomography aims to retrieve the three-dimensional distribution of the cross-sections in the sample based on projections taken at different angular views of the sample. Several reconstruction strategies exist.

1.4.1 Direct, analytical method: Filtered backprojection

Consider the recorded projection data of a slice through the sample. From the Beer-Lambert law (eq. 1.3), the negative natural logarithm of the recorded transmission profile is the integral of the macroscopic cross-section along a set of parallel lines through the sample onto the detector. Mathematically, the *Radon transform* describes the formation of the parallel projection P of an object function - in our case the macroscopic cross-section - under an angle θ :

$$P_{\theta}(t) = \int_{-\infty}^{\infty} \int_{-\infty}^{\infty} \Sigma(x, y) \delta(x \cos \theta + y \sin \theta - t) dx dy, \quad (1.9)$$

with (x, y) coordinates in the slice plane and t the coordinate of the projection. It can be shown [14] that the one-dimensional Fourier transform of this profile

$$S_{\theta}(w) = \int_{-\infty}^{\infty} P_{\theta}(t) e^{-j2\pi wt} dt \quad (1.10)$$

equals the profile along a line at angle θ of the *two dimensional* Fourier transform of our object function

$$S(u, v) = \int_{-\infty}^{\infty} \int_{-\infty}^{\infty} \Sigma(x, y) e^{-j2\pi(ux+vy)} dx dy. \quad (1.11)$$

This is known as the *Fourier slice theorem*, it is a cornerstone of the reconstruction algorithm and is illustrated in figure 1.10. Performing this step for all sample projection angles θ , one completely fills up two-dimensional Fourier space. One is then left with taking the inverse 2D Fourier transform to end up with the distribution of the macroscopic cross-section $\Sigma(x, y)$ in real space.

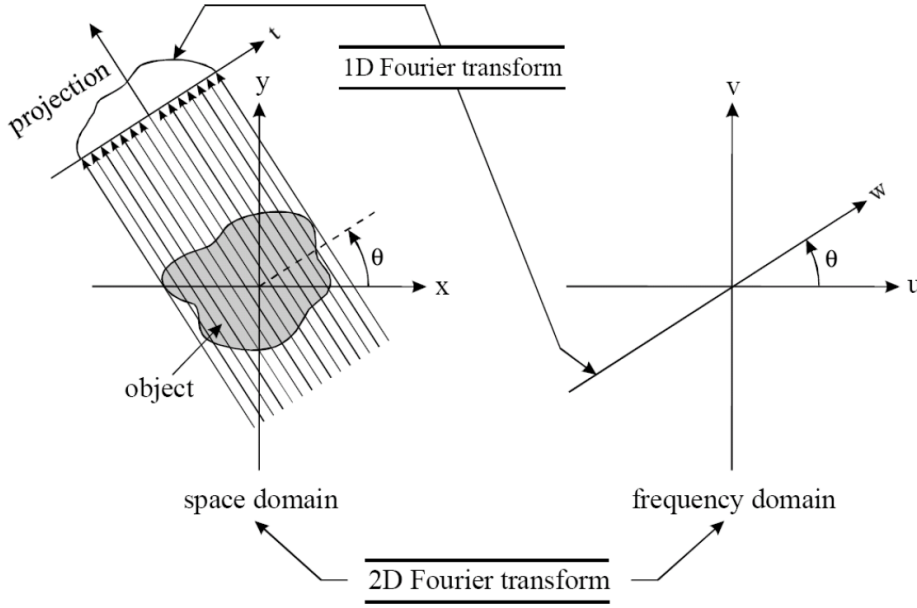


Figure 1.10: Illustration of the Fourier slice theorem (taken from [15]).

The practical implementation of the reconstruction procedure is known as the filtered back-projection algorithm. After rewriting and combining the Fourier slice theorem and two dimensional Fourier transform [14], the unknown cross-section distribution is found as

$$\Sigma(x, y) = \int_0^\pi Q_\theta(t) d\theta, \quad (1.12)$$

with

$$Q_\theta(t) = \int_{-\infty}^{\infty} S_\theta(w) |w| e^{2\pi j w t} dw. \quad (1.13)$$

Equation 1.13 represents a *filtering* of the projection data P_θ in the frequency domain: $S_\theta(w)$ is modulated by the ramp filter $|w|$. The filtered profiles at all angles θ are subsequently *backprojected* and added (equation 1.12). Implemented using the fast Fourier transform, this direct method for reconstructing the cross-section is very fast, a typical dataset being reconstructed in the order of minutes. A schematic illustration is given in figure 1.11.

1.4.2 Algebraic reconstruction techniques

A completely different approach is to write out the image formation process as a series of algebraic equations, going from a series of unknowns (the cross-sections throughout the sample) to given projection data. The main advantage compared to direct analytical methods lies in their superior performance when dealing with a limited number of projections or non-equiangular spaced ones [16] and the ability to include more physics into the reconstruction (e.g. imposing that the cross-section can not be negative).

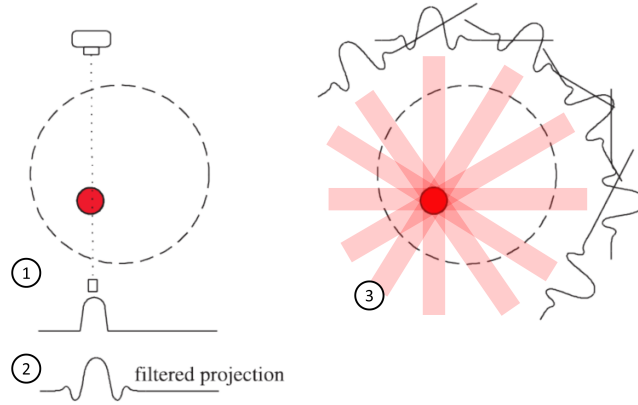


Figure 1.11: The filtered backprojection reconstruction algorithm: the recorded transmission profile (1) is filtered in the frequency domain (2). Filtered profiles for all acquisition angles are then backprojected and summed in real space (3). Image edited from [15].

The unknown sample content can be discretised on a grid of N cells, each attributed an unknown macroscopic cross-section Σ_j . The integrated cross-section seen by a detector pixel p_i , is then the sum of all Σ_j encountered by a "fat" neutron ray - its width being the same as the pixel - weighted by the fractional area of the fat ray within each cell j :

$$\sum_{j=1}^N w_{ij} \Sigma_j = p_i \quad (1.14)$$

and this for each one of the M detector pixels i . The acquisition process according to this principle is shown schematically in figure 1.12.

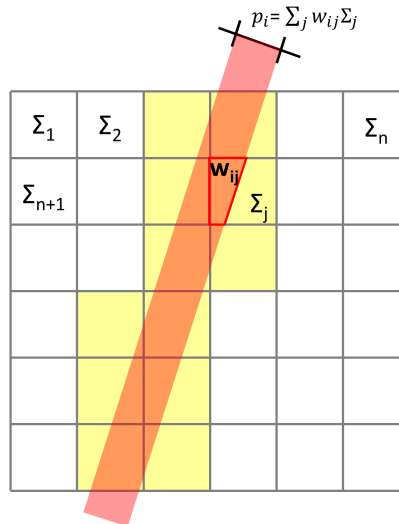


Figure 1.12: The algebraic reconstruction technique: rewriting the image formation process as a series of algebraic equations.

In other words, one has obtained a matrix equation

$$[w]^{M \times N} [\Sigma]^{N \times 1} = [p]^{M \times 1} . \quad (1.15)$$

These matrices tend to be huge however (M usually being on the order of at least 1024×1024 pixels and N a similar number). Direct inversion is out of the question and one has to rely on iterative methods to solve for Σ . Substantial computing power and time is required, even though recent advances have been made in implementation on Graphics Processing Units (GPUs) allowing for immense parallelization and significant speed up [17]. Still, several hours are required in order to reconstruct a typical dataset. Different solution strategies exist:

ART (algebraic reconstruction technique) - In most ART implementations, the weights w are simply replaced by 1s and 0s, depending whether or not a ray runs through the corresponding cell. This binarization makes the implementation easier and faster, but causes considerable salt and pepper noise. Moreover, the difference between each observed and computed ray impact is calculated and corrected for each ray sequentially. Changes made by one ray in a cell can thus be overwritten by the next.

SIRT (simultaneous iterative reconstruction techniques) - In response, the SIRT method [18] calculates the corrections for each ray before simultaneously updating all cells with the average of all proposed changes at once. Resulting reconstructions look better with much of the noise smoothed out, at the expense of slower convergence.

SART (simultaneous algebraic reconstruction techniques) - In order to reduce the discretization error, the SART method [19] uses bilinear elements rather than a constant pixel basis. Just like in SIRT, all correction terms are applied simultaneously at the end of each iteration. A weighting window is introduced, favouring corrections near the center of the reconstruction compared to the edges, as this is where the objects of reconstruction are located.

1.5 Imaging beamline layout

Working with ionizing radiation, the experimental area is a heavily shielded bunker structure, composed out of concrete blocks lined with steel of up to 1 m thickness. An anteroom can be present to house all beam manipulation systems (monochromators, filters, grating systems), separating them from the rest of the experimental (sample) area as they tend to get activated and become a source of γ radiation. A labyrinth type entrance avoids radiation seepage by neutrons scattered on sample and surroundings.

A shutter system stands in between the neutron source and the sample (e.g. [20]). When these are opened, access to the experimental area is prohibited. Over a meter of steel is required to stop the high energy neutrons. Thermal and cold neutrons are stopped using Boron, Lithium and Gadolinium.

Neutron imaging is ideally performed with a parallel beam. Due to the vast dimensions of neutron sources, no magnified imaging as with micro-focus X-ray tubes is possible. Moreover,

a strategy of using lenses to reshape the neutron trajectory is hindered by a lack coherence and electric charge. Some strategies exist [21, 22, 23], though still in their infancy and not used in practice in neutron imaging. Thus, the beam is shaped by having an aperture of diameter D in the neutron source shielding and performing the imaging experiment at a distance L away from it. The final divergence is quantified by the so called L/D ratio and it has a direct impact on the image resolution.

Imagine a sample with a perfectly sharp edge at a distance l from the detector. In a parallel beam, this would give rise to a step in the transmission profile. However, if the beam is originating from an aperture, diameter D , at a distance L , the recorded edge profile will be smeared out over a distance

$$d = l \left(\frac{L}{D} \right), \quad (1.16)$$

as illustrated schematically in figure 1.13. An example from practice is presented in figure 1.14.

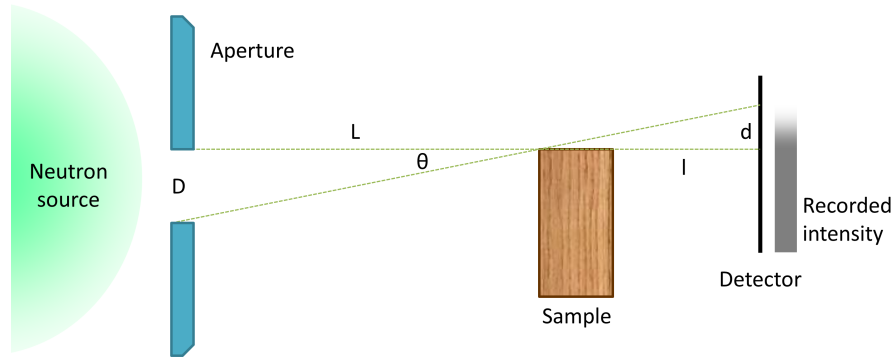


Figure 1.13: Effect of a pinhole of diameter D at a distance L from the sample on the edge blur d recorded at a detector at position l behind the sample.

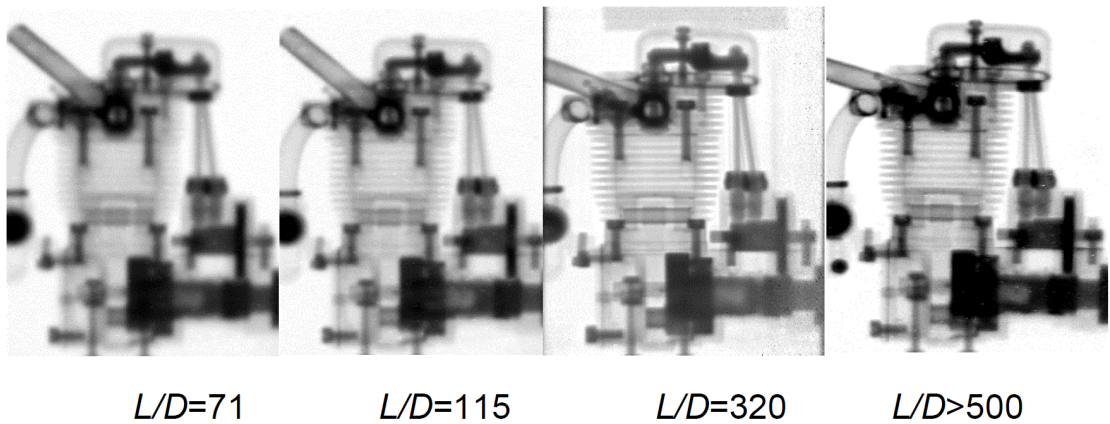


Figure 1.14: Radiographies of a small motor demonstrating the effect of the L/D ratio on image sharpness [4].

Chapter 1. Neutron imaging

Though reducing the pinhole size can lower the geometric unsharpness, it will also reduce the neutron flux. Increasing the beam path length comes with a bigger field of view and L/D ratio, but again a lower flux. In practice, usually two measurement positions are available and a choice between different aperture sizes. Typical numbers for the ICON beamline are given in table 1.1, summarizing the L/D ratios, corresponding divergence angles and neutron flux [24].

Aperture	1 mm	10 mm	20 mm	40 mm	80 mm
L/D	6864	686	343	172	86
θ	0.5'	5'	10'	20'	40'
Flux [$n\ s^{-1}\ cm^{-2}\ mA^{-1}$]	-	3.2×10^6	1.3×10^7	-	1.4×10^8

(a)

Aperture	1 mm	10 mm	20 mm	40 mm	80 mm
L/D	12083	1208	604	302	151
θ	0.28'	2.8'	5.7'	11.4'	22.8'
Flux [$n\ s^{-1}\ cm^{-2}\ mA^{-1}$]	-	-	3.9×10^6	-	5.2×10^7

(b)

Table 1.1: Beam divergence and flux at the ICON measurement position L=6.864 m (a) and L=12.083 m (b).

Between aperture and sample, the neutron beam goes through vacuum flight tubes. These limit intensity losses, background increase and activation of the surroundings predominantly caused by scattering from air molecules (mainly by the N_2 gas and humidity, i.e. H_2O). More than 5 percent of beam intensity is lost per meter for 5 Å neutrons [25]. However, the higher the vacuum, the thicker the entrance and exit windows of the flight tubes need to be and the higher the neutron beam attenuation by them.

Additional motorized slits are installed to limit the beam size to the sample dimensions. This avoids unnecessary activation and scattering of the surroundings leading to increased background.

The sample stage needs to account for three categories of motion. Firstly, translation with respects to the beam center allows to move a sample in and out of the beam (taking flat field images) or moving it up and down (measuring tall samples by stitching). Secondly, a goniometer corrects for sample tilt to have the rotation axis perpendicular to the beam. Lastly, a rotation stage is present, a prerequisite for tomographic acquisitions.

It is placed as close to the detector as possible in order to limit geometrical blurring, i.e. minimizing l in equation 1.16.

The typical required infrastructure for neutron radiography and tomography is illustrated using the ICON beamline, where most experiments presented in this work were performed. Its layout is representative for a typical neutron imaging beamline. A sketch of the beamline is provided in figure 1.15 with the most important components designated.

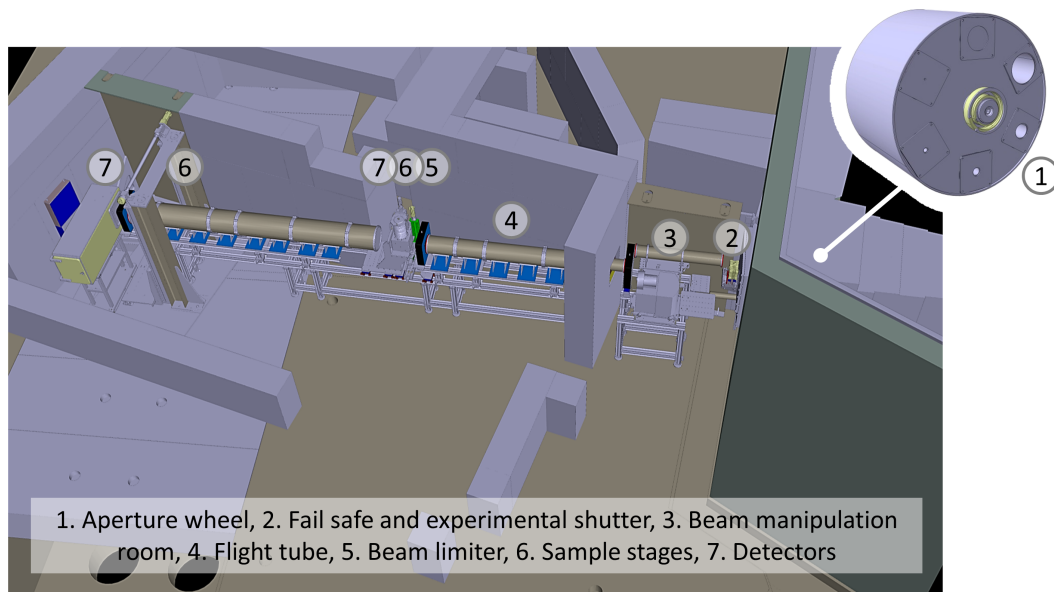


Figure 1.15: Layout of the ICON beamline as a typical imaging instrument, with neutrons coming from the right. Several shielding blocks have been omitted for clarity.

1.6 Imaging detector systems

Neutron imaging detectors are position sensitive detector systems featuring high spatial resolution and relatively large field of view. Two main digital categories can nowadays be distinguished: scintillator based systems convert neutrons to visible light detected with a camera and microchannel plate detectors, converting the neutrons into secondary charged particles for detection.

1.6.1 Film and imaging plates

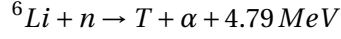
First neutron imaging was performed using X-ray films, made sensitive to neutron radiation by covering them with a conversion material such as a thin layer of Gadolinium. High spatial resolution can be obtained ($\sim 20 \mu$) this way, though the dynamic range is limited and non-linear. A new film is required for each radiograph. The result is an analog image on film, that can later on be digitized [26].

Imaging plates [27], feature a film of BaFBr:Eu. Neutron irradiation excites it to a meta-stable state. Afterwards, the imaging plates are placed in a scanner, where upon laser illumination the material de-excites. Photons are emitted in the process and collected, their number being a measure for the initial number of incident neutrons at that point. An intense white light erases the imaging plate, which is thus reusable.

The *ex-situ* development of film and imaging plates makes them impractical for tomographic purposes and they are nowadays but rarely used.

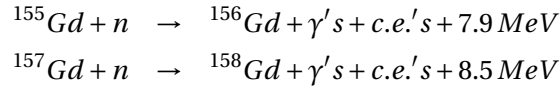
1.6.2 Scintillator based systems

This type of imaging detector system relies on a scintillator screen to convert the neutrons into visible light. The most common one is the ${}^6\text{LiF ZnS:Ag}$ one. Here, ${}^6\text{Li}$ acts as a converter, creating charged particles through the nuclear reaction



The triton and alpha particles induce ionizations along 40-150 μm and 5-10 μm path length in solid [28]. These will stimulate photon emission from the ZnS:Ag phosphor crystals, which are mixed together with the LiF crystals in an organic binder and coated on an aluminium substrate. The large difference in refractive index between the ZnS and LiF (2.4 *versus* 1.4, [29]) causes multiple reflections of the generated light on its way out of the scintillator and makes it rather opaque to its own light. The thicker the scintillator screen is made, the higher the neutron conversion efficiency by the ${}^6\text{LiF}$, but from around 450 μm on, the light yield does not follow this trend anymore [30]. The increased light diffusion that comes with thicker scintillators also reduces the spatial resolution that can be obtained. In practice, ${}^6\text{LiF ZnS:Ag}$ scintillators of 50 μm -300 μm are used.

To obtain higher spatial resolution, one thus needs very thin scintillators. However, the conversion efficiency of ${}^6\text{Li}$ would then be too low. Therefore, one switches to $\text{Gd}_2\text{O}_2\text{S}$ (Gadox) scintillators. Natural gadolinium has a 50 times higher absorption cross-section for thermal neutrons than ${}^6\text{Li}$ (even 270 times higher for the ${}^{157}\text{Gd}$ isotope). The thermal neutron capture reactions



produce low energy conversion electrons *c.e.* (the most probable K level conversion electron has an energy of 30 keV). As a result, they have a very short ionization range ($\sim 5 \mu\text{m}$) [31], meaning lower light yield, but the light also originates closer to the point of neutron interaction and higher spatial resolution is obtained. Typical Gadox scintillator thicknesses lie between 10 μm – 30 μm .

The scintillation light is then reflected *via* a 45° mirror to a high sensitivity CCD or CMOS camera outside the direct neutron beam to limit irradiation damage. However, γ 's generated in interactions of neutrons with sample and surroundings can still reach the camera chip and create *white spots* or *zingers* in the radiographs. Depending on the number of pixels on the camera chip and the size of the scintillator area focused onto that chip with optical lenses, different effective pixel sizes can be obtained. The whole is packed in a light tight box to prevent stray light from the experimental area to falsify results.

Typical exposure times are in the order of seconds, the dynamic range large (typically 16bit or 65535 grey levels) and linear. The resultant images are most importantly digital, with huge advantages for computed tomography, image processing, data storage.

In case of fast cyclic processes, stroboscopic imaging using a gated CCD with image intensifier is used [32, 33]. To avoid motion blurring of the cyclic process, very short exposure times are chosen. The recorded light intensity is correspondingly low, requiring photon multiplication and triggering at the same moment in every cycle, allowing to stack the radiographs and obtain sufficient image statistics.

At ICON, a whole range of such systems are available, covering a wide range of sample sizes and resolutions: the so-called *maxibox*, *midibox*, *micro set-up* [24, 34] and the *neutron microscope* under development (figure 1.16). Generally, the higher the spatial resolution, the longer the exposure times, as one focusses the light of smaller scintillation areas, generated using thinner scintillators onto a larger number of pixels.

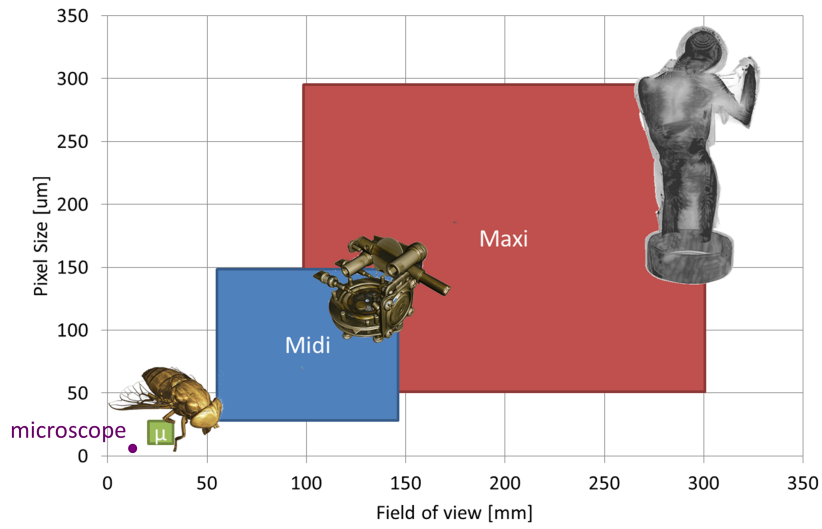
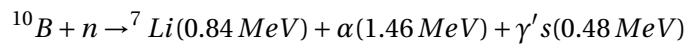


Figure 1.16: Range of possible sample sizes and spatial resolution for the different neutron imaging detector systems at the ICON beamline.

1.6.3 Microchannel plate detectors

A completely different class of neutron imaging detectors are based on Microchannel Plate (MCP) technology. A microchannel plate is a thin slab (\sim mm) of resistive material under high voltage, perforated with microscopic channels ($\sim 10 \mu\text{m}$, regularly spaced apart). Incident photons or charged particles that hit the walls knock out electrons which will be accelerated in the electric field and in turn knock out even more electrons, starting an electron avalanche within that pore. By doping MCP glass with ^{10}B , it becomes sensitive to neutron capture through the reaction



generating the required charged particles. The event location is registered with an underlying pixellated detector readout chip. A schematic overview is provided in figure 1.17. The main difference compared to coating a converter material such as ^{10}B or Gd straight on such a chip,

also used in neutron imaging [35], is the higher spatial resolution and signal intensity. As the charge build-up is limited to a single pore, one can perform event centroiding and reach resolutions down to $\approx 10\mu\text{m}$ [36] compared to $\approx 100\mu\text{m}$. Its noiseless character and fast time resolution ($\approx 1\mu\text{s}$) make it an ideal detector for time-of-flight neutron imaging.

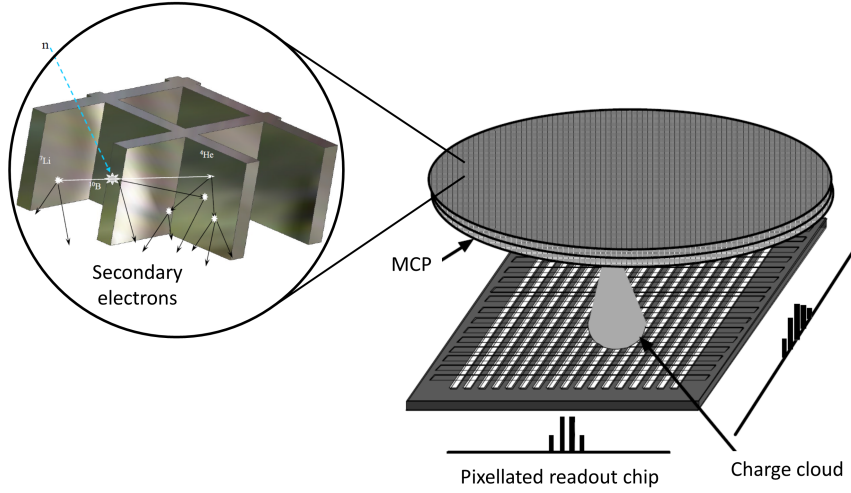


Figure 1.17: Schematic overview of a microchannel plate detector for neutron imaging. Charged particles are generated by neutron capture in borated glass, resulting in an electron avalanche detected on an underlying pixellated readout chip (adapted from [37]).

1.7 The need for energy-selective neutron imaging

So far, we've considered a single constant value for the cross-section in the Beer-Lambert law. However, reality is more complex and the cross-section, representing the neutron-matter interaction processes that cause the beam attenuation, is wavelength dependent. Thus, the Lambert-Beer law should be applied separately to each wavelength λ in the incident beam spectrum s , each with its own cross-section $\Sigma(\lambda)$. The recorded sample transmission will thus be:

$$T = \frac{\int_s I_0(\lambda) e^{-\Sigma(\lambda)d} \epsilon(\lambda) d\lambda}{\int_s I_0(\lambda) \epsilon(\lambda) d\lambda}, \quad (1.17)$$

with $\epsilon(\lambda)$ the wavelength dependent detector efficiency. The above equation is in fact an averaging operation of the wavelength dependent sample interaction over the incident beam spectrum.

In the case of crystalline material, this wavelength dependency of the cross-section can be very pronounced. The ability to perform neutron imaging at a single wavelength would allow the investigation of the spatial variation in crystalline properties of the sample. In the next chapter we investigate the interaction of neutrons with matter, absorption and scattering, concentrating on the wavelength range of relevance to neutron imaging. It will shed light on which crystalline properties are accessible and what their wavelength dependent cross-section exactly looks like.

2 Neutron interaction with matter

The probability of interaction between a neutron beam and the sample material is energy-dependent. Especially in the presence of an ordered structure of atoms, it can vary dramatically. In this chapter, we discuss the different types of interaction - absorption and scattering, both coherent and incoherent, elastic and inelastic - and their energy dependences. It will help us to understand which sample properties are newly accessible to us in energy-selective neutron imaging as well as how best to measure them.

2.1 Cross-sections

In neutron imaging, we assume an ideally parallel beam of thermal or cold neutrons incident on the sample nuclei. It is described by its wave vector \mathbf{k} , of the same direction as the neutron and of magnitude $2\pi/\lambda$. It can either undergo no interaction, be absorbed and removed from the beam or it can be scattered, changing its direction and/or energy as described by an outgoing wave vector \mathbf{k}' . These interaction mechanisms are investigated in great detail in further sections. Standard neutron imaging studies the spatial variation in transmitted beam intensity. However, as we will see in chapter 6, under certain conditions one can also perform imaging using a specific form of scattered neutrons, namely *diffracted neutrons*. The interaction geometry for neutron imaging in all modalities is shown in figure 2.1.

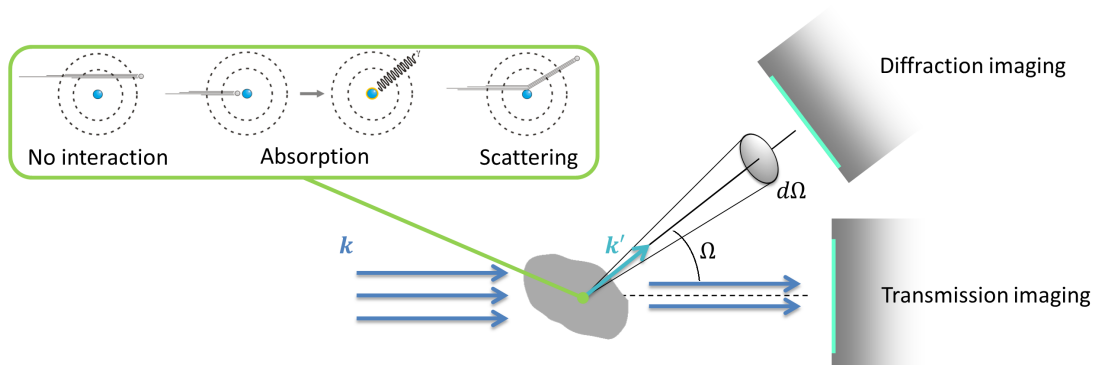


Figure 2.1: Reaction geometry showing incident beam, target, scattered and transmitted beam

The probability for an interaction to occur between neutron and nucleus is stated by the corresponding *microscopic cross-section* σ :

$$\sigma = \frac{\text{number of neutrons undergoing interaction per target nucleus [n/s]}}{\text{incident neutron flux [n/s/cm}^2\text{]}}$$

This material property has the dimensions of an area and is usually expressed in units of barn ($1 \text{ barn} = 10^{-28} \text{ m}^2$). One can picture it as the area of a virtual disk around the nucleus' position, with interaction occurring when a neutron passes through it and no interaction when the neutron flies by unperturbed further away¹.

The *macroscopic cross-section* Σ takes into account the density of nuclei N in a target material of interest, $\Sigma = N\sigma$.

In case we are only registering the number of outgoing interacted neutrons in a certain direction Ω with solid angle $d\Omega$ subtended by a detector, we can investigate the angular dependence of the interaction process as represented by the *differential cross section*

$$\frac{d\sigma}{d\Omega} \quad (2.1)$$

The differential cross-section e.g. manifests itself in diffraction imaging experiments. The total microscopic cross-section is then found again through simple integration over all angles. Conversely, one can also define the differential energy cross-section distinguishing between outgoing neutrons by the energy range dE they fall into and do not by their direction:

$$\frac{d\sigma}{dE} \quad (2.2)$$

This is what we observe in energy-selective transmission imaging, making a series of radio-graphs at different wavelengths.

Finally, the *double differential cross-section* gives the probability of observing the interacted neutron in the angular range $d\Omega$ and energy range dE :

$$\frac{d^2\sigma}{d\Omega dE} \quad (2.3)$$

2.2 Interaction with a single nucleus

2.2.1 Absorption

When a neutron hits a nucleon of the atom's core, the recoil nucleon and neutron will hit other nucleons which will recoil themselves and hit other nucleons in turn and so on. Rapid energy sharing thus occurs and a *compound nucleus* is formed, which quickly de-excites by prompt gamma radiation. The resultant compound nucleus is however not necessarily stable and radioactive decay (or a chain of decays) will occur until a stable end state is reached. The time scale for this process is highly dependent on the initial type of target nuclei and can range from seconds to millions of years. Therefore it is important prior to neutron imaging experiments,

¹The basic unit originates in the approximate geometric cross-section of a Uranium nucleus [38].

to check possible sample activation on the nuclide chart (e.g. [39]) as it might compromise its release by radiation safety authorities.

Resonances exist for energy states of the compound nucleus in the keV-range, characterised by a high cross-section and narrow energy width [40]. Each isotope has a unique resonance pattern 'finger print', which is exploited in resonance neutron imaging possible at a few pulsed sources only [41].

The primary absorption mechanism is radiative capture, the cross-section σ_r is given by the Breit-Wigner formula for a single isolated resonance [42, 43]:

$$\sigma_r = \frac{\lambda^2}{4\pi} g_J \frac{\Gamma_n \Gamma_\gamma}{(E - E_R)^2 + \Gamma_R^2} \quad (2.4)$$

with λ the wavelength of the incident neutron and g_J the spin factor for the compound state of total angular momentum J . Γ_n is the neutron width dependent on the density of final states available to the incident neutron and thus proportional to the neutron velocity $\Gamma_n \propto v$. Γ_γ is the emitted gamma width independent of the neutron velocity as for a compound nucleus the incident and exit channel are decoupled. Finally, $E \propto v^2$ is the neutron energy and E_R the energy of the resonance of width Γ_R . For thermal and cold neutrons, far from resonance, the equation 2.4 tends to the familiar $1/v$ law. More qualitatively, one can state that the slower the neutron, the more time it has for interacting with the nucleus and thus the higher the cross-section. Figure 2.2 illustrates the radiative capture cross-section for ^{27}Al over a large energy range retrieved from the ENDF/B-VII.1 database using JANIS [39].

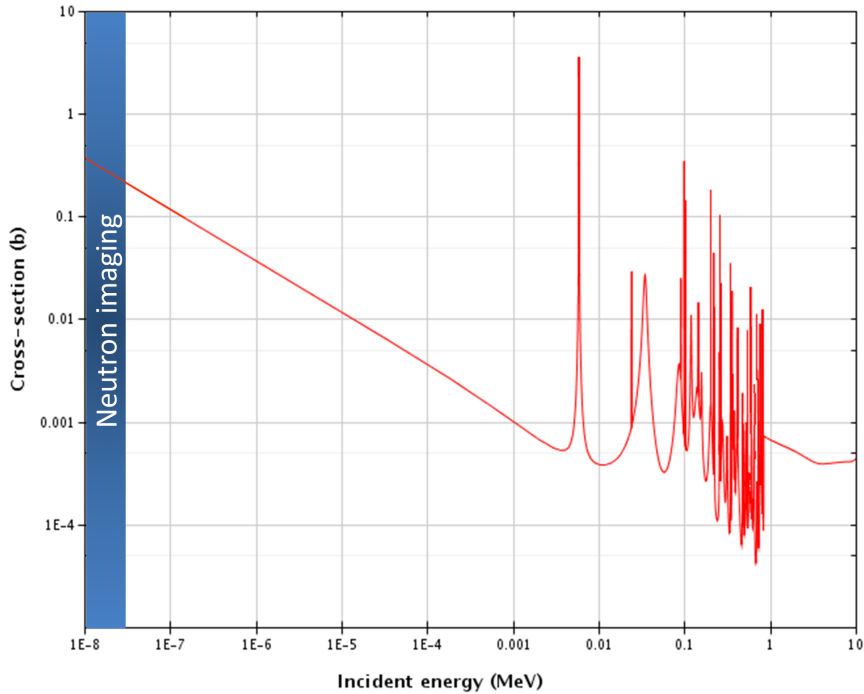


Figure 2.2: Radiative capture cross-section for ^{27}Al .

A few isotopes also have a resonance in the thermal range (e.g. ^{157}Gd at 1.67 Å or ^{113}Cd at 0.66 Å). These are typically used in neutron detectors or as shielding material (shutter, beam limiters, beam dump...) in neutron imaging and scattering experiments due to their high capture efficiency.

2.2.2 Scattering

However, more than absorption, neutron scattering is the dominant interaction mechanism for a large number of materials. For a selected number of materials, reappearing as samples in this work, their respective absorption and scattering cross-section are shown in figure 2.3. An important consequence is that, though the Beer-Lambert law assumes all interacted neutrons (absorbed or scattered) removed from the beam, some of these scattered neutrons will still reach the detector. The number of observed neutrons is thus higher than expected from applying the Beer-Lambert law on a straight path through the sample, leading to quantification errors. The issue is dealt with in more detail in chapter 4.

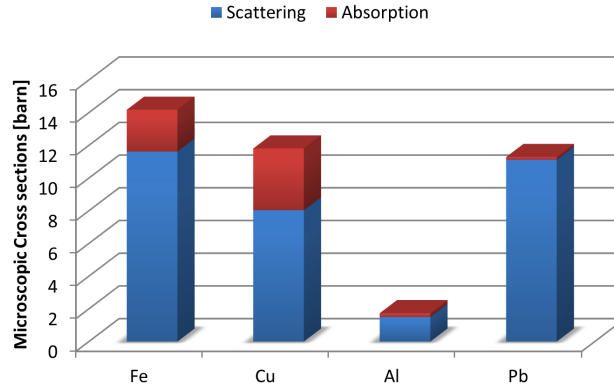


Figure 2.3: Tabulated [44] total microscopic scattering and absorption cross-sections for selected materials.

First, we investigate the scattering from a neutron of wave vector \mathbf{k} from a single, fixed nucleus at position $\mathbf{r} = 0$. We make use of the particle-wave duality for the incident neutron and represent it by a plane wave $e^{i\mathbf{k}\cdot\mathbf{r}}$. As the force exerted by the nucleus is central, the scattered wave can be decomposed in eigenfunctions of angular momentum. Now consider the incident neutron (mass m , velocity v) striking just at the surface of the nucleus, at $r = R$, being in the range of a few femtometers. The angular momentum involved in the impact is $m v R$. Quantum mechanics dictates it is quantized, so

$$m v R = \hbar \sqrt{\ell(\ell + 1)}, \quad (\ell = 0, 1, 2, 3, \dots) \quad (2.5)$$

so for thermal and cold neutrons ($v = 2200 \text{ m/s}$ and below), only $\ell = 0$ or S-wave scattering is possible, which is isotropic. Equation 2.5 shows that $\ell = 1$ or P-wave scattering does not set on until energies in the MeV range, far above the energy range considered in this work. Thus the

wave function associated with the scattered neutron is

$$\psi(\mathbf{r})|_{r>R} = f \frac{e^{i\mathbf{k}\cdot\mathbf{r}}}{r}, \quad (2.6)$$

f being the scattering amplitude. The total flux of scattered neutrons can be found integrating over a virtual sphere of radius r around the nucleus:

$$v \cdot 4\pi r^2 \cdot |f \frac{e^{i\mathbf{k}\cdot\mathbf{r}}}{r}|^2 = 4\pi v |f|^2 \quad (2.7)$$

The incident flux being

$$v \cdot |e^{i\mathbf{k}\cdot\mathbf{r}}| = v \quad (2.8)$$

The scattering cross-section, or chance that an incident neutron is scattered from the nucleus is then given by the ratio of (2.7) to (2.8):

$$\sigma_s = 4\pi |f|^2 \quad (2.9)$$

The bound² scattering length b is defined as

$$b = -f, \quad (2.10)$$

and can be interpreted geometrically as the radius R of an impenetrable rigid sphere at which scattering occurs. In this strongly simplified model, the total wave function

$$\psi(r) = e^{i\mathbf{k}\cdot\mathbf{r}} - b \frac{e^{i\mathbf{k}\cdot\mathbf{r}}}{r} \quad (2.11)$$

needs to become zero at the interface, resulting in $R = b$. The minus sign in (2.10) is introduced by convention to take into account the 180° phase shift between incident and outgoing wave and obtain positive values for the scattering length for scattering from an impenetrable rigid sphere³. However, in practice it is often simply interpreted as the proportionality constant between incident and scattered wave.

In principle it is possible to find the scattering length by solving the Schrödinger equation in the nuclear potential and joining the wave function between incident and scattered wave. However in practice, nuclear theory does not yet provide a description for the potential

²Also a free scattering length can be defined. It corresponds to the situation of neutron scattering from a free nucleus instead of a rigid one, in which case a recoil has to be taken into account. However, passing on to the center of mass system, this problem is equivalent to scattering of a neutron of reduced mass $m' = mM/(m+M)$ from a fixed nucleus and we will not consider it further here.

³A few isotopes exist with a negative scattering length (e.g. ⁷Li, ⁴⁸Ti, ⁵⁵Mn,...). Instead of an infinite potential associated with an impenetrable sphere, the *Fermi model* describes the nucleus as simple potential well of constant depth $V \approx -40\text{MeV}$ and width $R[\text{fm}] = 1.2A^{1/3}$, with A the atomic mass number. Solving the Schrödinger equation for this potential and joining the wave functions inside and outside the nucleus, the scattering length is found again as the zero of what is now the extrapolated outer wave function [45]. A few atomic masses (and corresponding potential well widths) will give rise to resonances between the wave functions and will have a negative root [46].

Chapter 2. Neutron interaction with matter

accurate enough. Experimental values are used instead, determined through experiments involving diffraction, neutron interference, refraction, reflection or even gravitometry [47]. They are tabulated and can be found e.g. in [47, 44].

A priori suggesting an isotropic scattered wave solution (eq. 2.6), one can propose a potential

$$\hat{V}(r) = \frac{2\pi\hbar^2}{m}\delta(r) \quad (2.12)$$

which yields the correct result when deriving the scattering cross-section through application of Fermi's golden rule for calculating the interaction probability on quantummechanical grounds [48]:

$$\frac{d^2\sigma}{d\Omega dE} = \frac{k'}{k} \left(\frac{m}{2\pi\hbar^2} \right)^2 \sum_{\xi,\chi} p_{\xi} p_{\chi} \sum_{\xi',\chi'} | \langle \mathbf{k}' \xi' \chi' | \hat{V} | \mathbf{k} \xi \chi \rangle |^2 \delta(\hbar\omega + E_{\chi} - E_{\chi'}), \quad (2.13)$$

with the initial neutron wave vector \mathbf{k} , spin state ξ and target state χ , their final states denoted by \mathbf{k}' , ξ' , χ' ; p the probabilities of those states and $\hbar\omega$ the change in neutron energy. Inserting (2.12) into this equation for the case of an unpolarized beam and no energy exchange with the target nucleus, again we find $\sigma_s = |b|^2$.

\hat{V} is however not a true potential but rather a *pseudo potential*, since the solution is found in the Born approximation which is violated for such a strong potential as one containing a δ -function. It is rather an artifice constructed such as to yield the correct result in this approximation and outside the nucleus.

Instead of a gamma ray, a neutron can also be re-emitted after neutron absorption⁴. The nuclear potential scattering cross-section (equation 2.9) should be corrected by addition of a resonance term and interference term [43]. However, far from resonances, these terms become independent of the neutron energy. Moreover, the compound nucleus model implies isotropic particle emission as the incident neutron direction is "forgotten". This reaction channel can thus be incorporated in the experimental constant scattering length b .

2.3 Scattering from a rigid array of nuclei

Consider an array of N nuclei, with the l^{th} nucleus at \mathbf{R}_l . The Fermi potential then becomes

$$\hat{V}(\mathbf{r}) = \frac{2\pi\hbar^2}{m} \sum_l b_l \delta(\mathbf{r} - \mathbf{R}_l) \quad (2.14)$$

⁴Charged particle emission for slow neutron capture is only found for a few lighter elements, e.g. $^3\text{He}(n,p)$, $^6\text{Li}(n,\alpha)$, $^{10}\text{B}(n,\alpha)$.

Thus $\langle \mathbf{k}' | \hat{V} | \mathbf{k} \rangle$ becomes, expanding the bra-ket notation,

$$\langle \mathbf{k}' | \hat{V} | \mathbf{k} \rangle = \frac{2\pi\hbar^2}{m} \sum_l b_l \int e^{-i\mathbf{k}' \cdot \mathbf{r}} \delta(\mathbf{r} - \mathbf{R}_l) e^{i\mathbf{k} \cdot \mathbf{r}} d\mathbf{r} \quad (2.15)$$

$$= \frac{2\pi\hbar^2}{m} \sum_l b_l e^{i\boldsymbol{\kappa} \cdot \mathbf{r}}, \quad (2.16)$$

with $\boldsymbol{\kappa} = \mathbf{k} - \mathbf{k}'$. Introducing it into equation (2.13), with the quantum numbers χ for a rigid lattice referring only to the isotope and nuclear spin distribution and the energy of the lattice system to a very good approximation independent of this so as to be dealing with elastic scattering, we find:

$$\frac{d\Sigma_s}{d\Omega} = \sum_{l,l'} \overline{b_{l'}^* b_l} e^{i\boldsymbol{\kappa} \cdot (\mathbf{R}_l - \mathbf{R}_{l'})}, \quad (2.17)$$

with

$$\overline{b_{l'}^* b_l} = \sum_{\lambda} p_{\lambda} \langle \lambda | b_{l'}^* b_l | \lambda \rangle \quad (2.18)$$

the averaging over the isotope and nuclear spin distribution. The scattering length b_l depends on the isotope and nuclear spin of the nucleus associated with position \mathbf{R}_l . As there is no correlation between the nuclei at \mathbf{R}_l and $\mathbf{R}_{l'}$,

$$\overline{b_{l'}^* b_l} = \begin{cases} |\bar{b}|^2 & , l \neq l' \\ |\bar{b}|^2 & , l = l' \end{cases} \quad (2.19)$$

Hence, equation (2.18) can be split up into two terms

$$\overline{b_{l'}^* b_l} = |\bar{b}|^2 + \delta_{l,l'} (|\bar{b}|^2 - |\bar{b}|^2), \quad (2.20)$$

so the differential cross-section (2.17) can be rewritten as the sum of a *coherent* term

$$\left(\frac{d\Sigma}{d\Omega} \right)_{s,coh} = |\bar{b}|^2 \left| \sum_l e^{i\boldsymbol{\kappa} \cdot \mathbf{R}_l} \right|^2, \quad (2.21)$$

with \bar{b} often referred to as the coherent scattering length, and an *incoherent* term

$$\left(\frac{d\Sigma}{d\Omega} \right)_{s,inc} = N(|\bar{b}|^2 - |\bar{b}|^2) = N|\bar{b} - \bar{b}|^2. \quad (2.22)$$

Physically, this can be interpreted as follows. Due to the presence of different isotopes and nuclear spin states with different scattering lengths, the array of nuclei is not truly periodic. However, it can be seen as a superposition of a periodic array with mean scattering length and (random) corrections. Where the former gives rise to an interference factor - making the coherent scattering cross-section highly dependent on the geometry of the system - the incoherent scattering cross-section is simply proportional to the mean-square of the deviation and isotropic.

Chapter 2. Neutron interaction with matter

Neglecting the nuclear spin, for different isotopes ξ of abundance c_ξ ,

$$\bar{b} = \sum_{\xi} c_{\xi} b_{\xi} \quad (2.23)$$

Next, we consider a single isotope only. In the interaction of a neutron with spin $1/2$ and a nucleus of spin I , states of total angular momentum $J^+ = I + 1/2$ or $J^- = I - 1/2$ with multiplicity $2J + 1$ and corresponding scattering length b^+ , b^- are available to the neutron. Occupation of each of these states is equiprobable, so the chance of interaction with J^+ is:

$$\frac{2I + 2}{(2I + 2) + 2I} = \frac{I + 1}{2I + 1} \quad (2.24)$$

and for J^- :

$$\frac{2I}{(2I + 2) + 2I} = \frac{I}{2I + 1}, \quad (2.25)$$

so that

$$\bar{b} = \left(\frac{I + 1}{2I + 1} \right) b^+ + \left(\frac{I}{2I + 1} \right) b^- \quad (2.26)$$

Combining (2.23) and (2.26) we can find a general expression for \bar{b} and *mutatis mutandis* $|\bar{b}|^2$:

$$\bar{b} = \sum_{\xi} c_{\xi} \frac{1}{2I_{\xi} + 1} \left[(I_{\xi} + 1) b_{\xi}^+ + I_{\xi} b_{\xi}^- \right] \quad (2.27)$$

$$|\bar{b}|^2 = \sum_{\xi} c_{\xi} \frac{1}{2I_{\xi} + 1} \left[(I_{\xi} + 1) |b_{\xi}^+|^2 + I_{\xi} |b_{\xi}^-|^2 \right] \quad (2.28)$$

Tabulated are the so called *bound (in)coherent scattering cross-sections* for single nuclei [44]. These are defined as:

$$\sigma_{coh} = 4\pi |\bar{b}|^2 \quad (2.29)$$

$$\sigma_{inc} = 4\pi (|\bar{b}|^2 - |\bar{b}|^2) \quad (2.30)$$

Equation (2.30) corresponds to the total microscopic incoherent scattering cross-section - integrating equation (2.22) over the unit sphere and normalizing to a single nucleus. The tabulated bound coherent scattering cross-section (eq. 2.29) does not take the interference factor implied by the periodic structure into account. It is rather a constant describing its strength.

The tabulated bound coherent and incoherent scattering cross-sections are illustrated in table 2.1 for some materials typically encountered in neutron imaging and scattering. Hydrogen has a nuclear spin of $1/2$ and spin incoherence dominates dramatically. Likewise, for Vanadium, the coherent scattering lengths b^+ and b^- have opposite sign and are present in almost equal ratio $9/2:7/2$. Iron on the other hand is a strong coherent scatterer as one isotope of spin zero is highly abundant.

2.4. Scattering from a rigid crystal lattice

Element	Isotope (abundance [%])	Nuclear spin	σ_{coh} [b]	σ_{inc} [b]	σ_a [b]
H		1/2	1.77	80.26	0.33
Al			1.495	0.0082	0.231
V	^{51}V (99.75)	7/2	0.032	5.08	5.08
Fe			11.3	11.6	2.25
	^{54}Fe (5.84)	0	2.2	2.5	2.59
	^{55}Fe (91.68)	0	12.8	12.8	2.48
	^{56}Fe (2.17)	1/2	0.64	2.0	1.28
Cu			7.49	0.55	3.78

Table 2.1: A selection of single atom scattering cross-sections for materials typically encountered in neutron imaging and scattering, the absorption cross-section is given for completeness. (from [44, 48]).

2.4 Scattering from a rigid crystal lattice

2.4.1 Describing a crystal lattice

In this section, we consider our array to be a crystal lattice and further develop the formulation for the coherent cross-section. The incoherent cross-section (eq. 2.30, independent of the nuclei positions) remains unchanged.

A crystal is a periodic repetition of a *unit cell* in space. The unit cell is described by its subtending *base vectors* \mathbf{a}_1 , \mathbf{a}_2 and \mathbf{a}_3 and has a volume $V_0 = \mathbf{a}_1 \cdot (\mathbf{a}_2 \times \mathbf{a}_3)$. The *lattice vector* \mathbf{l} denotes moving from one unit cell to the next: $\mathbf{l} = l_1 \mathbf{a}_1 + l_2 \mathbf{a}_2 + l_3 \mathbf{a}_3$, with l_1, l_2, l_3 integers. The position of different atoms within the unit cell are described by the vector $\mathbf{d} = d_1 \mathbf{a}_1 + d_2 \mathbf{a}_2 + d_3 \mathbf{a}_3$, with d_1, d_2, d_3 rational numbers. All lattice sites are thus described by the vector $\mathbf{R}_{ld} = \mathbf{l} + \mathbf{d}$. An example of the crystal lattice and its descriptors is given in figure 2.4.

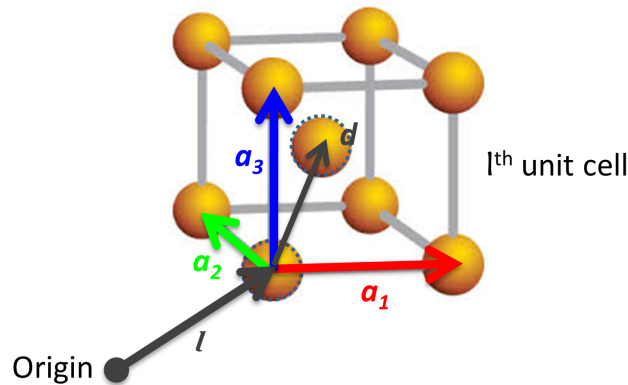


Figure 2.4: A set of base vectors for a body-centered cubic lattice for which the unit cell contains two atoms at $\mathbf{d} = 0$ and $\mathbf{d} = 1/2(\mathbf{a}_1 + \mathbf{a}_2 + \mathbf{a}_3)$.

Chapter 2. Neutron interaction with matter

An equivalent *reciprocal lattice* of vectors $\boldsymbol{\tau}$ can be defined by

$$e^{i\boldsymbol{\tau} \cdot \mathbf{l}} = 1 \quad (2.31)$$

The reciprocal lattice is then described by $\boldsymbol{\tau} = t_1 \boldsymbol{\tau}_1 + t_2 \boldsymbol{\tau}_2 + t_3 \boldsymbol{\tau}_3$, with the reciprocal base vectors

$$\boldsymbol{\tau}_1 = \frac{2\pi}{V_0} \mathbf{a}_2 \times \mathbf{a}_3 \quad (2.32)$$

$$\boldsymbol{\tau}_2 = \frac{2\pi}{V_0} \mathbf{a}_3 \times \mathbf{a}_1 \quad (2.33)$$

$$\boldsymbol{\tau}_3 = \frac{2\pi}{V_0} \mathbf{a}_1 \times \mathbf{a}_2. \quad (2.34)$$

The volume of a unit cell in reciprocal space is then

$$\boldsymbol{\tau}_1 \cdot (\boldsymbol{\tau}_2 \times \boldsymbol{\tau}_3) = \frac{(2\pi)^3}{V_0}. \quad (2.35)$$

Crystal lattice planes and crystallographic directions are often represented by a set of three integers h, k, l , referred to as the *Miller indices*. (hkl) denotes the plane defined by its intercepts with the base vectors at \mathbf{a}_1/h , \mathbf{a}_2/k and \mathbf{a}_3/l . A zero index represents a plane parallel to the corresponding base vector (or equivalently intersecting it at infinity). $[hkl]$ denotes the direction $h\mathbf{a}_1 + k\mathbf{a}_2 + l\mathbf{a}_3$. The families of planes and directions equivalent due to crystal symmetry are denoted as $\{hkl\}$ and $\langle hkl \rangle$ respectively.

2.4.2 Single crystal cross-section

For a crystal lattice with N atomic positions \mathbf{l} , equation (2.21) is simply rewritten as

$$\left(\frac{d\Sigma}{d\Omega} \right)_{s,coh} = |\bar{b}|^2 \left| \sum_{\mathbf{l}} e^{i\boldsymbol{\kappa} \cdot \mathbf{l}} \right|^2. \quad (2.36)$$

The cross-section is large when the scattering vector $\boldsymbol{\kappa}$ coincides with a reciprocal lattice point $\boldsymbol{\tau}$ whereas it drops off rapidly when $\boldsymbol{\kappa}$ moves away from such points. In the limit for a large crystal

$$\left| \sum_{\mathbf{l}} e^{i\boldsymbol{\kappa} \cdot \mathbf{l}} \right|^2 \propto \delta(\boldsymbol{\kappa} - \boldsymbol{\tau}), \quad (2.37)$$

the proportionality constant found through equating and integrating both sides. The differential coherent scattering cross-section thus becomes [48]

$$\left(\frac{d\Sigma}{d\Omega} \right)_{s,coh} = \frac{N(2\pi)^3}{V_0} |\bar{b}|^2 \sum_{\boldsymbol{\tau}} \delta(\boldsymbol{\kappa} - \boldsymbol{\tau}). \quad (2.38)$$

In the case of multiple atoms per unit cell, it is generalized to:

$$\left(\frac{d\Sigma}{d\Omega} \right)_{s,coh} = \frac{N(2\pi)^3}{V_0} \sum_{\boldsymbol{\tau}} F(\boldsymbol{\tau}) \delta(\boldsymbol{\kappa} - \boldsymbol{\tau}), \quad (2.39)$$

with the *structure factor* F defined as

$$F(\boldsymbol{\tau}) = \sum_{\mathbf{d}} \bar{b}_d e^{i\boldsymbol{\tau} \cdot \mathbf{d}}. \quad (2.40)$$

The condition for coherent scattering can be represented graphically by the *Ewald construct* depicted in figure 2.5. Here, the incident neutron is represented by the wave vector \mathbf{k} impinging at the origin O of the reciprocal lattice. As the scattering is elastic, the wave vector \mathbf{k}' for the scattered neutron must have the same magnitude. Therefore, starting at the same point A as \mathbf{k} , its end point must lie on a circle with center A and radius $|\mathbf{k}| = |\mathbf{k}'| = k$. Only for the intersections of this circle with the reciprocal lattice, is the condition for coherent elastic scattering (also known as *diffraction* or *Bragg scattering*) $\boldsymbol{\kappa} = \boldsymbol{\tau}$ fulfilled. From figure (2.5), it can be seen that

$$\sin(\theta) = \frac{\tau}{2k} \quad (2.41)$$

As the reciprocal lattice vector is perpendicular to the lattice planes in real space and has a magnitude $\tau = n2\pi/d$, with d the lattice plane spacing and n an integer, this can be reformulated as

$$2d \sin \theta = n\lambda, \quad (2.42)$$

the well known *Bragg law*.

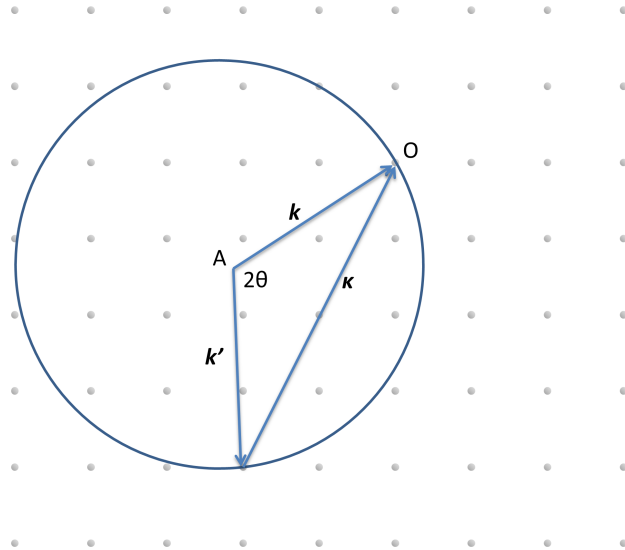


Figure 2.5: Ewald construct showing the condition for Bragg scattering

Alternatively, Bragg's law can also immediately be derived in real space. From figure 2.6, it is clear that if the path difference between the scattered neutron waves is a multiple of the wavelength $n\lambda$, $n = 1, 2, 3, \dots$, the scattered waves are in phase. Trigonometry reveals the path difference to be $2d \sin \theta$ and the condition for constructive interference thus leads to equation 2.42 again. For any deviation from this condition, the waves are no longer in phase and the reflected intensity quickly falls to zero.

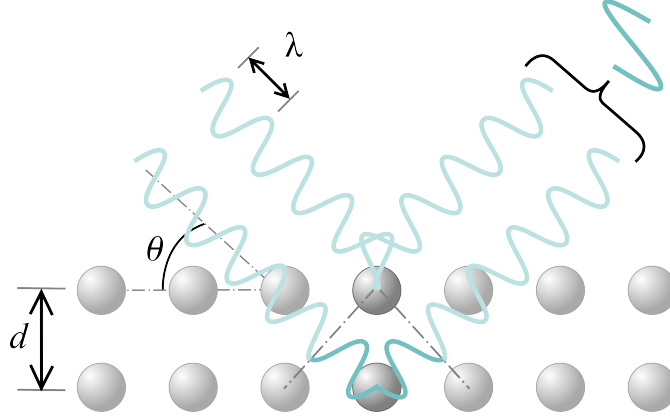


Figure 2.6: Derivation of Bragg's law in real space, with a neutron beam of wavelength λ incident under an angle θ on a crystal lattice of plane spacing d .

The total cross-section is then found by integration of equation (2.39) over $d\Omega$, or equivalently over $d\mathbf{k}'/|\mathbf{k}'|$:

$$\Sigma_{s,coh} = N \frac{(2\pi)^3}{V_0} \frac{2}{k} \sum_{\mathbf{\tau}} |F(\mathbf{\tau})|^2 \delta(\tau^2 - 2k\tau \sin \theta), \quad (2.43)$$

the delta function being equivalent to the fulfilment of the Bragg law. Thus, wavelength-dependent neutron imaging of single crystals will feature sharp dips in the transmission spectrum due to coherent elastic scattering wherever the Bragg condition is met.

As an illustration to equation (2.43), the transmission pattern of a copper single crystal is shown in figure 2.7. Apart from their location, equation (2.43) tells us how the Bragg dips become more pronounced for longer wavelengths ($\Sigma_{s,coh} \propto 1/k$). Their number decreases and separation increases for longer wavelengths. This can be understood in the context of the Ewald sphere again: with short wavelengths, a large Ewald sphere is associated, with many intersection possibilities with the reciprocal lattice. With increasing wavelengths, the Ewald sphere grows smaller and intersections more scarce. From a certain point on, it will be so small that no intersections are possible anymore. Energy-selective transmission imaging of single crystals is thus best performed using cold neutrons, allowing for higher contrast and placing less stringent demands on the energy-resolution required to separate the peaks. We will get back to this in chapter 5, with newly developed methods and applications for extracting single crystal properties at high spatial resolution.

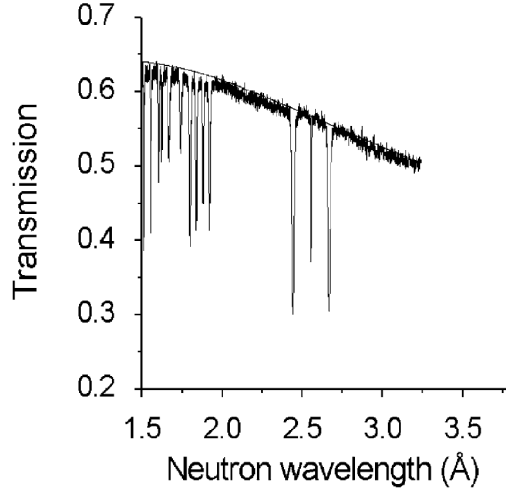


Figure 2.7: Transmission spectrum of a copper single crystal (taken from [32]).

2.4.3 Powder cross-section

A powder or an ideal polycrystalline material can be considered an ensemble of single crystals in all random orientations. With typical crystallite sizes in the order of $\mathcal{O}(10\text{ }\mu\text{m})$ [49] and sample diameters of $\mathcal{O}(1\text{ cm})$, a thousand crystallites are present in the beam direction. The formula for coherent scattering can thus be found through averaging the one for a single crystal (equation 2.39) over all orientations of $\boldsymbol{\tau}$:

$$\left(\frac{d\Sigma}{d\Omega}\right)_{s,coh} = \frac{2\pi^2 N}{k^2 V_0} \sum_{\boldsymbol{\tau}} \frac{1}{\tau} |F(\boldsymbol{\tau})|^2 \delta\left(1 - \frac{\tau^2}{2k^2} - \cos\theta\right). \quad (2.44)$$

The argument of the δ -function represents a cone of opening angle 2θ . Neutrons can scatter in all directions defined by these so-called *Debye-Scherrer cones*. Again, the total cross-section can be found through integration:

$$\Sigma_{s,coh} = \frac{4\pi^3 N}{k^2 V_0} \sum_{\boldsymbol{\tau}} \frac{\tau^{<2k}}{\tau} |F_{\boldsymbol{\tau}}|^2, \quad (2.45)$$

which can be rewritten in more common terms of wavelength λ and lattice spacings as d_{hkl} :

$$\Sigma_{s,coh} = \frac{\lambda^2 N}{2V_0} \sum_{d_{hkl}}^{2d_{hkl} < \lambda} d_{hkl} |F_{hkl}|^2. \quad (2.46)$$

The cross-section will increase quadratically with increasing wavelengths - promoting the use of cold neutrons - and feature sharp *Bragg edges* at $\lambda = 2d_{hkl}$. For larger wavelengths, the (hkl) lattice planes can no longer scatter neutrons out of the direct beam and the cross-section drops sharply. Past the largest $2d_{hkl}$ coherent scattering can no longer occur, this is the *Bragg*

cut-off. Equation (2.45) is illustrated in figure 2.8 for a rigid Body Centered Cubic (BCC) lattice of cube side a .

It should be noted that preferred orientation or texture [50] can lead to large deviation of this pattern [51, 32]. Orientations that are overrepresented compared to the random distribution will lead to increased scattering (higher cross-section) for the corresponding Bragg wavelength at the expense of underrepresented orientations.

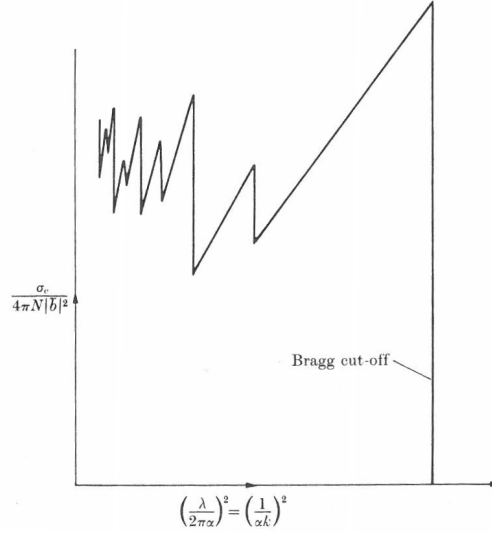


Figure 2.8: Total coherent scattering cross-section for a theoretical rigid body-centered cubic lattice of cube side length a (taken from [48]).

2.5 Scattering from a crystal lattice with thermal motion

2.5.1 Phonons and the Debye model

So far, we have assumed a rigid crystal lattice. However, in reality, the sample is at a certain temperature and associated nuclei oscillate around an equilibrium position. This makes it possible for the neutron to exchange some of its energy with the crystal, setting it into oscillation or absorbing energy from the crystal vibrations. The part of the cross-section involving energy exchange is referred to as the *inelastic* cross-section, whereas for the *elastic* cross-section the energy of incident and scattered neutron remain the same.

The nature of these vibrations have been studied extensively, development of different models driven by their ability to explain the evolution of the volumetric specific heat capacity with temperature. The oldest model developed by Dulong and Petit (1819), assumes the nuclei as vibrating independently around their equilibrium lattice position. The energy associated with these vibrations resembles the classical case of a mass-on-a-spring harmonic oscillator. A continuum of potential energies is possible, $E = \frac{1}{2} kx^2$, k the effective spring constant and x the deviation from equilibrium. However, though the model describes the atomic mass dependency of the specific heat capacity fairly well, it also states it erroneously to be independent of temperature.

2.5. Scattering from a crystal lattice with thermal motion

Einstein introduced a quantum mechanical treatment of the harmonic oscillator (1917), the energy associated with the vibrations now quantized as *phonons* - similar to photons for electromagnetic field oscillations - with $E = \hbar\omega(n + 1/2)$. Here, ω represents the angular frequency of the phonon and n the quantum state number. Though the Einstein model describes the temperature dependence of the specific heat capacity well at moderate and room temperature, it breaks down in the low temperature limit.

Debye solved this issue by renouncing the concept of independent vibrations. Oscillations of nuclei in one lattice plane also have an impact on the movement of neighbouring planes and vice versa[52, 53]. This interdependent vibration of nuclei can be broken down into modes, schematically illustrated in figure 2.9 together with the other models. The shortest possible wavelength or highest order mode (maximum angular frequency ω_D) of such joint oscillation then corresponds to twice the interatomic distance in the 1D case. Any shorter wavelength is irrelevant, as unlike electromagnetic waves, the phonon concept is only meaningful at the nuclei's positions, being defined as the movement of nuclei. The associated temperature $\theta_D = \hbar\omega_D/k_B$ is called the Debye temperature, with $k_B = 1.38 \cdot 10^{-23} \text{ J/K}$ the Boltzmann constant. It marks the transition from collective thermal lattice vibrations to the independent atomic vibrations considered before. Physically, materials with high θ_D feature strong bonds and many collective vibration modes, the Dulong-Petit model will as such be a bad descriptor. A low Debye temperature on the other hand indicates weak bonds, little interaction between the nuclei's position, the Dulong-Petit and Einstein model of independent vibrations being a good descriptor. Throughout the rest of this section, the Debye phonon model is used.

2.5.2 Elastic scattering cross-section

In the presence of vibrations of the nuclei, the differential coherent elastic scattering cross-section is formed by correcting equation (2.38), derived for a rigid lattice, by the Debye-Waller factor

$$\left(\frac{d\Sigma}{d\Omega}\right)_{s,coh}^{el} = \frac{N\sigma_{coh}}{4\pi} \frac{(2\pi)^3}{V_0} |\bar{b}|^2 \sum_{\mathbf{\tau}} \delta(\mathbf{\kappa} - \mathbf{\tau}) e^{-2W(\mathbf{\kappa})}, \quad (2.47)$$

where $2W$ corresponds to the mean square displacement of a nucleus, weighed by κ^2 [48]. Thus, the Debye-Waller factor decreases with increasing temperature and larger κ . The height of the Bragg edges for higher (hkl) reflections at smaller wavelengths will generally decrease and the coherent elastic scattering eventually tend to zero in contrast to figure (2.8).

The **total elastic coherent scattering cross-section** then becomes (using the Debye model to evaluate the Debye-Waller factor) [54]:

$$\sigma_{coh}^{el}(E) = \sigma_{coh} \frac{\pi^2 \hbar^2}{2mEV_0} \sum_{\tau \neq 0}^{\leq 2k} \frac{w(\tau)}{\tau} e^{-\frac{3\hbar^2 \Phi_1(\theta)}{2Mk_B \theta_D} \tau^2}, \quad (2.48)$$

with m the neutron mass, M the nuclei's mass, $\theta = T/\theta_D$ the temperature relative to the Debye temperature and the function

$$\Phi_m(\theta) = \int_{-1}^1 \frac{\epsilon^m}{e^{\epsilon/\theta} - 1} d\epsilon. \quad (2.49)$$

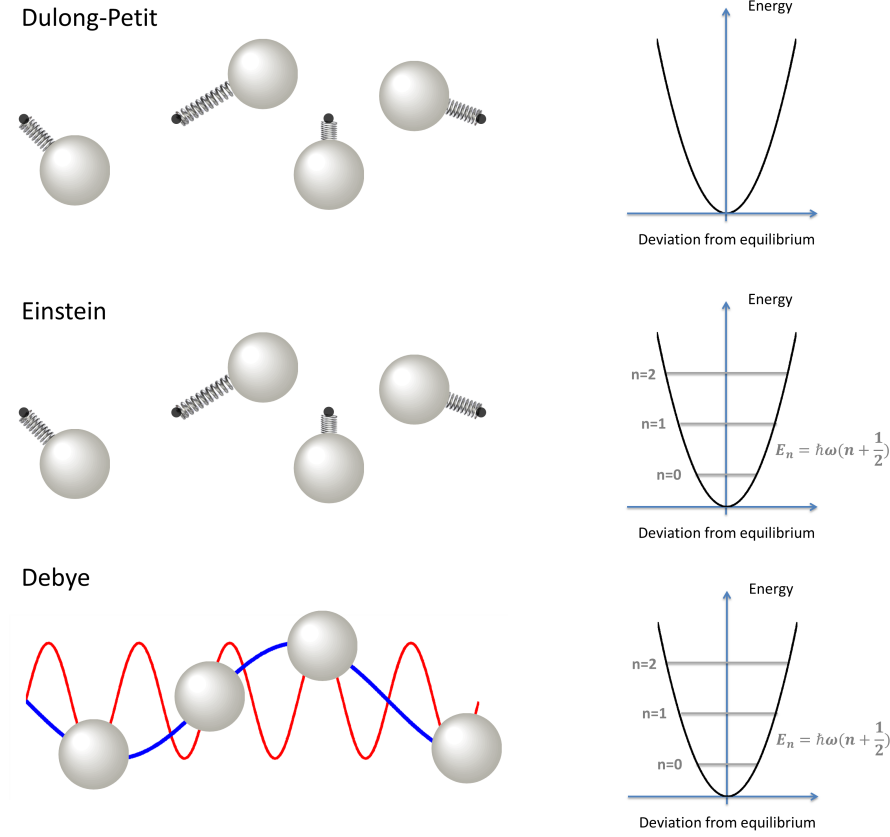


Figure 2.9: Schematic representation of the different lattice vibration models and associated energies. An example of a mode in the Debye model is shown by the blue line, the red one being an alternative albeit meaningless one above the Debye temperature.

The exponential Debye-Waller factor in equation (2.48) was also rewritten by Vogel in terms of an isotropic displacement factor B_{iso} to lend itself better to Rietveld refinement of Bragg edge transmission patterns in his BETMAN code [55], an approach overtaken by Boin in his more recent nxs simulation library [56]:

$$e^{-2W(\mathbf{\kappa})} := e^{-\frac{B_{iso}}{4d_{hkl}^2}}, \quad B_{iso} = \frac{3\hbar^2\Phi_1(\theta)}{Mk_B\theta_D}. \quad (2.50)$$

Likewise, the differential incoherent scattering cross-section for the static lattice is adjusted to

$$\left(\frac{d\Sigma}{d\Omega}\right)_{s,inc}^{el} = \frac{N\sigma_i}{4\pi} e^{-2W(\mathbf{\kappa})} \quad (2.51)$$

2.5. Scattering from a crystal lattice with thermal motion

and the **total elastic incoherent cross-section** becomes [54]

$$\sigma_{inc}^{el}(E) = \sigma_{inc} \frac{1}{12} \frac{M}{m} \frac{k_B \theta_D}{E \Phi_1(\theta)} \left(1 - e^{-12 \frac{m}{M} \frac{E}{k_B \theta_D} \Phi_1(\theta)} \right) \quad (2.52)$$

2.5.3 Inelastic scattering cross-section

A straightforward approach after deriving the elastic neutron scattering cross-section in which no energy with the crystal is exchanged, would be to consider interactions with the emission or absorption of only one phonon, then two, three, etc. However, the convergence of such a multiphonon expansion quickly worsens and its terms grow increasingly complex as the neutron energy increases [57]. Instead, Placzek suggested a mass expansion for the total incoherent cross-section of polycrystals built out of heavy nuclei [58, 59], later generalized by Wick [60] to include light nuclei:

$$\sigma_{inc}^{tot} = \sigma_{inc} \sum_{n=0}^{\infty} \left(\frac{m}{M} \right)^n A_n(E, \theta), \quad (2.53)$$

and the coefficients A_n are tabulated (e.g. in [48]) or can be calculated [54]. It is a rapidly converging series and usually only the first three terms are taken into account. The evaluation simplifies in the epithermal range - but also applicable over the thermal energy range - to [54]

$$\sigma_{inc}^{tot}(E) \approx \sigma_{inc} \left(\frac{M}{m+M} \right)^2 \left[1 + \frac{3mk_B \theta_D}{4ME} \Phi_3(\theta) \right]. \quad (2.54)$$

The **total inelastic incoherent cross-section** is then found by subtracting (2.52) from (2.54),

$$\sigma_{inc}^{inel} = \sigma_{inc}^{tot} - \sigma_{inc}^{el}. \quad (2.55)$$

For coherent inelastic scattering involving a single phonon, the allowed interactions are strongly restricted by the laws of conservation of energy and momentum, the one phonon cross-section being strongly peaked around certain scattered neutron energies and directions. However, for two or more phonons involved, much more scattering channels are open to the neutron and the coherent inelastic scattering cross-section becomes a smoothly varying function with negligible interference effects. Moreover, looking at the total cross-section introduces additional averaging over all solid angles and scattered neutron energies [45] and the scattering behaviour can be considered incoherent. This is known as the incoherent approximation, introduced by Placzek [61] in the limits of short and long wavelengths. Binder [62] found these approximations to be suitable also in the thermal region.

The **total inelastic coherent cross-section** is found as

$$\sigma_{coh}^{inel}(E) = \frac{\sigma_{coh}}{\sigma_{inc}} \sigma_{inc}^{inel}(E). \quad (2.56)$$

The partial cross-sections for the different interaction channels (absorption as well as scattering, both coherent and incoherent, elastic and inelastic) were simulated for iron using the `nx`s code [51], which is based on the formulas covered in this section.

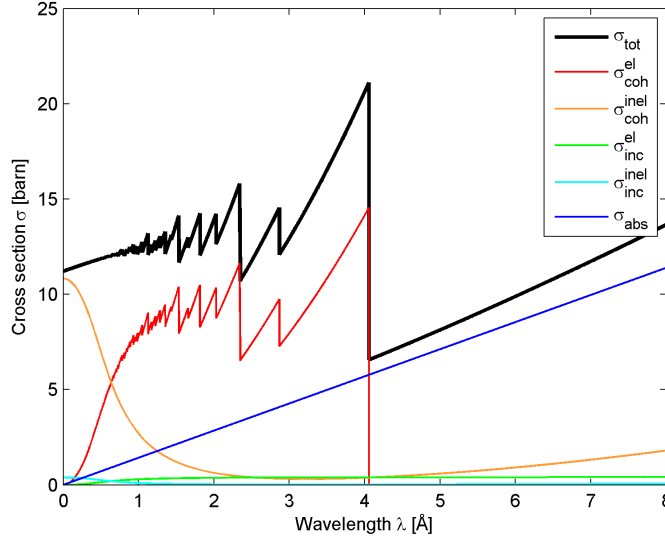


Figure 2.10: Total and partial cross-sections for α -iron simulated with nxs.

2.6 Application to neutron imaging

Now that we know what mechanisms are behind the final observed transmission spectrum, we can consider what information can be extracted from it. In other words, which sample properties can be mapped at high spatial resolution through energy-selective neutron imaging.

The Bragg edge pattern depends on the crystallographic phase. By comparing monochromatic radiographies at wavelengths slightly shorter and longer than a Bragg edge of a particular phase, one can enhance radiographic contrast for that phase compared to other phases with no Bragg edge at that position and a more slowly varying cross-section [32, 63].

Radiography at a wavelength slightly longer than the last and highest Bragg edge features increased sample penetration depths as the cross-section is lowest here. For instance, lead has an average microscopic cross-section of 11.4 barn in a polychromatic thermal spectrum versus only 1.4 barn at 6 Å, past the Bragg cut-off, increasing the penetration depth from 6 cm to 50 cm). Conversely, one can increase sensitivity of neutron imaging by radiography at wavelengths just short of the Bragg cut-off, where the cross-section is at its highest.

Preferred orientation or texture [50] can lead to large deviation of the Bragg edge pattern [51, 32]. Orientations that are overrepresented compared to the random distribution will lead to increased scattering (higher cross-section) for the corresponding Bragg wavelength at the expense of under-represented orientations. Mapping of texture variations across a sample of interest is thus possible [64].

Energy-selective neutron imaging past the Bragg cut-off, means scattering is suppressed and one becomes insensitive to the sample's crystallography. This strategy is exploited in chapter 4 and is shown to yield better quantitative results in specific cases.

The Bragg edge position itself is determined by the lattice spacing, which becomes smaller

or larger under compression or tension. The local shift in observed Bragg edge position is a measure for mapping strain across a sample [65, 66].

A schematic summary of the different modes of energy-selective imaging around Bragg edges is given in figure 2.11.

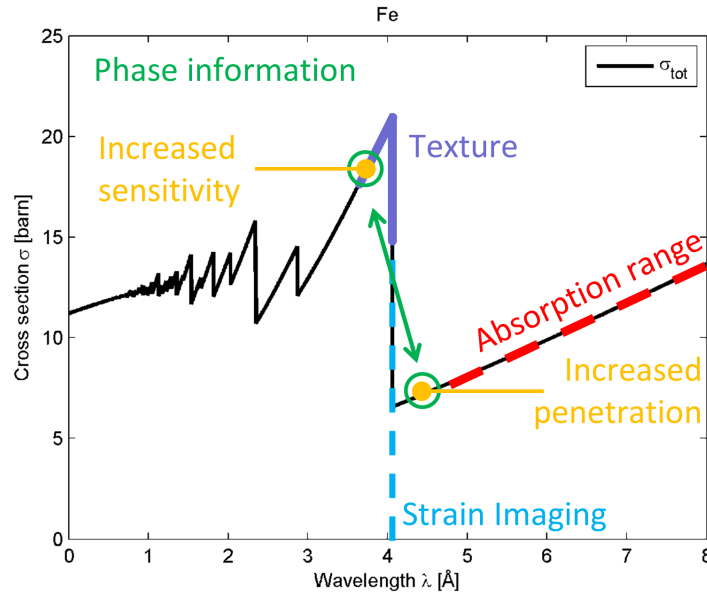


Figure 2.11: Schematic overview of the different modes of energy-selective neutron imaging of polycrystalline material.

In case of single crystals one no longer observes Bragg edges, but rather distinct Bragg peaks. The peak positions pattern can be used to map spatial variation in crystal orientation and the peak width is a measure for the local mosaicity. A limited number of pattern overlap (multiple crystallites in the beam direction) can be tolerated. Imaging strategies and applications in this regime are treated in chapter 5.

At the same time, when a single crystal undergoes diffraction and is fully illuminated by the neutron beam, Bragg's law implies that all these diffracted neutrons follow the same direction. One thus obtains a parallel projection of the single crystal in that direction, formed by diffracted neutrons at positions dependent on the crystal orientation. Even tomographic extension is possible, if data under multiple sample rotation angles is acquired. Chapter 6 discusses this unconventional neutron imaging modality, its advantages and disadvantages in more detail.

A schematic juxtaposition of both modes of crystal(lite) imaging is shown in figure 2.12.

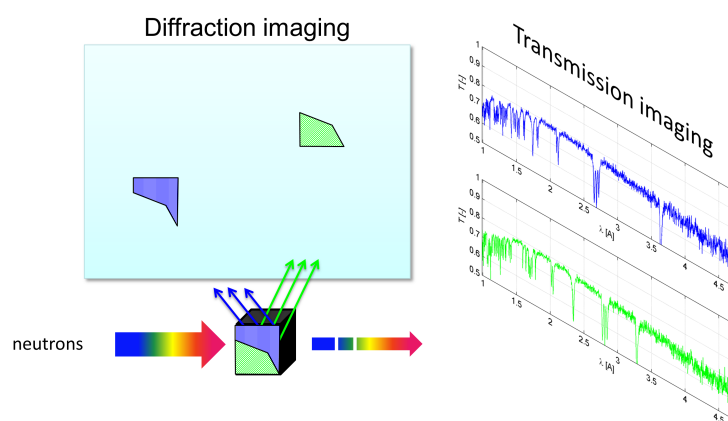


Figure 2.12: Schematic overview of neutrons of particular wavelengths being diffracted on the lattice planes of large crystallites, forming projections themselves used in diffraction imaging and intensity losses studied in transmission imaging.

3 Energy-resolving capability for neutron imaging

A prerequisite for energy-selective neutron imaging is the limitation of the wavelength band used in recording a radiograph, as otherwise the energy-dependency of the cross/section is averaged out over the incident polychromatic beam spectrum. This can be achieved in several ways.

At pulsed sources, one can use the time lag between the source pulse and the neutron arrival at the detector, which is representative for the neutron velocity i.e. its energy: the so called Time-of-Flight (TOF) method.

At continuous neutron sources however, one has to use a monochromator device to select the desired wavelength out of the incident polychromatic spectrum that is provided by the neutron source. Several types exist and most of them have their origin in neutron scattering, using a narrow pencil beam. However, it was found that their use with a broad, slightly divergent neutron beam as in neutron imaging will induce a spatial variation in delivered spectrum across the field of view. In this chapter, several monochromators are investigated and characterized w.r.t. energy-selective neutron imaging. After neutron filters, a mechanical neutron velocity selector is discussed, a double crystal monochromator and finally the newly developed *TESI* monochromator. The majority of the presented findings and conclusions have already appeared in publications by the author in [67, 25, 68].

3.1 Time of flight

If a pulse of neutrons is generated at time $t = 0$ and the neutrons are allowed to travel a certain distance L , then their arrival time t is indicative of their speed $v = L/t$, with L the flight path length. Using the De Broglie relation, one can link it to the neutron wavelength:

$$\lambda = \frac{h}{m_n L} t, \quad (3.1)$$

with h Planck's constant and m_n the neutron mass. Recording a radiograph with very short exposure time at time t means making a monochromatic image at wavelength λ .

E.g. Engin-X comes with a flight path of 50 m [69], so from eq. 3.1, a 0.01 Å wavelength bin around 1.8 Å corresponds to a radiograph of 125 μs exposure time, taken 22.7 ms after the pulse. Repeating the process for a series of periodic pulses and stacking the results, ensures sufficient neutron statistics. Typically such measurements are performed with a gated CCD

[32] or an MCP detector as described in section 1.6. The latter detector was also used for the time of flight imaging performed at ISIS (UK) that will be presented in chapter 5.

Alternatively, if one is only interested in the spectrum and no spatial information is required, one can use a ^3He counter [70] as well. This method is e.g. applied for determining the transmission spectra of the different monochromators characterized in the following sections.

The initial neutron pulse can be generated in several ways. At spallation sources, one can have pulses of protons hitting the spallation target, generating in turn pulses of neutrons. The final neutron pulse width depends on the initial proton pulse width and its further broadening in the moderator, due to the uncertainty on the number of collisions and path length of the neutrons in the moderator. However schemes exist to minimize such broadening, e.g. by having a decoupled moderator [9, 71] .

Also pulsed nuclear reactors have been built. The JINR institute in Dubna (Russia) operates the IBR-2 reactor, feeding several neutron scattering beamlines and with a project to develop one for neutron imaging newly initiated [72]. Its unique reactor design features a rotating reflector near a PuO_2 core, producing intense neutron pulses by making the reactor periodically super- and subcritical [73, 74].

At continuous sources, one has to use a chopper to make use of the time-of-flight method. A rotating disk, opaque to neutrons and featuring a narrow opening slit, chops up the continuous neutron beam into pulses.

The pulses should be sufficiently separated to avoid pulse overlap: the fastest neutrons in a pulse overtaking the slowest ones from the previous pulse. The wavelength uncertainty is directly related to the timing uncertainty (detector time bins and neutron pulse width), as from eq. 3.1 it directly follows $\Delta\lambda/\lambda = \Delta t/t$. Electronics offset and precise path length are usually calibrated for with a transmission wavelength scan of materials with a well-known Bragg edge, usually beryllium is taken with a Bragg cut-off at 3.959 \AA .

At pulsed sources using TOF imaging, capturing the whole field of view as a single time frame for a monochromatic image, the spectral distribution is inherently uniform across the field of view. Of course, the parallax of the field of view comes with a certain difference in path length for the neutrons hitting the center compared to the sides. However, the effect is negligible as a numeric calculation shows. For our 50 m flight path and taking a field of view of 10 cm, the path length difference is only $50 - \sqrt{50^2 + 0.05^2} = 25 \cdot 10^{-6} \text{ m}$, so for a thermal neutron travelling at 2200 m/s, a time difference of 11 ns only, well below the initial neutron pulse width and detector time binning in the order of tens of microseconds.

3.2 Filters

The simplest although coarsest and least flexible way of energy selection is having a filter of a material that cuts off part of the spectrum. This can either be by exploiting a strong neutron resonance (e.g. cadmium for filtering out thermal neutrons) or the Bragg cut-off. For the latter, one relies on the fact that the cross-section is higher on the lower wavelength side of the final Bragg edge than on the higher wavelength side. Having a sufficiently long neutron path

length through the material ensures only neutrons of wavelengths larger than the Bragg cut-off remain. The filter performance can be improved by cooling with e.g. liquid nitrogen. This will reduce the inelastic scattering component of the cross-section and increase transmission of wavelengths longer than the Bragg cut-off. By selecting the right material, one can tweak the wavelength cut-off, e.g. beryllium for 3.95 Å, graphite for 6.7 Å.

Working with the transmitted beam through the filter, the properties for imaging are not affected, apart from a reduced intensity. An example of a beryllium-filtered spectrum (recorded at ICON using the time-of-flight method, with a chopper and ^3He counter) and its practical realization at the ICON beamline is shown in figure 3.1. For technical reasons (design and reliability in an activated and inaccessible position), it is not cooled.

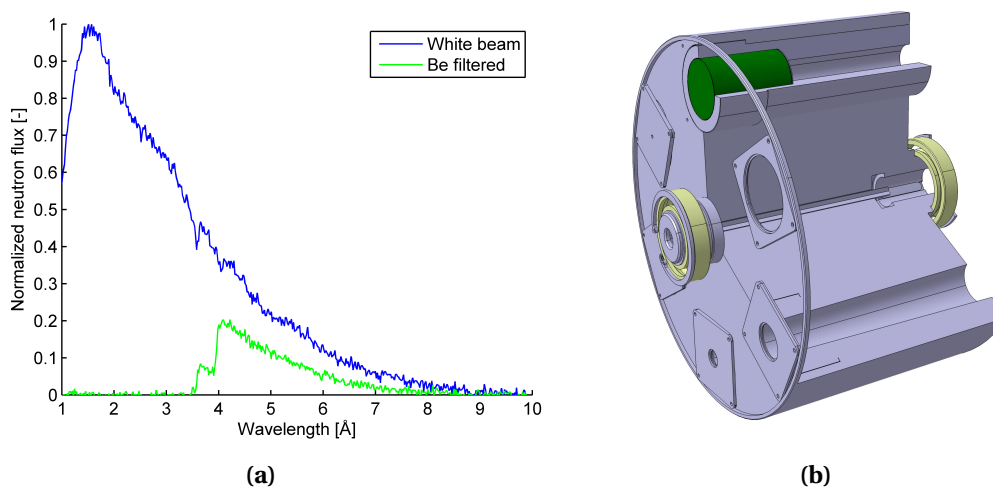


Figure 3.1: Recorded spectrum at ICON with a 100 mm thick beryllium filter in the neutron beam (a) and a 3D rendering of its incorporation (the green cylinder) in the aperture wheel (b).

3.3 Mechanical neutron velocity selector

3.3.1 Principle

A Mechanical Neutron Velocity Selector (MVS) consists of a rotating drum with twisted lamellae coated with a strong neutron absorber. Depending on its rotation speed, only neutrons of the right velocity or energy will pass through the device [75]. The resulting monochromaticity $\Delta\lambda/\lambda$ is given by the ratio of the opening angle of the blades over their twist angle. As such it is a fixed design property and usually on the order of 10%-15%. There is a limit to the shortest wavelength that can be chosen, lying around 2.5 Å- 3 Å, imposed by the maximum rotation speed of the device. Though the spectral width is quite wide, it also implies a reasonably high flux and limited increase in exposure time, making it the most suitable choice for investigating slowly varying energy-dependent effects – e.g. imaging across the Bragg cut-off at long wavelengths where the source intensity is low. The field of view is usually large (~ 10 cm). Such a device has been available at ICON since 2008 [24] and has been included in the ANTARES II upgrade at FRM II in München (Germany), online as of spring 2014.

The velocity selector type monochromator is common at Small Angle Neutron Scattering (SANS) beamlines [76] and has only recently been put to use at imaging beamlines as well. The broad beam characterizing the latter instead of a pencil beam has some important implications that will be discussed in this section.

Such a device has already been experimentally characterized in terms of (1) its positive influence on spatial resolution coming from additional beam collimation [77], and (2) the determination of central beam divergence by time-of-flight measurements of the output spectrum [78] as well. However, no information on the spectral distribution over the field of view is available but non-uniformities have clearly been observed [79, 80]. Here, the spatial and spectral neutron distributions are characterized, along with explanations of their origin and discussion on the implications for imaging data analysis.

3.3.2 Experiments

Three series of measurements were performed to characterize the change in wavelength over the field of view when using a neutron velocity selector, the results of which are presented and explained in the sections below. The experiments were conducted at the ICON beamline (PSI, Switzerland).

In the **first experiment**, an energy scan was made of an iron plate of 95 mm by 95 mm, with 5 mm thickness. Images of the sample and open beam were recorded from 2.8 Å to 6.0 Å in steps of 0.1 Å. A 100 μ m thick ^6Li ZnS scintillator was used in combination with an Andor CCD camera of 1024 \times 1024 pixel. Any shift in the incoming neutron wavelength distribution over the iron plate implies a change in the transmitted spectrum which affects the Bragg edge position measured as a function of the velocity selector wavelength setting. This Bragg edge position was determined pixel by pixel by the position of the minimum of the derivative of the measured wavelength-dependent cross-section. The principle is schematically depicted in figure 3.2. The comparison of the physically constant (110) Bragg edge at 4.05 Å with the experimental data yields a wavelength shift map for this wavelength.

In a **second experiment**, the evolution of the wavelength shifts over the field of view is studied for all wavelengths in comparison to the 4.05 Å ((110) reflection) using the method described above. An energy scan was made of a 95 mm \times 90 mm \times 3 mm vanadium plate. This material is predominantly an incoherent scatterer with negligible coherent scattering cross-section (see section 2.3). As such, the total cross-section of Vanadium exhibits no Bragg edges and is monotonously increasing according to a linear function of the wavelength (Figure 3.3). Thus any difference in incident beam wavelength distribution over the plate results in a different transmission wavelength-integrated intensity on the detector. Transmission images were obtained with the same detector set-up as above for wavelengths from 2.8 Å to 6.0 Å in steps of 0.1 Å.

In a **third experiment**, the shift in wavelength over the field of view for a 4 Å velocity selector wavelength setting was determined through time-of-flight. A chopper running at 50 Hz was used in combination with a ^3He counter tube. Its entrance window was 29.2 mm \times 25.5 mm

and flight path length 7098 mm. The monochromatic beam spectrum was measured for five steps of 25.5 mm in the vertical direction. The vertical slit entrance window of the chopper does not allow for horizontal stepping.

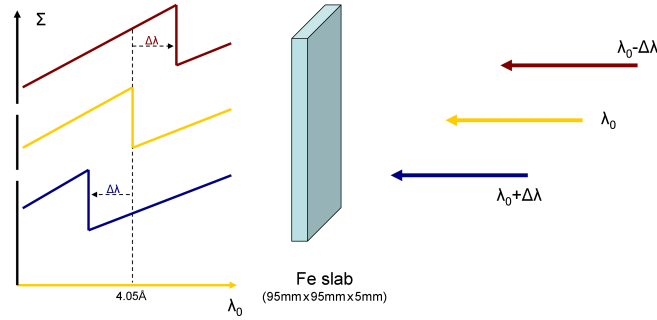


Figure 3.2: The wavelength shift ($\Delta\lambda$) over the field of view is measured by macroscopic cross-section (Σ) across a 5 mm thick iron plate setting a series of velocity selector wavelengths (λ_0).

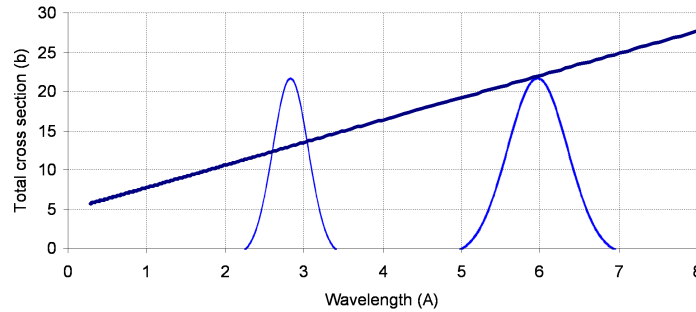


Figure 3.3: Total wavelength-dependent cross-section of vanadium (dark blue line) together with simulated beam wavelength distributions at two specific velocity selector frequencies as illustration.

3.3.3 Device description

The mechanical neutron velocity selector available at the ICON beamline is mounted at position 1, close to the beam port (see figure 3.4) at 2.5 m from the beam entrance aperture. It was originally constructed at Risø (Denmark) in 1980 to be used on a SANS machine and later on recycled at ICON. It is a user-friendly device mounted on rails to easily slide it in and out of the beam.

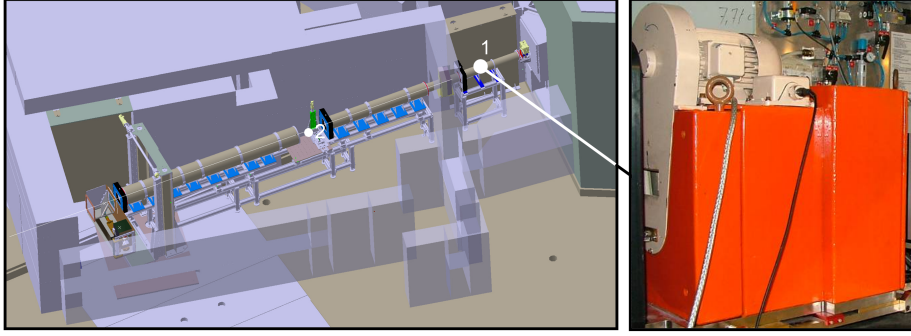


Figure 3.4: ICON beamline layout (left) equipped with the mechanical velocity selector (right).

The wavelength setting is integrated to the beamline operating software. The device has been calibrated at the beam center through time of flight measurements using a chopper and a ^3He counter (figure 3.5). The minimum wavelength lies at 2.75 \AA and monochromaticity $\Delta\lambda/\lambda$ at 15%.

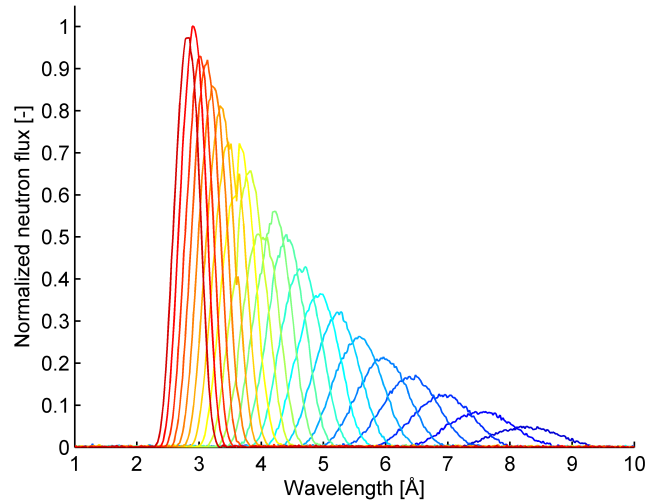


Figure 3.5: Beam spectra after monochromatization with the mechanical neutron velocity selector at the ICON beamline.

The relevant velocity selector parameters are listed in Table 3.1 , with turbine blade subtending angle (α), drum length (L), average blade radius (R) and number of lamellae (N). The opening angle β between to blades is given by $360^\circ/N$.

α	L	R	N
12.5°	400 mm	82.5 mm	156

Table 3.1: Velocity selector parameters at the ICON beamline.

A wavelength change over the field of view is inherent to the use of a neutron velocity selector. The wavelength shift is generated by the change in horizontal divergence over the field of view. Following the framework suggested by Hammouda [76], the neutron wavelength and monochromaticity after beam passage through the velocity selector is given by:

$$\lambda = \frac{\alpha_{eff} h}{L m_n \omega} \quad (3.2)$$

$$\frac{\Delta \lambda}{\lambda} = \frac{\beta}{\alpha_{eff}} \quad (3.3)$$

$$\alpha_{eff} = \alpha + \gamma \frac{L}{R} \quad (3.4)$$

where λ is the neutron wavelength after the velocity selector, ω the rotation frequency and γ the horizontal tilt (with sign) of the incoming neutron beam with respect to the velocity selector rotation axis - or in the reference frame of the velocity selector, the divergence of the incident neutrons w.r.t. the central ray. The constants h and m_n denote Planck's constant and the neutron mass respectively. The relation (3.2) is obtained by equating the neutron flight time over the distance L to the opening time of the revolving skewed turbine blades. The monochromaticity is found as the ratio of the opening angle of the blades compared to the blade tilt and for the numbers in table 3.1, estimated as $\Delta \lambda / \lambda = 18\%$.

For these experiments, conducted at position 2 (7.1 m from the aperture), the maximum horizontal divergence γ_{max} of the incoming neutrons that hit the side of a 100 mm x 100 mm field of view is approximately 0.4° . Using the parameter values listed in table 3.1 it is possible to calculate the horizontal wavelength shift expected when setting the device to calibrated rotation frequency for 4.05 Å. An estimate of 1.3 Å wavelength shift over the field of view is obtained.

3.3.4 Results and discussion

A map of the wavelength deviation $\Delta \lambda$ over the field of view with respect to the velocity selector's calibrated wavelengths at the beam center is given in figure 3.6a. For each pixel, the transmission intensity across the iron plate versus the set wavelength was recorded, and the measured wavelength setting for the (110) Bragg edge was determined and compared to the known real physical value of 4.05 Å to get the shift map. The experimental Bragg edge position was determined by fitting a Gaussian to the derivative of the transmission spectrum, with a final uncertainty of about 2%. In summary, a shift in incident wavelength over the field of view is observed to be 1.3 Å over 95 mm horizontally and 0.5 Å over 95 mm vertically.

Experimental data are in good agreement with estimated values in the previous section. However, assuming a symmetrical horizontal divergence γ , the above formalism does not provide any explanation for the diagonal trend observed in the shift map.

The measurement has been repeated with the iron plate rotated by 90° around its normal axis. However, no significant change in the results has been observed, ruling out the possibility of it being due to spatial inhomogeneity of any kind (e.g. texture) within the iron plate.

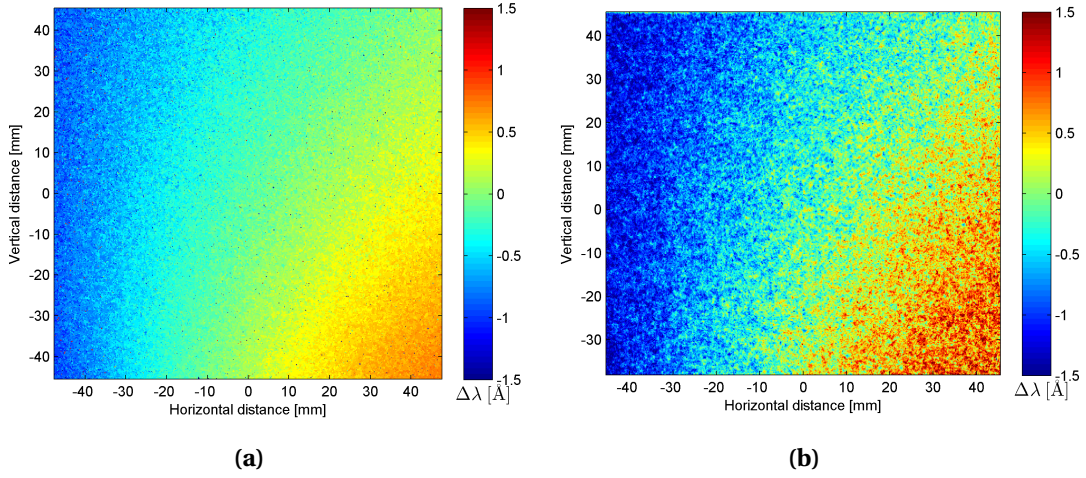


Figure 3.6: (a) Wavelength shift map at 4.05 Å determined from the Fe Bragg edge measurements and (b) wavelength shift map at 6 Å determined from the vanadium plate measurement.

The incident horizontal and vertical beam divergence was measured by rotating a 10' neutron Soller collimator [81] in these respective planes. Such a collimator exists of a series of neutron absorbing gadolinium foils, parallel to each other and with a certain spacing in between which determines the collimator's acceptance angle. The beam divergence was found symmetric, even though the beam port insert itself (so called "Zapfen unit") is slightly asymmetric [82]. The diagonal trend must therefore be attributed to the device itself.

A misalignment of the velocity selector drum (of the device as a whole or given its history of the drum within the device) with the incident beam is thus expected to be the cause.

Moreover, the implications of having the velocity selector entrance window on the upper side of the device should be considered. It is thus sensitive to horizontal divergence and spatial variation in central wavelength lies dominantly in the horizontal direction. Conditions for energy-selective tomography are thus not ideal. Reconstruction algorithms, as covered in section 1.4, assume a constant averaged scalar cross-section in each sample volume element. However, under rotation the projected position of such a volume element changes horizontally within the field of view. The neutron wavelength traversing the volume element thus also changes under rotation and with that the recorded cross-section contribution to the projection. A tomography covering 360° is therefore recommended instead of 180°, as it will tend to better average out the arising artifacts.

However, the effective wavelength bandwidth that affects the reconstructed cross-section will be broader than the original velocity selector monochromaticity. Changes in incident spectrum across the field of view have been studied extensively by the X-ray community, where the so-called *heel effect* [83] occurs when using a directional X-ray tube: X-rays leaving the target head in one direction travel a longer distance through the target than in another direction and their spectrum is hardened more.

The wavelength shift over the field of view at other wavelengths, was determined from the vanadium plate energy scan, setting different wavelength values. As the vanadium macroscopic cross-section is a monotonous linear increasing function of the neutron wavelength, the measured transmission over the plate can directly be related to the incident beam wavelength. A correction for neutron scattering contributions was preliminarily made by comparing a vanadium transmission image at 4.05 Å to the iron plate shift map; the latter being based on the measurement of the Bragg edge position so that the influence of scattering can be neglected. As the scattering cross-section for vanadium is approximately constant over the energy range under investigation, 2.8 Å- 6 Å, the single calibration at 4.05 Å can be applied to the whole set of data.

As an illustration, the wavelength shift over the field of view at 6 Å is shown in figure 3.6b. In comparison with the data of the iron plate, the higher noise levels are caused by a larger sensitivity to noise in original transmission data (lower flux at longer wavelengths) and by additional contribution of the Bragg edge based shift map noise induced by the calibration method.

Exploiting equations 3.2 and 3.4, it is possible to derive the relation between the wavelength shift map $\Delta\lambda_1$ and its calibrated beam center wavelength λ_1 ,

$$\frac{\Delta\lambda_1}{\lambda_1} = \frac{\gamma L}{\alpha R} \quad (3.5)$$

The right side of the equation is constant at each position over the field of view, so that, once a single shift map $\Delta\lambda_0$ at λ_0 is determined, it is possible to derive it for any other wavelength setting:

$$\frac{\Delta\lambda_1}{\lambda_1} = \frac{\Delta\lambda_0}{\lambda_0} \quad (3.6)$$

Figure 3.7 plots $\Delta\lambda/\lambda$ of vanadium at two extreme positions of the field of view scanned over the whole 2.8 Å- 6.0 Å wavelength range. The positions are the top left and bottom right corner (see figure 3.6), since they exhibit the largest negative and positive shifts respectively, illustrating equation 3.6. Uncertainty bars denote the standard deviation on the data obtained as a 10 x 10 pixel average and is largely due to noise. Thus, it suffices to measure the wavelength shift map over the field of view only once, e.g. with the Bragg edge method, and derive it for all wavelengths through pixelwise evaluation of equation 3.6.

Finally, the wavelength shift in the vertical direction was measured with TOF. Results are summarized in table 3.2, together with the results of the iron Bragg edge based method, averaged over the time of flight window for direct comparison.

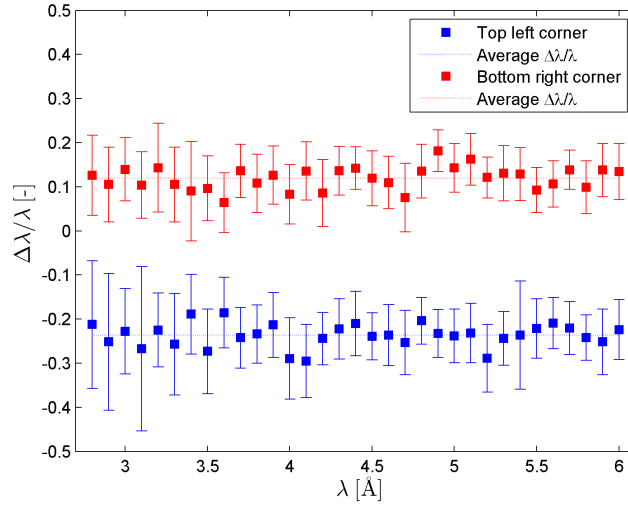


Figure 3.7: $\Delta\lambda/\lambda$ at top left and bottom right position for the vanadium plate wavelength scan as given in figure 3.6.

Vertical position	Time of flight	Fe ₍₁₁₀₎ Bragg edge
35.4 mm	0.21 Å	0.20 Å
17.7 mm	0.10 Å	0.08 Å
0.0 mm	-0.03 Å	-0.03 Å
-17.7 mm	-0.17 Å	-0.14 Å
-35.4 mm	-0.24 Å	-0.23 Å

Table 3.2: Vertical wavelength shift measurement determined through time of flight, compared to results obtained through iron Bragg edge measurement.

3.3.5 The velocity selector at ANTARES

A new mechanical neutron velocity selector has been installed at the ANTARES II beamline, developed by ASTRIUM GmbH. For comparison, its spectral non-uniformity has been investigated in the same way. The main construction parameters are given in table 3.3. For a field-of-view of 15 cm at 9 m from the pinhole, the maximal beam divergence is $\pm 0.49^\circ$. The expected difference in central wavelength across it, using equations (3.2) and (3.4), is then 0.36 Å. The monochromaticity is estimated according to eq. (3.6) as $\Delta\lambda/\lambda = \frac{360^\circ/144}{23.5^\circ} = 10.6\%$, close to the 10% listed by the manufacturer in its specification sheet.

α	L	R	N
23.5°	250 mm	115 mm	144

Table 3.3: Velocity selector parameters at the ANTARES II beamline.

Figure 3.8 shows the mapping of the experimental deviation in central wavelength compared to the 4.05 Å Fe(110) Bragg edge position, which is indeed of that magnitude. It is notable that here the pattern is indeed symmetric and the wavelength gradient is now in the vertical direction. As can be seen from a photograph of the device, the neutron beam goes through the left side of it, *i.e.* the blades lie horizontally w.r.t. the neutron beam and it is the vertical divergence that causes the shift in central wavelength. The horizontal divergence causes the slightly stronger gradient on the right side of the map than on the left, as a slightly different velocity selector radius is seen by these neutrons (eq. 3.4). In this case, the effective spectral distribution affecting the reconstructed tomographic slices will not be broadened and corresponds to the velocity selector's monochromaticity. However, a gradient will be present along the reconstructed sample's height.

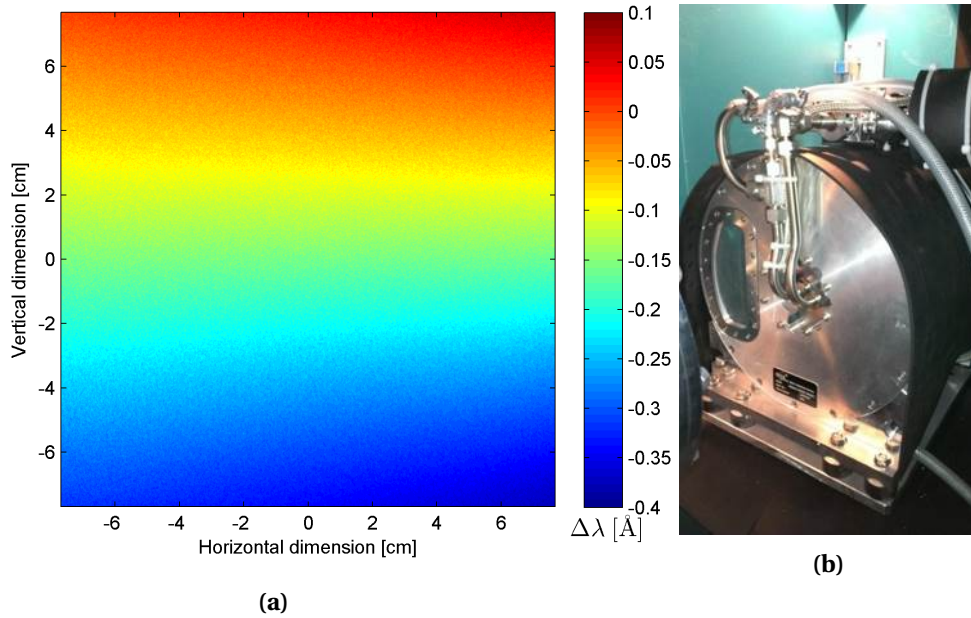


Figure 3.8: (a) Deviation between the observed central wavelength setting λ_{obs} and the actual constant physical one for the (110) iron Bragg edge at 4.05 Å. (b) Photograph of the velocity selector installed at the ANTARES II beamline.

3.3.6 Conclusion

The variability in the incident neutron beam wavelength distribution over the field of view, related to using a mechanical velocity selector monochromator was determined by the combination of three different experiments. A difference in measured Bragg edge position of an iron plate resulted in a wavelength shift map at 4.05 Å. Time of flight measurements confirmed the result. A wavelength scan of a vanadium plate demonstrated that from one wavelength shift map, it is possible to extrapolate the maps for other beam center selected wavelengths.

The knowledge of the shift map is the first crucial step towards correcting energy-selective radiographies and tomographies of large objects experiencing different incident beam wave-

lengths over the full sample. For small samples and fields of view ($\sim 15 \text{ mm} \times 15 \text{ mm}$), as are typical in high-resolution tomography, the wavelength change can be ignored.

Alternatively, the different incident beam wavelength over the field of view can also be exploited to make short wavelength scans by simply translating the sample over the field of view. A clear advantage of this method is the need of one open beam image only to calculate wavelength-dependent transmission, instead of taking one at every velocity selector wavelength setting, effectively increasing the wavelength scan speed.

3.4 Double Crystal Monochromator

Some applications (e.g. residual stress mapping), need a higher energy-resolution. Here, a Double Crystal Monochromator (DCM) might be used instead. It is based on obtaining the desired wavelength by Bragg reflection from a crystal:

$$2d \sin \theta = n\lambda, \quad (3.7)$$

d being the used crystal plane spacing, θ the set crystal angle, λ the reflected wavelength of order $n = 1, 2, 3, \dots$. A second crystal is then used to diffract the beam back to its original direction, although now translated compared to the original one. This is the so-called $(+n, -n)$ configuration. The non-reflected neutrons are absorbed on a beam dump. In neutron imaging, generally pyrolytic graphite's (002) reflection is used with higher order reflections $\lambda/2, \lambda/3, \dots$ ($n=2, 3, \dots$ in equation 1) suppressed with a Be filter [84, 85]. The monochromaticity is in general 2%-5% depending on the set wavelength and mosaicity of the crystals used.

Also here, the use of a broad, slightly divergent beam has consequences on the spatial variation of the final incident wavelengths over the field of view.

3.4.1 Device description

A double crystal monochromator is installed at the BOA beamline, its design shown in figure 3.9. The crystals are made of pyrolytic graphite with a mosaicity of 0.6° . The $32 \text{ 1} \times 2 \text{ cm}^2$ crystals are placed in two holders (one for each reflection) constituted of two rows of 8 crystals each. Without any collimation downstream from it, the DCM provides a rather homogeneous field of view of about $5 \times 5 \text{ cm}^2$. Only by adding a 10' vertical collimation the Field Of View (FOV) no longer appears homogeneous due to the limitation of divergence-based smearing and shows a distinct minimum corresponding to the vertical separation of the two crystal rows. In the horizontal direction such an effect is not visible. The device was upgraded in summer 2014, with the replacement of the small crystals with two $10 \times 5 \text{ cm}^2$ crystals of 0.8° mosaicity in order to provide a more uniform field of view. The wavelength range of this device is $2.4\text{-}6 \text{ \AA}$, with a peak width (full width at half maximum) of $\approx 0.05 \text{ \AA}$ measured by time of flight.

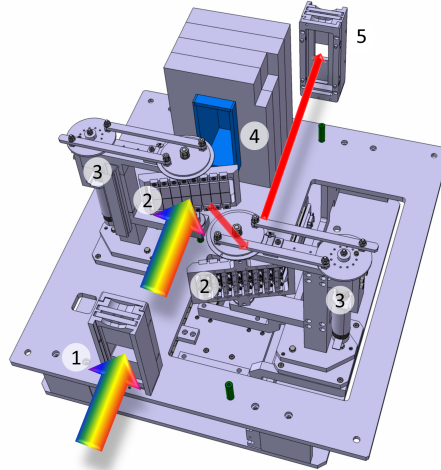


Figure 3.9: Schematics of the layout of the DCM available at BOA. In this figure, the main components are highlighted: the entrance slit (1), the two crystal rows providing the energy selection (2), the linear and rotation motors providing control over the position and angle of the crystals (3), the beam dump (4) and the exit slit (5). The casing and the magnets providing the guiding field are not drawn for clarity. The arrows show the neutron path.

3.4.2 Spatial variation of the spectrum across the field of view

Working with a large field of view means a slightly different angle for neutrons illuminating one edge of the field of view *versus* neutrons hitting the opposite edge. This small change in incidence angle on the crystals, translates in a small change in reflected wavelength, following Bragg's law (eq. 3.7). As with the velocity selector, the broad neutron beam that marks neutron imaging, will also cause a small variation of the spectrum across the field of view. The effect is illustrated schematically in figure 3.10.

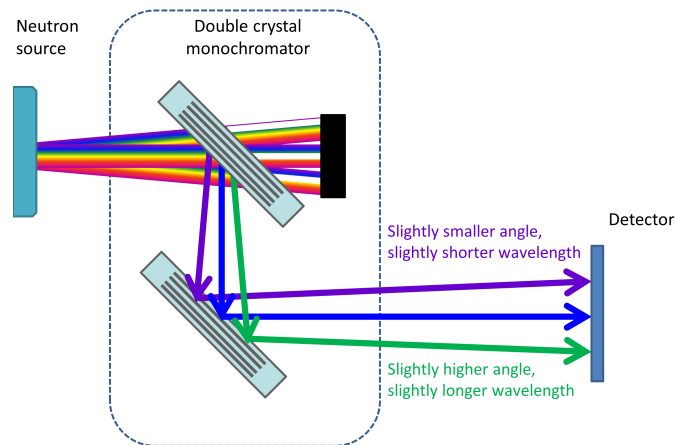


Figure 3.10: Schematic top-down view on the BOA double crystal monochromator. Neutrons hitting the left of the detector-screen (looking downstream) have a slightly smaller Bragg angle w.r.t. the crystals, selecting out a slightly smaller wavelength than the central neutron rays. The opposite is true for neutrons hitting the right of the field of view.

As the crystals are mounted vertically at BOA, the wavelength gradient will be in the horizontal plane. The spectrum was recorded with the time-of-flight method, using a combination of a chopper and ^3He counter for set monochromator wavelengths of 3 Å, 4 Å, 5 Å and 6 Å. The mean incident wavelength varied by ~ 0.05 Å over 5 cm, see figure 3.11a. For a two dimensional mapping of the wavelength variation, again the Bragg edge of an iron plate was scanned. It illustrates nicely how only the horizontal beam divergence plays a role. Results agree with an estimate based on Bragg's law (eq. 3.7): with $d_{PG(002)}=3.36$ Å, a wavelength of $\lambda=4.05$ Å is selected by setting a Bragg angle of $\theta_B=37.06^\circ$. With the detector at 6 m downstream of the aperture and a field of view of -3 cm to 5 cm around the beam center, the actual Bragg angles for neutrons hitting the left and right of the scintillator screen are corrected by $-\text{atan}(3/600) = -0.286^\circ$ and $\text{atan}(5/600) = 0.477^\circ$. The selected wavelengths thus vary by 0.072 Å.

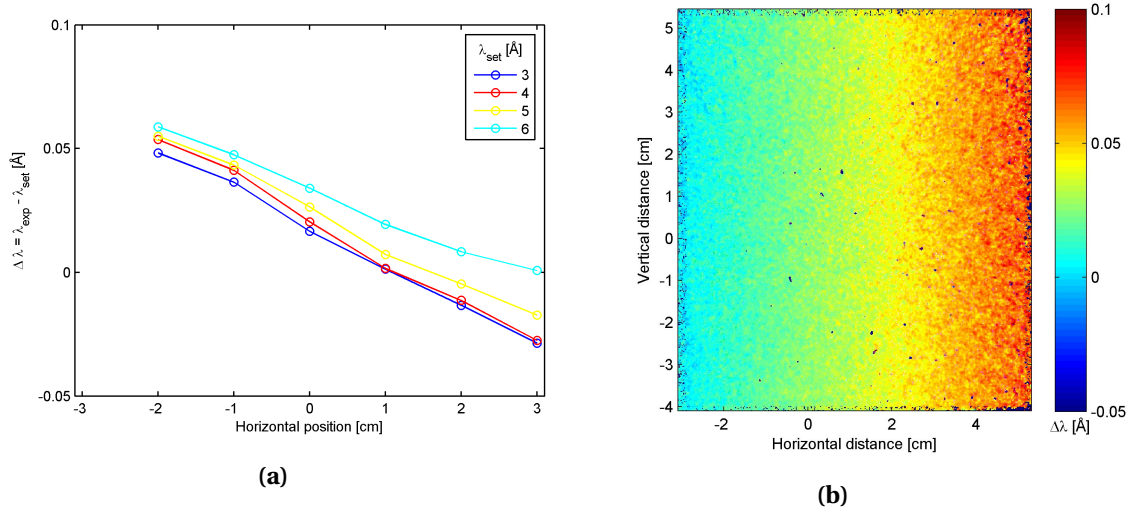


Figure 3.11: Horizontal variation across the field of view of the peak wavelength selected by the double crystal monochromator as determined through time-of-flight (a) and a two dimensional mapping of the peak wavelength position through scanning of the iron (110) Bragg edge.

3.4.3 Higher order contamination of the spectrum

The second effect is due to the higher order Bragg diffraction that occurs in the crystal for $n = 2, 3, \dots$ in the Bragg's formula (eq. 3.7). For an angle that should diffract the wavelength λ , the Bragg condition is also fulfilled by $\lambda/2$ and $\lambda/3$ (and so on), resulting in spurious contributions from higher energy neutrons in the spectrum. This effect is unavoidable in a $(-n, +n)$ configuration. Given the incident spectrum of BOA, this effect becomes very substantial at higher wavelengths, when the flux is low and the second order wavelength falls in a region of the spectrum where the flux is high. This effect was measured, and proved to be non-negligible as shown in figure 3.12. Here, the recorded spectra for four different settings of the double crystal monochromator are plotted, together with the relative intensity contribution of the different orders to the total number of registered neutrons. It is clear that the amount of contamination from higher order diffraction increases with the wavelength, becoming actually higher than the first order component at 6 Å. Little neutron flux is available at this

3.4. Double Crystal Monochromator

long wavelength, whereas the incident BOA spectrum reaches its maximum right around 3 \AA at the wavelength of the second order component. Figure 3.13 shows a measured transmission spectrum through a 5 mm thick nickel plate and a 4 mm thick BCC iron single crystal as measured with the double crystal monochromator. Spurious Bragg edges and Bragg dips are clearly observed due to higher order contamination: no diffraction for BCC iron is possible above 4.05 \AA and yet a Bragg dip is observed at 5.4 \AA , a reproduction of the dip at 2.7 \AA by second order diffraction. Thus, the use of filters (e.g. beryllium) is highly recommended when using the double crystal monochromator.

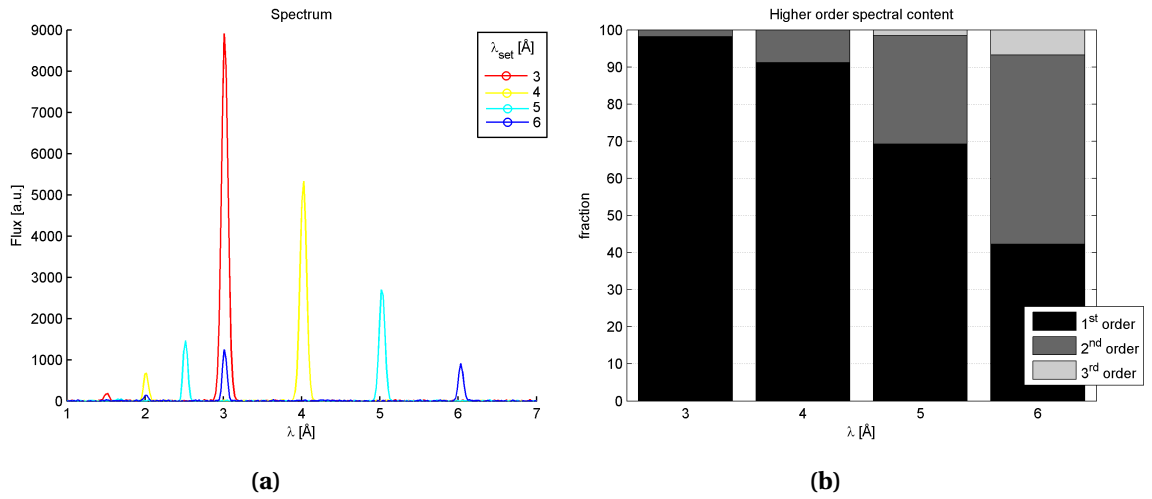


Figure 3.12: Recorded time of flight spectra for the double crystal monochromator set to 3 \AA , 4 \AA , 5 \AA and 6 \AA (a), with the relative contributions of the higher order components to the total number of neutrons as registered by an imaging detector.

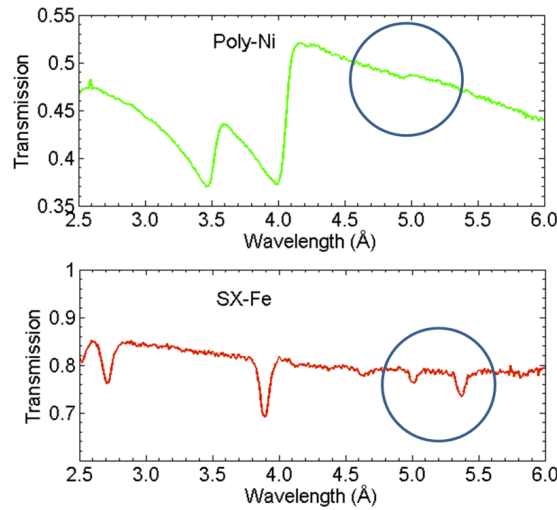


Figure 3.13: Transmission spectrum through 5 mm polycrystalline nickel (top) and 4 mm single crystalline BCC iron (bottom). Spurious Bragg edges and Bragg dips due to higher order contamination of the spectrum are marked.

Alternatively, $\text{Si}_{(111)}$ and $\text{Ge}_{(311)}$ monochromators have their 2nd order reflections forbidden based on crystallographic grounds as the corresponding structure factor equals zero. However, such crystals are of such high quality and reflect such a narrow spectral band that exposure times would be impractical for imaging purposes. Deformation by hot bending and flattening does increase the mosaicity [86], though such treatment is not really available off the shelf and would be very costly (in terms of time and money). Therefore the choice falls on pyrolytic graphite for neutron imaging and a Be filter to remove higher order contributions for first order wavelengths above 4 Å at the cost of increased attenuation. Alternatively, one can use a third pyrolytic graphite crystal set to scatter out the second order contribution.

3.5 TESI - a Transmission based monochromator for Energy-Selective Imaging

In this section, we present a newly developed type of monochromator, named Transmission based Energy-Selective Imaging (TESI), where a set of crystals is used to flexibly filter the MVS spectrum of $\Delta\lambda/\lambda \approx 15\%$ further down to $\Delta\lambda/\lambda \approx 2 - 5\%$ through the out-scattering of undesired wavelengths. As such, one can work with the transmitted beam of high monochromaticity without higher order contamination and keeping the original divergence (and thus spatial resolution). The beam is not displaced which eases compatibility with other present imaging plugin devices (e.g. for grating interferometry).

3.5.1 Principle

A schematic representation of the TESI principle can be found in figure 3.14. First the rotation frequency of the MVS is set to the desired central wavelength λ . The resulting Gaussian wavelength pass-band is still quite wide with $\Delta\lambda/\lambda \approx 15\%$ (figure 3.14a). They are removed by adding a pair of crystals of low mosaicity $\Delta\theta_1$, set to diffract a small wavelength band before and after the peak in MVS spectrum at $\lambda \pm \delta\lambda_1$ (figure 3.14b) will reduce the width of the central peak in the transmitted beam spectrum. However, two secondary wavelength peaks or side lobes at $\lambda \pm \delta\lambda_2$ are still present as the remainder of the original broad MVS spectrum. By adding a second pair of crystals and setting them to diffract these wavelengths out of the original beam direction (figure 3.14c). Being further away from the central peak, one can use crystals of higher mosaicity $\Delta\theta_2$ that can diffract out a larger wavelength range without compromising the central peak. A third and a fourth crystal pair can be added to further suppress the induced side lobes (particularly at long wavelengths). Using the beam transmitted through matched pairs of crystals in combination with a MVS, the collimation of the monochromatized beam that reaches the sample are unchanged and its spectrum does not contain higher-order contributions.

3.5. TESI - a Transmission based monochromator for Energy-Selective Imaging

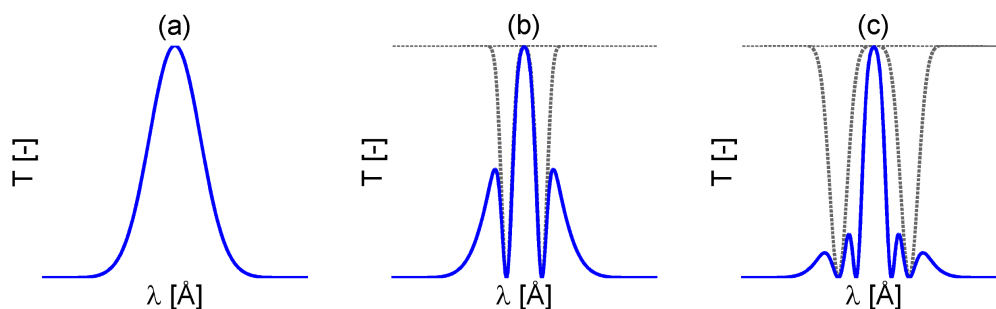


Figure 3.14: TESI principle: starting from the transmission spectrum of the mechanical velocity selector (a), a first crystal pair of low mosaicity is added (b) after which a second crystal pair of higher mosaicity is added to lower the side lobes (c). The total transmission spectrum is indicated by the solid blue line and the crystal transmission spectra by the dashed gray one.

3.5.2 Design

TESI is designed as a plug-in device that can easily be mounted in front of the MVS at the ICON beamline. It has capacity for ten crystals, mounted on independently controllable rotation stages with an accuracy of 0.005° . The control of the stages is integrated in the beamline operating system for user-friendly remote manipulation of the positions. Unused crystals can be flipped out of the beam instead of being removed from the device, so as to preserve calibration. Currently eight highly oriented pyrolytic graphite crystals of varying mosaicity (see calibration subsection 3.5.3) are installed, measuring $40 \text{ mm} \times 10 \text{ mm} \times 5 \text{ mm}$ (width x height x thickness). A shielding unit, comprising of 32 mm boron carbide plastic and 30 mm of lead featuring a $10 \text{ mm} \times 10 \text{ mm}$ window, is present to protect the motors and electronics from radiation damage and activation. A 3D drawing of the device is shown in figure 3.15.

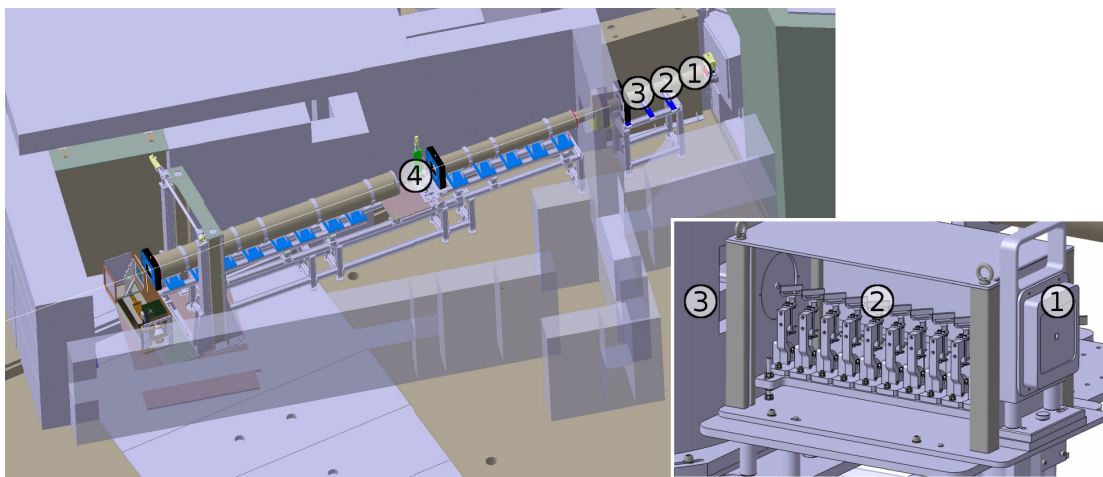


Figure 3.15: TESI (right, inset) device installed at the ICON beamline (left). Neutrons enter the device from the right, passing through shielding aperture (1), crystals (2), mechanical velocity selector (3) and detected at position (4).

3.5.3 Calibration

All crystals have been characterized using the time-of-flight technique and their alignments within the TESI device calibrated. To this end, a chopper was used spinning at 7.17 m upstream of a synchronized ^3He counter tube having 512 time bins of $35\ \mu\text{s}$, providing a resolution of $0.019\ \text{\AA}$ per bin.

The transmission spectrum was recorded for each crystal separately and for diffraction wavelengths λ_{set} from $3\ \text{\AA}$ - $6\ \text{\AA}$ in steps of $0.25\ \text{\AA}$. Subsequently, it was fitted over a relevant wavelength range $\lambda_{set} - 3\sigma_{MVS} \leq \lambda \leq \lambda_{set} + 3\sigma_{MVS}$, with σ_{MVS} the standard deviation of the MVS Gaussian transmission spectrum. The crystal behaviour can then be summarized by a constant transmission level in combination with a Gaussian profile for neutron diffraction from the (002) planes. Pyrolytic graphite crystals, however, are not single crystals, their crystal planes are aligned only in one direction, $[00\ell]$, and scattering from non-(00 ℓ) planes can occur for wavelengths until $4.25\ \text{\AA}$ causing reduced transmission and possible asymmetry around the (002) diffraction wavelength [87]. The continuous fit function thus becomes:

$$\begin{cases} T_l - Ae^{-\frac{(\lambda-\lambda_0)^2}{2\sigma^2}} & \lambda \leq \lambda_0 \\ T_r - [A + (T_l - T_r)]e^{-\frac{(\lambda-\lambda_0)^2}{2\sigma^2}} & \lambda > \lambda_0 \end{cases} \quad (3.8)$$

Here, T represents the general transmission level left ($T_l, \lambda \leq \lambda_0$) and right ($T_r, \lambda > \lambda_0$) of the observed central wavelength λ_0 differing from λ_{set} thus giving information on angular offsets that can be used for calibration. The amplitude A characterizes the filtering strength of the crystal and the standard deviation σ is representative for the filter width (mosaicity). An example of the fitted transmission spectrum is presented in figure 3.16.

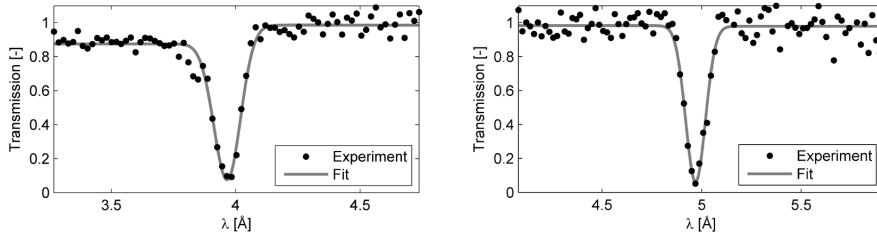


Figure 3.16: Recorded and fitted transmission profile of crystal 2, set for diffraction at $\lambda_{set}=4\ \text{\AA}$ (left) and $5\ \text{\AA}$ (right).

The obtained mosaicities of the different crystals are summarized in table 3.4, converted from fitted $\sigma\ [\text{\AA}]$ to the more commonly used $\Delta\theta\ [^\circ]$, the full width at half maximum of the Gaussian diffraction intensity versus crystal angle profile using equation 3.7.

Crystal No.	1	2	3	4	5	6	7	8
$\Delta\theta\ [^\circ]$	0.4	0.5	0.4	0.4	1.1	1.0	1.7	1.7

Table 3.4: Experimentally determined mosaicities of the used pyrolytic graphite crystals.

3.5.4 Imaging characteristics

Spectrum

Once all crystals have been characterized and calibrated, the angles for the first (low-mosaicity) crystal pair are set to generate a narrow central peak and the Nelder-Mead simplex algorithm [88] is subsequently used to find the optimal angles for the other crystals that minimize the spectral content in the side lobes.

Figure 3.17a shows the recorded spectra from 3 Å to 6 Å using all 8 crystals. The available wavelength range is limited on the short wavelength side by the MVS reaching its maximum rotation speed and on the long wavelength side by the pyrolytic graphite diffraction range. The reduced intensity because of the spectral filtering by non-(00 ℓ) reflections can clearly be observed below 4.25 Å, whereas longer wavelengths follow the tapering of the ICON spectrum. The monochromaticity $\Delta\lambda/\lambda \approx 15\%$ of the MVS was drastically reduced to 3.7 % in this scan (approximately constant as in this case also the high-mosaicity crystals were used at short wavelengths with smaller MVS spectral bandwidth, filtering wavelengths in side lobe and central peak). However, the final spectral width is not a fixed monochromator property like it is for an MVS or DCM. Rather, having a set of rotatable crystals of different mosaicity as filters, TESI offers a very flexible spectrum shaping capability. Any spectral width up to $\Delta\lambda/\lambda \approx 15\%$ set by the MVS can be obtained, as exemplified in figure 3.17b, with a monochromaticity of resp. 7.7 %, 6.3 %, 4.4 % and 2.4 %. It offers the freedom to flexibly compromise between flux and energy-resolution, depending on the application. One can even imagine a more exotic spectrum, e.g. an asymmetric peak spectrum (figure 3.17c) by filtering out wavelengths on one side of the MVS spectrum only. Such a spectrum could be useful e.g. for crystallographic phase contrast imaging around a Bragg edge with high energy resolution and high flux.

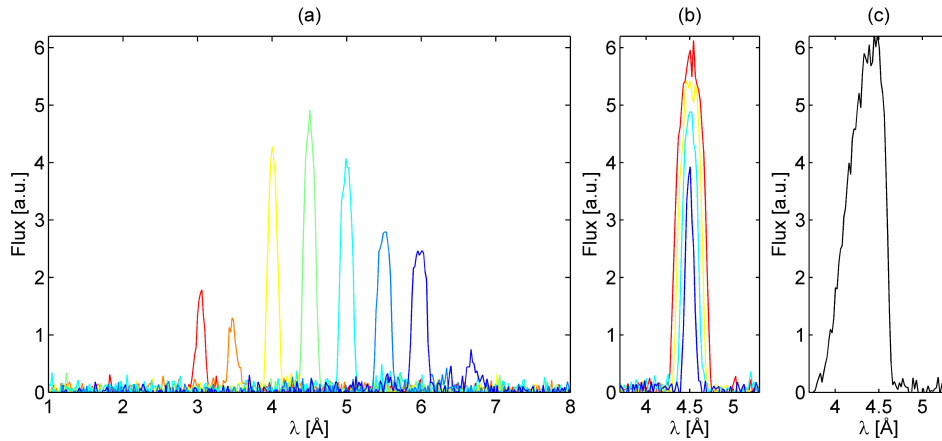


Figure 3.17: Beam spectra for an energy scan from 3 Å to 6 Å per 0.5 Å (a), for 4 different set monochromaticities (b) and for an asymmetric peak profile (c).

Intensity and field of view

Further performance of the monochromator was tested under typical imaging conditions. An area measuring $125 \times 125 \text{ mm}^2$ of a $100 \mu\text{m}$ thick ^6Li -based scintillator was focused using a 50 mm optical lens onto a $1024 \times 1024 \text{ pixel}^2$ Andor DW-434 CCD camera in order to record

beam intensity and profile. An energy scan without sample was made with TESI set for 5 % monochromaticity.

As expected due to the higher level of monochromaticity, the exposure rates are quite low: 15 - 40 gray levels $\text{pixel}^{-1} \text{s}^{-1}$ at a proton beam current of 1.5 mA, evolving with the wavelength similarly to the flux profiles recorded with time-of-flight in figure 3.17. Typical exposure times are thus in the order of 3-5min/image to obtain sufficient statistics for imaging, which is on par with the performance of double crystal monochromators.

The flat field image of neutrons passing through the monochromator set-up (MVS + TESI) is shown in figure 3.18. One can clearly distinguish the rectangular region of lower intensity corresponding to the projection of the crystals at the detector position and the flux decrease by narrowing of the spectrum. The fully illuminated area bears the asymmetric marking of the internal beam port structure, imaged through the TESI shielding acting as a pinhole.

Clearly, the desired beam spectrum will only be realized in the center region, with neutrons having passed through all the crystals. Nonetheless it is useful to make an analysis of the spatial variation in spectral contamination across the field of view. To this end, a Bragg edge scan of a 5 mm thick iron plate was made covering the entire field of view. The resultant transmission spectrum was at each point compared to the central one. The region of less than 10 % normalized root mean square error between recorded spectra is delimited by the contour overlay in figure 3.18. Outside of this region, spurious Bragg edges start appearing due to a mismatch between crystal setting and the non-uniform distribution of the MVS spectrum [67]. Depending on the application and sample dimensions, one can opt to slit down the beam to cover only the central region or have larger samples wholly scanned at once, albeit only with the central region at the highest spectral purity.

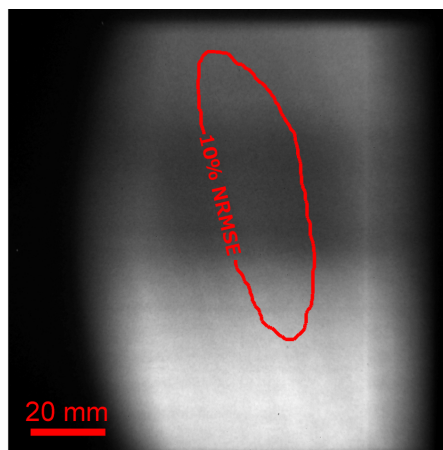


Figure 3.18: Radiograph of the neutron illuminated area at the ICON middle position. Also indicated is the contour of 10 % NRMSE of a Bragg edge scan at each position compared to the center, indicative of the spectral purity across the field of view.

Bragg edge measurement

As an illustration of the increased energy resolution that can be obtained using TESI to further narrow down the MVS spectrum, the Bragg edges for an iron and a lead plate were measured

3.6. Discussion and conclusion: energy-selective imaging at pulsed or continuous sources?

between 3 Å and 5 Å using the imaging set-up described above. The spectral width using TESI was set to $\Delta\lambda/\lambda = 5\%$ as a typical test compromise between energy-resolution and exposure time. The Bragg edges are resolved much sharper than in the case of the MVS alone, where $\Delta\lambda/\lambda = 15\%$ (figure 3.19). The wavelength scan was repeated with a standard DCM for imaging at the BOA beamline [25], featuring two pyrolytic graphite crystals in (+n,-n) configuration and fixed $\Delta\lambda/\lambda = 2.5\%$ at 4 Å. The measured evolution in microscopic cross-section is in good agreement to each other, with the Bragg edges resolved slightly sharper by the DCM delivering a beam of narrower albeit fixed wavelength spread. The cross-section evolution for an ideal polycrystal was calculated using NXS [51] and added as a reference.

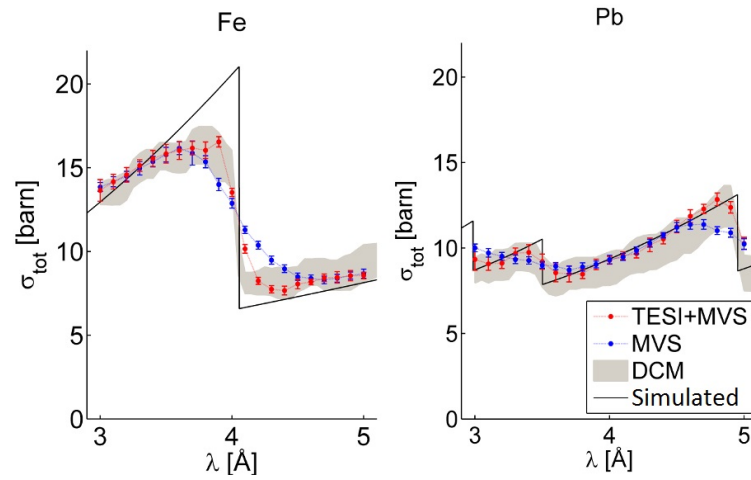


Figure 3.19: Wavelength-dependent cross-section of an iron (left) and lead (right) plate measured with and without the TESI insert and compared to a measurement with a double crystal monochromator (shown by the uncertainty band of the measurement) and NXS calculations.

3.6 Discussion and conclusion: energy-selective imaging at pulsed or continuous sources?

Several methods enabling energy-selective neutron imaging have been discussed. Each has its own advantages and disadvantages. Prosaically phrased, one has to select the right method for the right job: time-of-flight at pulsed sources or a monochromator at continuous sources, high energy resolution and long exposure times or lower energy resolution but faster acquisition. But also the experimenter's locality and scarce availability of neutron sources, pulsed or continuous, play a role.

Imaging at pulsed sources using the time-of-flight method offers the best wavelength resolution for energy-selective imaging. Moreover, it can very flexibly be traded off for imaging statistics (and total exposure time) by simply recording fewer frames of larger exposure time for each pulse. At continuous sources, one has to select the proper monochromator as a function of energy-resolution *versus* exposure time: a velocity-selector with $\Delta\lambda/\lambda \approx 15\%$ and ~ 1 min exposure time or a double crystal monochromator or, more flexibly, TESI with $\Delta\lambda/\lambda \approx 2 - 5\%$

Chapter 3. Energy-resolving capability for neutron imaging

and ~5 min exposure time.

To make a wavelength scan, one selects a single wavelength, discarding all others, to record one wavelength frame of the scan. This has to be repeated for each frame.

At pulsed sources on the other hand, a wavelength scan can be performed very efficiently, as for each pulse all time (or equivalently wavelength) frames of the scan can be recorded simultaneously.

This feature is an important drive for all the imaging beam lines currently being built or planned at pulsed sources. However, when monochromatic imaging at a single wavelength only is required, imaging at a continuous source has the advantage that this wavelength is continuously provided for. At pulsed sources, it only comes at the pulse repetition rate. Though the peak neutron flux at pulsed sources is orders of magnitude higher than at continuous sources, the average flux is actually lower [89].

Use of a monochromator for imaging at a continuous source inevitably comes with a change of the spectral distribution across the field of view, whereas time-of-flight imaging at pulsed sources suffers no such non-uniformities. It is therefore advisable for each experiment to make a calibration scan of an iron plate as described in previous section so a true pixelwise characterization or correction is possible.

As a practical reference guide to the future user, table 3.5 lists some of the typical characteristic values for different energy selection methods at the SINQ spallation source at Paul Scherrer Institut. White beam numbers are given for completeness. The time-of-flight (TOF) values are based on experiences measuring at ISIS at the Rutherford Appleton Laboratory in the UK. It should be noted that the field of view was limited by the MCP detector, not by the beam size. Exposure times are considerably longer - the time averaged neutron flux is lower by one order of magnitude [90] - but in this time the monochromatic radiographies spanning the whole spectrum are recorded in parallel.

	Monochromaticity	Field of view	Exposure time	Wavelength shift
White	-	15 × 15 cm ²	5 s	-
MVS	15 %	10 × 10 cm ²	1 min	1 Å
DCM	2.5 %	10 × 10 cm ²	5 min	0.1 Å
TESI	2-15 %	2.5 × 6 cm ²	5 min - 1 min	-
TOF	< 0.5 %	2.5 × 2.5 cm ²	2.5 h	-

Table 3.5: Typical values for neutron imaging with a white beam and using monochromators (MVS: mechanical velocity selector, DCM: double crystal monochromator) at SINQ and time of flight (TOF) imaging at ISIS.

The opportunities for energy-selective imaging using time-of-flight at pulsed sources are thus clear. Therefore, since 2008, a series of yearly workshops called NEUWAVE was initiated to promote the hitherto absent neutron imaging at pulsed sources. Today, IMAT at ISIS (UK)

3.6. Discussion and conclusion: energy-selective imaging at pulsed or continuous sources?

and RADEN at JPARC (JP) are near completion, VENUS at SNS (US) is under construction and ODIN at the future ESS (SE) has been approved as a day one instrument.

However, again, also at continuous sources, neutron imaging in general and energy-selective imaging in particular still has a major role to play. For the newly developed imaging methods discussed in the following chapters, also its application options at the different types of neutron sources is analyzed.

4 Quantification by energy-selective neutron imaging

Beam hardening and scattering contributions hinder quantitative analyses in neutron imaging. In this chapter the problem is discussed and current remedies reviewed. A new strategy is proposed: energy-selective imaging at wavelengths past the Bragg cut-off. It is first demonstrated for digital neutron radiography of an iron step wedge and computed tomography of a stepped iron cylinder. Two practical applications are given for illustration: the determination of alloy composition in Renaissance bronzes (previously published in [91]) and the integrity of copper discs prior to machining as linear accelerator cavity structures.

4.1 The trouble with quantification

Investigating a sample with neutron imaging, one looks at the spatial variation in attenuation based on changes in local thickness and different constituting materials based on their different cross-sections. This often suffices for morphological analyses, e.g. shrapnel in medieval cannon balls [92].

However, if one wants to perform quantitative analyses of material compositions or derive a quantity (i.e. "put a number on it"), certain aspects of the physics of the measurement might falsify the results.

A major challenge is correcting for the neutron scattering contributions to the digital radiographs. For many materials, scattering forms the dominant contribution to the total cross-section. Some neutrons scattered inside the sample or from the surroundings, may still hit the detector and are misinterpreted as a higher transmission along a straight neutron flight path from source through sample to detector. As a result, if left uncorrected, the measured cross-section or material content, will be an underestimation compared to tabulated values or describing formulas (chapter 2). A schematic overview is given in figure 4.1, showing neutrons (top to bottom) undergoing multiple scattering, scattering without hitting the detector, scattered neutrons still hitting the detector, neutrons being transmitted without undergoing any interaction, absorption and scattering from the surroundings. A cross marks the scattering contributions that give rise to quantification errors.

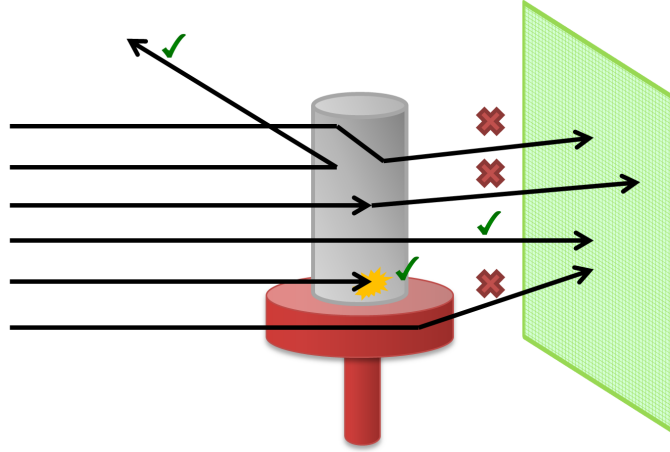


Figure 4.1: Neutron interactions during an experiment, some of which falsify the transmission measurement (marked with a cross).

A second effect originates in the use of a polychromatic neutron beam spectrum in combination with a wavelength-dependent cross-section, as figure 4.2 illustrates for the ICON spectrum and the total microscopic cross-section of iron. After transition through a thin slab of iron, the shorter wavelengths in the spectrum will be attenuated more than the longer ones. Upon traversing macroscopic sample thicknesses (an assembly of the considered thin slabs), the average of the final transmitted beam spectrum is shifted towards longer wavelengths. With it, also the observed macroscopic cross-section changes. The mechanism is called *beam hardening* [93], a term coined in the X-ray community where the attenuation coefficient decreases with increasing energy and the X-ray beam energy spectrum shifts to higher average energies (hard X-rays). It should be pointed out that in neutron imaging, depending on the presence and magnitude of Bragg edges, the opposite trend ("beam softening") can occur: a shift to longer wavelengths or lower energies as in this case for iron. To illustrate the effect, the expected mean neutron wavelength for the ICON spectrum s is calculated after traversing several thicknesses d of iron:

$$\lambda_{avg} = \frac{\int_s \lambda I(\lambda) e^{-\Sigma_{Fe}(\lambda)d} d\lambda}{\int_s I(\lambda) e^{-\Sigma_{Fe}(\lambda)d} d\lambda}. \quad (4.1)$$

The result is shown in table 4.1 and shows a clear increase in mean neutron beam wavelength after filtering through increasingly thick iron slabs.

Thickness [cm]	0	0.5	1.0	1.5	2.0	2.5
λ_{avg} [Å]	2.86	2.91	2.98	3.07	3.17	3.27

Table 4.1: The mean neutron beam wavelength increases by filtering through increasingly thick iron slabs.

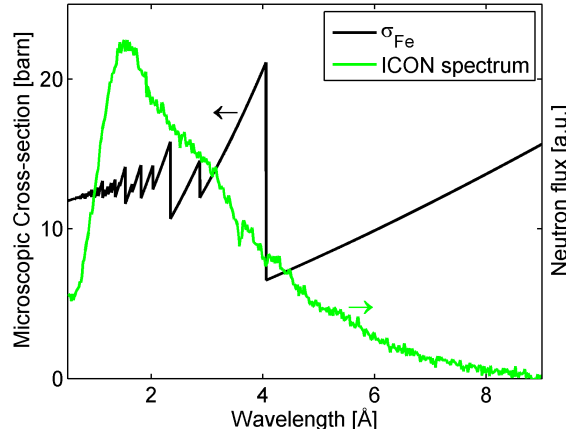


Figure 4.2: Illustration of the beam hardening effect: given the iron cross-section, the shorter wavelengths in the ICON spectrum will be attenuated more than the longer wavelengths. Upon transition through layers of iron, the beam spectrum will gradually shift to longer wavelengths.

4.2 Existing quantification strategies

Several strategies already exist to take into account the above mentioned hindrances for quantification.

A first approach is a hardware correction, where a honeycomb-type collimator of a neutron-absorbing material is placed in between sample and detector. Neutrons following a straight path through the sample reach the detector, while scattered neutrons hit the walls of the collimator and are removed from the beam. The principle has been around from early days of modern neutron imaging [94] and is still in use today [95, 96]. A set-up for scatter reduction using a microchannel plate as collimator has been developed as an instrumental plugin at PSI in 2014 [97]. It assumes no prior sample knowledge, but requires a careful alignment with the beam, increased sample-detector distance leading to a loss in spatial resolution and the decreased image intensity because of the duty cycle of the channel plate collimator. Moreover, the parallel neutron beam that is let through the collimator can still suffer from beam hardening.

A second method can be dubbed as a *black body* correction [98]. A radiograph is made of the sample, containing a certain scattering contribution. Subsequently, another radiograph is made with part of the sample covered with a small strip of a strong neutron absorbing material. The detector contribution in the region behind it is then coming solely from the neutrons scattered in sample and surroundings. This measure for the scattering contribution is then used to correct the original radiograph. This method works well, though requires more radiographs, especially for complex shaped samples.

A third strategy is to add the extra measurement of a calibration sample (e.g. a step wedge of the relevant sample material) to the experimental program. As such, one can derive a recalibration curve between observed and theoretical cross-section [99].

A fourth approach is to use Monte Carlo codes to simulate the imprint of beam hardening and scattering contribution to the radiography. This method was e.g. pursued by Hassanein [100, 101]. Based on a parameterization of experimental set-up and a simplified sample description, so-called point-scatter functions are calculated for each pixel, i.e. the detection probability for neutrons scattered in a homogeneous material layer and originating from a point-like source. All these scattering contributions are then subtracted from the original image to give a corrected image. An advantage of this method is its post-processing nature, no additional measurement time is required.

A principle disadvantage is the need for detailed *a priori* knowledge of the double differential cross-section, required for accurate simulation. They are however not always well-known and usually derived for idealized materials, which can differ greatly from actual sample conditions (e.g. the presence of texture). Moreover, the uncertainty becomes large for very short sample to detector distances and large scattering contributions to the radiographs. Further practical disadvantages are the required access to MCNP which is export controlled and that the method is computationally expensive. It is mainly developed for isotropic scattering of water in the thermal regime however, not for the cold energy range with directional scattering occurring. Though MCNP only includes double differential cross-sections for a few materials, advances are made in developing routines capable of simulating Bragg edges [102] for arbitrary materials. An interesting alternative is the open source code McStas [103, 104] for neutron ray tracing. It has the capability of simulating both Bragg edges from neutron scattering in polycrystalline material *and* further tracking of the scattered neutrons [105]. It might be an excellent candidate for further developments of a simulation based quantification tool for cold neutron imaging of polycrystalline material.

4.3 Principle of energy-selective imaging past the Bragg cut-off

A different strategy for quantification of polycrystalline material lies in energy-selective neutron imaging at wavelengths longer than the *Bragg cut-off*. This is the longest wavelength at which coherent elastic scattering or diffraction can occur, corresponding to twice the largest crystal lattice spacing. Bragg's law can no longer be fulfilled for longer wavelengths. Instead of using hardware to eliminate the scattered neutron component in the beam or using software to simulate and correct scattering and beam hardening effects, one can thus avoid their occurrence in the first place.

The reduced wavelength bandwidth and the more slowly varying cross-section in this wavelength range greatly suppress beam hardening.

As no coherent elastic scattering can occur at such long wavelengths, neutron imaging becomes insensitive to spatial variation in crystallography-based properties such as texture and grain size that can cause strong deviations of the assumed ideal cross-section (section 2.4).

For many structural materials, coherent elastic scattering is by far the most dominant scattering mechanism. By experimentally avoiding its occurrence, the effect of scattering contributions is largely abated. Only the much smaller incoherent scattering component remains. Iron for instance, has a tabulated coherent scattering microscopic cross-section of 11.22 barn, whereas the incoherent scattering cross-section is only 0.4 barn. Absorption by neutron cap-

4.3. Principle of energy-selective imaging past the Bragg cut-off

ture is dominant at wavelengths longer than the Bragg cut-off, dubbing it the *absorption range*.

Quantitative neutron imaging in the absorption range comes at the price however. Exposure times increase by an order of magnitude, as one monochromatizes the beam at long wavelengths where flux is low. Moreover, its applicability is limited to polycrystalline material with low incoherent scattering which persists at wavelengths past the Bragg cut-off.

4.3.1 Proof of principle: radiography of an iron step wedge

The transmission profile of a α -iron step wedge was examined at the ICON beamline for imaging with cold neutrons. Having a Bragg cut-off at 4.05 \AA , the availability of cold neutrons is a prerequisite. The sample measured $10 \text{ mm} \times 25 \text{ mm}$, with the thickness varying from 5 mm to 25 mm in steps of 5 mm (figure 4.3a).

Using a $100 \mu\text{m}$ thick $^6\text{Li ZnS}$ scintillator, the neutron signal was converted into visible light and detected with a $1024 \times 1024 \text{ pixel}^2$ CCD camera. The sample was positioned with its flat back pressed against the scintillator.

The transmission profile was recorded for two different incident beam spectra: (a) the polychromatic ICON spectrum already shown in figure 4.2 and (b) a reduced wavelength band after the Bragg cut-off centered around 5.0 \AA . The latter was realized using a Mechanical Neutron Velocity Selector providing a Gaussian wavelength band of monochromaticity $\Delta\lambda/\lambda = 15\%$. As no high energy-resolution is required and short exposure times are preferential, this is the monochromator of choice. The result is shown in figure 4.3b.

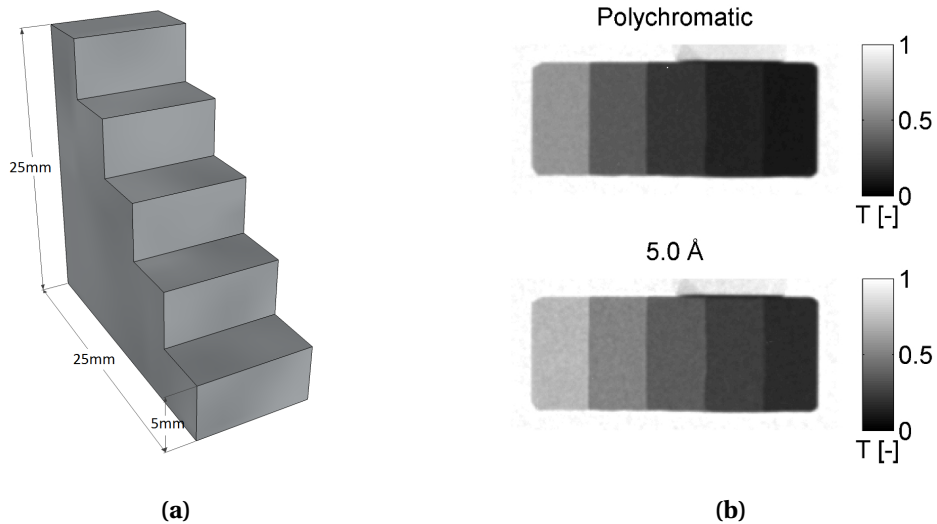


Figure 4.3: Iron step wedge sample (a) and corresponding digital radiographs for a polychromatic beam spectrum and using the velocity selector for imaging with a reduced wavelength band around 5 \AA (b).

The observed microscopic cross-section σ was thereupon calculated based on the Beer-

Lambert law (equations 1.3 and 1.4):

$$\sigma = -\frac{1}{Nd} \ln T \quad , \quad (4.2)$$

for each step of the wedge (of assumed known design thickness d). The nuclei density used was calculated based on the standard iron mass density and molar mass.

$$N = \frac{7.874[\text{g}/\text{cm}^3]}{55.85[\text{g}/\text{mole}]} \cdot 6.022 \cdot 10^{23}[\text{nuclei}/\text{mole}] = 8.49 \cdot 10^{22} \text{ nuclei}/\text{cm}^3 \quad (4.3)$$

It was repeated for both a polychromatic beam spectrum ($\sigma_{exp,poly}$) and the one with the velocity selector in place ($\sigma_{exp,5.0\text{\AA}}$). The result is shown in figure 4.4. On the one hand, a clear violation of the Beer-Lambert law is observed for the polychromatic data: the microscopic cross-section is not constant, but decreases with thickness. On the other hand, the results for energy-selective imaging past the Bragg cut-off are independent of the thickness.

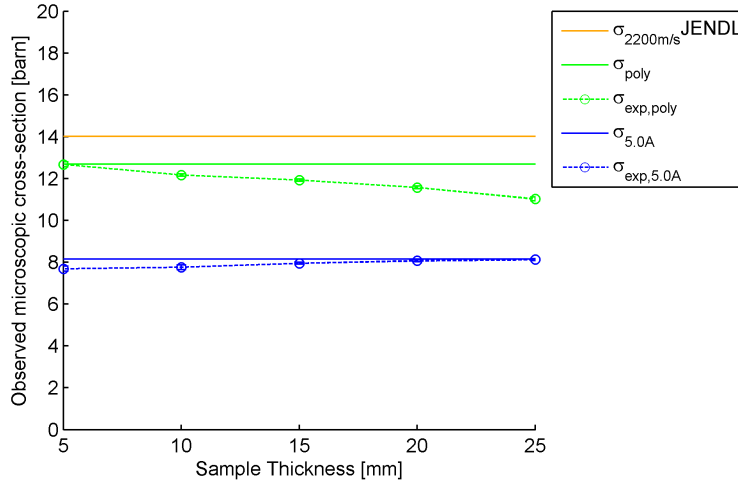


Figure 4.4: Microscopic cross-sections of iron as a function of thickness: experimental values (σ_{exp}) and calculated spectral averages (σ) for polychromatic ($poly$) and monochromatized (5.0\AA) beam spectra. Error bars fall within the data point markers.

A typical quantification task is the determination of material thickness from digital radiography:

$$d = -\frac{1}{N\sigma} \ln T \quad (4.4)$$

The question boils down to which reference cross-section is to be used. It can be taken from tabulated data, e.g. several cross-section databases exist depending on the nation such as JENDL (Japanese), JEF (European), ENDF-B (USA), BROND (Russia) or CENDL (China) [106]. It should be noted that these are assumed constant values for a Maxwellian thermal spectrum. Clearly, deviations when using a cold neutron beam are to be expected. Using NXS [51], the wavelength-dependent cross-section of ideal iron (random orientation of the crystallites) is

4.3. Principle of energy-selective imaging past the Bragg cut-off

simulated. The averages over the two beam spectra used in the experiment are then calculated for use as a more accurate reference. Comparison to experimental data (figure 4.4) shows good agreement at 5 \AA , but in case of a polychromatic beam spectrum the agreement only holds for the thinnest layers as a result of neutron scattering and beam hardening.

The thickness of the step wedge is thus calculated and shown in figure 4.5. The sharp variation in cross-section across each step edge indicates there is little cross-talk through scattering between the steps, justifying the pragmatic choice of a single step wedge measurement instead of five radiographs of single slabs of different thicknesses. Energy-selective neutron imaging at wavelengths longer than the Bragg cut-off reproduces the design profile. Standard polychromatic imaging shows deviation of up to 13% at 25 mm thickness, due to aforementioned problems of scattering and beam hardening.

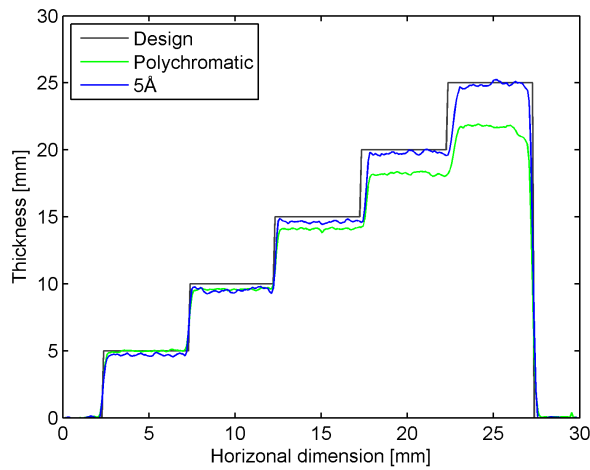


Figure 4.5: Thickness profile of the iron step wedge, *per* design, derived from standard white beam digital radiography and from energy-selective imaging in the absorption range at 5 \AA .

4.3.2 Proof of principle: tomography of a step cylinder

In computed tomography, beam hardening and scattering lead to *cupping artifacts*: virtual volume slices show a reconstructed cross-section profile decreasing inwardly. The cross-section at the innermost voxels is reconstructed based on neutron rays that have had the largest path lengths through the sample. Thus they have seen the most beam hardening and scattering contributions, lowering the observed cross-section.

To illustrate the effect, a tomography was made of an iron step cylinders in a white beam and energy-selective in the absorption range. The step cylinder was 20 mm high and its diameter varied from 5 mm to 20 mm in 4 steps. A total of 375 projections were made for the white beam tomography and 225 for the energy-selective tomography. The measurements were performed at the BOA beamline [25]. The energy-selective tomography was performed using the double crystal monochromator with a Beryllium filter to eliminate the higher-order contamination of the spectrum. As the wavelength band is more narrow than for a velocity selector as used

in the previous subsection, a shorter wavelength closer to the Bragg edge was chosen, where flux is higher: 4.5 Å. A 200 μm thick ^6Li ZnS scintillator was used and the pixel size was 135 μm . Figure 4.6a shows a 3D rendering of the sample surface from the reconstructed white beam tomography. The line profiles of the reconstructed cross-section through the bottom step are shown next to it for both spectra. The expected constant cross-section profile are given for comparison. Like for the step wedge radiography, they were derived from simulation of the wavelength-dependent cross-section using NXS and taking the average over the respective beam spectra. Good agreement is found for neutron imaging at 4.5 Å with severe cupping artefacts present in the polychromatic measurement. The reconstructed cross-section profile through the other steps show similar trend, though less pronounced as the amount of material is also less.

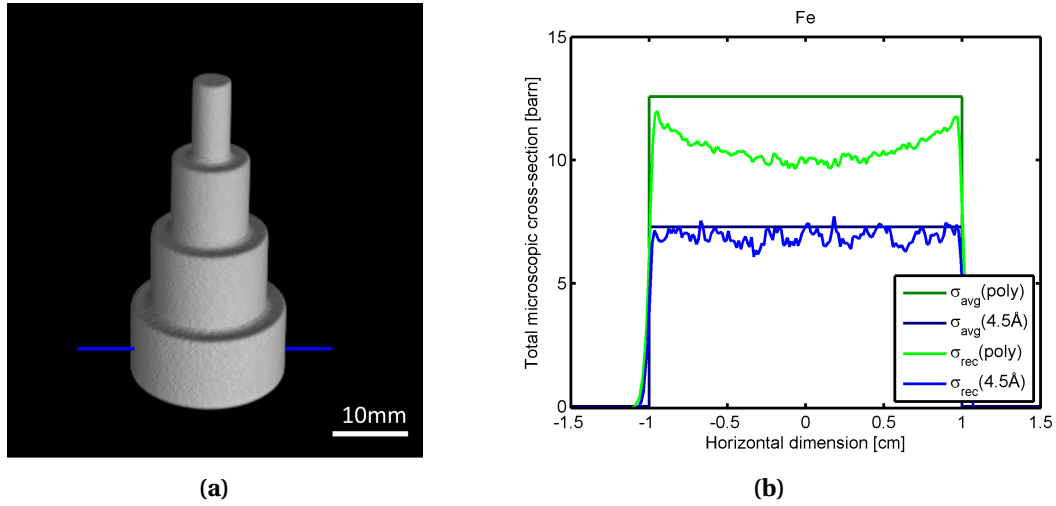


Figure 4.6: Volume rendering of the reconstructed iron step cylinder (a), the profile of the reconstructed cross-section along the blue line is shown in (b).

4.3.3 Discussion and outlook

The question remains open which mechanism is mostly responsible for quantification errors: scattering contributions or beam hardening? At cold neutron wavelengths, scattering will tend towards back reflection, limiting scattering contributions on the detector. However, Bragg edges in the cross-section are more pronounced compared to thermal neutron wavelengths, worsening the effect of beam hardening. Conversely, for thermal neutron wavelengths, scattering is in the forward direction, but the cross-section exhibits an approximately flat wavelength-dependent profile, with Bragg edges limited in height.

Repeating the above mentioned quantification experiments at NEUTRA (thermal), ICON (thermal and cold) and BOA (cold) for comparison would therefore be highly interesting. An MCP-type collimator could be used to separate the scattered neutron contribution from the beam hardening effect.

4.4 Application 1: Historical copper alloy composition

4.4.1 Problem setting

The Rijksmuseum Amsterdam holds an important collection of Renaissance bronze statuettes which were being studied from both art historical and scientific point of view.¹ Until some decades ago this and similar collections were only studied from a stylistic point of view. That approach started to change in the last quarter of the 20th century when interdisciplinary studies from both a scientific and art history took place. Thus numerous studies have led to new attributions which consequently have been published in museum catalogues or scholarly papers [107, 108, 109]. In the vast majority of these studies researchers made use of traditional analytical equipment. Stylistic features and covered parts of a sculpture were studied with the naked eye, microscopy, videoscapy or X-radiography. For the determination of alloys Atomic Absorption Spectroscopy (AAS), Inductive Coupled Plasma (ICP) and X-ray Fluorescence (XRF) measurements have been used most frequently. The alloy composition of ancient artefacts is important to archaeometallurgy, as it can be linked to a place of manufacturing and date [110, 111].

However, except for XRF, these methods all require sample taking, which museum curators prefer to avoid as renaissance bronzes are often very precious objects. XRF is thus used in museums more easily since it requires a simple set up and relatively little cost, as many museums nowadays operate hand held X-ray Fluorescence (XRF) devices. However, it is only a surface analysis technique and will penetrate the copper alloy up to a maximum of approximately 20-30 μm [112]. Several drawbacks of this method appear. Primarily, the surface has to be completely clean before a measurement can take place, taking segregation effects of an alloy into consideration [113]. Secondly the data obtained by XRF research has proven to be inconsistent after an inter laboratory research among XRF users in museums [114].

In search for different Non-destructive Testing (NDT) methods neutron tomography was found to provide bulk information on alloy heterogeneity without any prior sample preparation. Earlier studies have proven that neutron imaging can be used to detect different materials (casting remains and soldering repairs) within a Renaissance bronze sculpture (figure 4.7). However, results were limited to a qualitative indexing of macroscopically separated regions of different materials (bronze approximated as copper and a core material) [115, 116]. As a result, this new study took place to quantitatively distinguish different copper alloys directly in neutron imaging based on the attenuation. Samples are cast according to traditional casting techniques and the copper alloys have been selected according to contemporary treatises.

¹The term Renaissance bronze is used throughout this paper to reflect the type of objects. Bronze usually consists of a copper tin/lead alloy yet Renaissance bronzes can also consist of copper zinc alloys which are indeed brasses.



Figure 4.7: Photo (a) and neutron tomography surface (b) and volume (c) rendering of a Renaissance Bronze from the Rijksmuseum depicting a Striding Nobleman (reference BK-16083, about 35 cm height), showing different attenuation of the neutrons as a result of different composition at the ankles, knees and shoulder part.

4.4.2 Experimental set-up

For the purpose of this study 19 copper binary alloys have been reconstructed where the alloyed metal with copper was either tin, lead or zinc as given in table 4.2. All samples with an average size of $4.5 \times 8 \times 50 \text{ mm}^3$ have been cast and cooled down to ambient temperature and subsequently cut down to the same dimensions in thickness ($4.1 \times 7.0 \times 45 \text{ mm}^3$). The alloys are composed according the occurrence of historical alloys based on contemporary literature. Neutron imaging of these specific copper alloys was performed at the NEUTRA and ICON beamlines at PSI.

Neutron imaging with a polychromatic thermal spectrum was first performed at NEUTRA. A cooled highly-sensitive $2048 \times 2048 \text{ pixel}^2$ CCD camera was looking onto a $100 \mu\text{m}$ $^6\text{LiF ZnS}$ scintillation screen for neutron detection, with exposure times of 20s.

Based on these experiments and due to beam time constraints, a number of alloys were selected for further energy-selective neutron imaging measurements at ICON: Cu-Sn alloys 5, 6, 7, 8 and Cu-Zn alloys 15, 16, 17, 18. In this case a $1024 \times 1024 \text{ pixel}^2$ CCD camera was looking was used, again in combination with a $100 \mu\text{m}$ $^6\text{LiF ZnS}$ scintillator. The mechanical neutron velocity selector was used for monochromatization.

The sample to detector distance was in both cases 1 cm given by the holder size.

4.4. Application 1: Historical copper alloy composition

Alloy no.	Composition [%]			
	Cu	Sn	Zn	Pb
1	99	1	0	0
2	97	3	0	0
3	95	5	0	0
4	93	7	0	0
5	90	10	0	0
6	85	15	0	0
7	80	20	0	0
8	75	25	0	0
9	70	30	0	0
10	99	0	0	1
11	97	0	0	3
12	95	0	0	5
13	93	0	0	7
14	95	0	5	0
15	90	0	10	0
16	85	0	15	0
17	80	0	20	0
18	75	0	25	0
19	70	0	30	0

Table 4.2: Copper alloy compositions under investigation with thermal neutrons.

4.4.3 Evaluation strategy

Both scattering and absorption of neutrons occurs in the sample. In the thermal wavelength region many and little pronounced Bragg edges are present (as seen in section 2.4.3) and the wavelength-dependent microscopic cross-section of isotope i can be approximated by a tabulated mean scattering cross-section term σ_i^{scatt} and an absorption cross-section term proportional to the neutron wavelength, typically determined from tabulated $\sigma_{i,2200m/s}^{abs}$ (the microscopic absorption cross-section of a thermal neutron, i.e. having a velocity of 2200 m/s) [44]:

$$\sigma_i(\lambda) = \sigma_i^{scatt} + \frac{\sigma_{i,2200m/s}^{abs}}{1.798} \lambda [\text{\AA}] \quad (4.5)$$

The density of nuclei N_i in an alloy can be calculated as

$$N_i = \frac{x_i \rho N_A}{M_i}, \quad \rho = \frac{1}{\sum_i x_i / \rho_{i,0}} \quad (4.6)$$

with x_i the alloy components weight fraction, M_i its molar mass, N_A Avogadro's constant, ρ the density of the alloy calculated based on the natural densities $\rho_{i,0}$ of the components

brought together in the alloy. The final macroscopic cross-section that governs the attenuation becomes

$$\Sigma = \sum_i N_i \sigma_i(\lambda) \quad (4.7)$$

When making a standard radiography, all wavelengths present in the used neutron beam spectrum s contribute to an effective recorded intensity (neglecting the wavelength-dependent efficiency of the set-up) with sample of thickness d in place, I_{eff} and without it, $I_{0,eff}$:

$$I_{eff} = \int_s I_0(\lambda) e^{-\Sigma(\lambda)d} d\lambda, \quad I_{0,eff} = \int_s I_0(\lambda) d\lambda \quad (4.8)$$

From which an effective macroscopic cross-section can be calculated as

$$\Sigma_{eff} = -\frac{1}{d} \ln \left(\frac{I_{eff}}{I_{0,eff}} \right), \quad (4.9)$$

a quantity that allows us to distinguish between alloys.

4.4.4 Results and discussion

Thermal white beam measurements at NEUTRA

Figure 4.8 depicts the theoretical and experimental values of Σ_{eff} for the measured alloys listed in table 4.2. The theoretical values were calculated according to the formulations above: calculating the microscopic cross-section according to equation (4.5) based on the data library and atomic density according to equation (4.6), the recorded effective transmitted intensity can be found (equation (4.8)) as well as effective macroscopic cross-section (equation (4.9)). The experimental values were determined as the mean Σ_{eff} value in its distribution over the entire sample image (after open-beam corrections and background removal). Error bars indicate the 1σ uncertainty limits.

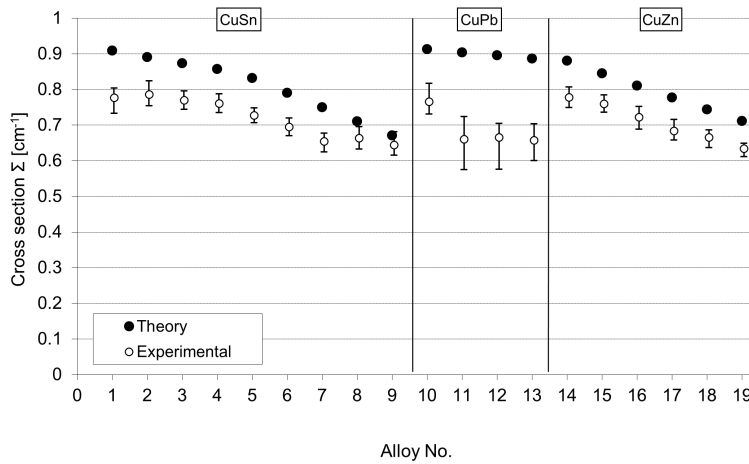


Figure 4.8: Overview of the effective cross-section theoretically expected (filled circles) and determined from measurements (empty circles)

4.4. Application 1: Historical copper alloy composition

The measured effective cross-section nicely follows the theoretical behaviour, though a systematic offset exists because of scattering contributions and beam hardening. Qualitatively, this has little influence on the relative discrimination between different copper alloys, as can e.g. be present in historical bronzes when mended after their construction [113].

A clear deviation from the expected trend can be found for the lead-rich alloys 11, 12 and 13. This can be explained from the theoretical calculation assumption that these alloys consisted fully out of copper and lead, while in truth air pockets, porosities appear in bronze materials of such high lead concentrations (figure 4.9). Though hardly visible on the sample surface, they clearly appear in the bulk-sensitive neutron radiographies. A maximum of 0.4 % of lead can exist in the solid copper [117]. This increased sample heterogeneity also leads to increased uncertainty for these alloys. Here, a computed tomography would be necessary to separate both material thickness and cross-section in the reconstructed slices, as the outer sample thickness no longer corresponds to the true material thickness.

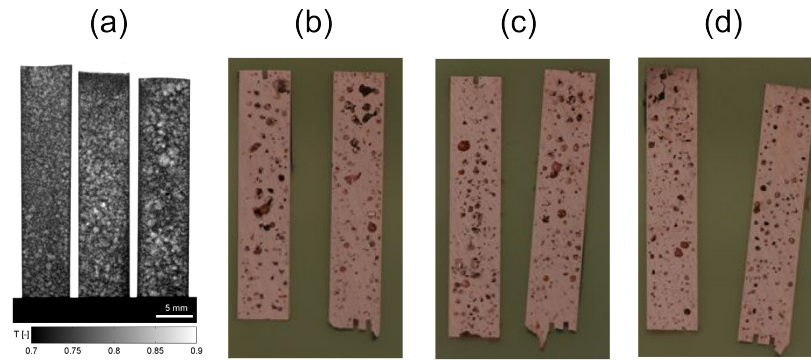


Figure 4.9: Impression of porosity in historically cast copper/lead alloys: neutron transmission measurement of alloys 11, 12 and 13 (a, right to left) as well as photographs of the alloys embedded in resin and subsequently cut open - alloy 11 (b), alloy 12 (c) and alloy 13 (d) – to demonstrate the presence of porosities in the bulk.

Energy-selective measurements with cold neutrons at ICON

In the absorption range, equation (4.5) can again be applied to describe the cross-section, though σ_i^{scatt} is now limited to $\sigma_{i,inc}^{scatt}$, the incoherent scattering component (also tabulated). The scattering contribution to the transmission radiograph is negligible in the absorption range for the alloy component materials Cu, Sn, Zn and Pb. Hence, no scatter correction is necessary, making it ideal for quantitative studies as ours.

An illustration of the recorded wavelength-dependent cross-section evolution is presented in figure 4.10 for the case of alloy number 7. The wavelength spread is too large to separate the (111) and (200) Bragg edges and they are seen as a single edge ranging from 3.5 Å to 4.5 Å. Better wavelength resolution would be required to resolve these edges, e.g. by using a double crystal monochromator or TESI. However, in the absorption range, the broad wavelength spread is an advantage since it means a higher neutron flux on the sample in wavelength regions of limited source flux and simple linear cross-section behaviour. Image exposure times increased to 60 s only.

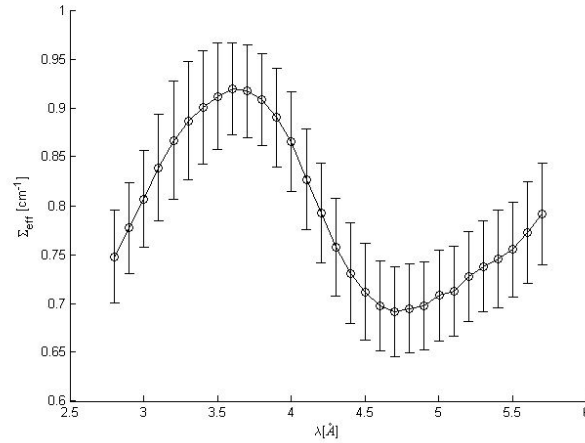


Figure 4.10: wavelength-dependent cross-section example as measured for the $\text{Cu}_{0.8}\text{Sn}_{0.2}$ alloy No. 7.

The alloy composition was again determined through comparison of measured and theoretical cross-section values in the absorption range. All data points above 5 \AA were used for increased statistics. No scattering correction was made. Results are summarized in figure 4.11. Very good agreement with production values exists. Uncertainty on the composition was around 1 % only.

It was not possible to distinguish between Sn and Zn as secondary alloy component through energy-selective imaging, as they are both taken up in the copper Face Centered Cubic (FCC) phase and as such do not form any new and distinguishable Bragg edges. One could nevertheless work with a “Sn equivalent” alloy component as proposed in [118]. Moreover, composition reconstruction for binary alloys where one knows in advance the present secondary alloy element (e.g. through XRF) pose no problem. Often historical objects are first analyzed to exclude any metal present that will negatively influence the half-life of the objects after exposure to neutrons.

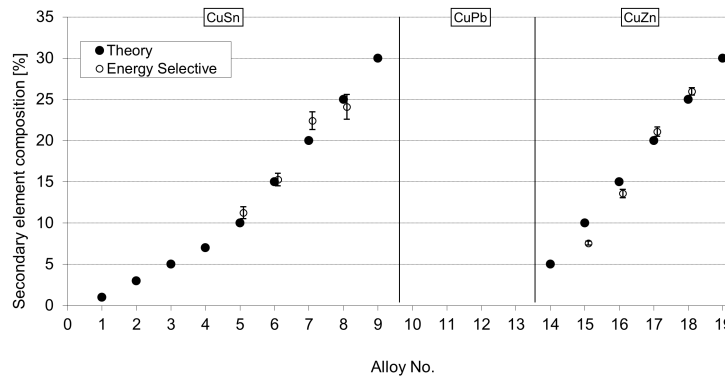


Figure 4.11: Alloy component weight fractions from theory and energy-selective imaging in the absorption range. A small horizontal offset has been introduced for clarity.

4.4.5 Conclusion

Neutron imaging was used to quantitatively determine historically-relevant binary copper alloy composition. Radiographies using the full polychromatic beam spectrum showed a clear need to correct for neutron scattering contributions if one wants to draw quantitative rather than qualitative conclusions. Radiographies in the absorption domain allowed to successfully retrieve composition information without needing any scatter correction at the cost of limited increase in exposure time. As a result, the way is now paved for quantitative tomography in the absorption range for 3D spatially localized composition information in historical bronze sculptures.

4.5 Application 2: Integrity of copper discs for SwissFel C-band cavity production

4.5.1 Problem setting

The linear accelerator for the SwissFEL free electron laser is composed of a series of copper cavities, soldered together and put under a high RF field to accelerate an electron beam. These cavities are custom built, by precise machining out of 99.99 % pure copper discs (113 mm diameter, 23 mm thickness) that were forged to preclude occurrence of porosities from casting.

However, pitting was observed on the surface of the final product (figure 4.12a). It would have a detrimental effect on the accelerator performance, as a smooth cavity surface is required to prevent electrical discharges.

To address the question if these are due to the machining or the result of porosities already present in the pristine copper discs, several such discs were inspected using neutron imaging (figure 4.12b). The large sample thickness impeded the use of X-rays as transmission would be too low (around 1 % only at 100 keV).

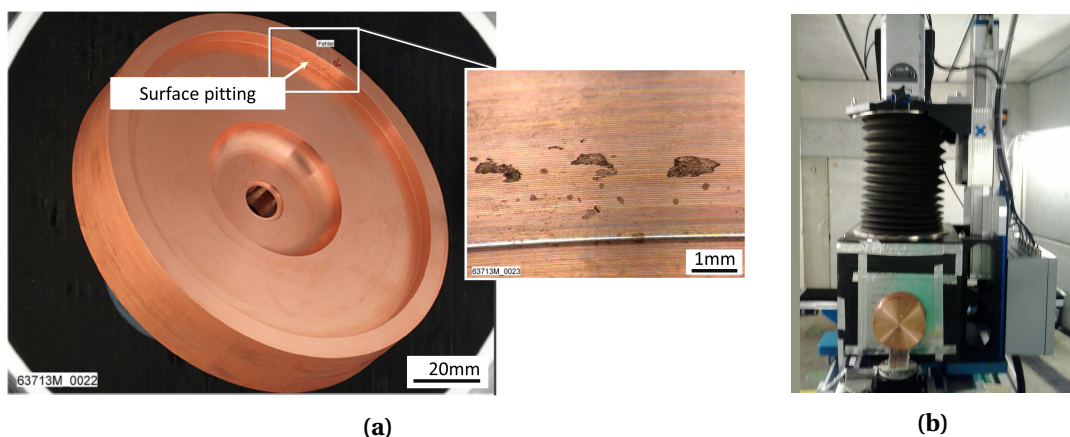


Figure 4.12: Copper cavity segments showing surface pitting after machining (a) and neutron radiography set-up of a pristine forged copper disc (b).

4.5.2 Initial examination at NEUTRA

Initial examination took place using a polychromatic thermal neutron spectrum at the NEUTRA imaging beamline at PSI. Experimental parameters are listed in table 4.3. Radiographies were made with the sample in contact with the scintillator surface to obtain the highest spatial resolution.

Large spatial variations in transmission are observed over the sample (figure 4.13). Clear cupping artifacts due to scattering contributions are visible: the observed transmission tapers off at increasing disc radius. The effect is aggravated by the close contact between sample and detector.

In order to calculate the thickness (equation 4.4), a constant macroscopic cross-section of $\Sigma=0.9 \text{ cm}^{-1}$ is assumed, found by averaging the theoretical copper cross-section over the NEUTRA spectrum. A thickness of 15 mm is found in the center of the disc, a gross underestimation of the reality. Moreover, thickness variations of over a millimetre are found superposed to the cupping profile, unrealistically large to be attributed to production flaws. Therefore, spatial variation in macroscopic cross-section instead of thickness is suspected to exist, as crystallography (e.g. texture and grain size) and density might vary due to the manufacturing process.

Scintillator	50 μm $^6\text{LiF ZnS}$
Field of view	129.6 \times 153.6 mm
Pixel size	60 μm
Exposure time	60 s

Table 4.3: Experimental parameters for the neutron imaging of SwissFEL copper discs at NEUTRA.

4.5.3 Energy-selective neutron imaging at BOA

The hypothesis formulated above is verified by energy-selective imaging at wavelengths longer than the Bragg cut-off for copper (i.e. the (111) Bragg edge at 4.17 Å). At such long wavelengths, coherent elastic scattering is no longer possible and the cross-section (and *a fortiori* the neutron digital radiograph) becomes insensitive to the sample's crystallography. The experiment was conducted at the BOA beamline, using the double crystal monochromator in combination with a Beryllium filter. Further experimental parameters are listed in table 4.4.

Wavelength	4.5 Å
Scintillator	200 μm $^6\text{LiF ZnS}$
Field of view	138 \times 138 mm
Pixel size	135 μm
Exposure time	195 s

Table 4.4: Experimental parameters for the energy-selective neutron imaging of SwissFEL copper discs at BOA.

Indeed, the transmission image at 4.5 \AA now appears homogeneous. A small horizontal gradient is present due to the shift in incident wavelength across the field of view as discussed in chapter 3. Cupping artifacts are no longer present. The spatial variation in transmission observed for polychromatic thermal neutron radiography, can thus be attributed to spatial variation in the sample's crystallography instead of thickness or density variations. The nature of the variations in crystallography are however beyond the scope of this investigation. Taking the theoretical macroscopic cross-section of $\Sigma = 0.88 \text{ cm}^{-1}$ at 4.5 \AA , a thickness of $22.3 \pm 0.5 \text{ mm}$ is found. No porosities were detected.

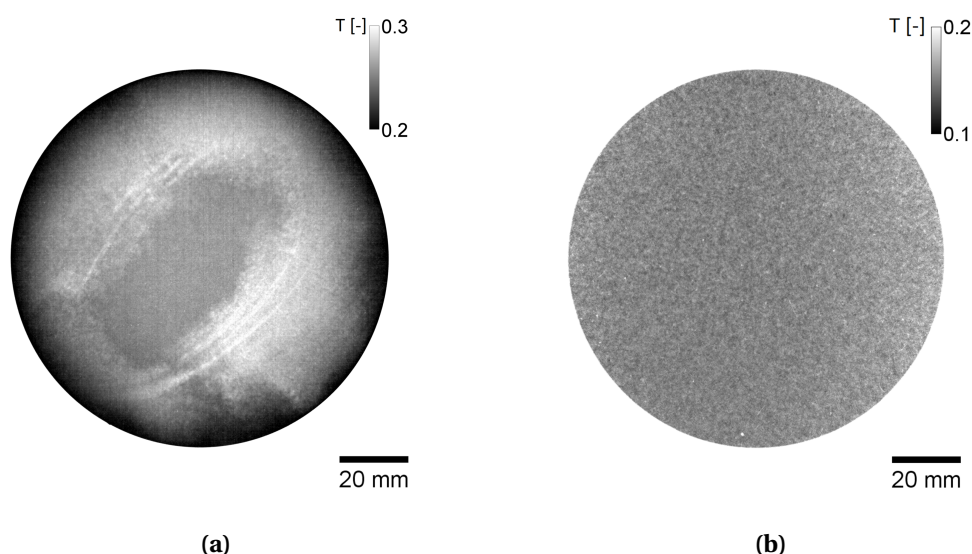


Figure 4.13: Radiographies of copper discs for SwissFEL linear accelerator cavities to be machined out of: measured using a polychromatic thermal spectrum at NEUTRA (a) and a monochromatic one at 4.5 \AA at BOA (b).

4.5.4 Conclusion

Polychromatic thermal neutron imaging is subject to artifacts as scattering contributions and sensitive to spatial variation in crystallography across the sample that impede quantitative determination of copper disc thickness and porosity presence. Energy-selective imaging in the absorption range yields correct thickness results and does not pick up any porosities above the noise level.

4.6 Summary

Energy-selective imaging of polycrystalline materials in the absorption range has been proposed to experimentally avoid effects hindering quantification. Beam hardening and scattering contributions are suppressed and one becomes insensitive to variations in crystallographic properties. The ICON and BOA beamline are suitable for such experiments as they feature the required cold neutron spectrum and energy-selective capability. Exposure times are however increased by one order of magnitude. Both proof-of-principle experiments and practical applications were shown.

5 Energy-selective neutron imaging of crystals

After polycrystals with a transmission spectrum featuring Bragg edges, we turn our attention to single crystals and ensembles of a few of them, *oligocrystals*. As the number of crystal orientations present in the neutron beam is now limited, a wavelength scan of such samples will exhibit distinct Bragg peaks in its cross-section.

In this chapter, we show how the pattern of Bragg peaks recorded at each pixel can be indexed to reveal an orientation map of the sample, which in turn can be used to segment the present crystallites - even overlapping ones in the beam direction. Mapping of the peak widths yields information on the mosaicity variations across the sample.

Two applications are shown for illustration. In a first one, energy-selective neutron imaging is used to map parameters of the (002) Bragg peak in the cross-section of pyrolytic graphite monochromator crystals. It demonstrates its capability as a fast crystal inspection tool with high spatial resolution.

A second example is one from geoscience: neutron radiography and tomography of a nickel-iron meteor with a limited wavelength band, revealing the large kamacite and taenite crystallites present (previously published in [119]).

5.1 Quantitative analysis of a single crystal wavelength scan

5.1.1 Experiment

The wavelength-dependent cross-section of single crystals was investigated by means of energy-selective neutron imaging.

The experiment was performed at the ROTAX beamline [90] at the ISIS pulsed spallation source, located at the Rutherford Appleton Laboratory in the UK. Originally designed as a multi-purpose diffractometer, it is nowadays used for in-house development and crystal alignment. It looks onto the methane moderator at 95 K of target station 1. The proton accelerator delivers 25 pulses per second, with 1 pulse out of 5 diverted to the new target station 2. A final integral flux of around 10^6 n/s/cm² is available at the sample position.

The MCP detector for neutron imaging developed at Berkeley [120] was used, having a round active area of 28 mm diameter and a pixel size of 55 μ m. A total of 1450 successive time bins of 10.24 μ s were recorded simultaneously and stacked for each pulse. A final exposure time of 2 hours was required to obtain sufficient image statistics. The flight path was calibrated to be 16 m, based on the Bragg edge positions of aluminium present from the flight tube

windows. Thus, the wavelength scan was performed with 0.0025 Å wide bins. The recorded beam spectrum is shown in figure 5.1.

Two iron single crystals of the BCC crystal structure were examined. One was shaped as a cube ($4 \times 4 \times 4 \text{ mm}^3$), the other as a cylinder (10 mm diameter, 40 mm height).

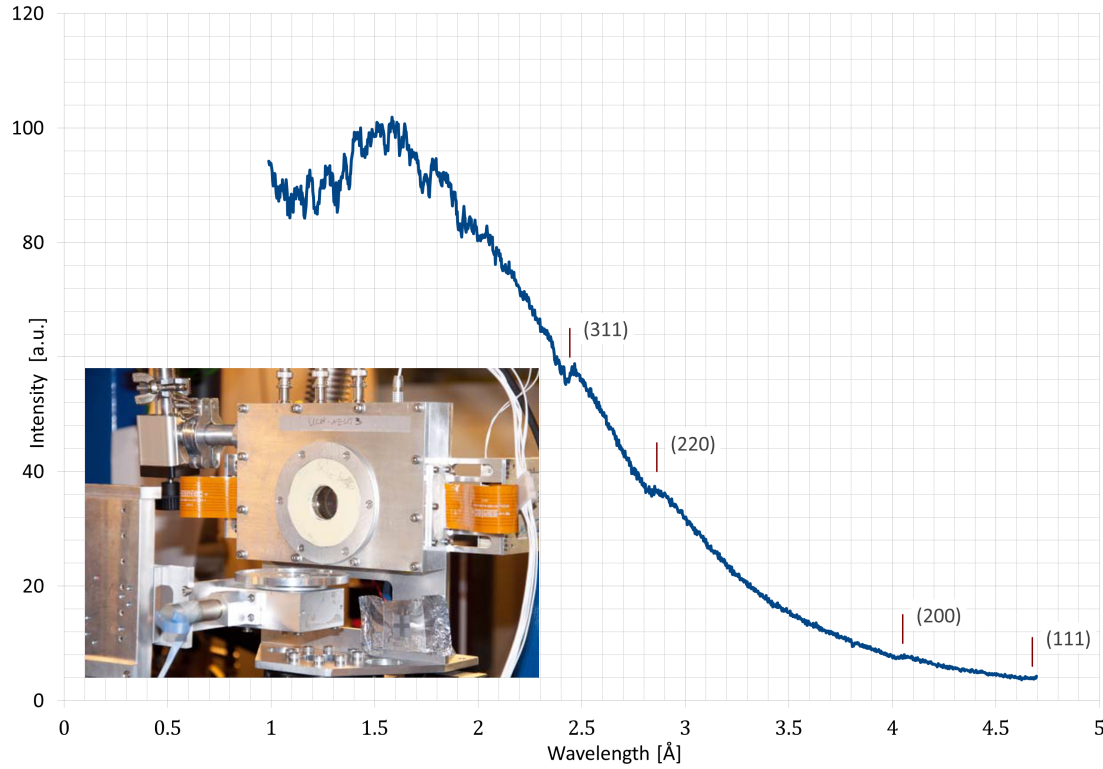


Figure 5.1: Measured spectrum at the ROTAX beamline (ISIS, UK), at the center pixels of the MCP detector (inset) used in this experiment. The four largest Bragg edges for Aluminium (from the traversed flight tube windows) used for calibrating the flight path length are marked.

5.1.2 Evaluation strategy

Separating the coherent elastic scattering contribution

A white beam (by integration of all wavelength frames) detector image, showing both crystals, is presented in figure 5.2a. For each pixel however, the transmission spectrum is available. It features sharp Bragg peaks from coherent elastic scattering on a smooth varying background formed by absorption and the other types of scattering. Based on the describing formulas derived in chapter 2, the wavelength dependence of their corresponding cross-section is approximated as:

5.1. Quantitative analysis of a single crystal wavelength scan

$$\Sigma_{abs} \propto \lambda \quad (5.1)$$

$$\Sigma_{coh}^{inel} \propto \Sigma_{inc}^{inel} \propto \frac{1}{\lambda} + \lambda \quad (5.2)$$

$$\Sigma_{inc}^{el} + \Sigma_{inc}^{inel} \propto \lambda^2 \quad (5.3)$$

The following fit function is then used for the cross-section of all but the coherent elastic scattering:

$$\Sigma_{tot} - \Sigma_{coh}^{el} = \alpha \cdot \frac{1}{\lambda} + \beta + \gamma \cdot \lambda + \delta \lambda^2 \quad , \quad (5.4)$$

with $\alpha, \beta, \gamma, \delta$ fit parameters. Thus, also any wavelength dependence in detector efficiency is taken into account. This part of the recorded cross-section can be used for investigating compositional and thickness variations across the sample, as any white beam radiography, though for the remainder of this chapter we focus on the information comprised within the coherent elastic cross-section. An example of the transmission spectrum of the cylindrical single crystal is shown in figure 5.2b, with contributions from coherent elastic scattering separated from the rest.

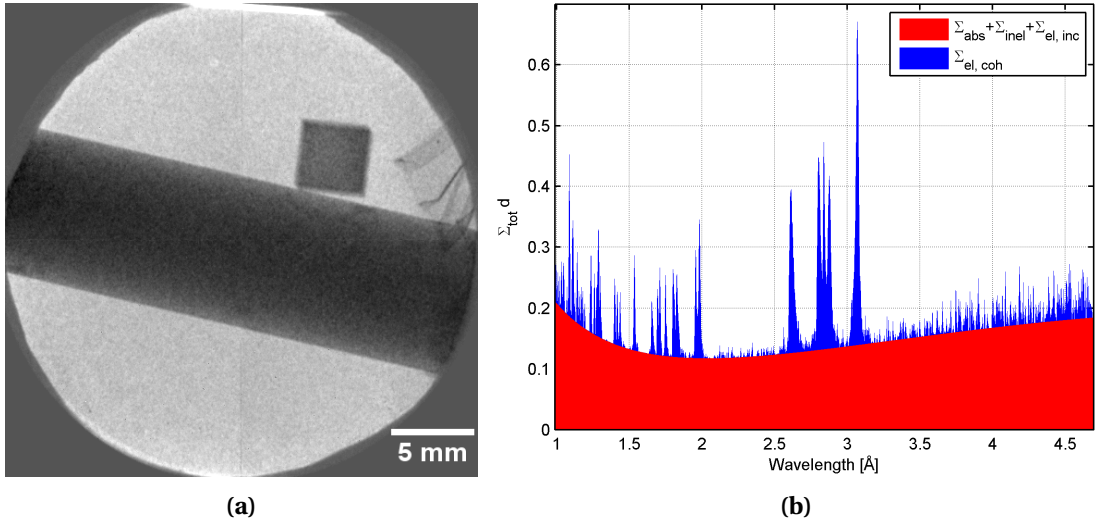


Figure 5.2: Detector image (integrated over all wavelength frames) showing the two single crystals (a) and the macroscopic cross-section behaviour at the center pixels, with the contribution from the coherent elastic scattering separated from the other interaction types (b).

Indexation strategy

The starting point for the indexation of the Bragg peaks is the consideration [121] that an $\{hkl\}$ lattice plane can only give rise to a Bragg peak up to $\lambda = 2d_{hkl}$, which follows from Bragg's law (eq. 2.42). For a BCC iron crystal, the three longest upper wavelength bounds are listed in table 5.1. This puts a limit on the number of lattice plane families the longest wavelength peak can belong to. In case of the pattern from figure 5.2b, the rightmost Bragg peak λ_1 has to be a $\{110\}$ peak.

Now that the lattice plane responsible for the first Bragg peak is known, one can derive the angle θ_1 between the incident neutron beam and the lattice plane normal \mathbf{n}_{110} , i.e.

$$\theta_1 = \arccos(\lambda_1 / 2d_{110}) \quad (5.5)$$

In the crystal reference system, this means the incident beam direction is restricted to the envelope of a cone of semi-angle θ_1 around \mathbf{n}_{110} . Only one degree of freedom is left, ϕ , the angle describing the cone envelope. For each possible beam direction \mathbf{n}_ϕ , all Bragg peak wavelength positions λ_{hkl} for all hkl lattice plane normals \mathbf{n}_{hkl} are calculated:

$$\lambda_{hkl} = 2d_{hkl} \cos \theta_{hkl}, \quad (5.6)$$

with

$$\theta_{hkl} = \arccos(\mathbf{n}_{hkl} \cdot \mathbf{n}_\phi). \quad (5.7)$$

For our iron single crystal, the geometry is illustrated in figure 5.3a. It should be pointed out that turning to the crystal reference system instead of the lab reference system, has the advantage that the freedom of rotation of the crystal around \mathbf{n}_{110} is already encompassed within ϕ .

$\{hkl\}$	$2d_{hkl}$
$\{110\}$	4.05 Å
$\{200\}$	2.87 Å
$\{211\}$	2.34 Å

Table 5.1: Upper wavelength bounds for the occurrence of the three largest $\{hkl\}$ families of BCC iron.

Similarity between calculated and experimental pattern

The calculated Bragg peak pattern is subsequently compared with the experimental one. De Gelder *et al.*, [122] define the similarity S_{fg} between two patterns f and g as

$$S_{fg} = \frac{\int w_{fg}(r) c_{fg}(r) dr}{\sqrt{\int w_{ff}(r) c_{ff}(r) dr \int w_{gg}(r) c_{gg}(r) dr}}, \quad (5.8)$$

with

$$c_{fg}(r) = \int f(x) g(x+r) dx \quad (5.9)$$

the cross-correlation function between the two patterns and

$$w_{fg}(r) = \begin{cases} 1 - |r|/l & |r| < l \\ 0 & |r| \geq l \end{cases} \quad (5.10)$$

a triangular weighted window function. It takes into account that two patterns can bear much resemblance, but have peak positions slightly offset w.r.t. each other, something that would be

5.1. Quantitative analysis of a single crystal wavelength scan

ascribed a low correlation value but has a high similarity. This will be due to e.g. insufficient accuracy in the TOF to wavelength conversion, the initial choice of lattice parameter (typically from literature values which can also vary by a few percent) and inevitably the discretization step for ϕ . The normalization by the denominator in equation 5.8 ensures comparability of similarity values for all ϕ . The evolution of the similarity for our iron crystal case study is shown in figure 5.3b. The Bragg cone envelope angle ϕ corresponding to its maximum, fixes the incident beam direction w.r.t. to the crystal reference system. Oversampling of ϕ will lead to increased computation times, while for undersampling one might miss the similarity peak and lose accuracy. Good results have been obtained with sampling at 1° intervals. A final coordinate transform brings us back to the lab reference system.

If more than one candidate plane existed for the longest wavelength Bragg peak, one would have to consider all of them and retain the one yielding the highest similarity to the experimental pattern.

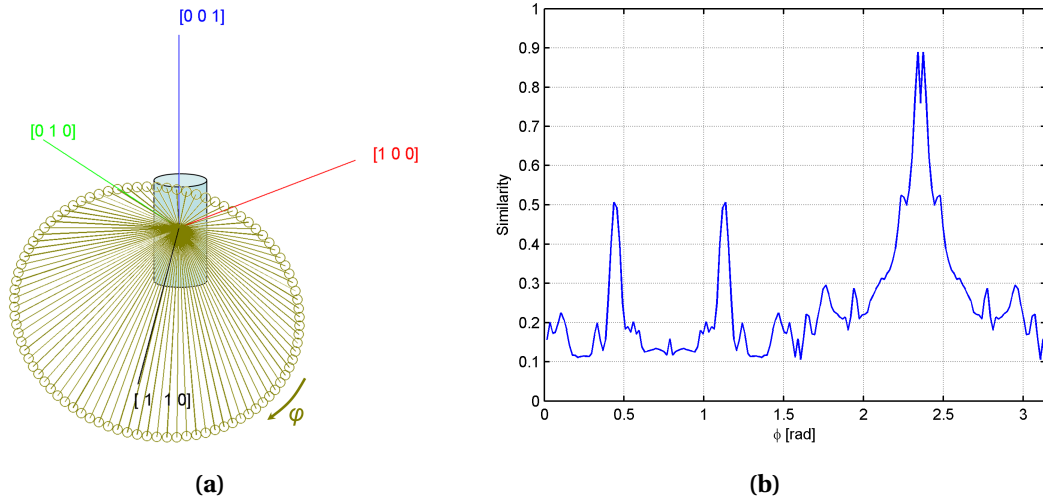


Figure 5.3: Possible beam directions w.r.t the single crystal upon considering the longest wavelength Bragg peak as $\{hkl\}$ (a) for which the similarities between calculated and experimental patterns are calculated (b).

Orientation and mosaicity mapping

For each pixel, the coherent elastic cross-section pattern is now indexed: it is known which crystal lattice plane gives rise to which Bragg peak (figure 5.4a) and what the orientation of the crystal is (figure 5.4b). The cylindrical single crystal was indeed put with its $[100]$ direction facing the beam port during the experiment, whilst the crystal cube was put in randomly and by chance both crystals orientations turned out to be misaligned by 15° only.

More information can be extracted from the pattern however. The peak width for instance, is a direct measure for the mosaicity of the crystal, which can also be mapped across the field of view (figure 5.5). Many single crystals are not perfect across their entire volume, but rather consist of small blocks that are slightly misaligned, which broadens the Bragg peak. Though the effect is ignored here, one should in principle deconvolve the instrumental broadening due

to finite neutron pulse width and detector time binning (e.g. [123]) as well as beam divergence, in order to obtain the through sample mosaicity.

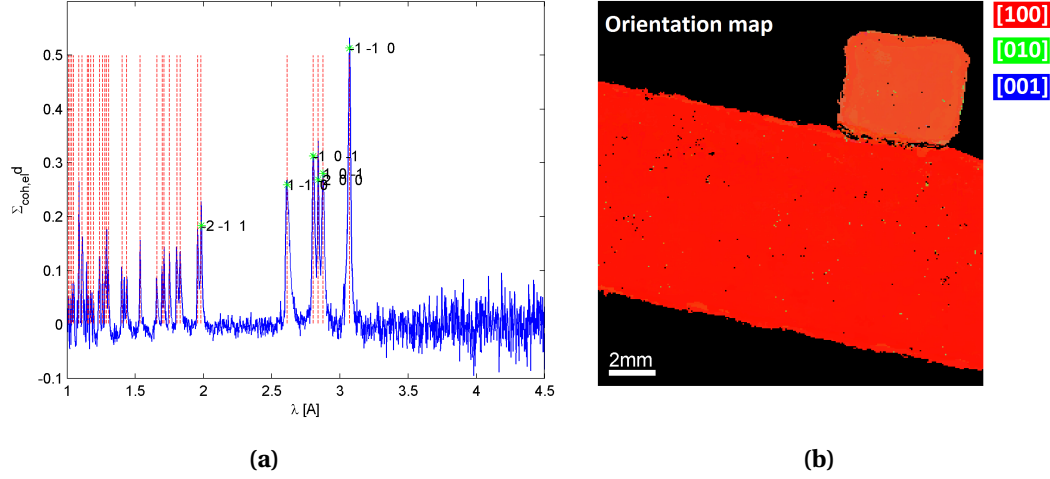


Figure 5.4: Indexed coherent elastic scattering cross-section, with the experimental pattern in blue, calculated Bragg peak positions in red (a). An orientation map is shown next to it (b), with RGB color values corresponding to the direction cosines of the beam direction w.r.t. the principal crystallographic axes.

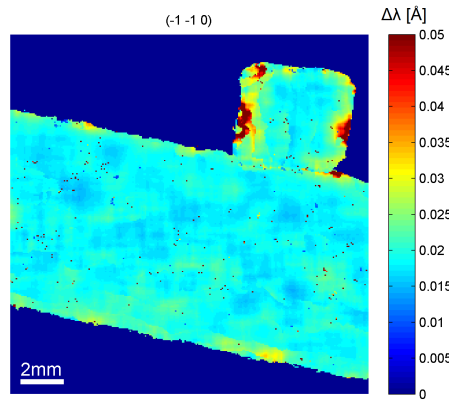


Figure 5.5: Peak width $\Delta\lambda$ (Full width at half maximum) of the Bragg peak given rise to by the (-1 -1 0) crystal plane.

In case there is more than one single crystal in the beam direction, i.e. a sample of multiple crystal(*lites*), pattern overlap will occur. The indexation scheme does not require much modification however. All experimental peak positions are put in a queue. Again, the longest wavelength peak is taken as a basis for indexation. As it will be due to one of the present crystallites, the highest similarity will be found between calculated single crystal pattern and experimental Bragg peaks due to that same crystallite. These peaks are indexed and removed from the queue. There is a new longest wavelength peak in the queue now and the indexation process is repeated until the queue is empty.

The two crystals were rotated to have them partially overlapping in the transmission direction. The indexed spectra at a detector region behind the cylinder alone, the cube alone and behind the both of them, is shown in figure 5.6.

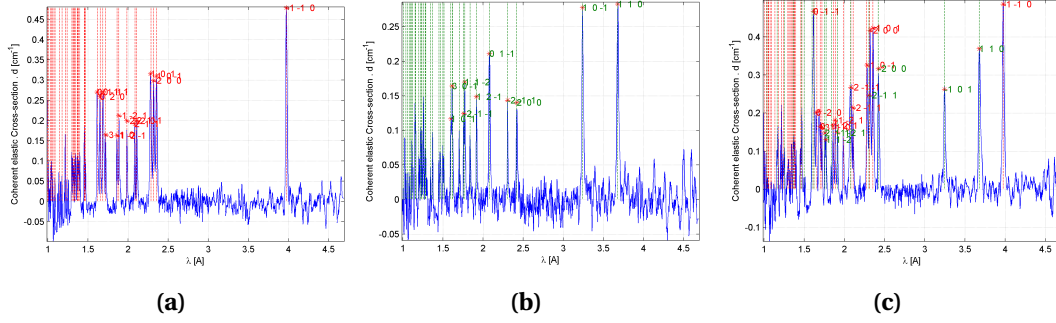


Figure 5.6: Indexed spectrum of the coherent elastic cross-section recorded behind the cylindrical single crystal (a) and the cube shaped crystal (b). Also in the region of crystal overlap, Bragg peaks are correctly identified as belonging to different grains, in this case two of them are identified and indexed.

Segmentation

With multiple crystals present, next to or behind (causing pattern overlap) each other, segmentation of the crystals is not straightforward. A modified version of the segmentation by fast scanning and adaptive merging algorithm [124] is developed.

We define a crystallite as a spatially connected region of similar crystal orientation. Typically, a high-angle grain boundary is characterized by a misorientation by more than $\delta=15^\circ$ across it [50].

The segmentation algorithm is illustrated schematically in figure 5.7. Consider an $M \times N$ matrix of pixels (coordinates i, j). The first pixel is by default classified as a first grain, $GrainID = 1$ (fig. 5.7a). We now run over all pixels, increasing the column index until the last one is reached, then turning to the next row (fig. 5.7a-l). At pixel (i, j) , each orientation indexed is compared to the ones for the pixel above it $(i - 1, j)$ and to its left $(i, j - 1)$.¹ If the misorientation with one of these is smaller than a set value δ , the pixel is registered under the same $GrainID$ (fig. 5.7b, for a pixel position with only one indexed orientation; fig. 5.7d,e in case of grain overlap). Otherwise, a new $GrainID$ is initiated (fig. 5.7c for a pixel position with only one indexed orientation; fig. 5.7f in case of grain overlap). In the case of one crystallite bulging out into the other one in the direction of smaller column indices, the protrusion will at first erroneously be considered a new grain (fig. 5.7). This is however set straight later on at higher pixel indices: in case the misorientation of pixel (i, j) with its neighbours at $(i - 1, j)$ and $(i, j - 1)$ is in both cases smaller than δ and yet the two neighbours have a different $GrainID$, the two segmented grains are merged (fig. 5.7h). Upon completion of the algorithm, having run once over all pixels and orientations, one ends up with a segmented grain map for the entire recorded field of view (fig. 5.7i). The orientation maps of the segmented crystallites are shown in figure 5.8, in this case the two single crystals were rotated to have partial overlap in transmission.

¹Only one of these for pixels bordering the edge of the matrix.

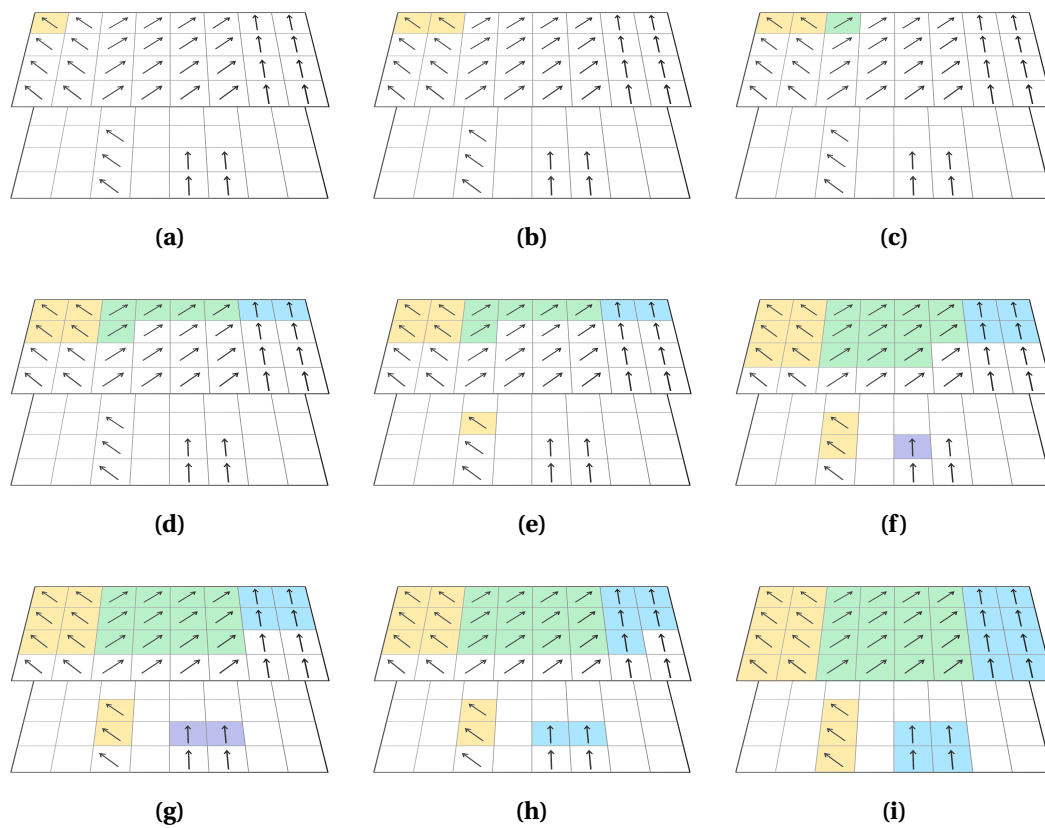


Figure 5.7: Illustration of the crystallite segmentation algorithm for the simplified case of three crystallites with no more than two crystallites overlapping. The neutron beam would be coming from the top.

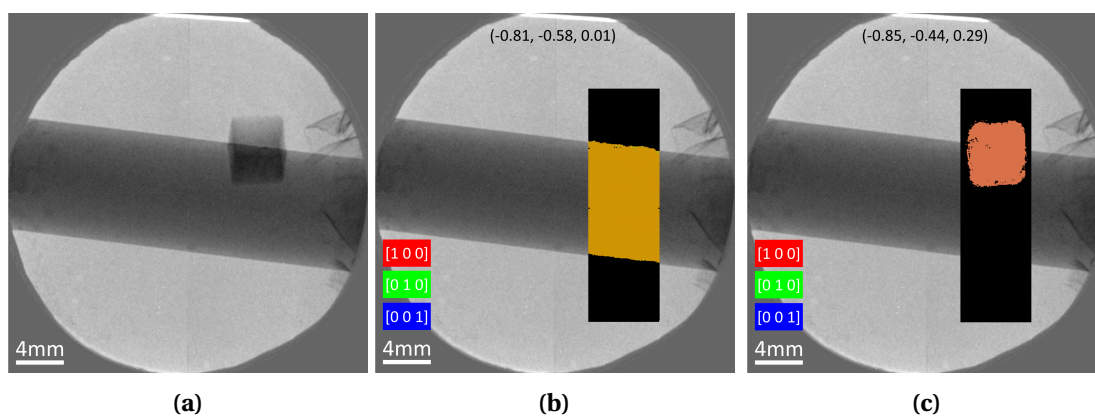


Figure 5.8: White beam transmission radiograph of two BCC iron single crystals, partially overlapping (a). The two crystals can be segmented and an overlay of their respective orientation maps is shown in (b) and (c). RGB values correspond to the direction cosines of the listed beam direction w.r.t. the principal crystallographic axes.

5.1.3 Considerations for tomographic extension

The long acquisition time for such a high wavelength-resolution scan, in combination with the requirement to record them under various sample rotation angles, puts a restraint on the tomographic extension of the method developed above. Nevertheless, in light of ongoing developments to increase neutron flux (new sources such as ESS [125], focusing guides [126]), it is useful to consider the options.

The recorded transmission spectrum is the result of joint attenuation by all crystallites i of thickness d_i present in the beam direction:

$$T(\lambda) = \prod_i e^{-\Sigma_i(\lambda)d_i} \quad (5.11)$$

Taking the negative natural logarithm and explicitly separating contributions from coherent elastic scattering:

$$-\ln T(\lambda) = \left[\Sigma_{abs}(\lambda) + \Sigma_{inc}(\lambda) + \Sigma_{coh}^{inel}(\lambda) \right] d + \sum_i \Sigma_{coh,i}^{el}(\lambda) d_i, \quad (5.12)$$

with $d = \sum_i d_i$ and assuming a single material element for simplicity.

The first term on the right hand side is independent of crystal orientation. Integrated over the entire recorded wavelength range, the resultant radiograph is sensitive only to the traversed material type and thickness. If available over a set of sample rotation angles, it can - as in standard white beam tomography - be used to reconstruct the sample's 3D material distribution.

Regarding the second term, we have seen how to separate the Bragg peaks belonging to the different grains and segment the different crystallites. Each term i of the summation can be integrated over the wavelengths of the Bragg peaks attributed to crystallite i , $\mathfrak{s}_{B,i}$,

$$\Sigma_{coh}^{el} d_i = \int_{\mathfrak{s}_{B,i}} \Sigma_{coh,i}^{el}(\lambda) d_i d\lambda \quad (5.13)$$

yielding a set of radiographs of the individual crystallites. The individual Bragg peak heights depend on the wavelength (eq. 2.43) and thus on the rotation angle (eq. 2.42). Integrating over all peaks not only increases crystallite projection image statistics, but also averages out wavelength/angular-dependence before tomographic reconstruction. Alternatively, one can correct for the wavelength-dependence and reconstruct a normalized value at the Bragg wavelength, e.g. $\Sigma_{coh,i}^{el}(\lambda_{110,i}) d_i / \lambda_{110,i}$, or renormalize the crystallite projections under different angles w.r.t. each other, as they all represent the same diffracting volume. Collecting either quantity for all rotation angles, one can reconstruct the three-dimensional crystallite shape.

A first theoretical glance, suggests also tomographic reconstruction of the mosaic spread in a single crystal is feasible. The observed Bragg peak at a certain pixel, follows a Gaussian distribution centered on λ_{obs} and of standard deviation σ_{obs} (representative of the mosaicity of the crystal plane giving rise to that Bragg peak): $\mathfrak{G}(\lambda_{obs}, \sigma_{obs}^2)$. It is the result of the additive contri-

bution of the cross-section in each of N voxels v traversed by the neutron beam before striking that pixel, each of which can also be associated with a Gaussian wavelength-dependence: $\mathfrak{G}(\lambda_v, \sigma_v^2)$. As a sum of Gaussian distributions is again a Gaussian distribution

$$\sum_{v=1}^N \frac{1}{N} \mathfrak{G}(\lambda_v, \sigma_v^2) = \mathfrak{G}\left(\sum_{v=1}^N \frac{1}{N} \lambda_v, \sum_{v=1}^N \left(\frac{1}{N} \sigma_v\right)^2\right) = \mathfrak{G}(\lambda_{obs}, \sigma_{obs}^2), \quad (5.14)$$

one can reconstruct the mosaicity at each voxel, σ_v from projection maps, σ_{obs} , under different angles. However, more in-depth investigation is still required, e.g. finding the proper wavelength normalization here too, though outside the scope of this work.

It should be noted that the above only holds in the kinematic approximation [127], with no extinction occurring, so the cross-section for coherent elastic scattering is independent of sample thickness and the recorded Bragg peak amplitude $\Sigma_{coh}^{el}(\lambda_{B,i})d_i$ is directly proportionate to the crystal thickness.

5.2 Monochromatic imaging of oligocrystals

In the previous section, we analysed the full transmission spectrum and Bragg peak pattern at each pixel to map orientation and mosaicity. However, such wavelength scans at high spatial and temporal resolution are very time consuming. What information can already be obtained from a single radiograph of reduced wavelength bandwidth?

Again we turn to Bragg's law (eq. 2.42). Suppose we have two neighbouring crystallites (sufficiently large to be spatially resolved by our imaging set-up). By definition, they are misoriented w.r.t. each other. As such, they will diffract at different wavelengths. By restricting the beam spectrum to a narrow wavelength band, one will observe a region of reduced intensity in the digital radiograph, corresponding to projections of the crystallite oriented as such as to diffract at a wavelength within that band. Information on crystallite morphology can thus readily be obtained (see section 5.4 for examples), without the need for time-consuming energy-scans at high energy resolution.

Choosing a wavelength band above the Bragg cut-off, no diffraction by the crystallites is possible anymore and one only observes a change in the elemental distribution within the sample².

The principle is illustrated schematically in figure 5.9³.

²See chapter 4 for more details on imaging in this wavelength range.

³The transmission data shown, was recorded for the iron crystal cube at 0° and 10°, with sample and experimental conditions already described in section 5.1.1.

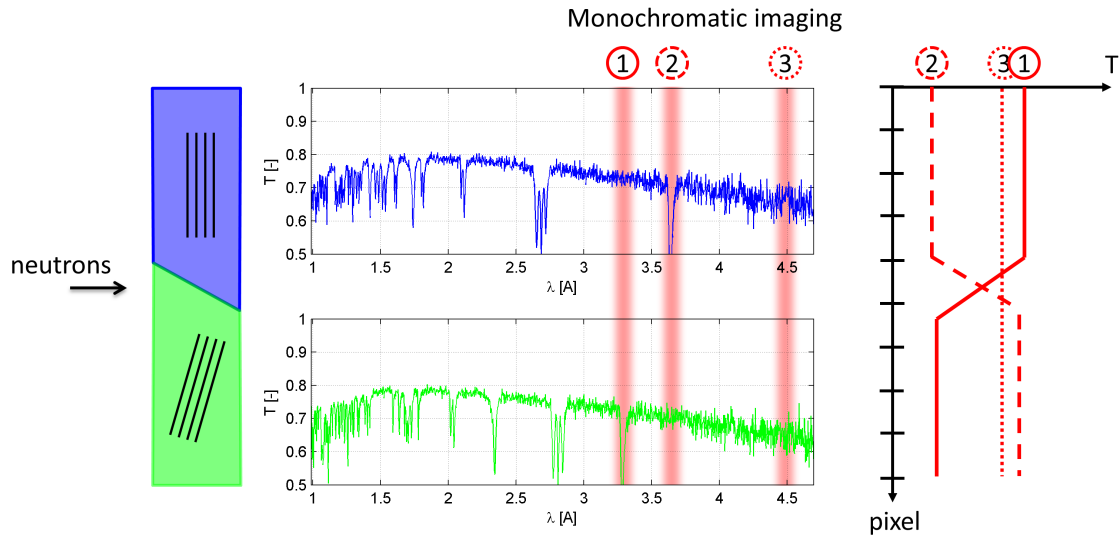


Figure 5.9: Principle of imaging with a reduced wavelength band in case of few, large crystallites. Depending on the chosen wavelength, diffraction can occur from a crystallite, resulting in a region of reduced intensity in the digital radiograph, corresponding to the projection of that crystallite (case 1 for the bottom crystallite, case 2 for the top one). At long wavelengths past the Bragg cut-off, no crystallite contrast can be observed (case 3).

5.3 Application 1: monochromator crystals for CAMEA

5.3.1 Introduction

CAMEA, short for *Continuous Angle Multi-Energy Analysis*, is a new concept for a time-of-flight inelastic neutron spectrometer at ESS [128]. Such instruments are used for the studies of phonon and magnon excitations by studying the direction and the energy of scattered neutrons. Current time-of-flight spectrometers only analyze at a single energy of scattered neutrons.

CAMEA on the other hand, would use a set of crystals placed behind each other in the scattered beam direction, each one selecting out a different energy to analyze. The spectrometer's efficiency would thus be boosted significantly, allowing studies of weaker interactions or fast investigations of dynamic processes.

The currently foreseen design is sketched in figure 5.10. The instrument will include 15 analyzer-detector banks, each one counting 10 analyzers of at least 5 pyrolytic graphite crystals, measuring $5\text{-}10 \times 1 \text{ cm}^2$.

Given the difficulties in producing large homogeneous pyrolytic graphite crystals and the amounts to be procured, a fast quality assurance method is required. The option of energy-selective neutron imaging is investigated to this end.

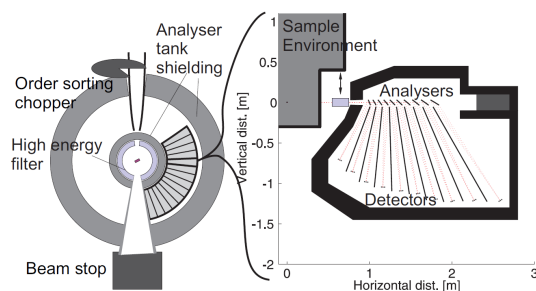


Figure 5.10: Simplified view on the CAMEA time-of-flight spectrometer considered for ESS. A close up of one of the 9 angular segments, reveals it to consist of 10 consecutive analyzer-detector banks, each analyzer constructed out of several pyrolytic graphite crystals. (Image taken from [128])

5.3.2 Experiment

Three pyrolytic graphite monochromator crystals were investigated. They were manufactured by Panasonic, each measuring $10 \times 50 \times 1 \text{ mm}^3$, two of them having a mosaicity of 1° and one of 1.3° . They were fixed with their back sides pressed against a single 0.5 mm thick flat aluminium plate so that they could be imaged together.

The experiment was conducted at BOA, using a double crystal monochromator in combination with a Beryllium filter to suppress the higher-order spectral contamination. The crystals were turned to a Bragg angle of 38.8° w.r.t. the incident neutron beam, to have them diffracting at 4.2 \AA - a wavelength in the typical CAMEA working range. The incident wavelength was then stepped from 4 \AA to 4.4 \AA per 0.02 \AA . For the imaging itself, a $100 \mu\text{m}$ thick ^6Li -based scintillator screen was used together with the Andor Ikon-M CCD camera, having $1024 \times 1024 \text{ pixel}^2$ focused on a $109 \times 109 \text{ mm}^2$ field-of-view. The exposure time for a single image was 195 s. Photographs of the experiment are shown in figure 5.11.

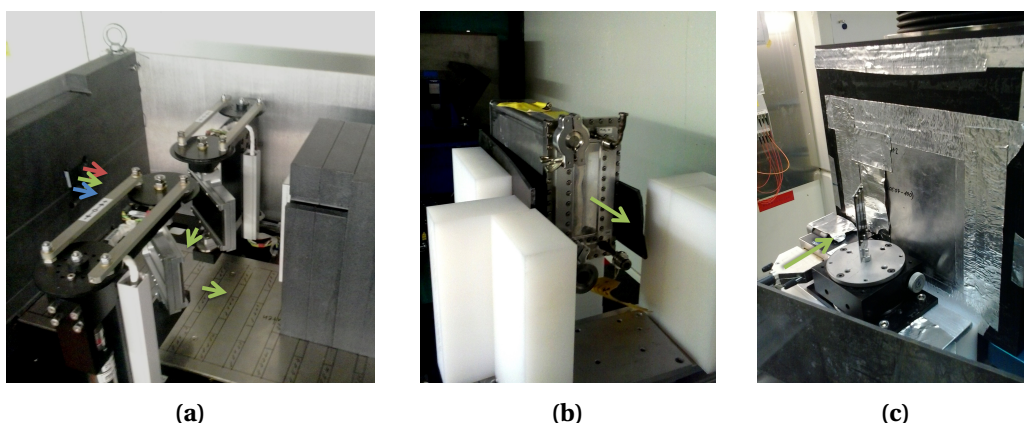


Figure 5.11: Experimental set-up with (a) the double crystal monochromator (with the cover removed), (b) the Beryllium filter and (c) the three crystals mounted together on a rotation stage in front of the *midibox* imaging set-up. Arrows indicate the neutron beam direction.

5.3.3 Results and discussion

At first, the (110) Bragg edge of a 5 mm thick iron plate was scanned to determine and correct the wavelength shift w.r.t. monochromator setting at each pixel (see chapter 3).

The measured macroscopic cross-section exhibits a Gaussian behaviour as a function of wavelength. For each pixel, it is fitted for improved accuracy of the defining parameters (figure 5.12). Note that due to the wavelength shift correction, experimental points no longer correspond to the set wavelength interval from 4 Å to 4.4 Å per 0.02 Å.

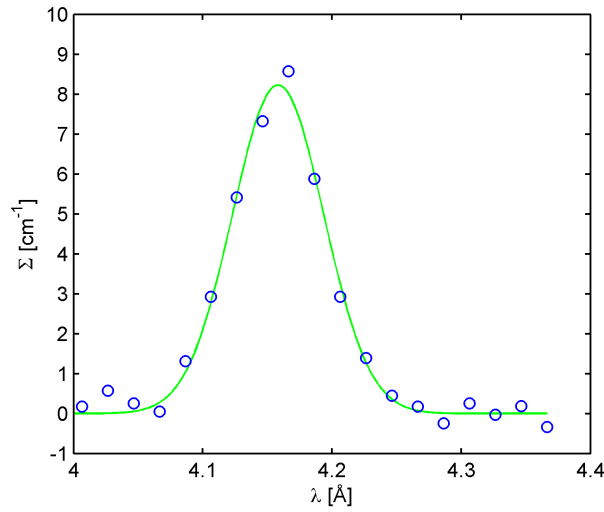


Figure 5.12: Observed variation in macroscopic cross-section (blue circles) and fitted Gaussian profile (solid green line) for an arbitrary pixel behind the right-most crystal in figure 5.13.

Figure 5.13 shows a map of the fitted amplitude A , a measure for the variation in reflective power. The recorded peak position λ_0 is influenced by local variation in either orientation or lattice spacing (Bragg's law, eq. 2.42). The map of the fitted Gaussian's standard deviation σ_λ is affected by variations in mosaicity. One should disregard the region around the outer nodges where the crystals were screwed to the aluminium backing.

All three crystals were homogeneous in their reflectivity and mosaicity. It can immediately be inferred that the middle crystal was the one of 1.3° mosaicity and the outer ones of 1°. The mapped Bragg peak position however shows some interesting features. The left most crystal has an average Bragg wavelength offset of 0.05 Å compared to the other two. Following Bragg's law and a $d_{002}=3.36$ Å, this corresponds to a misalignment of 0.5° of the crystal planes w.r.t. the sample surface, though a systematic error in the screw mount can not be ruled out. Alternatively, a 1 % smaller lattice plane spacing would have a similar effect.

In the middle crystal, a clear split in Bragg wavelength is observed between its left and right half. No mounting offset can be invoked to explain such a dichotomy. Rather, it is a property of the sample itself and most likely the result of non-uniform crystal growth.

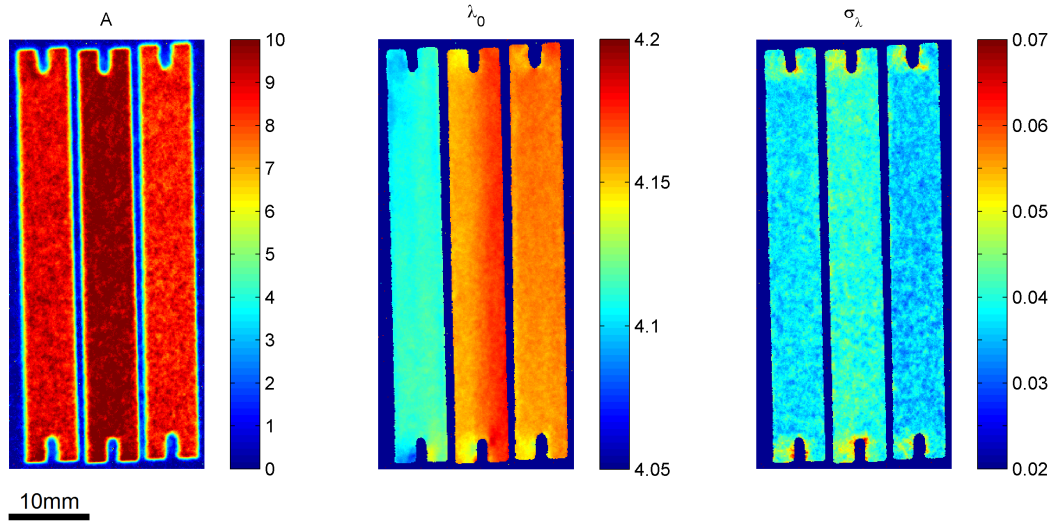


Figure 5.13: Map of the fitted Gaussian amplitude A , peak position λ_0 and standard deviation σ_λ of the three investigated pyrolytic graphite crystals.

5.3.4 Conclusion

The conducted experiment shows that energy-selective neutron imaging can be used for the investigation of monochromator crystal quality at high spatial resolution. Information is obtained for each sample point simultaneously, *versus* the scanning with a pencil beam approach at diffractometers and spectrometers. In short time spans of around 1.5 hours, it is possible to inspect over $10 \times 10 \text{ cm}^2$ of projected monochromator surface for spatial variation in reflectivity, mosaicity and orientation/lattice spacing at a resolution of $\approx 100 \mu\text{m}$.

5.4 Application 2: morphological and phase analysis of iron-nickel meteorites

5.4.1 Introduction

In order to univocally characterize a metallic material, a textural analysis is a mandatory requirement. Traditionally this necessity is satisfied by means of microscope observation on specifically prepared portions of the sample. For this purpose, portions of the sample have to be cutted, polished, chemically or electrochemically etched, etc. making this analysis intrinsically destructive. Therefore, traditional metallographic analysis is not suitable when performed on rare and unique objects of high scientific and economic value. Lots of interesting items fall in this category: sculptures and artistic goods, archaeological finds, rare coins and meteorites.

In the case of metallic meteorites, namely iron meteorites, the study of texture is extremely important since it provides data regarding the formation and the minero-chemical evolution of the asteroids and planetary systems. Iron meteorites are the biggest and heaviest examples of extraterrestrial material that fall to earth. They are constituted by Fe-Ni alloys, mainly kamacite (metallic iron BCC structure with up to 7.5 % nickel in solid solution) and taenite

5.4. Application 2: morphological and phase analysis of iron-nickel meteorites

(metallic iron, FCC structure with nickel ranging from 25 to 70 %). Few other compounds such as sulfides (troilite and daubreelite), phosphides (schreibersite) and oxides (chromite, spinel) generally account for less than 5 % by volume. Nevertheless these tiny amounts are important indeed since they provide useful indications for meteorite classification.

Slowly cooling of the meteorite's parental body below about 900°C gives rise to the exsolution of taenite bands from bulk kamacite resulting in a fine intergrown of these two phases named Widmanstätten patterns, a peculiar feature characteristic of iron meteorites. Observing the relative thickness of the taenite bands, a fundamental geochemical parameter such as parental body cooling rate, can be profitably inferred [129, 130].

Texture and phases investigation using penetrative radiation such as X-rays and neutrons offer an advantage in respect to the classical approach being not destructive. While radiography and tomography is similar in principle for both beams, it is very complementary in practice due to the different interaction mechanisms: X-rays interact with the electronic shell while the chargeless neutrons with the atomic nuclei.

In this section we present the results of an in depth tomographic study performed on a iron meteorite (Mont Dieu meteorite) by means of energy-selective neutron imaging. This method has already been reported to be sensitive to crystalline properties of metallic objects [131, 32], which is now for the first time applied to iron-nickel meteorites and extended with the use of advanced 3D reconstruction methods.

Mineral inclusions, oxidation crust and main iron body can be studied in 3D. Moreover different phases and crystallites can be identified and orientation characterised. This technique allows to determine the relative 3D distribution of compositionally very similar phases such as taenite and kamacite providing evidence of the capability of this non-destructive technique to allow a 3D metallographic analysis without sample preparation.

5.4.2 Materials and experimental set-up

The meteorite sample (figure 5.14) was obtained from the Museo di Scienze Planetarie di Prato (catalogue n° MSP-PL 1412)⁴. The meteorite was found in July 1994 in the forest of Mont Dieu (Ardenne, France) and the name Mont Dieu was officially attributed by the Meteoritical Society [132]. Bulk metal composition is the following: 0.4 wt% Co, 7.5 wt% Ni, remaining Fe [133]. According to the original description, the meteorite is constituted by taenite and kamacite intergrowth and it is characterized by the presence of troilite (FeS) and schreibersite ((Fe,Ni)₃P) along with rare chromite (Cr₂O₃).

⁴We gratefully acknowledge its curator Dr. Vanni Moggi-Cecchi for providing the sample.



Figure 5.14: Photograph of the investigated Mont Dieu meteorite sample mounted on its holder.

Neutron imaging on the meteorite has been performed at the ICON beamline at the Paul Scherrer Institut [24]. A monochromatic beam was produced by inserting a mechanical velocity selector in the beamline, close to the aperture. The transmitted neutron beam is converted into visible light using a $100\text{ }\mu\text{m}$ thick $^6\text{Li ZnS}$ scintillator, which is then guided via a mirror to an Andor DW434 CCD camera with 1024×1024 pixels. The field of view was $110\text{ mm}\times 110\text{ mm}$ with $107\text{ }\mu\text{m}$ pixel size, allowing to image most of the sample. Using different light focusing optics, a $55\text{ mm}\times 55\text{ mm}$ image was obtained at $54\text{ }\mu\text{m}$ pixel size, for a high resolution measurement of the meteorite tip.

Radiographies were taken at mean wavelengths of $3.0\text{ }\text{\AA}$, $3.2\text{ }\text{\AA}$, $3.4\text{ }\text{\AA}$, $3.6\text{ }\text{\AA}$, $3.8\text{ }\text{\AA}$, $4.0\text{ }\text{\AA}$, $4.2\text{ }\text{\AA}$ and $5.0\text{ }\text{\AA}$, for both described resolution settings. Subsequently, two energy-selective tomographies at $5.0\text{ }\text{\AA}$ and $3.6\text{ }\text{\AA}$ were made. Projections were obtained for 376 sample rotation angles equiangularly spaced from 0° to 180° , with a projection exposure time of 38 s.

An isotope analysis by gamma spectroscopy was carried out on the sample after the initial wavelength scan to make sure no radioactive isotopes with a long half-life would be formed during future tomographies and the sample could be returned safely to the museum.

5.4.3 Principle

As discussed in section 5.2, a different beam attenuation is expected across the meteorite sample depending on the local lattice plane orientation of the different crystallites towards the primary beam. By varying the incoming neutron wavelength or by changing the sample

5.4. Application 2: morphological and phase analysis of iron-nickel meteorites

scattering angle, i.e. rotating the sample with respect to the incoming beam, one can get different crystallites come into contrast. This is demonstrated in the next subsection.

The largest lattice plane distances for the present kamacite and taenite phases as determined from previous neutron diffraction experiments [134] are listed in table 5.2, implying a Bragg cut-off at 4.14 Å.

Lattice plane	d-spacing
(110)	2.027 Å
(200)	1.433 Å
(a) Kamacite	
Lattice plane	d-spacing
(111)	2.071 Å
(200)	1.794 Å
(220)	1.268 Å
(b) Taenite	

Table 5.2: Two largest lattice spacings of Kamacite (a) and the three largest ones of Taenite (b).

5.4.4 Results and discussion

Wavelength radiographic scan

Figure 5.15 shows neutron transmission radiographies of the meteorite for different wavelengths yielding contrast between differently oriented grains. A radiography at 5.0 Å allows to distinguish between elemental (e.g. mineral inclusions) and crystallographical sample features as no diffraction can occur at this wavelength for the present crystalline phases, i.e Bragg's law cannot be fulfilled. Two different types of morphology can be distinguished: convex crystallites of centimetre size (probably kamacite) and needle-type structures of sub-millimetre thickness (the lamellar Widmanstätten patterns of taenite and kamacite). The wavelength scan also holds basic orientation information of the crystallites. Selecting some specific crystallites and supposing them to be single crystals or highly oriented polycrystals, the wavelength of minimum transmission corresponds to the fulfilment of the diffraction condition and can thus be related to the crystallite orientation with the incident beam through equation 2.42. As an example, the crystallite indicated in figure 5.15 with the top arrow exhibits a fitted minimum transmission at 3.74 Å (inset). Attributing this needle-like crystallite to the Taenite phase on morphological grounds, the application of Bragg's law together with table 5.2, tells us this attenuation can only happen by diffraction from the (111) crystal planes under a Bragg angle $\theta=64.5^\circ$. With the incoming neutron beam normal to the meteorite surface, the (111) direction is thus at 25.5° normal to the surface.

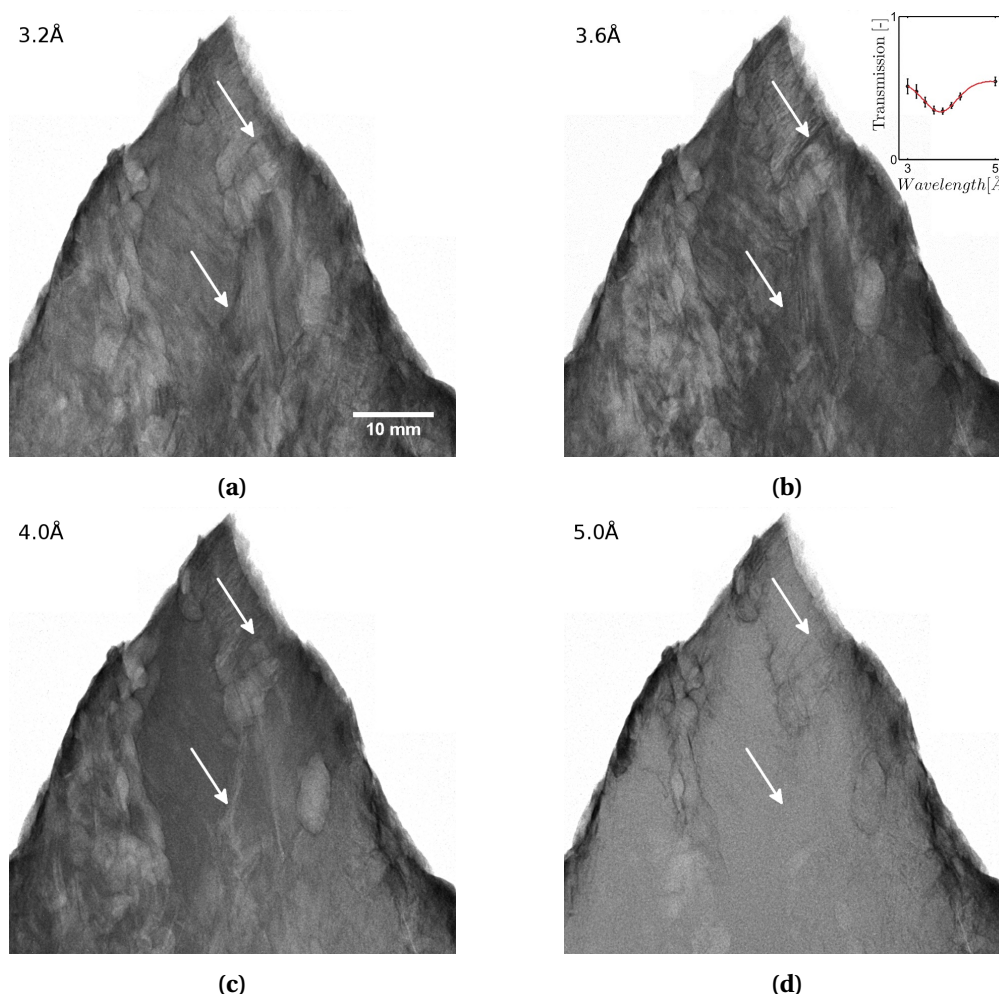


Figure 5.15: Radiographies taken at different mean neutron wavelengths. Arrows illustrate crystallites coming in and out of contrast with the inset showing the transmission variation for the grain indicated by the top arrow.

Tomography at 5 Å

At 5.0 Å, the Bragg law can no longer be fulfilled for the phases present in the meteorite, having lattice spacings as in tables 5.2a and 5.2b. As such, diffraction at the crystallites is no longer possible and no contrast between them is observed anymore. In this wavelength regime, the isotope dependent absorption contrast dominates. Tomographic reconstruction using the standard filtered back projection algorithm allows for segmentation of the different material regions present in the sample: main iron-nickel body, the outer oxide crust and mineral inclusions. A 3D volume rendering of the sample together with a virtual slice through the meteorite are presented in figure 5.16. These features can then be further quantified for future meteor classification. E.g. in the above mentioned figure, the oxidated layer on the left side is only 1.7 mm thick, while on the right side it is penetrating over 1 cm into the bulk and the volume fraction of supra-millimetre mineral inclusions (attributed to FeS nodules [133] and characterized by the lower macroscopic cross-section) was determined to be 3%.

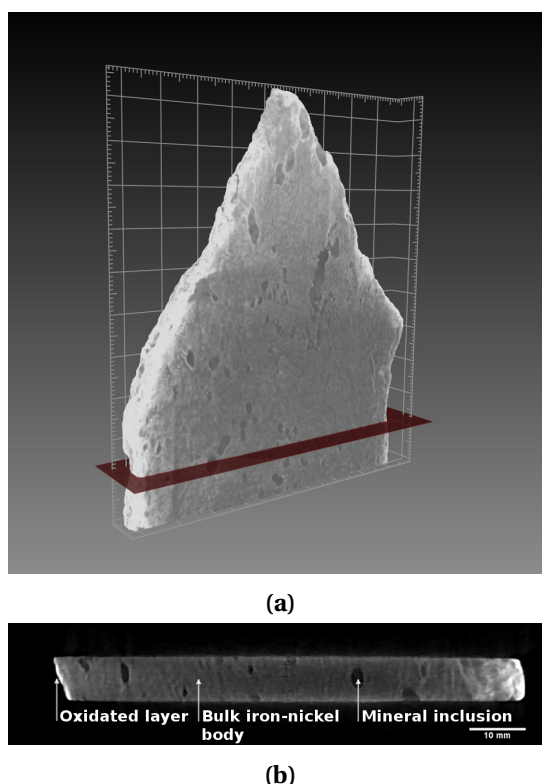


Figure 5.16: Threedimensional volume rendering of the investigated meteor sample (a) - grid lines are 10 mm apart – with the virtual cutting plane for the slice shown in (b).

Tomography at 3.6 Å

At 3.6 Å diffraction effects are visible in the transmission signal. During sample rotation, crystallites will move in and out of contrast depending on their orientation with respect to the incoming neutron beam. This is illustrated for the marked crystallite in figure 5.17, where again by applying Braggs Law one can determine this (Kamacite, based on morphology) crystallite has its (110) direction at 27.4° with respect to the incident beam.

In such case, simply reconstructing the full tomographic dataset would lead to erroneous results, as the attenuation induced by each sample volume element changes with its orientation in the beam and does not contribute to every projection as assumed in the standard reconstruction algorithm.

A solution is found in selecting from all the acquired projections the ones where a crystallite of interest contributes to. The crystallite's volume is then reconstructed based on those projections by means of algebraic reconstruction techniques (chapter 1, section 1.4.2). In this class of algorithms, the reconstruction task is rewritten as the matrix equation $Ax = b$, with x being the unknown 3D volume, b the recorded projections and A the projection system matrix. The problem is generally underdetermined and is solved iteratively. Though computationally more intensive, it offers superior performance when reconstructing objects using a limited number of non-equiaugular projections and allows to include additional reconstruction

constraints [135]. In this work, reconstruction was performed with the ASTRA-toolbox [136] using the SIRT algorithm. The available reconstruction at 5 Å was used as a mask for the sample geometrical outline. As such, the crystallite rendered in figure 5.18 was reconstructed using the projections acquired between 12° - 46°, 58° - 107° and 129° - 153° only.

Though not applied here, one could rescale the absorption cross-section profile obtained from the tomography at 5 Å to 3.6 Å according to the $1/v$ -law and subtract it from the 3.6 Å slices to end up with only the reconstructed scattering cross-sections responsible for crystallite contrast.

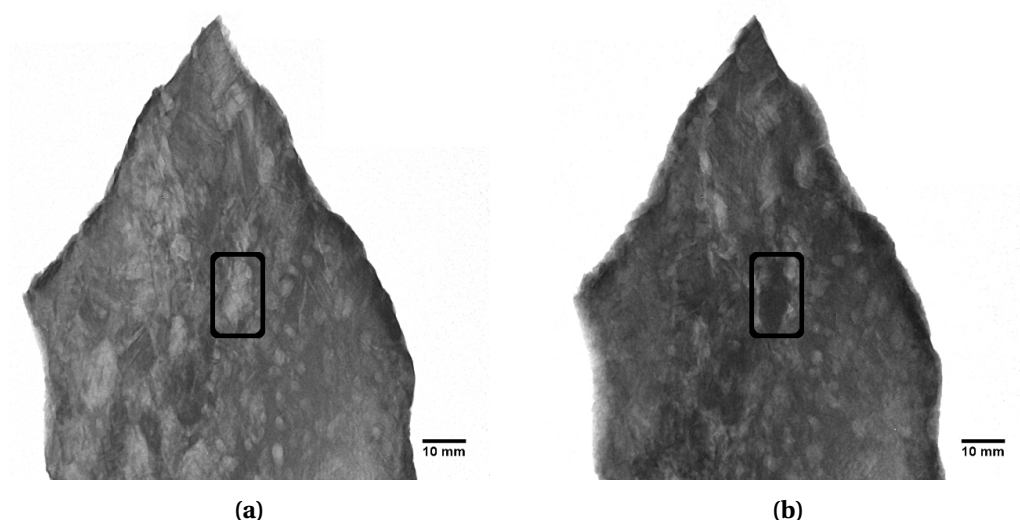


Figure 5.17: Projections at 0°(a) and 21.5°(b) illustrating the changing crystallite contrast. An iterative reconstruction of that crystallite is shown in figure 5.18.

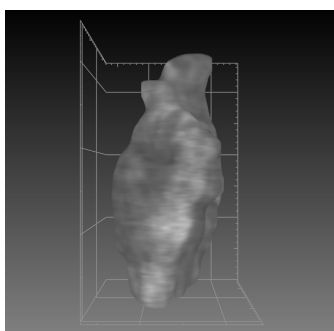


Figure 5.18: Threedimensional rendering after reconstruction of the crystallite marked in figure 5.17, with grid lines 5 mm apart.

A more detailed view on the difference in reconstruction is given in figure 5.19. Standard reconstruction using the filtered back projection algorithm over all projections from 0° - 180° shows several non-physical artefacts: stripes of reconstructed negative cross-section along the meteors' long axis due to zero recorded transmission in this direction (also called starvation artefact) and streaks of reconstructed material sticking out of the meteor due to missing

angular information with the diffracting grain not appearing in every projection included in the reconstruction. These artefacts can be avoided using the iterative reconstructor through the applied nonnegativity and mask constraints and more contrast at the grain region is obtained.

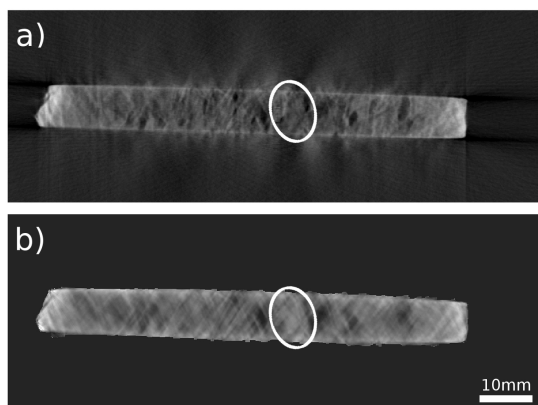


Figure 5.19: Reconstructed meteor slice using the filtered backprojection for $0^\circ - 180^\circ$ (a) and the SIRT algorithm over $12^\circ - 46^\circ$; $58^\circ - 107^\circ$; $129^\circ - 153^\circ$ (b).

The crystallite was selected for reconstruction based on visible inspection of acquired projections after the measurement. For future investigations one can envisage actively aligning diffraction vector and rotation axis to have a crystallite of choice in diffraction condition for all projections for the purpose of reconstruction, similar to [137]. Alternatively, as crystallites stay in diffraction contrast over tens of degrees due to the broad incident wavelength band, one could apply stereoscopy methods to obtain limited 3D spatial information as well.

In principle, one could also use the diffracted beam to obtain crystallite orientation and shape information, similar to the well established 3DXRD and DCT synchrotron methods [138, 139]. First attempts in this direction for neutrons are reported in the next chapter, though an initial examination of the Mont Dieu meteorite could not reveal sharp diffraction projections, the crystallite's mosaicity being too high.

5.4.5 Conclusion

Using energy-selective neutron imaging it was possible to identify morphology and location of mineral inclusions and oxidation crust of an iron-nickel meteorite in a non-destructive way. Moreover, using wavelengths that allow for diffraction to occur in the sample, one can distinguish between the differently oriented crystallites and even make a 3D crystallite reconstruction using algebraic reconstruction techniques. These results are of strong importance in the characterization of the evolution of meteorites and can give innovative data which might change in the future the classification criteria of meteorites.

6 Neutron diffraction contrast imaging

In this chapter, we perform neutron imaging investigations from a different perspective, using diffracted neutrons. Neutron imaging typically investigates the variation in transmitted neutron beam intensity through material and thickness dependent attenuation in the sample. The neutrons that are removed from the direct beam through absorption and scattering are ignored or deemed a nuisance (e.g. a hindrance to quantification). However, in this chapter, we will see how neutron imaging can be performed beneficially using neutrons that underwent a specific type of scattering, namely diffraction, yielding crystal orientation information. After outlining the advantages of the technique and the required set-up [140], an example of digital neutron diffraction radiography is given, followed by an 3D extension of the method for single crystals [141] and polycrystals [142].

6.1 Motivation

High energy-resolution is required to resolve all Bragg peaks of the transmission spectrum for indexation and orientation mapping, the Full Width at Half Maximum (FWHM) of the Bragg peaks of the iron crystals examined in the previous chapter (fig. 5.6) e.g. being on the order of 0.02 Å. Neutron imaging at such high energy-resolutions is only present at TOF facilities. At continuous sources, the peak broadening and overlap induced by the monochromator's energy-spread function (which stands around 0.1 Å FWHM for a typical DCM) greatly compromises the method.

Working with an incident wavelength bandwidth larger than the crystal's Bragg peak FWHM also leads to a loss of image contrast as the recorded transmission radiograph is defined by the ratio of the wavelength-integrated beam intensity with and without the crystal (eq. 1.17). Small variations in the crystal's local Bragg reflectivity will thus hardly be picked up.

However, one can think of the crystal as a monochromator in itself. Depending on its orientation in a white or pink neutron beam, it will diffract neutrons of specific wavelengths λ_B under an angle θ_B out of the direct beam. Bragg's law stipulates the relation between crystal lattice plane angle (plane spacing d_{hkl}) with the incident neutron beam θ_B and the diffracted wavelength λ_B :

$$2d_{hkl} \sin \theta_B = \lambda_B \quad . \quad (6.1)$$

With the whole crystal volume illuminated, these diffracted neutrons will form a projection of

that volume on any position-sensitive detector they fall on.

Working now outside the direct beam area, one only detects the diffracted neutrons¹, by default obtaining the highest possible intensity contrast for the coherent elastic scattering process.

The position of the diffraction projections on the detector is determined by the orientation of the crystal. A higher orientation sensitivity can be obtained than for the case of energy-selective transmission imaging. Consider e.g. a BCC iron crystal, with (110) plane oriented to diffract neutrons towards a detector at 90°. A misorientation of 0.1° will lead (taking the derivative of Bragg's law) to a change of the diffracted wavelength by 0.005 Å – a number hard to pick up even with TOF. On the other hand, the position of the diffracted neutron projection on that detector, placed 50 mm away, will change by 175 μm, well above the typical spatial resolution of neutron imaging detector systems.

Moreover, the angular separation of the diffraction projections of differently oriented crystallites, relaxes the upper limit on the number of crystallites that can be dealt with compared to transmission-based methods.

Diffraction imaging or topography² has a long history in the X-ray community since Berg obtained his first diffraction projections on rock salt in 1931 [144]. Stimulated by the availability of high-intensity synchrotron radiation beams, a multitude of variations nowadays exists at different dedicated beamlines [145, 146]. One can work with a polychromatic or monochromatic beam that can either fully encompass the sample or be limited to a line section through it. Extension to 3D also exists with X-ray diffraction tomography methods such as topo-tomography [137], Diffraction Contrast Tomography (DCT) [139] and 3DXRD [147]. But whereas X-rays interact with the electron shell of the atom, neutrons interact with the nucleus, yielding techniques similar in principle, though complementary in practice: neutrons generally offer bulk penetrability of metals, e.g. iron, nickel or lead crystals. Neutron topography has been carried out mainly in the '70s and '80s using X-ray films with a gadolinium convertor foil as also used for neutron radiography at that time [148].

The advent of digital methods at the dawn of the new millennium revolutionized neutron imaging and brought routine tomographic investigations. In the following sections, it is now extended to diffraction radiography and tomography using advanced algebraic reconstruction algorithms.

¹Apart from a background formed by scattering from the surroundings and incoherent sample scattering.

²The term *topography* was coined by Ramachandran in 1944 [143] and used throughout literature as a synonym to diffraction (contrast) imaging. To avoid confusion with topography in geoscience or the suggestion that it would only be a surface method, more and more preference is given to the term of diffraction contrast imaging, a trend which is followed in this work.

6.2 A double detector set-up for neutron diffraction contrast imaging

Transmission and diffraction imaging pose somewhat different detector demands. Transmission imaging is performed in the direct forward beam direction at the highest resolution possible. The diffracted neutron signal on the other hand does not follow the incident neutron beam direction anymore. In a cold neutron beam, the diffraction directions tend towards side and backscattering, illustrated in table 6.1.

	1 st reflection	2 nd reflection
Al	83.1°	99.9°
Cu	95.9°	118.1°
Fe (BCC)	99.8°	-
Ni	99.3°	123.2°

Table 6.1: Smallest two diffraction angles (w.r.t. the transmitted beam direction) formed by the two crystal planes of largest interplanar distance for typical engineering materials at the average wavelength of 3.1 Å of the ICON beamline.

Moreover, a large field of view is required to cover sufficient angular range at the cost of a loss in resolution. A solution to these conflicting demands has been found using a double detector set-up, combining the micro set-up for high resolution transmission imaging in the beam direction and the midi set-up on a movable stage aside from the direct beam, facing the sample, for diffraction imaging (figure 6.1).

Slight modifications have been introduced to allow for efficient imaging of backwards scattered neutrons (figure 6.2). The incident neutron beam is limited using a 4 cm thick block of borated plastic featuring an aperture the size of the micro set-up field of view. It is then allowed to traverse the mirror, which is a thin plate of polished aluminium measured to attenuate the beam by less than 5 %. A special scintillator has been produced with uncoated center, so back-reflected neutrons from the sample can still be converted into visible light with high efficiency by the coated region, without the incident beam being significantly attenuated. The neutron beam subsequently goes through the sample, with the transmission image recorded by the micro set-up and the diffracted neutrons forming grain projections on the midi set-up scintillator.

Camera trigger and feedback signals are logically combined and the whole is emulated as a single virtual camera in the existing beamline operating system. As such, both camera's can be triggered and start measuring simultaneously. The exposure times can be set independently and the camera with the longest acquisition time (exposure plus read-out time) will determine when the next trigger is sent. The set-up thus allows for simultaneous recording of transmitted and diffracted neutrons, making optimal use of the available beam time and providing easy sample aligning.

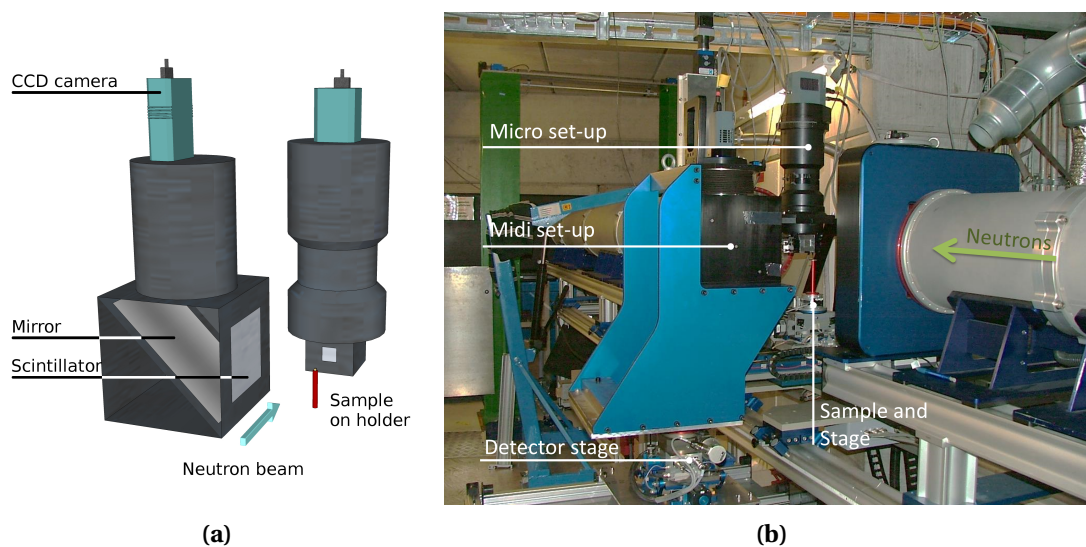


Figure 6.1: Schematic overview (to scale) of the double detector set-up for **sideways scattering** with the midi set-up on the left at 90° w.r.t. the sample for diffraction imaging and the micro set-up in the beam direction behind the sample for transmission imaging (a). A picture of the set-up installed at the ICON beamline is shown in (b).

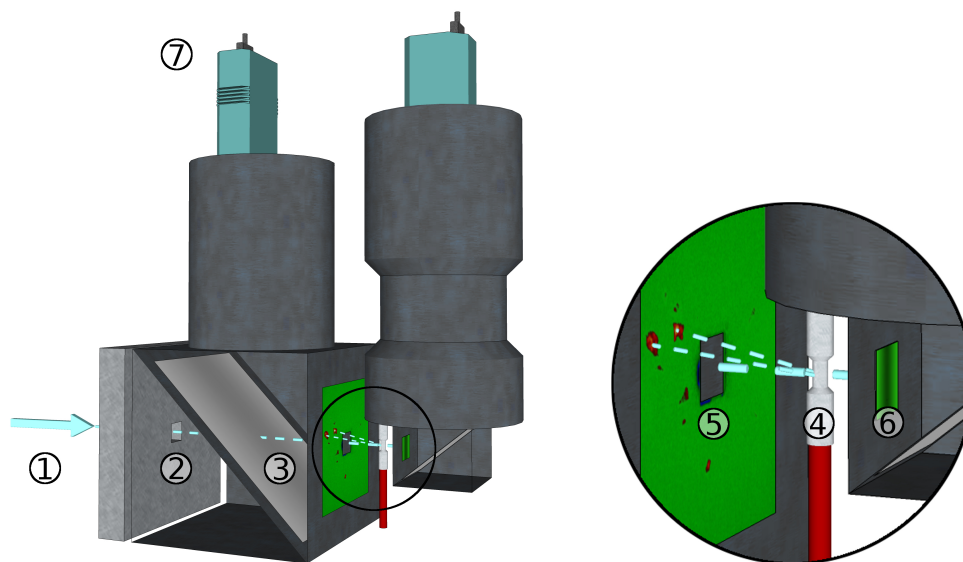


Figure 6.2: Schematic overview of the double detector set-up for **backwards scattering** with close-up on the right. Neutrons fly in from the left (1), beam size limited by an aperture (2), go through the mirror (3) and hit the sample (4). The transmission signal is subsequently captured on scintillator of the micro set-up (6) and the grain diffraction projections on the customized midibox scintillator (5). The light is then guided via the mirrors to the CCD camera on top (7).

6.3 Neutron diffraction contrast radiography

The strength of digital neutron radiography with diffracted neutrons is exemplified with an investigation of single crystal Nickel-base superalloy turbine blades.

6.3.1 Introduction

Jet engines and land-based gas turbines have the turbine blades subjected to the highest temperatures and loads carried out as single crystal Nickel-base superalloys. They are characterized by superior strength and resistance to creep, thermal fatigue and corrosion compared to conventionally cast blades, having their $\langle 001 \rangle$ crystallographic direction aligned to the blade axis of highest load [149, 150].

They are produced by pouring molten superalloy in a ceramic mold with a chiller at the base where solidification and grain nucleation starts. The top of the mold is situated in an oven, the unidirectional temperature gradient ensures that the grain growth, dendritic in nature, is columnar. The process is fastest for grains that have their $\langle 001 \rangle$ direction aligned to the temperature gradient. Already a few centimeters away from the chiller surface, one is left with only $\langle 001 \rangle$ oriented crystallites. The mold then narrows into a helical shaped grain selector. Only a few favorably oriented dendrites are able to grow into it and only one can emerge on the other end where the blade shaped part of the mold will start. The manufacturing set-up is shown schematically in figure 6.3.

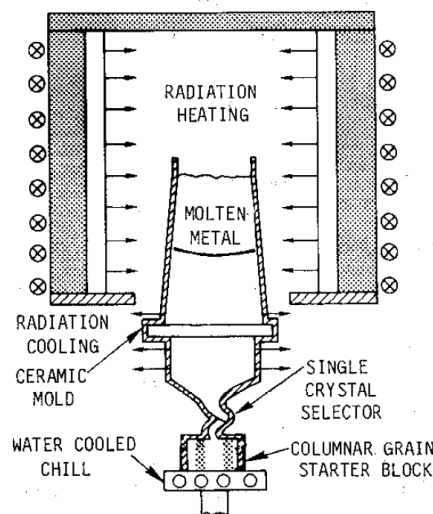


Figure 6.3: Schematic illustration of the casting process of single crystal superalloys, taken from [151].

The dendrite cores in the blade are typically spaced 200-600 μm apart and small misorientations of 0.1° - 1° will persist [152].

White beam synchrotron diffraction imaging has a.o. been used to investigate the change in mosaic structure that comes with different growth conditions [153, 154]. However, due to the high attenuation of X-rays in Nickel, such measurements were performed on thin slabs, typically a few hundred micron thick, cut out of the blade.

Tomimitsu [155] performed monochromatic neutron diffraction imaging measurements on a 3 mm thick slab of a prototypal turbine blade to verify the homogeneity of the "single crystal" (*sic*) and the suggested macroscopic growth direction in the different blade parts. An X-ray dental film and a Gadolinium (n, γ) converter foil were used in the experiment.

In this section, we explore white beam digital neutron diffraction imaging of a full commercial turbine blade as a tool for non-destructive testing of the mosaic structure in bulk.

6.3.2 Experiment

The experiments were conducted at the ICON beamline using the double detector set-up. In order to increase the neutron flux, the 40 mm aperture was selected. The full polychromatic beam spectrum was used. Three small single crystal Nickel-base superalloy turbine blades were obtained from the Sulzer company [156] for our investigation, two of them were grown along the vertical blade axis, a third one along the horizontal [157]. Detailed imaging parameters used for the different sample scans are listed in table 6.2. A tomography was made of blade No. 1, rotating it over 360° in 625 steps. Single radiographies were made of blades No. 2 and No. 3.

	Blade 1		Blade 2;3	
	Transmission	Diffraction	Transmission	Diffraction
Camera angle	0°	90°	0°	90°
Pixel size	27 μm	130 μm	27 μm	68 μm
Field of view	27.6×27.6 mm ²	102×102 mm ²	27.6×27.6 mm ²	102×102 mm ²
Scintillator	20 μm Gadox	100 μm ⁶ Li ZnS	20 μm Gadox	100 μm ⁶ Li ZnS
Exposure time	11 s	15 s	15 s ; 40 s	20 s ; 45 s
Sample distance		88 mm		69 mm ; 78 mm

Table 6.2: Parameters of the neutron imaging systems used for simultaneous imaging in transmission and diffraction mode.

6.3.3 Results and discussion

An example of a combination of transmission and diffraction image is presented in figure 6.4. A photograph of the sample under approximately the same angle as seen by the side scatter detector is provided as well, illustrating the interpretation of the diffraction image as a sample projection formed by the diffracted neutrons on the side detector. Other diffraction projections can be discerned too, emerging from neutron scattering of different wavelengths from different crystal lattice planes.

Laue pattern

A single crystal put in a white beam will produce a Laue pattern on a position sensitive detector and the investigated turbine blades are no different. The diffraction projections can likewise be indexed based on comparison between experimentally observed spot positions (taken

as the projection's center of mass) and simulated ones. The distance between them on the detector is minimized for multiple sample rotation angles, as the fairly large distance between sample and diffraction detector needed to avoid projection overlap will also limit the number of them observed on a single image.

The geometric procedure for simulating the Laue pattern was adapted from Marín [158] and generalized to account for arbitrary detector orientation. A list of all lattice plane normals is calculated for an arbitrary orientation of the crystal in the lab reference system. The directions of the diffracted beams are the ones of the incident beam rotated 180° around each of these normals. The Laue spots are then found as the intersections of the diffracted beams with the detector plane, discarding any that would fall outside of the detector's field of view.

The crystal lattice planes are described w.r.t. to the crystal base vectors \mathbf{a}_1 , \mathbf{a}_2 and \mathbf{a}_3 . There are many conventions to describe the orientation of a crystal in the lab reference system [50]. We adopt the use of Euler angles (ϕ_1, ϕ, ϕ_2) to describe the orientation matrix E , the matrix elements of which can be found in appendix B, equation B.1. The sample rotation during tomography is described by the rotation around the z-axis R_z in the lab reference system so that for each projection, the crystal base vectors are described by

$$\mathbf{a}'_i = R_z E \mathbf{a}_i, \quad i = 1, 2, 3. \quad (6.2)$$

The (hkl) crystal planes are subtended by the three points \mathbf{a}'_1/h , \mathbf{a}'_2/k and \mathbf{a}'_3/l . The normal vectors \mathbf{n}_{hkl} to those planes are found from the cross product

$$\mathbf{n}_{hkl} = \left(\frac{\mathbf{a}'_2}{k} - \frac{\mathbf{a}'_1}{h} \right) \times \left(\frac{\mathbf{a}'_3}{l} - \frac{\mathbf{a}'_1}{h} \right). \quad (6.3)$$

The Bragg diffracted beam vector \mathbf{c}_{hkl} equals the incident beam vector rotated by 180° around \mathbf{n}_{hkl} and taken in the opposite direction. Say the incident neutron beam follows the x-axis in the lab system, $\mathbf{1}_x$. That rotation then boils down to a coordinate transform that depicts \mathbf{n}_{hkl} onto the x-axis, $A_{n_{hkl}x}$ (appendix B), performing the 180° rotation R_x , followed by the transform back to the original system $A_{n_{hkl}x}^{-1}$ and taking the antivector:

$$\mathbf{c}_{hkl} = -A_{n_{hkl}x}^{-1} R_x A_{n_{hkl}x} \mathbf{1}_x. \quad (6.4)$$

the diffracted neutron path can be described by the parametric equation $s_{hkl} \mathbf{c}_{hkl}$, the scalar s_{hkl} being the distance of any point on it to the origin of the lab system. Where the diffracted beam intersects the detector plane - defined by a point \mathbf{O}_{det} and a normal vector \mathbf{n}_{det} - both $s_{hkl} \mathbf{c}_{hkl}$ and \mathbf{O}_{det} will lie in the same plane, perpendicular to \mathbf{n}_{det} , so

$$(s_{hkl} \mathbf{c}_{hkl} - \mathbf{O}_{det}) \cdot \mathbf{n}_{det} = 0, \quad (6.5)$$

so

$$s_{hkl} = \frac{\mathbf{O}_{det} \cdot \mathbf{n}_{det}}{\mathbf{c}_{hkl} \cdot \mathbf{n}_{det}}. \quad (6.6)$$

Chapter 6. Neutron diffraction contrast imaging

Where it only remains to be checked if the Laue spot position $s_{hkl}c_{hkl}$ on the detector plane also falls within the FOV.

The crystal plane responsible for the diffraction projection and the orientation of the crystal within the lab reference system is then found by looking for the euler angles that minimize the difference between simulated and experimental spot positions over multiple projections (i.e. changing R_z).

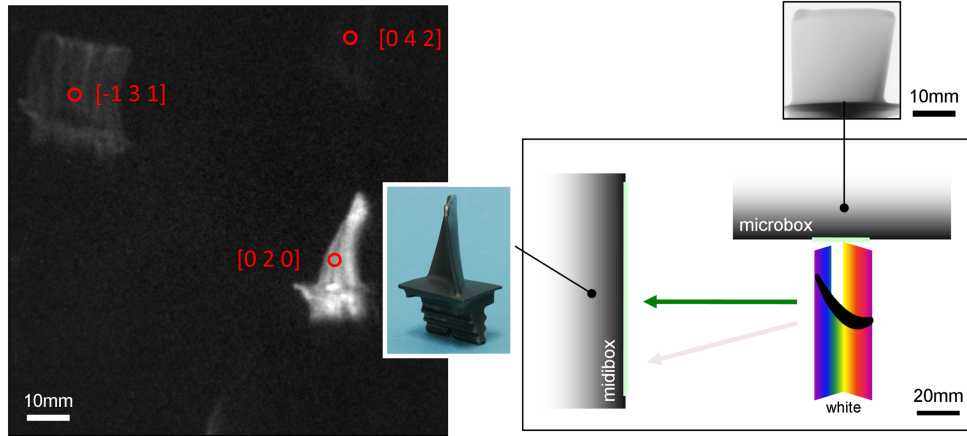


Figure 6.4: Diffraction image (left), transmission image (top right, same scale), photograph (middle) and a top-down set-up overview (bottom right) for measurement of a single crystal Nickel-base superalloy turbine blade.

The blade's crystal orientation thus obtained can then be combined with the standard tomographic reconstruction based on transmission projections (figure 6.5). Not surprisingly, we find the $[001]$ direction, the one that can withstand the highest loads, along the vertical blade axis.

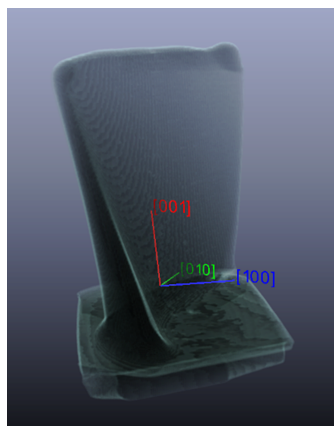


Figure 6.5: Threedimensional rendering of the tomographic reconstruction of a turbine blade based on transmission projections, together with its crystallographic orientation as indicated by the base vectors and determined based on indexed diffraction projections. The blade height was 22 mm.

However, much more information can be obtained. As can already be seen from the diffraction projection of weaker intensity in the upper left corner in figure 6.4, a columnar substructure is present. However, slices from the reconstructed transmission tomography reveal no cooling channels that might explain the intermittent dark columns through an absence of scattering material (figure 6.6).

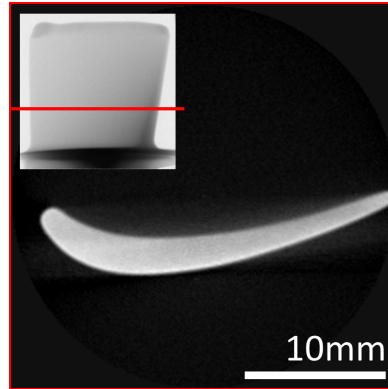


Figure 6.6: Virtual slice through the tomographic reconstruction of the transmission data of turbine blade No. 1. The inset shows the height in the blade that the slice corresponds to.

The dendritic microstructure

The small misalignment of the dendritic cores as described by Hussein *et al.* [152], will induce small differences in the direction of the diffraction projections of each dendrite, leading to regions of increased intensity where these overlap and an intensity loss where they diverge. The effect is schematically illustrated in figure 6.7. It gives rise to columnar diffraction projection features, following the growth direction as in this blade the vertical misalignment component does not give rise to diffraction projection overlap with horizontally neighbouring dendrites.

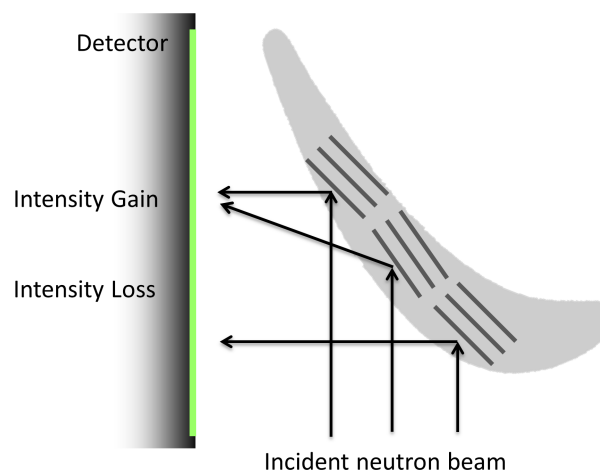


Figure 6.7: Schematic illustration of how regions with slightly different orientation can give rise to intensity gain and loss lines on a detector.

In order to verify the hypothesis, diffraction projections for two blades of different growth direction were inspected. A photograph, neutron transmission image and simultaneously recorded neutron diffraction projection for these two blades are shown in figure 6.8. The diffraction projections indeed exhibit a columnar structure, once in the vertical direction (indicative of vertical dendritic growth for blade No. 2) and once in the horizontal one (horizontal dendritic growth). Also noteworthy is the darker region where the base plate is expected for blade No. 2, caused by self-shielding in this thick Nickel-base part of the sample.

The two blades were thereupon cut with a diamond wire saw 5 mm below the top edge. They were embedded in resin, polished and etched using a solution containing 60 ml ethanol, 40 ml HCl and 2 g of Cu(II) chloride. The dendritic microstructure was analyzed using optical microscopy with green lighting. Micrographs (stitched together) of the blades' cross-sections are presented in figure 6.9. They reveal clearly that indeed, Blade No. 2 shows vertical dendritic growth while Blade No. 3 a horizontal one.

6.3.4 Conclusion

Neutron diffraction imaging offers a non-destructive insight in the crystallographic microstructure of single crystal turbine blades at very short measurement times. It can be performed in parallel to traditional transmission based tomography which reveals the material distribution (e.g. presence of cooling channels), making optimal use of available neutrons.

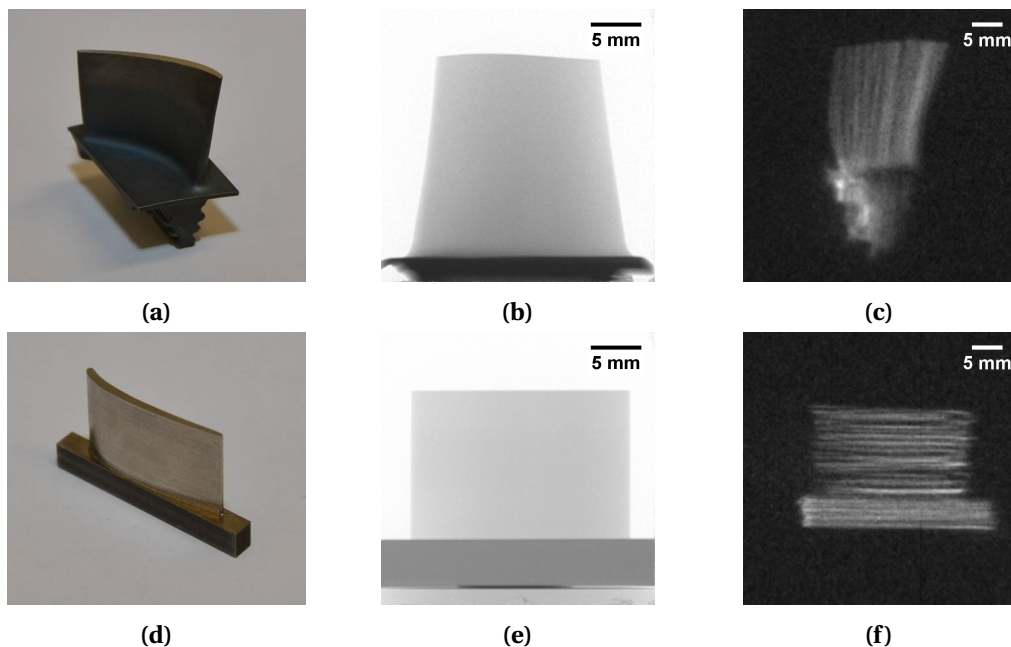


Figure 6.8: Inspection results of turbine blade No. 2 (top row) and No. 3 (bottom row): photograph (a,d), neutron transmission projection (b,e) and diffraction projection on the side detector (c,f).

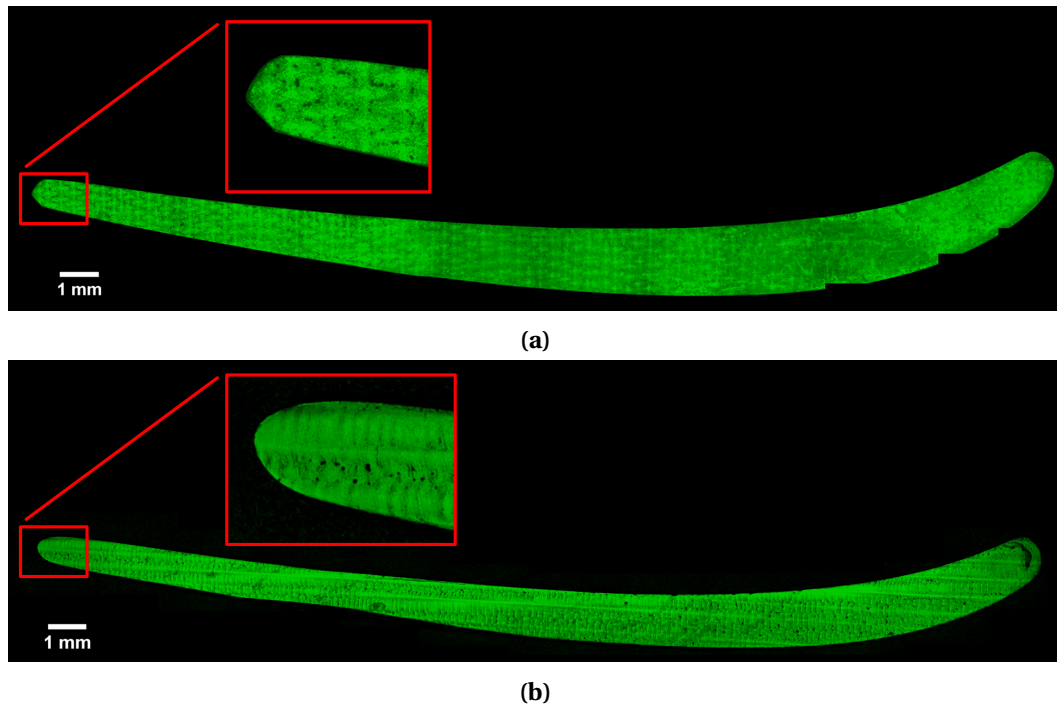


Figure 6.9: Optical micrographs of the cross-section of the vertically grown turbine blade No. 2 (a) and horizontally grown No. 3 (b).

6.4 Neutron diffraction contrast tomography of a single crystal

6.4.1 Experiment

To investigate going from single diffraction projections (i.e. radiography) to tomography, a cube shaped BCC iron single crystal, measuring $4\text{ mm} \times 4\text{ mm} \times 4\text{ mm}$ was rotated over 360° in 376 steps using a white beam³. The different imaging parameters used during this experiment are listed in table 6.3.

	Transmission	Diffraction
Camera angle	0°	90°
Pixel size	$13.5\text{ }\mu\text{m}$	$68.3\text{ }\mu\text{m}$
Field of view	$27.6 \times 27.6\text{ mm}^2$	$102 \times 102\text{ mm}^2$
Scintillator	$20\text{ }\mu\text{m}$ Gadox	$100\text{ }\mu\text{m}$ $^6\text{Li ZnS}$
Exposure time	70 s	80 s
Sample distance		70 mm

Table 6.3: Parameters of the neutron imaging systems used simultaneously in the transmission and diffraction tomography.

³The author would like to thank Prof. Dr. R. Schäfer from Leibnitz Institut für Festkörper- und Werkstofforschung (IFW) Dresden for providing the sample.

6.4.2 Method

Recorded signal components

Repetita iuvant, the in-beam detector records the attenuation of the neutron beam as it passes through the sample, following to a good approximation (in particular for small sample thickness) the Lambert-Beer law:

$$I = I_0 e^{-\int_d \Sigma dx}, \quad (6.7)$$

I being the recorded intensity profile, I_0 the incident beam profile on the sample and Σ the material and density dependent macroscopic cross-section averaged over the incident beam spectrum, the integral of which over the traversed neutron path d through the sample is recorded. Transmission was defined as I/I_0 , the ratio of the images with and without sample.

The intensity recorded with the side detector can be split into two classes. First, coherent elastic scattering from the single crystal sample that will give rise to recorded sample projections via diffraction. Under the approximation of kinematic diffraction, the local diffracted intensity for each point in the crystal adds up along the diffracted beam path through the sample. Changes in crystal quality (defects) induce an increased local scattering power or Bragg reflectivity as also neutrons that do not satisfy the Bragg condition in the crystal matrix can still diffract in the deformed region around the defect [159]. In the absence of strong internal orientation and strain gradients, parallel diffraction projections are thus formed. They move through the field of view as the sample is rotated, according to Bragg's law (eq. 6.1), the changing Bragg angle between crystal plane and the incident neutron beam equal to the angle between the plane and the exiting recorded diffracted beam.

The second component stems from incoherent sample scattering, which is approximately invariant under sample rotation if the sample's horizontal dimension change is small compared to the detector distance, together with scattering from the sample surroundings (air, concrete shielding, detection system and sample mount). As it is approximately constant as opposed to the moving first component, it is easily determined for each pixel taking the median over all acquired projections and can subsequently be subtracted to end up with only the sample neutron diffraction projections in our radiographs.

Projection segmentation

Next, all diffraction projections of the sample need to be segmented out of the recorded radiographs as future input for the reconstruction. As the recorded neutron signal is typically weak, this is performed in several steps. Firstly, all pixel regions with a Signal to Noise Ratio (SNR) above a threshold t_{high} are selected. A size criterion is subsequently applied to distinguish between sample diffraction projections and bright spots formed by gamma rays hitting the camera chip: connected pixel regions should have an area bigger than $S \text{ pixel}^2$. Region growing down to a t_{low} SNR threshold is then applied in order to also include the less intense parts of the diffraction projection. A closing and smoothing operation finalizes the segmentation. Typical values for these parameters are listed in the results section.

Set-up geometry

In order to identify at what direction through the sample the diffraction projections segmented previously were taken, their centers of mass at all sample rotations are identified and together with detector position, orientation relative to the sample holder and the sample rotation, these are transformed into a fixed, non-rotating sample coordinate system. The projection direction is then easily found as the vector connecting these points and the crystal's center of mass (determined geometrically for simple samples or from the transmission tomography for more complex sample shapes).

The sample's center of mass position w.r.t. the side camera needed for the reconstruction was refined further based on Friedel pair registration: if the (hkl) lattice plane fulfills the diffraction condition, then also (-h-k-l) will diffract (i.e. its *Friedel pair*) after turning the sample 180°. In the sample frame of reference, the two detected Friedel pair diffraction projections form a line through the diffracting crystal. Acquiring multiple Friedel pairs then yields the crystal's center as the intersection of these paths. As the sample rotation angles were not symmetric over 180° but over 360°, a standard often used in transmission tomography for higher spatial resolution, 20 more diffraction projections were recorded for sample rotation angles in the 180° - 360° interval symmetric to angles recorded in the prior tomography scan.

Reconstruction

The 3D spatial distribution of the macroscopic cross-section is reconstructed by applying the commonly used filtered back projection algorithm on the negative logarithm of the acquired transmission projections. Based on taking the Fourier transform of a projection intensity profile for each rotation angle (or Radon transform) followed by an inverse 2D Fourier transform yielding the spatially resolved reconstruction (Fourier slice theorem), the method is highly efficiently implemented using the fast Fourier transform [14].

The 3D distribution of the local scattering power can also be retrieved from its acquired integral footprint in the recorded segmented diffraction projections. Existing transmission imaging reconstruction algorithms can be used if one protracts the diffracted neutron path to a virtual parallel neutron source (see figure 6.10 for a schematic impression). A normalization of each projection to its integrated intensity is performed prior to reconstruction as they are all originating from the same diffracting volume, though different projections have different intensities because of different structure factors, spectral distribution of the incident neutron wavelength spectrum and different effective scintillator thicknesses for different diffracted neutron detector incidence angles. To reconstruct the – relative – local scattering power, we apply the three dimensional simultaneous iterative reconstruction technique (3D-SIRT) available in the ASTRA package [136]. The method relies on rewriting the reconstruction problem as an (underdetermined) matrix equation linking the unknown sample volume to the recorded projections and solving it iteratively (as explained in detail in section 1.4.2). Though computationally expensive, in particular with out of plane acquisitions requiring a full 3D approach, it offers superior performance dealing with few, non-uniformly spaced acquisition angles [16].

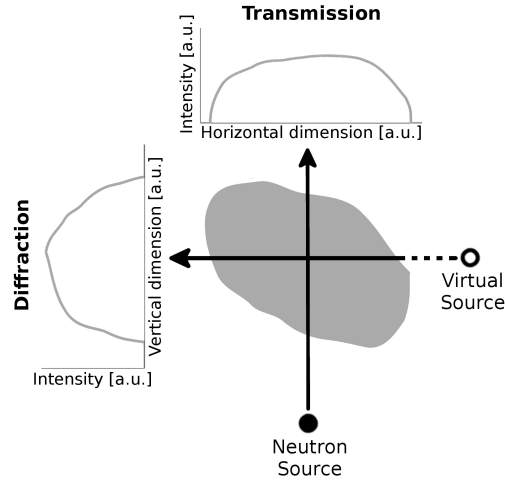


Figure 6.10: Schematic overview of the experiment geometry showing acquired neutron transmission signal and the diffraction projection profile that can be assumed to originate from a virtual source.

6.4.3 Results and discussion

Figure 6.11 shows a typical recorded image on the side detector, background corrected, with two sample diffraction projections segmented (indicated by the red circumference – $t_{high} = 5$, $t_{low} = 2$, $S = 20 \times 20 \text{ px}^2$).

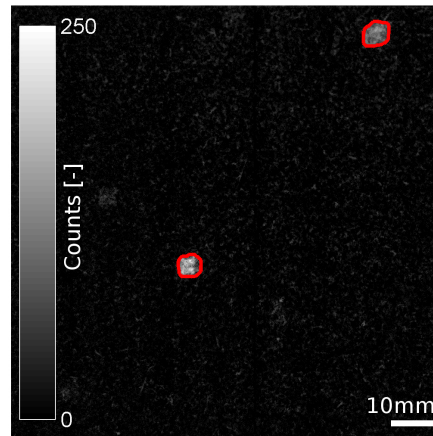


Figure 6.11: Background-corrected recorded signal on the side detector, for a sample rotation angle of 95.7° , with segmented sample diffraction projections (outlined in red).

Figure 6.12 shows all diffraction projection directions acquired on the unit sphere, with the sample axis system indicated by the (cyan, green, red)-tripod. It clearly shows a good angular coverage around the sample, however irregular and mostly out of plane requiring a full 3D algebraic reconstruction. A total of 522 diffraction projections were found, with a horizontal angular separation of 0.66° on average, with a maximum of 6.6° .

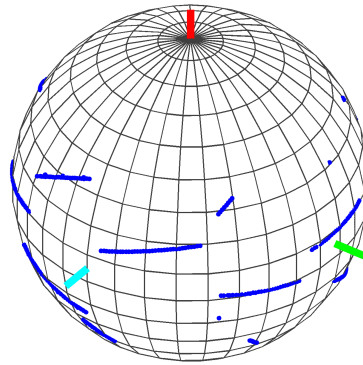


Figure 6.12: Segmented diffraction projection directions on the unit sphere in the sample frame of reference, indicated by the (cyan, green, red)-tripod. Grid line separation is 10° .

For the cubic sample in the same position as for figure 6.11, a close up of the two segmented diffraction projections is shown in figure 6.13, together with the transmission projection recorded simultaneously. As the sample induces an attenuation of the neutron beam, the transmission projection shows the sample as dark on a white background, whereas the diffraction projections are formed by an increase of detected neutrons and thus bright on a dark background. One can clearly recognize the cube's shape, even though statistics are low.

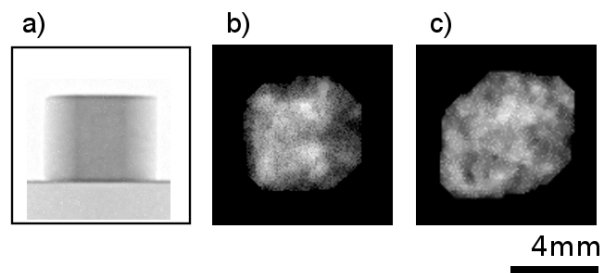


Figure 6.13: Transmission projection (a) and diffraction projections of the central (b) and top (c) segmented projections in figure 6.11 for the sample at 95.7° .

The subsequent reconstruction based on transmission and diffraction projections is illustrated in figure 6.14 by a 3D volume rendering. The object's shape, orientation and size are reconstructed correctly and consistently. The sample appears homogeneous in its macroscopic cross-section, i.e. its material distribution. The reconstructed distribution of local Bragg reflectivity however is higher on one side, implying reduced crystal quality there. Note the polycrystalline sample holder present in the transmission reconstruction and absent in the single crystal diffraction tomography.

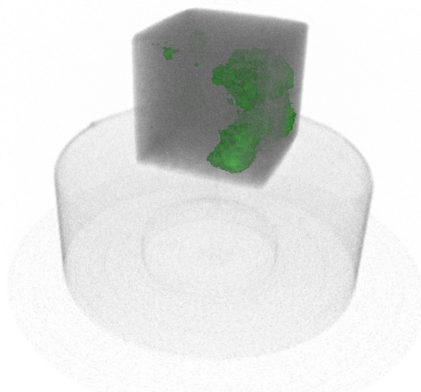


Figure 6.14: Volume rendering of the macroscopic cross section as reconstructed from transmission data (gray) and regions of increased local Bragg reflectivity (green).

A comparison of virtual slices through both reconstructions is given in figure 6.15. A distinct blur of the diffraction reconstruction can be observed. This is due to the incident beam divergence and finite source size - characterized in neutron imaging by the beamline's L/D , the ratio of source to sample distance over source size – in combination with a certain sample to side detector distance l . Though neutron imaging beamlines can to a good approximation be considered parallel for transmission imaging purposes, the standard $L/D=343$ also used in this experiment, together with $l=70\text{ mm} - 99\text{ mm}$ (diffraction projection in the center of the side detector versus in a corner) yields an observed sample point spread $l/(L/D)=200\text{ }\mu\text{m} - 290\text{ }\mu\text{m}$. Future care should be taken to work at the highest practical beam collimation and lowest sample to side detector distance possible.

A higher local Bragg reflectivity is registered towards the outer edges of the sample. This is however an artifact ascribed to the virtual source assumption applied on a large sample of non-negligible neutron attenuation. As the source-facing side of the sample sees higher incident beam intensity than the back, also the diffracted intensity coming from this side will be higher. Incorporating all acquired sample orientations will result in lower reconstructed central scattering power compared to the outer edges, much similar to cupping artifacts due to beam hardening in transmission imaging. However, though beyond the scope of this work, the attenuation information contained within the transmission tomography could in principle be included in the diffraction reconstruction.

The used approach bears resemblance to existing monochromatic synchrotron diffraction contrast tomography methods such as topo-tomography [137] where the local Bragg reflectivity is reconstructed using conventional filtered back projection after tedious alignment of the rotation axis with the diffraction vector so all diffraction projections fall on the same detector position. Here, we rotated a single crystal around its vertical axis in a white beam, resulting in many diffraction projections to reconstruct the local Bragg reflectivity from, without prior sample alignment and making more efficient use of the far lower neutron flux.

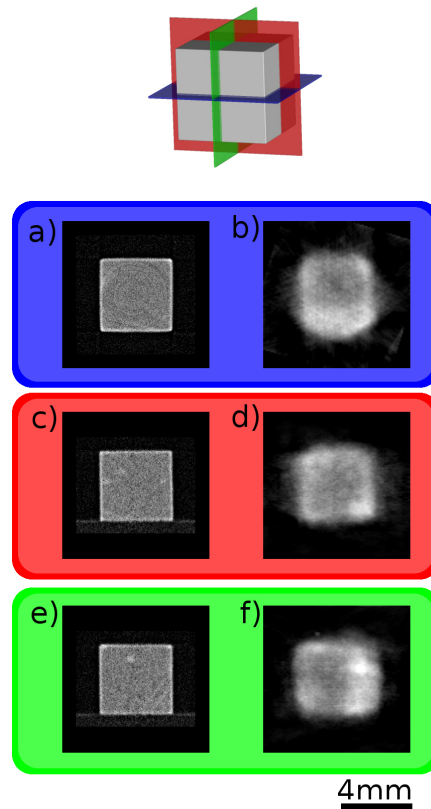


Figure 6.15: Horizontal, coronal and sagittal virtual slices through the sample from transmission (a,c,e) and diffraction contrast tomography (b,d,f). Reconstructed geometries agree well, though where the left column reflects material distribution, the right column shows the variation in relative Bragg reflectivity of the single crystal.

6.5 Neutron diffraction contrast tomography of a polycrystal

6.5.1 Introduction

Polycrystalline materials are omnipresent in modern society, from everyday metals and ceramics to increasingly complex alloys. Their properties such as behaviour under load can often be traced back to the crystallites that comprise them: their size and orientation. In order to understand materials' behaviour and develop new materials tailored to ever-higher industrial needs, it is of the utmost importance to be able to probe these crystallite properties (e.g. [160, 161, 162, 163]). Conversely, these properties can also yield information on ancient metal working methods long forgotten [164].

Optical and electron microscopy are standard tools in metallography that provide extensive information on the samples' microstructure. These are however surface methods, requiring extensive polishing and etching, and 3D information is only available through tedious serial sectioning - though nowadays largely automatized [165, 166]. Thus, there is a clear need for a faster, bulk, non-destructive alternative, particularly as this is required for *in-situ* experiments, or the study of priceless cultural heritage samples (e.g. [164, 167, 168]).

With the advent of synchrotron radiation, several such methods have appeared. Differential Aperture X-ray Microscopy (DAXM) [169] uses a polychromatic pencil beam and analyzer wire to scan the sample and record a Laue pattern for each point and derive an orientation map for the scanned volume. Three-dimensional X-ray Microscopy (3DXRD) [147, 138] and related X-ray diffraction contrast tomography (which will be referred here to as Syn-DCT) [139, 170] rotate the sample in a parallel monochromatic line- or box-beam, recording and indexing projections formed by diffraction from the illuminated grains. It allows the reconstruction of grain shape from the projected intensity profiles, and grain orientation from the projection positions on the detector. Recently, the method has been extended to more widely available polychromatic lab-based X-ray tube sources (Lab-DCT) [171].

The penetration depth of X-rays is however limited for common metals. Thicker samples can be probed using a neutron beam, particularly with respects to heavy metals. After treating a single crystal in the previous section, we now extend neutron Diffraction Contrast Tomography (nDCT) to polycrystalline material. After a description of the analysis method and set-up, the characterization of grain size, shape and orientation of a polycrystalline aluminium test sample is presented and compared to measurements with the well-established Syn-DCT.

6.5.2 Properties of a cold neutron imaging beam for DCT

Neutron imaging studies the spatial variation in the attenuation of the neutron beam across a sample of interest, which depends on the traversed material and path length. By recording such projections or radiographs under different sample rotation angles, one can retrieve the three-dimensional material distribution through tomographic reconstruction. The attenuation originates from the removal of neutrons from the beam through absorption and scattering, coherent or incoherent, elastic or inelastic.

Many metals feature dominant coherent elastic scattering or diffraction, occurring when Bragg's law (eq. 6.1) is fulfilled. The neutrons are diffracted in a direction of twice the Bragg angle w.r.t. the transmitted beam direction. With the whole sample illuminated by the neutron beam, they form a projection of the crystallite volume in that direction.

Neutron imaging makes use of large 2D position sensitive detection systems with high spatial resolution and a linear response with high dynamic range, qualifying it to be extended towards imaging diffracted neutron projections. Driven by neutron imaging beam properties, the developed nDCT method has many traits in common with either Syn-DCT or Lab-DCT, the principal set-up sketched in figure 1a and reflected upon further below.

Parallel beam

The neutron imaging beam is kept as parallel as reasonably possible, as any divergence would lead to image blurring [172]. A typical number is about 10' divergence. Given the nature of neutron sources and lack of neutron optics, a cone beam geometry is not possible. Thus, we will obtain parallel diffraction projections of the crystallites in the sample, much like Syn-DCT (illustrated in figure 6.16b) and without the mirrored and astigmatically magnified spot projection that are observed in Lab-DCT.

Moreover, a parallel beam will ensure Friedel pair symmetry, i.e. diffraction projections from

the (hkl) plane and the (-h-k-l) plane after 180° sample rotation will lie on a straight line through the grain of origin in the sample frame of reference. This principle serves as the backbone of the Syn-DCT indexing routine [139]. It is however violated in the Lab-DCT case, with the cone beam resulting in different beam incidence angles.

Polychromatic spectrum

Neutron imaging is typically performed using the full polychromatic beam spectrum from the source or white beam, a full tomography taking a few hours. Using either a mechanical neutron velocity selector or a double crystal monochromator, one can perform energy-selective neutron imaging with a bandwidth of $\Delta\lambda/\lambda=15\%$ or $2\%-5\%$ respectively. Though this bandwidth can be considered a pink beam by comparison to Syn-DCT standards ($\Delta\lambda/\lambda=0.01\%$), it is a compromise between exposure time and available neutron flux ($\approx 10^7$ neutrons/s/cm², whereas synchrotrons operate at 10^{17} photons/s/cm²).

In this respect, nDCT bears much resemblance to Lab-DCT. Whilst rotating the sample, the crystallites' lattice planes will be able to diffract neutrons (of different wavelengths) over a considerable angular range, depending on the incident beam spectrum. The crystallites' diffraction projections will form a curved trajectory on the detector and one has to follow a discrete angular stepping scheme in order not to induce any motion blurring. In contrast, with a monochromatic beam the projections must be integrated over the rotation angle to ensure all parts of a grain are imaged. As such, many more projections for tomographic reconstruction can be gathered from one lattice plane family and one can use much coarser angular stepping (typically a factor 10-20 \times , 1° versus 0.05-0.1°) than the monochromatic Syn-DCT case, partially making up for longer exposure times. The Bragg wavelength λ_B is not sufficiently restricted for refinement of the angular range (θ_B , based on Bragg's Law) in which to look for Friedel pairs or to recalibrate positions and tilts of detector and sample. In contrast, such geometric refinements can be made after grain indexing by comparing observed and predicted diffraction spot projections [170].

Figure 6.16c illustrates the grain diffraction projection trajectories accumulated over a 20° sample rotation (11 steps), with the spectrum bandwidth limited by a mechanical neutron velocity selector.

Cold neutron wavelengths

Syn-DCT and lab-DCT typically use rather hard X-ray energies, typically in the order of 40 keV. This corresponds to a wavelength of 0.31 Å. In addition, the structure factor for X-ray scattering, determining the intensity of the diffraction signal, is highest for low diffraction angles. These two characteristics favour the forward scattering geometry typically used for X-ray DCT. The average neutron wavelength at e.g. the ICON beamline for cold neutron imaging is however 3.1 Å [24]. As a result, in nDCT the diffraction angles are typically higher, tending towards side- and back-reflection. At the same time, the neutron scattering structure factor is rather independent of the diffraction angle, enabling other geometries to be exploited effectively. Detecting [140] and indexing [170] diffraction projections in such a geometry has already been shown to be feasible. Indeed, figure 6.16b and 6.16c show diffraction projections acquired in

back-reflection mode, with the incident beam passing through the detector center, onto the sample. The diffracted neutrons are captured on that detector and the transmission image is recorded on a second in-line detector (figure 6.16d).

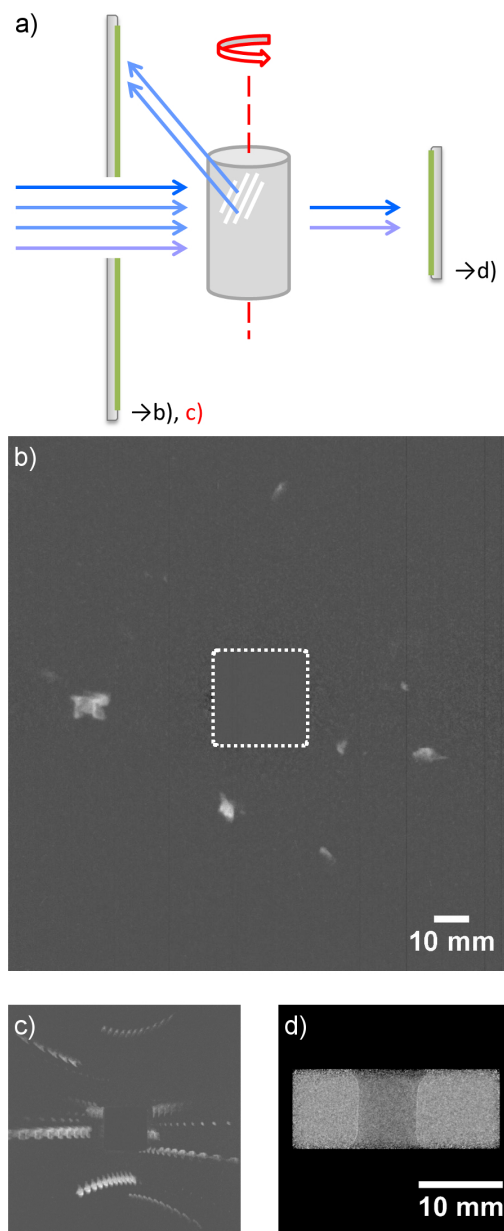


Figure 6.16: (a) Sketch of the set-up for cold neutron diffraction contrast tomography (see the next subsection for the detailed experimental realization). (b) Illustration of diffraction projections from an aluminium sample captured in back reflection. The dashed line marks the region where the beam passed through the detector. (c) Maximum intensity projection rotating the sample over 20° showing the curved spot trajectories. (d) Transmission projection captured on an in-line detector.

6.5.3 Experiment

The sample was a coarse-grained aluminium tensile test sample, cylindrical with a gauge volume of 7 mm diameter and 9 mm height. It was machined out of a pure aluminium casting, subsequently deformed to 5 % plastic strain and finally recrystallized for one hour at 500°C.

To avoid spot overlap and to limit the number of reflections, and to avoid ambiguity in assigning {hkl} types to diffraction spots, the experiment was not conducted with the full spectrum. Instead, two consecutive scans were performed in a cold pink beam provided by the mechanical neutron velocity selector. This provided Gaussian spectra with $\Delta\lambda/\lambda=15\%$ monochromaticity, centered around 4.3 Å and 3.7 Å respectively, in order that the {111} and {200} Debye-Scherrer rings aligned to the midibox custom scintillator center radius. The midibox scintillator was positioned 32 mm from the sample in order to image diffraction spots having angles from $115^\circ < 2\theta_B < 160^\circ$, for all azimuthal angles. At both wavelengths, the sample was rotated from 0° to 360° in 180 equiangular steps. The imaging parameters used during this experiment are listed in table 6.4.

	Transmission	Diffraction
Camera angle	0°	180°
Pixel size	27 μm	131 μm
Field of view	27.6×27.6 mm ²	142×154 mm ²
Scintillator	20 μm Gadox	200 μm ⁶ Li ZnS
Exposure time	115 s	125 s
Sample distance		32 mm

Table 6.4: Parameters of the neutron imaging systems used simultaneously in the transmission and diffraction tomography.

6.5.4 Data processing

The data processing route for nDCT is based on the standard algorithms of Syn-DCT and lab-DCT. The details of the beam geometry and spectrum described in subsection 6.5.2 imply certain choices, which are summarized here.

Preprocessing

The images acquired are preprocessed as normal to correct detector artifacts and to remove contrasts arising from the direct beam, leaving only diffraction spot contrasts. Diffraction spots are then segmented from the images using a marker-mask reconstruction approach to allow a low threshold value without over segmentation of noise. As in the case of lab-DCT, and in contrast to Syn-DCT, the segmentation is 2D, and intensities in consecutive images are not associated. The polychromatic illumination means that the whole of a grain diffracts in a given image, and it is not necessary to integrate over adjacent images.

Pair matching

Friedel pairs of spots are identified based on diffraction spot meta-data (position, size, intensity, etc). For a given spot, its pair spot is found offset by a sample rotation of 180° . In addition to this, the search area of the image in which the pair diffraction spot can be found is reduced because the grain must lie inside the sample volume. In the sample frame of reference, projecting the sample volume from the spot position onto the 180° rotated detector plane provides this reduced search area. In contrast to the monochromatic case, it is not possible to further reduce the search area by restricting the allowed $2\theta_B$ angles. The geometric construction based on the positions of the pair of spots provides the diffraction angles and a path through the sample upon which the grain center must be located. In the polychromatic case the $\{hkl\}$ family cannot be determined from the diffraction angle. It may be possible to identify the $\{hkl\}$ type if the beam spectrum can be restricted such that only one family of reflections is visible in a particular scan, or so that the $\{hkl\}$ type can be determined from the profile of diffracted intensity as a function of $2\theta_B$ for a line of spots arising from the same scattering vector [171].

Indexing

Indexing of the grain positions and crystallographic orientations is then performed using the INDEXTER algorithm, described in [139]. The function is configured to allow many pairs arising from the same (hkl) plane to be associated with a given grain. In contrast, in the monochromatic case this would be limited to two pairs per (hkl) for a 360° sample rotation.

Reconstruction

Finally, the reconstruction of grains is identical to the Syn-DCT case. The grains are individually reconstructed using again the 3D parallel beam SIRT algorithm [136], using the diffraction spots as projections. The grain reconstructions are assembled to form a 3D grain map. The radiographs recorded on the forward detector are used to reconstruct an absorption contrast tomogram of the sample. Finally, any gaps between reconstructed grains are eliminated using a 3D morphological dilation under the mask of the absorption reconstruction.

6.5.5 Results and discussion

Neutron DCT results

The final reconstructed grain volume is rendered in figure 6.17. Orthogonal slices through the volume showing the grains color-coded by their orientation are shown in figure 6.18. In total, 1895 $\{111\}$ and 1504 $\{002\}$ diffraction spots were identified from the two pink beam scans. Pair matching was performed on the two sets of spots, yielding 457 and 372 pairs respectively (approximately 50 % matching). The datasets were merged, to create a single pool of data from which to index and reconstruct grains. The INDEXTER algorithm identified 12 grains, using 633 spot pairs (76 % of those available). A forward simulation step (using the grain orientations and positions from indexing to simulate diffraction spot positions on the detector) was used to add remaining unassigned spots to grains. In total, 1492 diffraction spots were used for grain reconstructions (44 %). Unused diffraction spots tend to be smaller, weaker spots, often

affected by overlap with other spots or with the insensitive central region or edges of the detector.

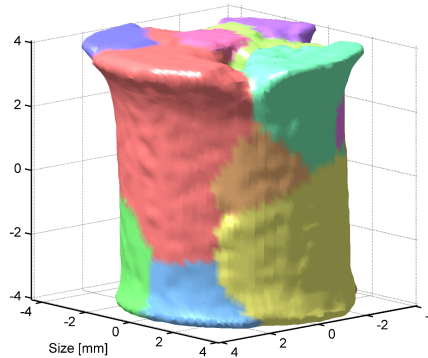


Figure 6.17: nDCT reconstruction of the grain volume (random colors).

Comparison to synchrotron DCT

In order to confirm the 3D grain shapes and orientations determined by nDCT the same sample was measured using the standard synchrotron technique at beam line BM05 of the ESRF. The validity of Syn-DCT in resolving grain boundary and orientation has been confirmed repeatedly, e.g. using phase contrast tomography [173] or EBSD [174]. A total of 3600 images were acquired using a detector with a pixel size of 13 microns placed 32 mm behind the sample, and a monochromatic beam energy of 30 keV and 0.01 % monochromaticity. The volume scanned was smaller than in the neutron case (7 mm diameter, 3.8 mm vertically). Figure 6.18 shows sections through the reconstruction for comparison to nDCT results. With the beam energy used, attenuation due to 7 mm of aluminium – corresponding to the total traversed path length by photons diffracted in the center – is almost 90 % (compared to 5 % for the neutron measurements). As a result, this region hardly contributes to any of the recorded grain projections, and the assumption that the diffraction spots represent linear projections of the grain volumes is violated. As such, the quality of the reconstruction is degraded, and the grain shapes are less accurate than would typically be the case. In contrast, the weaker interacting neutrons encounter no such problems, illustrating their potential for investigations of coarse grained bulk metallic samples.

However, the reconstructed grain map and grain orientations are sufficient to confirm the validity of neutron DCT result. To quantify the error in grain orientations, the seven grains common to the two datasets were used. A global rotation was applied to the synchrotron grain orientations in order to minimize the difference with the neutron grain orientations and allow for comparison between the two separate experiments, though this procedure also eliminated possible systematic orientation error. The remaining mean misorientation magnitude was 0.12° , representing the random part of the combined orientation errors in the two datasets.

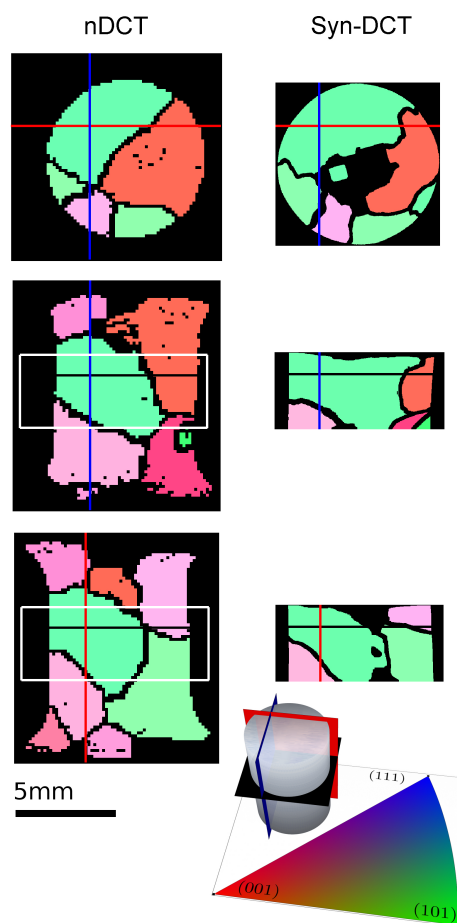


Figure 6.18: Ortho-slices through the neutron (left) and synchrotron (right) DCT reconstruction of the same aluminium sample, with the location of the cut planes clarified in the 3D legend. The crystallites are color coded by their orientation based on the inverse pole figure color map for a top view on the sample.

Discussion

It is useful to consider the potential scope of the nDCT technique compared to the established grain shape and orientation mapping methods.

The more weakly interacting neutron beam has the advantage it can penetrate much thicker samples, especially metallic ones, than its X-ray counterpart. Typical sample diameter can be in the centimetre range rather than the millimetre one.

The comprising grain size can also be much larger, ranging from the sample size (single crystal limit) down to about one millimetre. Given the available neutron flux at present and scheduled future neutron sources, the lower bound is determined mainly by the need for sufficient image statistics in the diffraction projections from the individual grains and not by spatial resolution achievable in neutron imaging. Current developments in neutron optics might mitigate the constraint by focusing the broad incident beam and subsequently defocusing it to a narrow parallel beam, gaining an order of magnitude of intensity in the process [126].

6.5. Neutron diffraction contrast tomography of a polycrystal

The intragranular mosaicity has a direct impact on the diffraction projection blur, detrimental to the grain shape reconstruction. Assume the grain can diffract an angular range α around the Bragg angle θ_B (this includes the added contribution of the beam divergence) and the detector is at a distance x from the sample. The blur can then be calculated as $2\alpha x \tan(2\theta_B)$ in the azimuthal and $2\alpha x / \cos(2\theta_B)$ in the radial direction for the Debye-Scherrer circles the diffraction projections lie on. A reasonable estimate for the typical geometry and dimensions used in this work would be an allowed mosaicity of 0.1° – 0.2° . Moreover, the smaller the grain, the larger the relative blur for the same mosaicity, underlining the grain size lower limit of one millimetre.

Whereas the Syn-DCT method is able to handle a few thousand grains per scan, this number is more restricted in the neutron case. Spot overlap is aggravated due to the larger wavelength bandwidth causing diffraction projections to persist over a larger angular range ($\mathcal{O}[15^\circ]$ versus $\mathcal{O}[0.1^\circ]$). This can be reduced to a few degrees by using a double crystal monochromator instead of a neutron velocity selector. However, apart from reducing the transmitted beam intensity, this limits the number of families that can be imaged simultaneously and might require additional scans. Taking into account above considerations, the number of grains that can be dealt with will be limited to a few hundred in the nDCT case. For samples with a large number of grains per cross section, one can limit the beam height and stack a series of reconstructions.

The comparison with synchrotron data demonstrates the advantage of nDCT compared to Syn-DCT for large samples with large and low mosaicity grains. Here, the high penetration depth of the neutron beam – even in the face of bulky metal samples – is advantageous. The two methods are thus rather similar in principle, though highly complementary in practice, with diffraction neutron imaging expanding the range of samples that can be probed. An overview of the different grain mapping techniques and their working area in terms of grain size and number is given in figure 6.19.

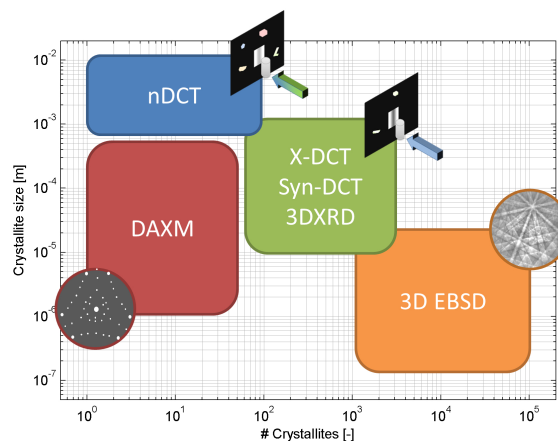


Figure 6.19: Application range in terms of sample crystallite size and number for the new nDCT technique and other methods mapping grain shape and orientation.

6.6 Summary

Diffraction contrast tomography was performed with neutrons for the first time using a double detector set-up, delivering information on the spatial distribution in crystal reflectivity and orientation. A new set-up was devised to this end, where the traditional transmission neutron tomography set-up is completed with a second imaging detector, recording projections formed by neutrons diffracted from the single crystal or crystallites.

7 Epilogue

Neutron imaging beamlines can be found around all major neutron sources, are under design, construction or commissioning. From its early days as a film-based inspection tool of engineering components, it has turned into a recognized scientific research method, to which this thesis work can be considered a contribution.

7.1 Summary

This work started with an overview of the requirements for neutron imaging, reviewing components from neutron source to detector, making considerations such as for spatial resolution and discussing data analysis like Computed Tomography (CT) algorithms. It is clear that neutron imaging is a very versatile technique, also reflected by its application as a research tool in numerous disciplines. With this work, an effort was made to further extend it by introducing new set-ups, methods, analysis strategies for the investigation of crystalline materials.

The principal interaction mechanisms of neutrons and matter relevant to neutron imaging were discussed, with an emphasis on coherent elastic scattering which is sensitive to crystalline structure. It exhibits strong variations in interaction probability, represented by the cross-section, as a function of the neutron energy.

In order not to average out the energy-dependent cross-section behaviour and the crystallographic sample information it contains, one needs to perform neutron imaging with a reduced wavelength band. As was seen, this is either done using the TOF method at pulsed neutron sources or with the aid of various kinds of monochromators at continuous sources. In case of the latter, the experimenter should be aware of the variation in incident energy across the field of view.

The fact that for many metals coherent elastic scattering is the dominant interaction mechanism and that it is characterized by a wavelength cut-off was exploited for quantification purposes: scattering is suppressed when using wavelengths longer than the final Bragg edge and one becomes insensitive to (variations in) the sample's crystallography.

Energy-selective imaging of single crystals and crystallites is then investigated in great detail. Analysis strategies for recovering orientation information and mosaicity at high spatial resolution are discussed for digital radiography, together with strategies to extend it to CT.

Conversely, such samples can also be investigated not by the footprint of a lack of neutrons

through diffraction at specific wavelengths in transmission, but instead by directly imaging these diffracted neutrons: diffraction contrast imaging.

The different modalities in which neutron imaging can be performed, including the ones developed in the frame of this work, are summarized in figure 7.1. Neutron imaging experiments can be classified - though not necessarily restricted to a single category - depending on the time scale of the sample changes, the dimensions probed (2D/3D), whether one images in transmitted or diffracted beam direction and beam manipulation to probe sample properties other than simple material distribution.

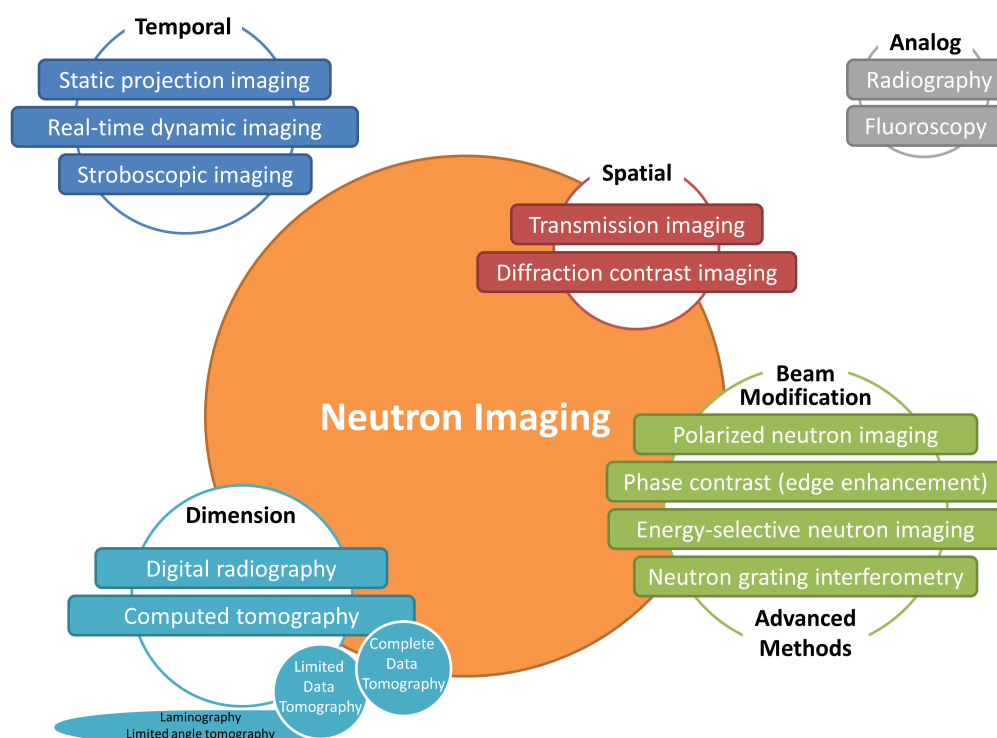


Figure 7.1: Overview of the multi-modal universe of neutron imaging and its terminology.

7.2 Transmission or diffraction? Continuous or pulsed?

The past two chapters both dealt with neutron imaging of single crystals and ensembles of them (coarse grained polycrystalline materials). But when to apply which? There is no straight answer: it depends on the sample, what information we are interested in, or simply which beam line we have been granted beam time at. In this section, we will dwell on the requirements and intricacies of both methods, so as to aid the reader in selecting the proper imaging modality for his experiment.

In energy-selective transmission imaging, the orientation of the crystal at each pixel position is found through indexation of the Bragg peaks in the wavelength-dependent transmission pattern. Very high energy-resolution is required, giving preference to a TOF imaging beam

7.2. Transmission or diffraction? Continuous or pulsed?

line. However, if one is only interested in a single Bragg peak (e.g. the Pyrolytic Graphite (PG) monochromator crystal in section 5.3), skipping the indexation step, using a monochromator at a continuous source will do just fine.

A cold neutron spectrum is preferred, since, as can be told from experimental data (figure 5.4a) or theoretical considerations (section 2.4.2), Bragg peaks become more pronounced and better separated for longer wavelengths, easing indexation. Still, overlap of a few crystallites in the beam direction will already give rise to too much Bragg peak overlap for this technique to remain useful.

Diffraction contrast imaging, features angular separation of the projections of the differently oriented crystallites, putting less constraints on the number of crystallites that can be treated. The experiments performed in the context of this dissertation featured side- and back reflection for working at a cold neutron imaging beamline. Nothing however speaks principally against performing diffraction contrast imaging with thermal neutrons. One then simply deals with forward diffraction angles. As an illustration, table 6.1 for the two smallest diffraction angles of selected materials at 3.1 Å is retaken for the thermal neutron wavelength of 1.8 Å in table 7.1.

	1 st reflection	2 nd reflection
Al	45.3°	52.8°
Cu	51.1°	59.7°
Fe (BCC)	52.7°	77.8
Ni	52.5°	61.4°

Table 7.1: Smallest two diffraction angles (w.r.t. the transmitted beam direction) formed by the two crystal planes of largest interplanar distance for typical engineering materials at the average thermal neutron wavelength of 1.8 Å.

Less energy-resolution is required, as the crystal will diffract only neutrons from a limited wavelength band out of the direct beam, the bandwidth in question depending on the crystal mosaicity.

However, this mosaicity should be quite low, as the corresponding angular range of the diffracted beam will blur any diffraction projections. Shorter sample to detector distances decrease the blur, though a certain minimum distance is required to cover sufficient angular range without projection angles becoming too oblique.

In energy-selective transmission imaging, the sample can be put as close to the detector as possible and an increased mosaicity will only result in an increased Bragg peak width in the cross-section pattern. The highest spatial resolution can be obtained this way.

It goes without saying that any method fit for continuous sources, can also be performed at pulsed sources, simply integrating the detected neutron counts over their arrival time. One can e.g. perform diffraction contrast tomography in TOF and use the additional wavelength stamp to determine the lattice plane family. However, one should take measurement time

constraints into account and strive for the highest efficiency.

If one needs an energy-scan, a TOF imaging beamline is the most efficient: all energy bins can be recorded in parallel. At a continuous source, one has to select a particular energy band with a monochromator, discarding the others in the process, record one image and move on to the next bin.

As its name suggests, a pulsed source produces neutrons in pulses, the time-averaged flux significantly lower than the peak one¹. If one only needs a single wavelength or a white beam, a continuous source is more efficient, the desired neutrons continuously being provided for.

A summary of the requirements and features of transmission and diffraction contrast imaging of crystals is given in table 7.2. The method applicability in terms of the sample is illustrated by figure 7.2.

	Transmission	Diffraction
Energy resolution	high	moderate
Spectrum	cold	thermal or cold
Number of Crystallites	low	moderate
Mosaicity	low-high	low
Spatial resolution	high	moderate
Field of view	small	large
	Pulsed	Continuous/Pulsed

Table 7.2: Features of transmission and diffraction contrast neutron imaging.

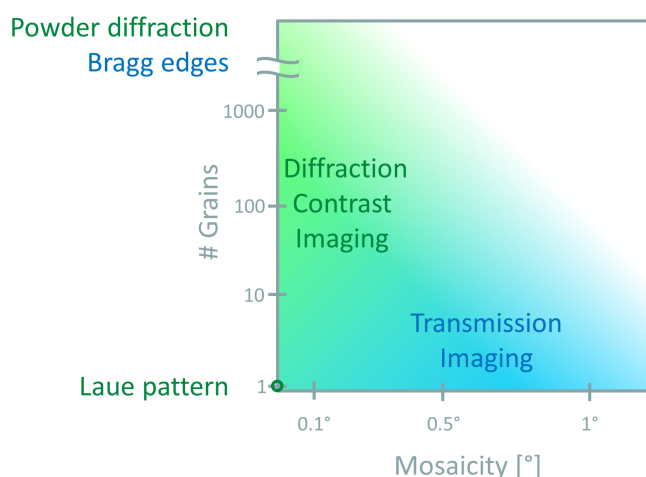


Figure 7.2: Method preference as a function of the sample's number of crystallites and their mosaicity.

¹Though ESS will still have a time-averaged flux on par with the currently strongest (continuous) neutron source at ILL [125].

7.3 Outlook

Critical in retrieving maps of crystal orientation and mosaicity at high spatial resolution from energy-selective transmission imaging is the indexation step. It is performed for each pixel by template matching to simulated single crystal transmission patterns. Currently, only the simple case of cubic systems can be treated and only the Bragg peak position is taken into account. Simulation options can still be extended to include any crystal structure and also yield ideal peak height information. Moreover, simulation and indexation routines should also be able to cope with the possibility of multiphase material to extend the number of samples and problems that can be treated.

To cope with low image statistics - at the required high energy resolution and small pixel sizes, one has a very low neutron count in each pixel - the quality of the experimental data can be improved by preprocessing prior to indexation. Advanced image processing methods such as the inverse scale space method [175] are able to filter out noise while preserving sharp gradients (the crystallite edge in the spatial dimension and the Bragg peaks in the temporal dimension). Wavelet-based methods [176] look promising for better identifying the Bragg peaks and their parameters (position, peak width) in experimental cross-section patterns obscured by noise.

Thus, the range of materials that can be treated would greatly be expanded and correlation between experimental and simulated patterns improved. In the presence of multiple crystallites in the beam direction and subsequent pattern overlap, robustness of the indexation and separation of the crystallites will thus be increased.

In transmission radiography, only the projection along the beam direction of the crystal properties (absorption, orientation, mosaicity) is mapped. The question on their 3D distribution naturally arises. However, tomographic reconstruction from energy-selective radiography at different projection angles is far from straightforward as the manifestation of these properties is also dependent on the orientation of the crystal in the beam. Appropriate reconstruction strategies such as normalization to angular-independent equivalent parameters are to be investigated. In case of multiple segmented crystallites, their respective projections must first be grouped for the different projection angles.

Also neutron diffraction imaging routines can still be improved on similar fronts such as the ability to analyze multiphase materials and arbitrary crystal structure. The virtual source approximation used to reconstruct the crystallites' shapes based on the diffraction projections breaks down in the case of large samples as beam attenuation is incorrectly taken into account. Two solution strategies can already be envisaged as worth pursuing: (1) an iterative scheme where diffraction projections are corrected based on the reconstructed macroscopic cross-section from the transmission tomography and beam path from prior diffraction reconstruction or (2) modification of the forward projector of the algebraic reconstructor used to the true beam path.

Key to the use and spreading of a new technique is the ease with which acquired data can be analyzed by the potential user, who usually has a different background than the method

developer. Therefore, a clear need exists for user-friendly evaluation and analysis software. It should moreover be flexible enough to allow for different experimental configurations that would promote the usage of the method and software at any existing neutron imaging beamline, such as at Paul Scherrer Institut.

Such a platform already exists for diffraction imaging with synchrotron radiation: FABLE [177], initiated at the Danish Technical University, which also features indexation and forward simulation routines. It should be investigated to which extent this software tool - which has the added advantage of being open source and freely available – can be expanded to deal with neutron diffraction imaging data.

The two initiated crystal analysis methods, neutron transmission and diffraction imaging, have initially been developed separately. However, they show a clear common ground: neutrons diffracted out of the direct beam causing a peak in the transmission cross-section spectrum, form the crystallite projection in diffraction imaging. It should therefore be investigated to which extent simulation of the single crystal transmission pattern and forward simulation of crystal diffraction projection positions can be merged.

If scalable to many crystallites, simulations of the diffracted neutrons can also be used to remove their contribution to the transmission images for better quantification of the reconstructed cross-section in tomography. An iterative procedure can be envisaged with a first tomographic reconstruction serving as a basis for simulating the scattering contributions, removing them from the transmission projections and reconstructing anew. The option of including it in algebraic reconstruction routines, which allows to incorporate much more a priori physics knowledge in the forward projector such as beam hardening [178], should also be explored.

A Total macroscopic cross sections

Group →	1	2	3	4	5	6	7	8	9	10	11	12	13	14	15	16	17	18
↓ Period																		
1	H 3.44																	He 0.02
2	Li 3.30	Be 0.79											B 101.6	C 0.56	N 0.43	O 0.17	F 0.20	Ne 0.10
3	Na 0.09	Mg 0.15											Al 0.1	Si 0.11	P 0.12	S 0.06	Cl 1.33	Ar 0.03
4	K 0.06	Ca 0.08	Sc 2.00	Ti 0.60	V 0.72	Cr 0.54	Mn 1.21	Fe 1.19	Co 3.92	Ni 2.05	Cu 1.07	Zn 0.35	Ga 0.49	Ge 0.47	As 0.67	Se 0.73	Br 0.24	Kr 0.61
5	Rb 0.08	Sr 0.14	Y 0.27	Zr 0.29	Nb 0.40	Mo 0.52	Tc 1.76	Ru 0.58	Rh 10.88	Pd 0.78	Ag 4.04	Cd 115.1	In 7.58	Sn 0.21	Sb 0.30	Te 0.25	I 0.23	Xe 0.43
6	Cs 0.29	Ba 0.07		Hf 4.99	Ta 1.49	W 1.47	Re 6.85	Os 2.24	Ir 30.46	Pt 1.46	Au 6.23	Hg 16.21	Tl 0.47	Pb 0.38	Bi 0.27	Po -	At -	Rn -
7	Fr -	Ra 0.34		Rf -	Db -	Sg -	Bh -	Hs -	Mt -	Ds -	Rg -	Uub -	Uut -	Uuq -	Uup -	Uuh -	Uus -	Uuo -
Lanthanides			La 0.52	Ce 0.14	Pr 0.41	Nd 1.87	Pm 5.72	Sm 171.47	Eu 94.58	Gd 1479.0	Tb 0.93	Dy 32.42	Ho 2.25	Er 5.48	Tm 3.53	Yb 1.40	Lu 2.75	
Actinides			Ac -	Th 0.59	Pa 8.46	U 0.82	Np 9.80	Pu 50.20	Am 2.86	Cm -	Bk -	Cf -	Es -	Fm -	Md -	No -	Lr -	

Figure A.1: Macroscopic cross section [cm^{-1}] for thermal neutrons.

Appendix A. Total macroscopic cross sections

Group →	1	2	3	4	5	6	7	8	9	10	11	12	13	14	15	16	17	18
↓ Period																		
1	H 0.02																	He 0.02
2	Li 0.06	Be 0.22											B 0.28	C 0.27	N 0.11	O 0.16	F 0.14	Ne 0.17
3	Na 0.13	Mg 0.24											Al 0.38	Si 0.33	P 0.25	S 0.30	Cl 0.23	Ar 0.20
4	K 0.14	Ca 0.26	Sc 0.48	Ti 0.73	V 1.04	Cr 1.29	Mn 1.32	Fe 1.57	Co 1.78	Ni 1.96	Cu 1.97	Zn 1.64	Ga 1.42	Ge 1.33	As 1.50	Se 1.23	Br 0.90	Kr 0.73
5	Rb 0.47	Sr 0.86	Y 1.61	Zr 2.47	Nb 3.43	Mo 4.29	Tc 5.06	Ru 5.71	Rh 6.08	Pd 6.13	Ag 5.67	Cd 4.84	In 4.31	Sn 3.98	Sb 4.28	Te 4.06	I 3.45	Xe 2.53
6	Cs 1.47	Ba 2.73		Hf 19.70	Ta 25.47	W 30.49	Re 34.47	Os 37.92	Ir 39.01	Pt 38.61	Au 35.94	Hg 25.88	Tl 23.23	Pb 22.81	Bi 20.28	Po 20.22	At -	Rn 9.77
7	Fr -	Ra 11.80		Rf -	Db -	Sg -	Bh -	Hs -	Mt -	Ds -	Rg -	Uub -	Uut -	Uuq -	Uup -	Uuh -	Uus -	Uuo -
Lanthanides				La 5.04	Ce 5.79	Pr 6.23	Nd 6.46	Pm 7.33	Sm 7.68	Eu 5.66	Gd 8.69	Tb 9.46	Dy 10.17	Ho 10.17	Er 11.70	Tm 12.49	Yb 9.32	Lu 14.07
Actinides				Ac 24.47	Th 28.95	Pa 39.65	U 49.08	Np -	Pu -	Am -	Cm -	Bk -	Cf -	Es -	Fm -	Md -	No -	Lr -

Figure A.2: Attenuation coefficient [cm⁻¹] for 100 keV X-rays.

B Matrix elements in simulating the Laue pattern

The relation between the Euler angles (ϕ_1, ϕ_2) and the elements of the equivalent orientation matrix E_{ij} is given by [50]:

$$\begin{aligned}
 E_{11} &= \cos \phi_1 \cos \phi_2 - \sin \phi_1 \sin \phi_2 \cos \phi \\
 E_{12} &= -\cos \phi_1 \sin \phi_2 - \sin \phi_1 \cos \phi_2 \cos \phi \\
 E_{13} &= \sin \phi_1 \sin \phi \\
 E_{21} &= \sin \phi_1 \cos \phi_2 + \cos \phi_1 \sin \phi_2 \cos \phi \\
 E_{22} &= -\sin \phi_1 \sin \phi_2 + \cos \phi_1 \cos \phi_2 \cos \phi \\
 E_{23} &= -\cos \phi_1 \sin \phi \\
 E_{31} &= \sin \phi_2 \sin \phi \\
 E_{32} &= \cos \phi_2 \sin \phi \\
 E_{33} &= \cos \phi
 \end{aligned} \tag{B.1}$$

To bring a random vector \mathbf{n} of elements (a, b, c) onto the x-axis, one can split up the total rotation into one over an angle α around the z-axis to bring it into the xz-plane, followed by one over β around the y-axis [158].

Illustrating the problem geometry in figure B.1, the angles are found as

$$\alpha = \begin{cases} -\text{atan}(b/a) & b \geq 0 \\ -\text{atan}(b/a) - \pi & b < 0 \end{cases} \tag{B.2}$$

and

$$\beta = -\text{atan}\left(\frac{c}{\sqrt{a^2 + b^2}}\right) \tag{B.3}$$

so the total transform A_{nx} is given by the two subsequent rotations

$$A_{nx} = \begin{bmatrix} \cos \alpha & -\sin \alpha & 0 \\ \sin \alpha & \cos \alpha & 0 \\ 0 & 0 & 1 \end{bmatrix} \cdot \begin{bmatrix} \cos \beta & 0 & -\sin \beta \\ 0 & 1 & 0 \\ \sin \beta & 0 & \cos \beta \end{bmatrix} \tag{B.4}$$

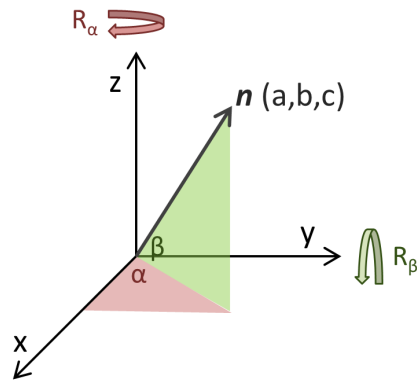


Figure B.1: Geometry for transforming a random vector onto the x-axis

Bibliography

- [1] A. Ziegler. *Reaktortechnik*. Springer, 2013.
- [2] <http://www.atomicarchive.com/Fission/Fission1.shtml>, retrieved on 17.06.2014.
- [3] <http://p5.focus.de/img/fotos/origs486343/8068736609-w552-h541-o-q75-p5/TUM-4.jpg>, retrieved on 17.06.2014.
- [4] B. Schillinger. ILL CRISP WIN workshop. In *ANTARES - State of the Art Neutron Imaging Instrument and Cultural Heritage applications*, 2014.
- [5] http://irfu.cea.fr/Images/astImg/2229_1.png, retrieved on 18.06.2014.
- [6] A. Krasa. Spallation reaction physics, 2010.
- [7] J. Frazer, R. E. Green, J. W. Hilborn, J. C. D. Milton, W. A. Gibson, E. E. Gross, and A. Zucker. Measured spallation neutron yield vs. proton energy for various targets. *Physics in Canada*, 21:17, 1965.
- [8] G. S. Bauer. Operation and development of the new spallation neutron source SINQ at the Paul Scherrer Institut. *Nuclear Instruments and Methods in Physics Research Section B: Beam Interactions with Materials and Atoms*, 139:65 – 71, 1998.
- [9] M. Arai and Crawford K. *Neutron imaging and applications*, chapter 2. Springer, 2009.
- [10] J. Chadwick. Possible existence of a neutron. *Nature*, 129:312, 1932.
- [11] Y. Kiyanagi. Review of projects of compact neutron sources in japan. In *1st UCANS, Beijing, China*, 2010.
- [12] P. Oberholzer, P. Boillat, R. Siegrist, A. Kaestner, E.H. Lehmann, G.G. Scherer, and A. Wokaun. Simultaneous neutron imaging of six operating PEFCs: Experimental set-up and study of the MPL effect. *Electrochemistry Communications*, 20:67 – 70, 2012.
- [13] Neutron imaging at the spallation source SINQ, information for potential users and customers. PSI Information Booklet, 2011.
- [14] A. C. Kak and M. Slaney. *Principles of Computerized Tomographic Imaging*, chapter 3: Algorithms for reconstruction with nondiffracting sources, pages 49–112. IEEE Press, 1999.

- [15] J. Vlassenbroeck. *Advances in laboratory-based X-ray microtomography*. PhD thesis, Ghent University, 2010.
- [16] A. C. Kak and M. Slaney. *Principles of Computerized Tomographic Imaging*, chapter 7: Algebraic Reconstruction Algorithms, pages 276–296. IEEE Press, 1999.
- [17] L. A. Flores, V. Vidal, P. Mayo, F. Rodenas, and G. Verdu. CT image reconstruction based on GPUs. *Procedia Computer Science*, 18(0):1412–1420, 2013. 2013 International Conference on Computational Science.
- [18] Peter Gilbert. Iterative methods for the three-dimensional reconstruction of an object from projections. *Journal of Theoretical Biology*, 36(1):105–117, 1972.
- [19] A. H. Andersen and A. C. Kak. Simultaneous algebraic reconstruction technique (SART): a superior implementation of the ART algorithm. *Ultrasonic Imaging*, 6:81–94, 1984.
- [20] G. Kühne, G. Frei, E. Lehmann, and P. Vontobel. CNR - the new beamline for cold neutron imaging at the swiss spallation neutron source SINQ. *Nuclear Instruments & Methods in Physics Research, Section A*, 542:264–270, 2005.
- [21] D. Liu, D. Hussey, M. V. Gubarev, B. D. Ramsey, D. Jacobson, M. Arif, D. E. Moncton, and B. Khaykovich. Demonstration of achromatic cold-neutron microscope utilizing axisymmetric focusing mirrors. *Applied Physics Letters*, 102:183508, 2013.
- [22] M. Yamada, Y. Iwashita, M. Ichikawa, T. Sugimoto, H. Tongu, H. Fujisawa, H. Shimizu, Ta. Ino, K. Mishima, K. Taketani, T. Yoshioka, S. Muto, Ta. Morishima, T. Oku, Ju. Suzuki, T. Shinohara, K. Sakai, H. Sato, K. Hirota, Y. Otake, Y. Seki, S. Kawasaki, S. Komamiya, Y. Kamiya, H. Otono, S. Yamashita, and P. Geltenbort. Development of modulating permanent magnet sextupole lens for focusing of pulsed cold neutrons. *Physica B: Condensed Matter*, 404(17):2646 – 2651, 2009.
- [23] U. Garbe, M. Yamada, Y. Iwashita, H. Tongu, W. Lee, S. Kennedy, H. Shimizu, K. Mishima, K. Hirota, M. Hino, M. Kitaguchi, T. Oda, P. Geltenbort, B. Guerard, and G. Manzin. Rotating sextupole lens as a neutron beam magnifier. Presented at the 7th International Topical Meeting on Neutron Radiography, 2012.
- [24] A. P. Kaestner, S. Hartmann, G. Kühne, G. Frei, C. Grünzweig, L. Josic, F. Schmid, and E. H. Lehmann. The ICON beamline - a facility for cold neutron imaging at SINQ. *Nuclear instruments and methods in physics research A*, 659:387–393, 2011.
- [25] M. Morgano, S. Peetermans, E. Lehmann, T. Panzner, and U. Filges. Neutron imaging options at the BOA beamline at paul scherrer institut. *Nuclear Instruments and Methods, section A*, 754:46–56, 2014.
- [26] E. H. Lehmann, P. Vontobel, G. Frei, and C. Brönnimann. Neutron imaging - detector options and practical results. *Nuclear instruments and methods in physics research A*, 531:228–237, 2004.

- [27] K. Takahashi, S. Tazaki, J. Miyahara, Y. Karasawa, and N. Niimura. Imaging performance of imaging plate neutron detectors. *Nuclear instruments and methods in physics research A*, 377:119–122, 1996.
- [28] M. J. Knitel. *New inorganic scintillators and storage phosphors for detection of thermal neutrons*. PhD thesis, Delft university of technology, 1998.
- [29] E. Schooneveld. Zns neutron detectors. In *International Neutron Scattering Instrumentation School (INSIS)*, 2012.
- [30] H. Iwase, M. Katagiri, and M. Shibayama. Optimization of the thickness of a zns/⁶lif scintillator for a high-resolution detector installed on a focusing small-angle neutron scattering spectrometer (SANS-U). *Journal of applied crystallography*, 45:507–512, 2012.
- [31] D. A. Abdushukurov. *Gadolinium foils as converters of thermal neutrons in detectors of nuclear radiation*. New York: Nova Science Pub. Inc., 2010.
- [32] W. Kockelmann, G. Frei, E. H. Lehmann, P. Vontobel, and J.R. Santisteban. Energy-selective neutron transmission imaging at a pulsed source. *Nuclear instruments and methods in physics research A*, 578:421–434, 2007.
- [33] C. Grünzweig, M. Wagner, J. Ruf, and D. Helmer. Visualisation of the oil distribution in a wet-running multi-disc clutch. *ATZ - Automobiltechnische Zeitschrift*, 3, 2013.
- [34] E. H. Lehmann, G. Frei, G. Kuehne, and P. Boillat. The micro-setup for neutron imaging: A major step forward to improve the spatial resolution. *Nuclear instruments and methods in physics research A*, 576 (2-3):389–396, 2007.
- [35] J. Jakubek, T. Holy, E. Lehmann, S. Pospisil, J. Uher, J. Vacik, and D. Vavrik. Spatial resolution of medipix2 device as neutron pixel detector. *Nuclear Instruments and Methods in Physics Research Section A: Accelerators, Spectrometers, Detectors and Associated Equipment*, 546(1-2):164 – 169, 2005. Proceedings of the 6th International Workshop on Radiation Imaging Detectors 2004.
- [36] A. S. Tremsin, J. B. J. B. McPhate, V. Vallergera, O. H. O. H. W. Siegmund, B. Feller, E. LehE. Lehmann, Kaestner, P. BoiP. Boillat, Panzner, and U. Filges. Neutron radiography with sub-15 μ m resolution through event centroiding. *Nuclear Instruments & Methods in Physics Research, Section A: Accelerators, Spectrometers, Detectors, and Associated Equipment*, 688:32–40, 2012.
- [37] A. S. Tremsin. High resolution energy resolved neutron imaging, transmission diffraction and resonance absorption imaging with MCP detectors. In *NEUWAVE-4 conference*, 2011.
- [38] D. Wackeroth and L. Belkora. High energy physics made painless. <http://ed.fnal.gov/painless/pdfs/cross.pdf>, retrieved on 01.09.2014.

Bibliography

- [39] Java-based nuclear information system, <http://www.oecd-neo.org/janis/>.
- [40] Kenneth S. Krane. *Introductory nuclear physics*. John Wiley and sons, 1988.
- [41] S. Vogel. Recent advancements in energy-dispersive neutron imaging at LANSCE. Neuwave-6 Conference, 2014.
- [42] G. Breit and E. P. Wigner. Capture of slow neutrons. *Phys. Rev.*, 49:519, 1936.
- [43] J. E. Lynn. *The theory of neutron resonance reactions*. Clarendon Press Oxford, 1968.
- [44] V. F. Sears. Neutron scattering lengths and cross sections. *Neutron news*, 3:26–37, 1192.
- [45] V. F. Turchin. *Slow neutrons*. Sivan Press, 1965.
- [46] K. W. Ford and D. Bohm. Nuclear size resonances. *Phys. Rev.*, 79:745–746, 1950.
- [47] L. Koester and A. Steyerl. *Springer Tracts in Modern Physics 80: Neutron Physics*. Springer Verlag, 1977.
- [48] W. Marshall and S. W. Lovesey. *Theory of thermal neutron scattering*. Oxford university press, 1971.
- [49] E. H. Kisi and C. J. Howard, editors. *Applications of neutron powder diffraction*. Oxford Science Publications, 2008.
- [50] O. Engler and V. Randle. *Introduction to texture analysis*. CRC Press, 2 edition, 2010.
- [51] M. Boin. NXS: a program library for neutron cross section calculations. *Journal of Applied Crystallography*, 45:603–607, 2012.
- [52] Charles Kittel. *Introduction to solid state physics*. Wiley & Sons, 2005.
- [53] J. Garai. Physics behind the Debye temperature. *ArXiv Physics e-prints*, February 2007.
- [54] J. R. Granada. Total scattering cross section of solids for cold and epithermal neutrons. *Z. Naturforsch.*, 39a:1160–1167, 1984.
- [55] S. Vogel. *A Rietveld-approach for the analysis of neutron time-of-flight transmission data*. PhD thesis, Christian-Albrechts-Universität (Kiel, Germany), 2000.
- [56] M. Boin. *Developments towards the tomographic imaging of local crystallographic structures*. PhD thesis, The Open University, 2011.
- [57] G. L. Squires. Multi-oscillator processes in the scattering of neutrons by crystals. *Proc. R. Soc. Lon. A*, 212:192–206, 1952.
- [58] G. Placzek. The scattering of neutrons by system of heavy nuclei. *Phys. Rev.*, 86:377–388, 1952.
- [59] G. Placzek. Incoherent neutron scattering by polycrystals. *Phys. Rev.*, 93:895, 1954.

-
- [60] G. C. Wick. The scattering of neutrons by system containing light nuclei. *Phys. Rev.*, 94:1228–1242, 1954.
- [61] G. Placzek and L. Van Hove. Interference effects in the total neutron scattering cross-section of crystals. *Il nuovo cimento*, 1:233–256, 1955.
- [62] K. Binder. Total coherent cross sections for the scattering of neutrons from crystals. *Phys. Stat. Sol.*, 41:767–779, 1970.
- [63] F. Salvemini, F. Grazzi, S. Peetermans, F. Civita, R. Franci, S. Hartmann, E. Lehmann, and M. Zoppi. Quantitative characterization of japanese ancient swords through energy-resolved neutron imaging. *Journal of Analytical Atomic Spectroscopy*, 27:1494–1501, 2012.
- [64] E.H. Lehmann, S. Peetermans, L. Josic, H. Leber, and H. van Swygenhoven. Energy-selective neutron imaging with high spatial resolution and its impact on the study of crystalline-structured materials. *Nuclear Instruments and Methods in Physics Research, Section A*, 735:102–109, 2014.
- [65] R. Woracek, D. Penumadu, N. Kardjilov, A. Hilger, M. Strobl, R. C. Wimpory, I. Manke, and J. Banhart. Neutron bragg-edge imaging for strain mapping under in situ tensile loading. *Journal of Applied Physics*, 109:093506–1 – 093506–4, 2011.
- [66] B. Abbey, S. H. Zhang, W. Vorster, and M. Korsunsky. Reconstruction of axisymmetric strain distributions via neutron strain tomography. *Nuclear instruments and methods in physics research B*, 270:28–35, 2012.
- [67] S. Peetermans, F. Grazzi, F. Salvemini, and E. Lehmann. Spectral characterization of a velocity selector type monochromator for energy-selective neutron imaging. *Physics Procedia*, 43:121–127, 2013.
- [68] S. Peetermans, M. Tamaki, S. Hartmann, A. Kaestner, M. Morgano, and E. H. Lehmann. A new transmission based monochromator for energy-selective neutron imaging at the ICON beamline. *Nuclear Instruments and Methods, section A*, 757:28–32, 2014.
- [69] <http://www.isis.stfc.ac.uk/instruments/engin-x/engin-x2900.html>, accessed on 17.07.2014.
- [70] G. F. Knoll. *Radiation detection and measurement*. J. Wiley and Sons, 1999.
- [71] C. G. Windsor. *Pulsed neutron scattering*. Taylor&Francis LTD, 1981.
- [72] G. D. Bokuchava, D. P. Kozlenko, A. M. Balagurov, and B. N. Savenko. Neutron imaging at IBR-2 pulsed reactor: first results and neutron imaging instrument project. ESS Neutron Imaging User Symposium, Bad Zurzach, Switzerland, 2012.
- [73] <http://flnp.jinr.ru/563/>.

Bibliography

- [74] E. P. Shabalin. *Fast pulsed and burst reactors*. Pergamon Press, 1979.
- [75] H. Friedrich, V. Wagner, and P. Wille. A high-performance neutron velocity selector. *Physica B*, 156&157:547–549, 1989.
- [76] B. Hammouda. Probing nanoscale structures - the sans toolbox. http://www.ncnr.nist.gov/staff/hammouda/the_SANS_toolbox.pdf, 2006.
- [77] S. Baechler, N. Kardjilov, M. Dierick, J. Jolie, G. Kühne, E. H. Lehmann, and T. Materna. New features in cold neutron radiography and tomography part 1: thinner scintillators and a neutron velocity selector to improve the spatial resolution. *Nuclear instruments and methods in physics research A*, 491:481–491, 2002.
- [78] N. Kardjilov, B. Schillinger, and E. Steichele. Energy-selective neutron radiography and tomography at FRM. *Applied Radiation and Isotopes*, 61:455–460, 2004.
- [79] F. Grazzi and et al. SINQ experimental report. project 10065, proposal number 20091243, 2010.
- [80] F. Grazzi, F. Salvemini, and S. Peetermans. SINQ experimental report. Project 11039, proposal number 20101255.
- [81] W. Soller. A new precision x-ray spectrometer. *Phys. Rev.*, 24:158–167, 1924.
- [82] L. Giller. Characterization of the cold neutron imaging beamline ICON at PSI. Master's thesis, Ecole Polytechnique Fédérale de Lausanne, 2006.
- [83] C. M. Fizez, P. Wambacq, P. Suetens, and E. Schoeters. Influence of heel-effect and of non-uniformity of emitted spectra on dual-energy subtraction in computed radiography. *SPIE*, 2708:588–598, 1996.
- [84] M. Schulz, P. Böni, E. Calzada, M. Mühlbauer, and B. Schilinger. Energy-dependent neutron imaging with a double crystal monochromator at the antares facility at frm ii. *Nuclear instruments and methods in physics research A*, 605:33–35, 2009.
- [85] W. Treimer, M. Strobl, N. Kardjilov, A. Hilger, and I. Manke. Wavelength tunable device for neutron radiography and tomography. *Applied Physics Letters*, 89:203504, 2006.
- [86] J. Schefer, M. Medarde, S. Fischer, R. Thut, M. Koch, P. Fischer, U. Staub, M. Horisberger, G. Böttger, and A. Dönni. Sputtering method for improving neutron composite germanium monochromators. *Nuclear instruments and methods in physics research A*, 372:229–232, 1996.
- [87] E. Frikkee. Application of pyrolytic graphite as a tunable neutron filter. *Nuclear Instruments & Methods*, 125:307–312, 1975.
- [88] J. C. Lagarias, J. A. Reeds, M. H. Wright, and P. E. Wright. Convergence properties of the nelder-mead simplex method in low dimensions. *SIQM J. Optim.*, 9:112–147, 1998.

-
- [89] R. Pynn. Lecture 2: Introduction and neutron scattering theory. *Los Alamos Neutron Science Center, Los Alamos Science*, 2014.
- [90] ROTAX technical information. <http://www.isis.stfc.ac.uk/instruments/rotax/technical-rotax-technical-information7345.html>. Retrieved on 25.07.2014.
- [91] S. Peetermans, R. van Langh, E. Lehmann, and A. Pappot. Quantification of the material composition of historical copper alloys by means of neutron transmission measurements. *J. Anal. At. Spectrom.*, 27:1674, 2012.
- [92] <https://www.hud.ac.uk/news/allstories/solvingthesubmergedsecretsofthemaryrose.php>.
- [93] A. B. Wolbarst. *Physics of Radiology*. Prentice-Hall International, 1993.
- [94] M. Tamaki, M. Oda, K. Takahashi, W. Tanimoto, and T. Funahashi. Study on neutron imaging techniques and processings for developing quantitative neutron radiography. *Nuclear instruments and methods in physics research A*, 377:102–106, 1996.
- [95] M. I. Silvani, R. T. Lopes, G. L. de Almeida, M. J. Gonçalves, and R. Furieri. On the impact of neutron beam divergence and scattering on the quality of transmission acquired tomographic images. *Nuclear instruments and methods in physics research B*, 263:253–257, 2007.
- [96] A. S. Tremsin, N. Kardjilov, M. Dawson, M. Strobl, I. Manke, J. B. McPhate, J. V. Vallerga, O. H. W. Siegmund, and W. B. Feller. Scatter rejection in quantitative thermal and cold neutron imaging. *Nuclear instruments and methods in physics research A*, 651:145–148, 2011.
- [97] M. Meyer. Kollimator positionierung an ICON. Technical report, Paul Scherrer Institut, 2014.
- [98] Y. Ikeda, M. Yokoi, M. Oda, M. Tamaki, and G. Matsumoto. Correction of scattering neutron effects on neutron ct. *Nuclear instruments and methods in physics research A*, 377:85–89, 1996.
- [99] M. Kang, H.Z. Bilheux, S. Voisin, L. Cheng C, E. Perfect, J. Horita, and J.M. Warren. Water calibration measurements for neutron radiography: application to water content quantification in porous media. *Nuclear Instruments & Methods in Physics Research, Section A*, 708:24–31, 2013.
- [100] R. Hassanein, E. Lehmann, and P. Vontobel. Methods of scattering corrections for quantitative neutron radiography. *Nuclear instruments and methods in physics research A*, 542:353–360, 2005.
- [101] R. Hassanein. *Correction methods for the quantitative evaluation of thermal neutron tomography*. PhD thesis, Swiss federal institute of technology Zürich, 2006.

Bibliography

- [102] F. Gallmeier. Private communication.
- [103] K. Lefmann and K. Nielsen. Mcstas, a general software package for neutron ray-tracing simulations. *Neutron news*, 10:20, 1999.
- [104] P. Willendrup, E. Farhi, and K. Lefmann. Mcstas 1.7 a new version of the flexible monte carlo neutron scattering package. *Physica B*, 350:735, 2004.
- [105] M. Boin. http://www.mcstas.org/download/components/contrib/Sample_nxs.html.
- [106] *Table of simple integral neutron cross section data from JEF-2.2, ENDF/B-VI, JENDL-3.2, BROND-2 and CENDL-2*. Nuclear Energy Agency, 1994.
- [107] V. Avery and J. Dillon. Renaissance and baroque bronzes of the fitzwilliam museum, cambridge. London: Daniel Katz Ltd, 2002.
- [108] J. Basset, J.P. Fogelman, D.A. Scott, and R. Schmidting II. The craftsman revealed, adriaen de vries sculptor in bronze. The Getty Conservation Institute, 2008.
- [109] F. G. Bewer. *A study of the technology of Renaissance bronze statuettes*. PhD thesis, University of London, University College, Institute of Archaeology, 1996.
- [110] O. Werner. Analysen mittelalterlicher bronzen und messingen i. Archäologie und Naturwissenschaften (Verlag de Römischen-Germanischen Zentralmuseums): 144-220, 1977.
- [111] J. Riederer. Metallanalysen augsburger bronze- und messingskulpturen des 16. jahrhunderts. Berliner Beiträge zur Archäometrie, Band 10:85-95, 1988.
- [112] L. D. Glinsman. *The Application of X-Ray Fluorescence Spectrometry to the Study of Museum Objects*. PhD thesis, Universiteit van Amsterdam, 2004.
- [113] R. van Langh, A. Pappot, S. Creange, L. Megens, and I. Joosten. The effect of surface changes in heat treated bronze samples analyzed by x-ray fluorescence spectrometry. In *Metal 2010, ICOM-CC metal working group. Charleston: 204-209*, 2010.
- [114] A. Heginbotham, A. Bezur, M. Bouchard, J.M. Davis, K. Eremin, J.H. Frantz, L. Glinsman, L. Hayek, D. Hook, V. Kantarelou, A.G. Karydas, L. Lee, J. Mass, C. Matsen, B. McCarthy, M. McGath, A. Shugar, J. Sirois, D. Smith, and R.J. Speakman. An evaluation of inter-laboratory reproducibility of quantitative xrf of historic copper alloys. In *Metal 2010, ICOM-CC Metal Working group, Charleston: 178-188*, 2010.
- [115] R. van Langh, E. Lehmann, S. Hartmann, A. Kaestner, and F. Scholten. The study of bronze statuettes with the help of neutron imaging techniques. *Analytical and Bioanalytical Chemistry*, 395:1949–1959, 2009.
- [116] E. H. Lehmann, E. Deschler-Erb, and A. Ford. Neutron tomography as a valuable tool for the non-destructive analysis of historical bronze sculptures. *Archaeometry*, 52:272–285, 2010.

-
- [117] W. Langenkamp. *Thermospannung bei der Rastertunnelmikroskopie der metallischen Heterostruktur Blei auf Kupfer (111)*. PhD thesis, Universität Duisburg-Essen, 2008.
- [118] E. Sidot, A. Kahn-Harari, E. Cesari, and L. Robbiola. The lattice parameter of α -bronzes as a function of solute content: application to archaeological materials. *Materials Science and Engineering A*, 393:147–156, 2005.
- [119] S. Peetermans, F. Grazzi, F. Salvemini, E. H. Lehmann, S. Caporali, and G. Pratesi. Energy-selective neutron imaging for morphological and phase analysis of iron-nickel meteorites. *Analyst*, 138:5303–5308, 2013.
- [120] A. S. Tremsin, J. B. J. B. J. B. McPhate, V. Vallerger, H. W. Siegmund, J. S. Hull, W. B. Feller, and E. Lehmann. Detection efficiency, spatial and timing resolution of thermal and cold neutron counting MCP detectors. *Nuclear instruments and methods in physics research A*, 604:140–143, 2009.
- [121] J. R. Santisteban. Time-of-flight neutron transmission of mosaic crystals. *Journal of applied crystallography*, 38:934–944, 2005.
- [122] R. De Gelder, R. Wehrens, and J. A. Hageman. A generalized expression for the similarity of spectra: application to powder diffraction pattern classification. *Journal of computational chemistry*, 22:273–289, 2001.
- [123] J. Santisteban, L. Edwards, A. Steuwer, and P. J. Withers. Time-of-flight neutron transmission diffraction. *Journal of applied crystallography*, 34, 2001.
- [124] J. J. Ding, C. J. Kuo, and W. C. Hong. An efficient image segmentation technique by fast scanning and adaptive merging. *CVGIP*, 2009.
- [125] Richard Hall-Wilton and Camille Theroine. Status of the european spallation source ESS AB, the instrument selection process, and a fundamental physics beamline at the ESS. *Physics Procedia*, 51(0):8 – 12, 2014. ESS Science Symposium on Neutron Particle Physics at Long Pulse Spallation Sources, NPPatLPS 2013.
- [126] Emmanouela Rantsiou, Tobias Panzner, Patrick Hautle, and Uwe Filges. Using parabolic supermirror lenses to focus and de-focus a neutron beam. *Journal of Physics: Conference Series*, 528(1):012009, 2014.
- [127] A. Authier, S. Lagomarsino, and B. K. Tanner, editors. *X-ray and Neutron Dynamical Diffraction - Theory and Applications*. NATO ASI Series B: Physics vol. 357. Plenum Press, 1996.
- [128] P. G. Freeman, J. O. Birk, M. Markó, M. Bertelsen, J. Larsen, N. B. Christensen, K. Lefmann, J. Jacobsen, Ch. Niedermayer, F. Juranyi, and H. M. Ronnow. CAMEA ESS - the continuous angle multi-energy analysis indirect geometry spectrometer for the european spallation source. 2014.

Bibliography

- [129] W. D. Hopfe and J. I. Goldstein. The metallographic cooling rate method revised: application to iron meteorites and mesosiderites. *Meteorit. Planet. Sci.*, 36:135–154, 2001.
- [130] K. L. Rasmussen, H. Haack, and F. Ulff-Møller. Metallographic cooling rates of group IIF iron meteorites. *Meteorit. Planet. Sci.*, 36:883–896, 2001.
- [131] E. H. Lehmann, G. Frei, L. Josic, N. Kardjilov, A. Hilger, W. Kockelmann, and A. Steuwer. The energy-selective option in neutron imaging. *Nuclear instruments and methods in physics research A*, 603:429–438, 2009.
- [132] J. N. Grossman. Catalogs and inventories: The meteoritical bulletin no. 81. *Meteorit. Planet. Sci.*, 32:A159–A166, 1997.
- [133] A. Desrousseaux, J. C. Doukhan, C. Fieni, C. Perron, J. P. Jeannot, B. Lavielle, D. Renaud, J. C. van Duysen and M. Caffee, and K. Nishiizumi. A new iron meteorite from france. *Meteorit. Planet. Sci.*, 31:A36, 1996.
- [134] F. Grazzi. ISIS Experimental report RB1160009, 2012.
- [135] Y. De Witte. *Improved and practically feasible reconstruction methods for high resolution X-ray tomography*. PhD thesis, Ghent University, 2010.
- [136] W. J. Palenstijn, K. J. Batenburg, and J. Sijbers. Performance improvements for iterative electron tomography reconstruction using graphics processing units (GPUs). *Journal of Structural Biology*, 176:250–253, 2011.
- [137] W. Ludwig, P. Cloetens, J. Härtwig, J. Baruchel, B. Hamelin, and P. Bastie. Three-dimensional imaging of crystal defects by ‘topo-tomography’. *Journal of Applied Crystallography*, 34:602–607, 2001.
- [138] D. Juul-Jensen and H.F. Poulsen. The three dimensional x-ray diffraction technique. *Materials Characterization*, 72:1 – 7, 2012.
- [139] W. Ludwig, P. Reischig, A. King, M. Herbig, and E. M. Lauridsen. Three-dimensional grain mapping by x-ray diffraction contrast tomography and the use of friedel pairs in diffraction data analysis. *Review of scientific instruments*, 80:033905, 2009.
- [140] S. Peetermans and E. H. Lehmann. A double detector set-up for simultaneous transmission and diffraction neutron imaging. *Physics Procedia*, 43:179–185, 2013.
- [141] S. Peetermans and E. H. Lehmann. Simultaneous neutron transmission and diffraction contrast tomography as a non-destructive 3D method for bulk single crystal quality investigations. *Journal of Applied Physics*, 114:124905, 2013.
- [142] S. Peetermans, A. King, W. Ludwig, P. Reischig, and E. Lehmann. Cold neutron diffraction contrast tomography of polycrystalline material. *Analyst*, 139:5765–5771, 2014.

-
- [143] B. N. Ramachandran. X-ray topographs of diamond. *Proc. Indian Acad. Sci. A*, 19:280–292, 1944.
- [144] W. Berg. über eine röntgenographische methode zur untersuchung von gitterstörungen an kristallen. *Naturwissenschaften*, 19:391–397, 1931.
- [145] B. K. Tanner and D. K. Bowen. Synchrotron x-radiation topography. *Materials Science Reports*, 8:369–407, 1992.
- [146] J. Baruchel, J. Härtwig, and P. Pernot-Rejmánková. Present state and perspectives of synchrotron radiation diffraction imaging. *J. Synchrotron Rad.*, 9:107–114, 2002.
- [147] H. F. Poulsen. *Three-Dimensional X-Ray Diffraction Microscopy*. Springer, 2004.
- [148] M. Schlenker and J. Baruchel. Neutron topography: a review. *Physica B*, 137:309–319, 1986.
- [149] T. M. Pollock and S. Tin. Nickel-based superalloys for advanced turbine engines: chemistry, microstructure and properties. *Journal of Propulsion and Power*, 22:361–374, 2006.
- [150] S. F. Gao, L. Liu, N. Wang, X. B. Zhao, J. Zhang, and H. Z. Fu. Grain selection during casting ni-base, single-crystal superalloys with spiral grain selector. *Metallurgical and materials transactions A*, 43A:3767–3775, 2012.
- [151] J. K. Tien et al., editor. *The development of single crystal superalloy turbine blades*, Metals Park (USA), 1980. TMS, American Society for metals, ASM Pub.
- [152] N. S. Hussein, D. P. Kumah, J. Z. Yi, C. J. torbet, D. A. Arms, E. M. Dufresne, T. M. Pollock, J. W. Jones, and R. Clarke. Mapping single-crystal dendritic microstructure and defects in nickel-base superalloys with synchrotron radiation. *Acta Materialia*, 56:4715–4723, 2008.
- [153] D. Bellet, P. Bastie, and J. Baruchel. White beam synchrotron topography and γ -ray diffractometry characterization of the crystalline quality of single-grain superalloys: influence of the solidification conditions. *J. Phys. D: Appl. Phys.*, 26:A50–A52, 1993.
- [154] N. Siredey, M. Boufoussi, S. Denis, and J. Lacaze. Dendritic growth and crystalline quality of nickel-base single grains. *Journal of Crystal Growth*, 130:132–146, 1993.
- [155] H. Tomimitsu, K. Iijima, K. Aizawa, and A. Yoshinari. Neutron diffraction topography observation of a ni-based superalloy single crystal. *Physica B*, 213&214:818–820, 1995.
- [156] <http://www.sulzer.com>.
- [157] F. Cheaitany. Oral communication.
- [158] C. Marín and E. Diéguez. *Orientation of single crystals by back-reflection Laue pattern simulation*. World Scientific Publishing Co. Pte. Ltd., 1999.

Bibliography

- [159] D. K. Bowen and B. K. Tanner. *High resolution X-ray diffractometry and topography*. Taylor & Francis, 1998.
- [160] S. I. Wright and D. P. Field. Recent studies of local texture and its influence on failure. *Materials science and engineering A*, 257:165–170, 1998.
- [161] V. Randle. The role of the grain boundary plane in cubic polycrystals. *Acta Materialia*, 48:1459–1480, 1997.
- [162] A. King, G. Johnson, D. Engelberg, W. Ludwig, and J. Marrow. Observation of intergranular stress corrosion cracking in a grain-mapped polycrystal. *Science*, 321:382–385, 2008.
- [163] M. Herbig, A. King, P. Reischig, H. Proudhon, E.M. Lauridsen, J. Marrow, J.-Y. Buffière, and W. Ludwig. 3d growth of a short fatigue crack within a polycrystalline microstructure studied using combined diffraction and phase contrast x-ray tomography. *Acta materialia*, 59:590–601, 2011.
- [164] R. M. Ehrenreich, E. Hamilton, and S. K. Nash. Far from barbaric: re-assessing the sophistication of merovingian metalworking. *JOM: The Journal of The Minerals, Metals & Materials Society*, 57:51–55, 2005.
- [165] J. Alkemper and P. W. Voorhees. Quantitative serial sectioning analysis. *Journal of Microscopy*, 201:388–394, 2001.
- [166] M. A. Groeber, B. K. Haley, M. D. Uchic, D. M. Dimiduk, and S. Ghosh. 3D reconstruction and characterization of polycrystalline microstructure using a FIB-SEM system. *Materials Characterization*, 57:259–273, 2006.
- [167] L. Margulies, G. Winther, and H. F. Poulsen. In situ measurement of grain rotation during deformation of polycrystals. *Science*, 291:2392–2394, 2001.
- [168] S. F. Li, J. Lind, C. M. Hefferan, R. Pokharel, U. Lienert, A. D. Rollet, and R. M. Suter. Threedimensional plastic response in polycrystalline copper via near-field high-energy diffraction microscopy. *Journal of applied crystallography*, 45:1098–1108, 2012.
- [169] W. Yang, B.C. Larson, J.Z. Tischler, G.E. Ice, J.D. Budai, and W. Liu. Differential-aperture x-ray structural microscopy: a submicron-resolution three-dimensional probe of local microstructure and strain. *Micron*, 35:431 – 439, 2004.
- [170] P. Reischig, A. King, L. Nervo, N. Vigano, Y. Guilhem, W.-J. Palenstijn, K.-J. Batenburg, M. Preuss, and W. Ludwig. Advances in X-ray diffraction contrast tomography: flexibility in the setup geometry and application to multiphase materials. *Journal of applied crystallography*, 46:297–311, 2013.
- [171] A. King, P. Reischig, J. Adrien, and W. Ludwig. First laboratory x-ray diffraction contrast tomography for grain mapping of polycrystals. *Journal of applied crystallography*, 46:1734–1740, 2013.

-
- [172] B. Schillinger, E. Lehmann, and P. Vontobel. 3d neutron computed tomography: requirements and applications. *Physica B*, 276-278:59–62, 2000.
- [173] W. Ludwig, A. King, P. Reischig, M. Herbig, E.M. Lauridsen, S. Schmidt, H. Proudhon, S. Forest, P. Cloetens, S. Rolland du Roscoat, J.Y. Buffière, T.J. Marrow, and H.F. Poulsen. New opportunities for 3d materials science of polycrystalline materials at the micrometre lengthscale by combined use of x-ray diffraction and x-ray imaging. *Materials Science and Engineering: A*, 524(1-2):69 – 76, 2009. Special Topic Section: Probing strains and Dislocation Gradients with diffraction.
- [174] M. Syha, A. Trenkle, B. Lödermann, A. Graff, W. Ludwig, D. Weynand, and P. Gumbsch. Validation of three-dimensional diffraction contrast tomography reconstructions by means of electron backscatter diffraction characterization. *Journal of Applied Crystallography*, 46(4):1145–1150, Aug 2013.
- [175] M. Burger, G. Gilboa, S. Osher, and J. Xu. Nonlinear inverse scale space methods. *Comm. Math. Sci.*, 4:179–212, 2006.
- [176] J. M. Gregoire, D. Dale, and R. B. van Dover. A wavelet transform algorithm for peak detection and application to powder x-ray diffraction data. *Review of scientific instruments*, 82:015105, 2011.
- [177] <http://sourceforge.net/projects/fable>.
- [178] L. Brabant, E. Pauwels, M. Dierick, D. Van Loo, M.A. Boone, and L. Van Hoorebeke. A novel beam hardening correction method requiring no prior knowledge, incorporated in an iterative reconstruction algorithm. *NDT & E International*, 51:68 – 73, 2012.

Index

- Absorption, 22
- Absorption Range, 69, 77
- Algebraic Reconstruction, 12, 101, 117, 126
- Aperture, 15
- Attenuation coefficient, 10

- Beam Hardening, 66
- Black Body Correction, 67
- Bragg Cut-off, 34, 38, 42, 68, 80
- Bragg Edge, 33, 38
- Bragg Peaks, 83, 85
- Bragg's Law, 31, 54, 105

- Collimator, 48, 67
- Cross Section, 8, 10, 137
 - coherent, 27, 28, 32, 33
 - coherent elastic, 84
 - elastic, 34
 - elastic coherent, 35
 - elastic incoherent, 37
 - incoherent, 27, 28
 - inelastic, 34
 - inelastic coherent, 37
 - inelastic incoherent, 37
 - macroscopic, 22
 - microscopic, 22, 70, 75
- Crystal, 29, 39
- Crystal Orientation, 87
- Crystallite, 89, 92, 101, 126
- Cupping Artifacts, 71, 80, 81

- Dark Current, 8
- Debye Temperature, 35
- Debye-Scherrer cone, 33
- Debye-Waller factor, 35

- Dendrite, 113
- Diffraction, 31
 - Imaging, 106
 - Tomography, 106
- Double Crystal Monochromator, 52
- Double Detector Set-up, 107

- Ewald construct, 31

- Filter, 42, 52
- Filtered Back Projection, 12
- Fission, 3
- Flight Tube, 16
- Friedel Pair, 117, 122, 126

- Imaging Plate, 17

- L/D, 15, 16
- Lambert-Beer law, 8, 20
- Laue pattern, 110

- Microchannel Plate, 19, 42, 67
- Miller indices, 30
- Moderator, 3, 42
- Monochromaticity, 43, 47, 125
- Monochromator, 41
- Monte Carlo simulation, 68
- Mosaicity, 87, 95, 129

- $(+n, -n)$ configuration, 52
- nDCT, 121
- Neutron
 - cold, 6, 32, 123
 - thermal, 3, 6, 42

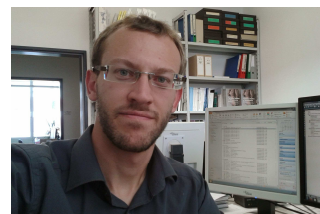
- Oligocrystals, 83

Index

- Open Beam, 8
- Orientation, 95, 106, 112
- Phonons, 35
- Polycrystal, 33
- Reactor, 3, 42
- Reflectivity, 95, 116, 119
- Resonance, 23
- Scattering, 24
 - amplitude, 25
 - coherent elastic, 68, 116
 - contributions, 65
 - length, 25
- Scintillator, 18
- Segmentation, 89, 116
- Similarity, 86
- Spallation, 5, 42
- Structure factor, 31
- Terminology, 132
- TESI, 56
- Texture, 34, 38, 68
- Time of Flight, 41, 42
- Tomography, 11
 - diffraction contrast, 115
 - Quantitative, 71
- Topography, 106
- Transmission, 8
- Turbine blade, 109
- Unit Cell, 29
- Velocity Selector
 - mechanical neutron, 43, 45, 56
- Wave vector, 21
- X-ray, 10

Steven Peetermans

Wallweg 5, 5210 Windisch, Switzerland
stevenpeetermans@gmail.com, +41 767 08 03 99



Education

Paul Scherrer Institut, Switzerland (Swiss nuclear science institute)

01.2011-12.2014 (*expected*): PhD on energy-selective neutron imaging. Enrolled in the department of materials science of the EPFL university, Switzerland.

Ghent University, Belgium

09.2008-07.2010: Master of Engineering Physics (major: nuclear engineering)
Graduated *summa cum laude*

Thesis title: *Windowless spallation target – proton beam interaction study in the MYRRHA reactor*, graded 19/20

09.2005-07.2008: Bachelor of Engineering Physics
Graduated *magna cum laude*

Awards & Certificates

11.2011. MCNP/MCNPX intermediate workshop

08.2011. Handling of radioactive sources (Swiss ministry of health)

12.2010. SCK•CEN (Belgian nuclear science institute) best master thesis award

Experience

Paul Scherrer Institut (Swiss nuclear science institute), Switzerland

01.2011-12.2014 (*expected*). PhD on energy-selective neutron imaging. Experienced with work at a neutron imaging beamline in all its facets: different imaging techniques, research and user support. Aside from building up the energy-selective imaging expertise in our group, I also developed the new method of diffraction contrast neutron imaging and designed the required set-up.

Centre for X-ray tomography of the Ghent University (UGCT), Belgium

09.2010-12.2010. Responsible for running EGS Monte Carlo simulations of the source target heads.

Paul Scherrer Institut (Swiss nuclear science institute), Switzerland

07.2010-09.2010. Summer internship during which I characterised the neutron grating interferometer set-up for differential phase contrast and dark-field imaging with neutrons. Outside the scope of the internship, I also checked the applicability of the grating-based synchrotron imaging reverse projection method.

Nuclear Physics Institute of the Academy of Science of the Czech Republic

07.2009-08.2009. Summer internship at the Czech nuclear physics institute, working on neutron activation analysis and the calibration of the germanium detector with various radioactive gamma sources.

PrimeLaserTech (industry), Greece

07.2008-08.2009. Summer internship at a spin-off company that uses lasers to weld solar boiler panels. Working in a team of local labourers, I gained hands-on workplace experience.

Skills

Languages

Dutch: mother tongue

English: excellent

German: very good

French: good

Russian: very basic

IT

General: Windows and Linux (ubuntu), Microsoft Office, Latex

CT Reconstruction: Octopus (commercial), MuhRec (PSI in-house), ASTRA (open-source)

Simulation: Matlab, McStas (good), EGS (good), MCNPX (basic)

Visualization: VGStudio, Paraview

Programming: Matlab, Labview, Java, JavaScript, Fortran95

Teaching & Coaching

09.2014. Professional bachelor student project 'PolyTom' for parallel instead of sequential neutron tomography of elongated samples.

06.2014. SISN Summer school 2014 on small angle neutron scattering and imaging: lectures and exercises on energy-selective neutron imaging and diffraction neutron imaging.

Conferences

10.2014. WCNR 10 (Switzerland), **[Organizing committee member]**

06.2014. NEUWAVE 6 (Germany), Analyzing crystalline structures by means of neutron imaging at pulsed and continuous neutron sources. [oral]

09.2013. Euromat (Spain), Energy-selective neutron imaging for materials science: bridging transmission and diffraction. **[keynote]**

07.2013. ICTMS 1 (Belgium), Attenuation, dark-field and diffraction neutron imaging of crystalline material [talk]

04.2013. NEUWAVE 5 (Sweden), (Energy-selective) neutron imaging in transmission and diffraction mode. [talk]

11.2012. ESS Science Symposium (Czech Republic), Neutron imaging for materials research. [talk]

06.2012. ITMNR 7 (Canada), A double detector set-up for neutron imaging [talk], Monochromators characterizations for energy-selective neutron imaging.[poster]

10.2011. NEUWAVE 4 (USA), A new monochromator for energy-selective neutron imaging [talk], Archaeometallurgical studies at ICON. [talk]

09.2011. Euromat (France), Energy-selective neutron imaging. [talk]

Publications

First author

Peetermans, S.; King, A.; Ludwig, W.; Reischig, P. & Lehmann, E. Cold neutron diffraction contrast tomography of polycrystalline material, *Analyst*, **2014**, 139, 5765-5771.

Peetermans, S.; Tamaki, M.; Hartmann, S.; Kaestner, A.; Morgano, M. & Lehmann, E. H. A new transmission based monochromator for energy-selective neutron imaging at the ICON beamline, *Nuclear Instruments and Methods, section A*, **2014**, 757, 28-32

Peetermans, S. & Lehmann, E. H. Simultaneous neutron transmission and diffraction contrast tomography as a non-destructive 3D method for bulk single crystal quality investigations. *Journal of Applied Physics*, **2013**, 114, 124905

Peetermans, S.; Grazi, F.; Salvemini, F.; Lehmann, E. H.; Caporali, S. & Pratesi, G. Energy-selective neutron imaging for morphological and phase analysis of iron-nickel meteorites. *Analyst*, **2013**, 138, 5303-5308

Peetermans, S. & Lehmann, E. H. A double detector set-up for simultaneous transmission and diffraction neutron imaging. *Physics Procedia*, **2013**, 43, 179-185

Peetermans, S.; Grazzi, F.; Salvemini, F. & Lehmann, E. H. Spectral characterization of a velocity selector type monochromator for energy-selective neutron imaging. *Physics Procedia*, **2013**, 43, 121-127

Peetermans, S.; van Langh, R.; Lehmann, E. & Pappot, A. Quantification of the material composition of historical copper alloys by means of neutron transmission measurements. *J. Anal. At. Spectrom.*, **2012**, 27, 1674

Co-author

King, A.; Reischig, P.; Adrien, J.; Peetermans, S. & Ludwig, W. *Polychromatic diffraction contrast tomography*, Materials Characterization, **2014**, 97, 1-10

Morgano, M.; Peetermans, S.; Lehmann, E.; Panzner, T. & Filges, U. Neutron imaging options at the BOA beamline at Paul Scherrer Institut, *Nuclear Instruments and Methods, section A*, **2014**, 754, 46-56

Mannes, D.; Lehmann, E.; Masalles, A.; Schmidt-Ott, K.; Przychowski, A.; Schaeppi, K.; Schmid, F.; Peetermans, S. & Hunger, K. The study of cultural heritage relevant objects by means of neutron imaging techniques *Insight - Non-Destructive Testing and Condition Monitoring, British Institute of Non-Destructive Testing (BINDT)*, **2014**, 56, 137-141

Lehmann, E. H.; Kaestner, A.; Grünzweig, C.; Mannes, D.; Vontobel, P. & Peetermans, S. Materials research and non-destructive testing using neutron tomography methods, *International journal of materials research*, **2014**, 105, 664-670

Lehmann, E.; Peetermans, S.; Josic, L.; Leber, H. & van Swygenhoven, H. Energy-selective neutron imaging with high spatial resolution and its impact on the study of crystalline-structured materials. *Nuclear Instruments and Methods in Physics Research Section A: Accelerators, Spectrometers, Detectors and Associated Equipment*, **2014**, 735, 102-109

Grünzweig, C.; Mannes, D.; Kaestner, A.; Schmid, F.; Vontobel, P.; Hovind, J.; Hartmann, S.; Peetermans, S. & Lehmann, E. Progress in Industrial Applications using Modern Neutron Imaging Techniques. *Physics Procedia*, **2013**, 43, 231-242

Cnudde, V.; De Boever, W.; Dewanckele, J.; De Kock, T.; Boone, M.; Boone, N.; Silversmit, G.; Vincze, L.; Van Rans, E.; Derluyn, H.; Peetermans, S.; Hovind, J.; Modregger, P.; Stampanoni, M.; De Buysser, K. & De Schutter, G. Multi-disciplinary characterization and monitoring of sandstone (Kandla Grey) under different external conditions. *Quarterly Journal of engineering geology and hydrogeology*, **2013**, 46, 95-106

Salvemini, F.; Grazzi, F.; Peetermans, S.; Civita, F.; Franci, R.; Hartmann, S.; Lehmann, E. & Zoppi, M. Quantitative characterization of Japanese ancient swords through energy-resolved neutron imaging. *Journal of Analytical Atomic Spectroscopy*, **2012**, 27, 1494-1501

Boone, M.; Vlassenbroeck, J.; Peetermans, S.; Van Loo, D.; Dierick, M. & Van Hoorebeke, L. Secondary radiation in transmission-type X-ray tubes: Simulation, practical issues and solution in the context of X-ray microtomography. *Nuclear Instruments and Methods in Physics Research, Section A*, **2012**, 661, 7-12

